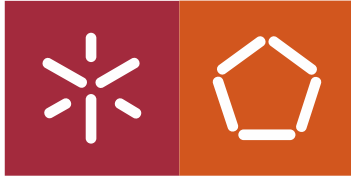**Universidade do Minho**
Escola de Engenharia

Ana Mafalda Meneses Costa

Multi-Functional Multi-Material Structures for Orthopedic Implants using Laser-Assisted Strategies

dezembro de 2021

Universidade do Minho
Escola de Engenharia

Ana Mafalda Meneses Costa

Multi-Functional Multi-Material Structures for Orthopedic Implants using Laser-Assisted Strategies

ACKNOWLEDGMENTS

Firstly, I would like to thank my supervisor Professor Georgina Miranda for the tireless work and dedication. Your shared knowledge, support, guidance, and all-time presence during these years were crucial for the success of this PhD thesis. Thank you for the opportunity.

To my co-supervisor Professor Filipe Samuel Silva whose enthusiasm, expertise and knowledge was essential to achieve this thesis. Thank you for the opportunity and I hope I have done what has never been done before.

I would like to express my gratitude to Dr. Flávio Bartolomeu for the endless support, friendship, and availability whenever I needed. To Dr. Óscar Carvalho, thank you for your enthusiasm and for always having a solution for my problems. To all members of the Microfabrication and Integrated Systems Laboratory for the team-spirit, shared knowledge, and encouragement. Thank you all for your friendship and for the fun we have had in these years. It was an absolute pleasure to meet you and to have you in this journey. A special thanks to Telma Dantas for being the roommate and friend I needed during these years.

To all people from other laboratories and institutions that in one way or another helped me developed this work, thank you.

Thank you to all my friends, especially to Sofia, for listening and always being present.

A special thanks to Francisco for your love and belief in me. Thank you for your patience, for cheering me up in my worst moments and for the words of encouragement throughout these years and every single day.

I would like to express my deeply gratitude to family, especially to my mother and father for the unconditional love and support. Thank you for being the best parents I could ever asked for, for always caring and doing everything to give me the best education possible. A special thanks to my sister Joana for being endless with me. Thank you for always giving me the right words, for constantly being supportive to pursue my dreams and for being an inspiration for me.

Statement of Integrity

I hereby declare having conducted this academic work with integrity. I confirm that I have not used plagiarism or any form of undue use of information or falsification of results along the process leading to its elaboration.

I further declare that I have fully acknowledged the Code of Ethical Conduct of the University of Minho.

University of Minho, 28 /12 /2021

_____

Ana Mafalda Meneses Costa

Resumo

Estruturas Multi-Material Multi-Funcionais para Implantes Ortopédicos utilizando Estratégias Assistidas a Laser

A artoplastia Total da Anca (ATA) é um procedimento largamente utilizado, que consiste na remoção e substituição da cabeça femoral e do acetábulo por uma prótese. Esta cirurgia pretende proporcionar ao paciente uma solução que restaure a funcionalidade da anca e a mobilidade sem dor. Nos últimos anos, o aumento do número de ATAs e cirurgias de revisão impulsionou a investigação de novas abordagens relativas ao design destas próteses. De todas as complicações que podem ocorrer após implantação, a principal causa de cirurgias de revisão está relacionada com a perda de fixação entre a prótese e o tecido ósseo circundante. A fraca adesão e osseointegração ao implante, a baixa resistência ao desgaste e a diferença entre os módulos de Young de implante e osso são as principais razões que levam à necessidade de recorrer a cirurgias de revisão.

Idealmente, um implante deve exibir biocompatibilidade de modo a não causar reações adversas ao organismo; bioatividade para induzir uma resposta biológica para promover formação, proliferação e integração óssea e, ao mesmo tempo, exibir propriedades mecânicas adequadas, i.e., ter um módulo de elasticidade adequado ao osso e resistência à corrosão e desgaste *in vivo*.

Neste sentido, esta tese de doutoramento foca-se no desenvolvimento de estruturas multi-funcionais multi-material com o intuito de superar os problemas acima referidos e assim aumentar a vida útil do implante. Para tal, estratégias de manufatura assistida por laser, nomeadamente ablação e fusão seletiva a laser, foram utilizadas para produzir soluções mono- e multi-material com multi-funcionalidade visando implantes de anca. Deste modo, foram produzidas soluções mono-material Ti6Al4V and NiTi, incluindo componentes estruturados ou superficialmente texturizados nos quais ainda foram incorporados novos materiais (fosfatos de cálcio ou PEEK). Esta abordagem visa adicionar novas funções a estes implantes ao introduzir conceitos como a bioatividade aliados a um desempenho mecânico e tribológico adequados. Estas soluções foram caracterizadas quanto ao seu desempenho bio-tribológico e interação biológica, demonstrando uma combinação de propriedades adequada para criar uma solução efetiva a longo prazo, de acordo com especificações locais.

Palavras-Chave: Fusão Seletiva a Laser, Texturização Laser, Prensagem Uniaxial a Quente, Prensagem e Sinterização, NiTi, Ti6Al4V, Fosfatos de Cálcio, PEEK, Implantes de Anca, Multi-Material

ABSTRACT

Multi-Functional Multi-Material Structures for Orthopedic Implants using Laser-Assisted Strategies

Total hip arthroplasty (THA) is a widespread procedure in which the diseased femoral head and acetabulum are removed and replaced by a prosthesis. This surgery aims to restore hip functionality and provide pain-free mobility to the patient. In the last few years, the increase in the number of THA and revision surgeries boosted the research on new approaches to this prosthesis design. Among all complications that can occur after implantation, the loss of fixation between implant and surrounding bone tissue is the one that causes the highest number of revision surgeries. Poor bone-to-implant bond and osseointegration, poor wear resistance and a Young's modulus (YM) mismatch between implant and bone are the main reasons that lead to revision surgeries.

Ideally, an implant should have biocompatibility and not cause any undesired reactions to the body; hold bioactivity to induce a biological response for bone formation, proliferation and integration with the implant, while displaying suitable mechanical properties, i.e., presenting a tailored elastic modulus to bone and corrosion and wear resistance *in vivo*.

In this sense, this PhD thesis is focused on the development of multi-functional multi-material structures to overcome all the abovementioned issues and increase hip implant lifetime. For that purpose, laser-assisted manufacturing strategies, namely Laser ablation and Selective Laser Melting were used to manufacture mono- and multi-material solutions with multi-functionality targeting hip implants. In this sense, mono-material Ti6Al4V and NiTi solutions, including structured or surface textured components were produced, in which new materials were further incorporated (calcium phosphates and PEEK). This approach aims to add new functions to these implants by introducing concepts like bioactivity allied to suitable mechanical and wear performance. These solutions were characterized bio-tribologically and biologically showing a suitable combination of properties to create a long-term and effective solution according to local requirements.

Keywords: Selective Laser Melting, Laser Surface Texturing, Hot Pressing, Press and Sintering, NiTi, Ti6Al4V, Calcium Phosphates, PEEK, Hip Implants, Multi-Material

CONTENTS

LIST OF SYMBOLS, ANNOTATIONS AND ABBREVIATIONS

A_f	Austenite-Finish Temperature
Al_2O_3	Alumina
ALP	Alkaline Phosphatase
AM	Additive Manufacturing
AR	Alizarin Red
A_s	Austenite-Start Temperature
ASTM	American Society for Testing and Materials
At. %	Atomic Percentage
ATA	Artoplastia Total da Anca
ATP	Adenosine Triphosphate
BCC	Body Centered Cubic
BMP-2	Bone Morphogenic Protein 2
CAD	Computer Aided Design
CaP	Calcium Phosphates
CoCr	Cobalt Chromium
COF	Coefficient of Friction
CW	Continuous Wave
DAA	Direct Anterior Approach
DED	Direct Energy Deposition
DGAV	Direção Geral de Alimentação e Veterinária
DLA	Direct Lateral Approach
DMEM	Dulbecco's Modified Eagle's Culture Medium
E_a	Energy absorption
EBM	Electron Beam Melting
ECM	Extracellular Matrix
EDS	Energy Dispersive X-Ray Spectroscopy
EIGA	Electrode Induction Melting Gas Atomization
EIGA	Electrode Induction-Melting Gas Atomization Technique
FBS	Fetal Bovine Serum
F_{max}	Maximum Push-Out Force

FOF	Flat-On-Flat
GT	Greater Trochanter
HAp	Hydroxyapatite
HCP	Hexagonal Closed Packed
hMSCs	Human Mesenchymal Stem Cells
HP	Hot Pressing
I	Implantation
J_{corr}	Corrosion Current Density
J_{pass}	Passivation Current Density
LASER	Light Amplification by Simulated Emission of Radiation
LDN	Low-dimensional Nanomaterials
LENS	Laser Engineered Net Shaping
LST	Laser Surface Texturing
MEM	Minimum Essential Culture Medium
M_f	Martensite-Finish Temperature
MOM	Metal-on-Metal
M_s	Martensite-Start Temperature
NiTi	Nickel-Titanium
Nitinol	Nickel-Titanium Naval Ordnance Laboratory
OA	Osteoarthritis
OCP	Open Circuit Potential
PA	Posterior Approach
PBF	Powder Bed Fusion
PBS	Phosphate-Buffered Saline
PCL	Polycaprolactone
PEEK	Poly-ether-ether-ketone
PFA	Paraformaldehyde
PM	Powder Metallurgy
PMMA	Polymethylmethacrylate
PS	Press and Sintering
RT	Room Temperature
SE	Superelasticity

SEM	Scanning Electron Microscopy
Sf	Static Final
Si	Static Initial
SLA	Sandblast-Acid Etching
SLM	Selective Laser Melting
SMA	Shape Memory Alloy
SME	Shape Memory Effect
SoFCOT	Société Française de Chirurgie Orthopédique et Traumatologique
SS	Stainless Steel
THA	Total Hip Arthroplasty
Ti	Titanium
Ti64	Ti6Al4V (Titanium-6Aluminum-6Vanadium)
TiH$_2$	Titanium Hydride
Tp	Tribological Performance
TTs	Transformation Temperatures
UV	Ultraviolet
wt. %	Weight Percentage
XRD	X-Ray Diffraction
YM	Young's Modulus
ZrO$_2$	Zirconia
αMEM	Alpha Minimum Essential Medium
βTCP	β Tricalcium Phosphate
ϕ_{corr}	Corrosion Potential

FIGURES

Chapter 3:

Chapter 4:

Chapter 5:

Chapter 6:

Chapter 7:

Chapter 8:

Chapter 9:

TABLES

CHAPTER 1

INTRODUCTION

The following chapter aims to highlight the purpose of this PhD project, by presenting a motivation subchapter that enlightens the most important issues that are further discussed in the ensuing chapters, followed by a list of objectives of this PhD project and finally an outline presenting the structure of this thesis.

1.1. Motivation

Total hip arthroplasty is one of the most performed surgeries, worldwide, aiming to restore joint functionality and pain-free mobility to patients, mainly suffering from osteoarthritis. Nevertheless, the decreasing age of patients performing these surgeries and the increase on life expectancy, demand an improved effort to assure a successful implantation and reduction on the need for revision surgeries.

Nowadays, guaranteeing a long-term success of the implant is extremely difficult due to all the problems arising with the current dense solutions. Loss of fixation within the first years of implantation is the major reported reason that leads to revision surgeries (that present more risks to patients and are usually more expensive).

Ti6Al4V is an extremely attractive material for such applications due to its suitable mechanical properties and biocompatibility, but its use for dense implants is associated with the loss of fixation, related to a poor bone to implant bond and osseointegration, elastic modulus mismatch (causing a reduction on the transferred stress to the bone), the poor wear resistance of this alloy and a non-uniform contact pressure between implant and bone.

This PhD thesis aim was to develop new solutions that take advantage of different materials and strategies to obtain multi-functional multi-material components that may overcome the current mentioned issues. In this sense, this project makes use of laser assisted techniques to create different designs for different purposes, as these assure a high design freedom for complex designs, conversely to conventional techniques. In this sense, Selective Laser Melting was used to produce complex components (cellular structures) that will fit more properly bone requirements in terms of elastic properties and improved mechanical interlocking (through bone ingrowth), while Laser Surface Texturing was used to enhance bone to implant bonding by altering surface design. Combined with other processing techniques, it was possible to introduce other materials into these components and thus create multi-material solutions that gathers and take advantage of several properties that a material alone would not be able to provide.

Thus, this PhD presents a range of potential solutions that can be integrated into a multi-functional implant with local specific properties.

1.2. Objectives

In accordance with what was stated in the Motivation Section, the main goal of this PhD thesis is to develop multi-functional multi-material solutions that aims to overcome the current implant limitations. For that purpose, it is necessary to assure and fulfill the following specific objectives:

Objective 1. Enhance bone to implant bond and osseointegration process

1.1. Design and manufacture Ti6Al4V and NiTi laser textured or cellular structured implants to promote a tailored elastic modulus and/or mechanical interlocking;

1.2. Introduce bioactivity without compromising these solutions overall integrity;

Objective 2. Improve the bio-tribological response of the multi-material structures

2.1. Design and manufacturing of mono- and multi-material structures (Ti6Al4V, NiTi and PEEK) to improve bio-tribological performance

1.3. Structure of the Thesis

This PhD thesis is organized as a compilation of research papers, that are published, accepted or submitted in international ISI journals. Before this sequence of research papers, the thesis also includes Chapter 1 and Chapter 2. In the first chapter, entitled Introduction, it is possible to find the motivation, the objectives and the structure of the thesis (present topic). The second chapter "State of the Art" presents a literature review regarding the main topics addressed in this thesis. In this sense, to contextualize the different readers from different backgrounds to aspects that are going to be discussed in the remaining chapters, in order to achieve a common level of knowledge about the topic, chapter 2 collects concepts about human skeletal system; hip joint and its diseases; total hip arthroplasty and the current adverse problems; biocompatible materials (bioinert and bioactive): advantages and drawbacks; powder metallurgy techniques: press and sintering and hot pressing; selective laser melting; and finally, laser surface modification.

The following chapters, from Chapter 3 to Chapter 9, as mentioned, are research papers that constitute all the work developed throughout this PhD project, being equally divided in the subsequent subchapters: Abstract, Introduction, Experimental details, Results and discussion, Conclusions, Acknowledgments and References.

Chapter 3 addresses the influence of multi-material βTCP-Ti6Al4V cellular structures design on physical and chemical aspects correlated with cellular response. Roughness, wettability, βTCP quantity and pH during cell culture were addressed and correlated with cellular response. This research paper is published in Materials Science & Engineering C, 2019, 98:705-716 (an Elsevier Journal with an impact factor of 7.328, Quartile 1).

Chapter 4 reports the corrosion behavior of multi-material Ti6Al4V-βTCP and Ti6Al4V-PEEK cellular structures. The effect of porosity and the incorporation of different materials inside the open cells were assessed and compared with bulk Ti6Al4V SLM samples. This research paper is published in Transactions of Nonferrous Metals Society of China, 2019, 29:2523-2533 (an Elsevier Journal with an impact factor of 2.917, Quartile 1).

Chapter 5 evaluates the tribological performance of Ti6Al4V-βTCP and hydroxyapatite-impregnated multi-material cellular structures by performing flat-on-flat reciprocating sliding tests against an alumina plate. This research paper is published in the Journal Mechanical Behavior of Biomedical Materials, 2019, 94:193-200 (an Elsevier Journal with an impact factor of 3.902, Quartile 1).

Chapter 6 investigates the tribological behavior of NiTi mono-material and NiTi-PEEK multi-material cellular structures. The specimens were tribological characterized in a ball-on-flat reciprocating sliding tests and the influence on different open-cell sizes, wall thicknesses and PEEK addition were evaluated. This research paper is published in Tribology International, 2021, 156:106830 (an Elsevier Journal with an impact factor of 4.872, Quartile 1).

Chapter 7 assesses the performance NiTi laser textured implants *in vivo* by implanting them in Sprague Dawley rats. Two different laser textured implants were manufactured and compared with bulk implants to assess their bonding and osseointegration behavior *in vivo*. Push-out tests and histological characterization were performed after 4 weeks and 12 weeks of implantation. This research paper is published in the Journal of Materials Science & Technology (an Elsevier Journal with an impact factor of 8.067, Quartile 1).

Chapter 8 evaluates *in vivo* performance of laser textured mono-material Ti6Al4V and multi-material Ti6Al4V- βTCP implants and compared them with non-textured implants. Similar to Chapter 7, this work evaluates the performance of the produced implants by implanting them *in vivo* in Sprague Dawley rats for 4- and 12-weeks being bone-implant bonding and osseointegration

assess in terms of push-out and histological characterization. This research paper is published in Advanced Materials Technologies (a Wiley Journal with an impact factor of 7.848, Quartile 1).

Chapter 9 deals with the manufacture of different mono- and multi-material NiTi and Ti6Al4V cellular structures and its characterization *in vitro* and bio-tribologically. NiTi mono- and Ti6Al4V mono-material structures were manufacture by selective laser melting and impregnated with βTCP or PEEK being characterized *in vitro* in terms of cell cytotoxicity, adhesion, differentiation and mineralization, under dynamic conditions. Its bio-tribological performance against bone femur was also assessed. This research paper is submitted in Applied Materials Today (an Elsevier Journal with an impact factor of 10.041, Quartile 1).

Finally, Chapter 10 presents the main conclusions that can be drawn from this PhD project, pointing suggestions for future works, and ending with further contributions to this thesis.

CHAPTER 2

STATE OF THE ART

This chapter presents a literature review on a series of concepts that are key to the subject of this PhD project. Accordingly, this chapter gathers information regarding human skeletal systems, narrowing the topic to bone femur and hip joint. Diseases commonly related to this joint, Total Hip Arthroplasty surgeries and its drawbacks are also addressed in this chapter. It is also introduced concepts like osseointegration, biocompatibility, bioinertness and bioactivity while discussing materials commonly used in implantology and new substitutes, showing their advantages and disadvantages and outlining a possible solution to overcome these drawbacks. Furthermore, Powder Metallurgy and Laser-Assisted Techniques like Selective Laser Melting and Laser Surface Modification are also adressed.

2.1. Human Skeletal System

The human skeletal system is composed of cartilage and bone, with cartilage promoting soft tissue support and providing a smooth surface for bone joints, while bone major functions are to support body against gravity, protect vital organs, playing a crucial role during body locomotion [1–6]. In addition, bone is also responsible for the production of blood cells, energy storage, being calcium and phosphorus reservoirs, which is extremely important in homeostasis process, nerve conduction, muscle contraction, etc [1,4–6].

Bone, a highly vascular and innervated tissue, has a hierarchical organization ranging from macro to nanoscopic level, as shown in Figure 2.1. At a macroscopic level, this calcified, connective, living tissue is divided into cortical and trabecular bone where the former represents 80% of the total weight of the human skeletal whereas the latter embodies 80% of bone surface area [2,4]. Cortical bone, also called compact bone, is denser, harder and more rigid than trabecular bone (spongy or cancellous), representing an outer shell surrounding the trabecular bone and has a function of stabilization and support [1,3–7]. Conversely, trabecular bone provides a suitable environment for tissue metabolism, containing within the bone marrow that in turn contain blood-forming cells [1,3,6,7]. On a microscopic level, cortical bone consists of osteons that are circular group of parallel mineralized collagen fibers (lamellae) that display Haversian canals, containing blood vessels, lymphatics and nerves, while trabecular bone is an interconnected framework of rod-like trabeculae constructs [3,6,8]. Lastly, at the nanostructural level, bone is divided in an organic and an inorganic (mineral) phase. The organic phase is mainly composed of type-I collagen and provides toughness to the bone, while the inorganic phase, which contains hydroxyapatite (HAp), $Ca_{10}(PO_4)_6(OH)_2$ nanocrystals is responsible for bone stiffness and tensile strength [2,3,6,8].
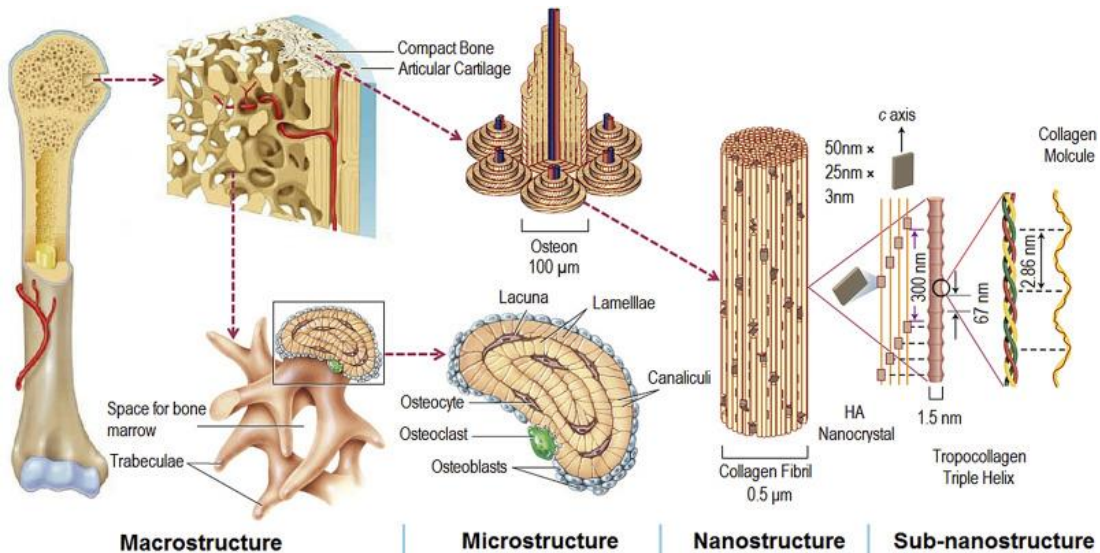
Figure 2.1 - Bone hierarchical structural organization at different scales. (reproduced from [7]).

Bone classification can be divided in long bones (tubular, e.g. femur, tibia), short (cuboidal, e.g. ankle, tarsus), flat (e.g. skull), irregular (e.g. face bones) and sesamoid bones (develop in tendons) [1]. For the interest of the present thesis, the morphology of the long bones, more specifically femur is defined. The femur, Figure 2.2(A), is the longest bone in the body and is constituted, as all long bones, by a cylindrical shaft called diaphysis (mainly composed by cortical bone) and two spherical ends named epiphysis (mainly characterized by trabecular bone and thin layer of surrounding cortical bone) [2,9,10]. The proximal epiphysis is, in turn, characterized by a head, neck and a greater and lesser trochanters [1,2,11]. In one hand, the latter are bone protrusions adhered to the muscles to impart motion to the hip, on the other, the spherical head at the end will interact with the acetabulum, a large cup-shape surface of the pelvic bone, forming the hip joint [1,2,10]. Attaching the femoral head with the shaft, there is a cylindrical structured called neck, projected with an inclination angle of around 125° [1,2].

The connection between bones that enable body motion and attach the human skeletal in a whole system, is termed joint, and can be divided in synovial and solid joints [1,11]. While on solid joints the bones are connected between them with a connective tissue, in synovial joints a cavity separates the bones from each other (Figure 2.2(B)). The bones are covered by a layer of cartilage (hyaline cartilage), not touching each other directly, displaying a joint capsule characterized by an outer and inner fibrous and synovial membrane, respectively. The fibrous membrane, a dense connective tissue, surrounds the joint and provides its stabilization, whereas the synovial membrane, a highly vascular membrane, is the responsible for synovial fluid production [1,12]. This fluid aims to provide a nourished and lubricated region inside the joint [1,11].
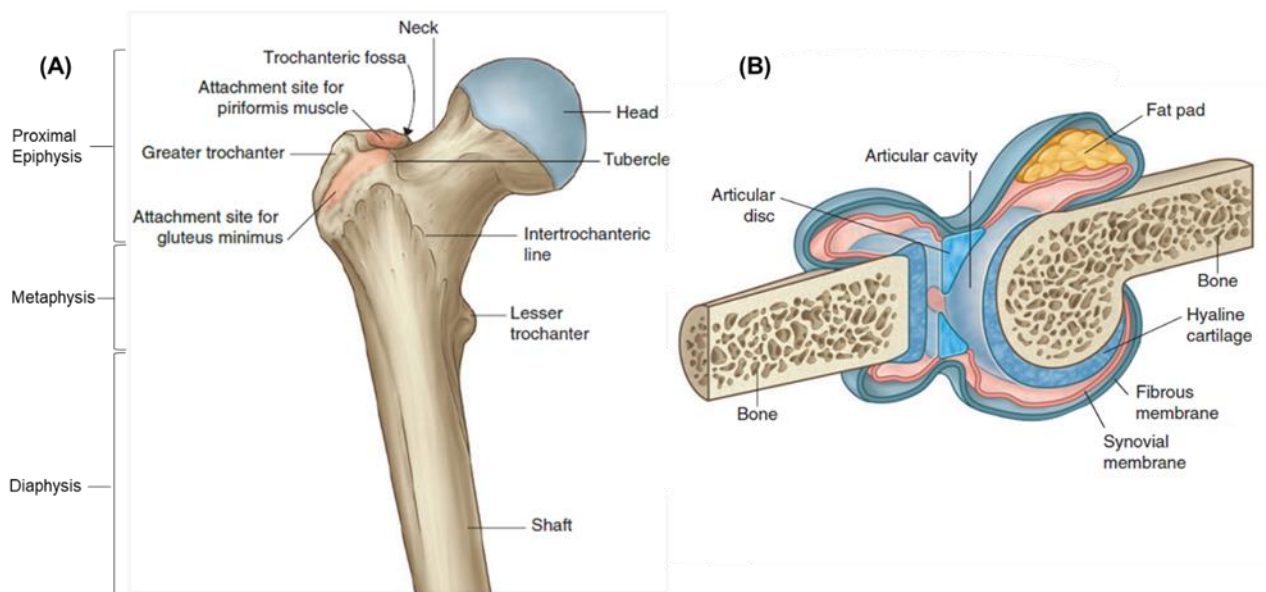
Figure 2.2 - Schematic representation of (A) Proximal end of the femur and (B) synovial joints (adapted from [1]).

2.2. Hip Joint

Hip joint is a synovial ball and socket joint, connecting the upper and lower limb, and is responsible for weight-bearing, promoting body stability and playing a crucial role in locomotion [1,10,13,14]. This ball and socket joint provides multiple planes of motion like flexion/extension, abduction/adduction, medial and lateral rotation and circumduction [1,9,13]. In this joint, the head of the femur acts as ball and the acetabular component of the pelvis as socket, having a ligament of the head of the femur connecting these two structures that are, in turn, as all synovial joints, covered by a synovial membrane [1]. Figure 2.3 displays a schematic representation of hip joint anatomy. As already mentioned, surrounding the joint surface there is a smooth tissue, called articular cartilage (hyaline cartilage), that is responsible for friction reduction and shock absorption during motion of the femoral head inside the acetabulum [10,11,15,16].

Articular cartilage is nourished by diffusion and, being an avascular tissue, it does not possess any blood vessels, lymphatics or nerves, which means that its ability for self-repair is limited [1,16,17]. In this sense, lesions in this tissue may lead to severe complications, once, when damaged, it makes the bone unprotected against normal wear and the joint will no longer function smoothly [11]. Moreover, when an inflammation on the surrounding tissues occur, the muscles around the joint start to weaken and the overall hip joint function may be compromised [11].
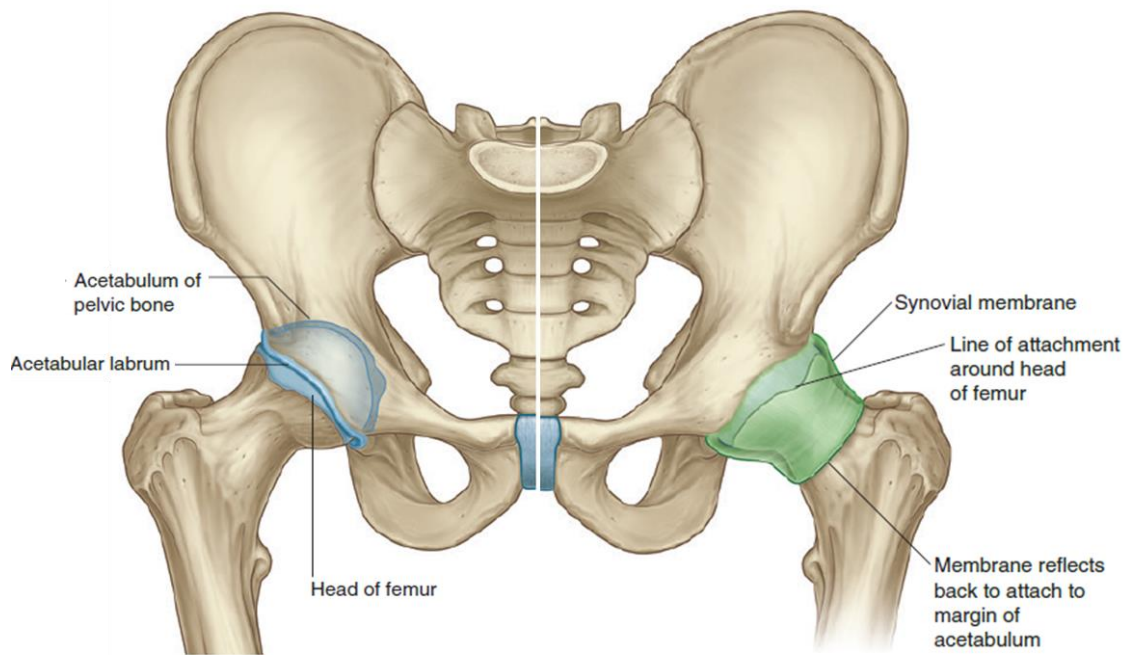
Figure 2.3 - Hip joint anatomy: left side represent articular surfaces and right side shows synovial membrane (adapted from [1]).

There are many pathologies that can affect the hip, such as osteoarthritis, rheumatoid arthritis, inflammation, osteolysis, post-traumatic arthritis, avascular necrosis, arthritis secondary to childhood disease, tumors, trauma, dysplasia, among others [4,11,13,15]. Among these different diseases, osteoarthritis (OA), besides being the most usual type of arthritis, it is also the most common to occur, leading patients to undergo total hip joint replacement [11,14,15,18,19]. OA is a degenerative joint disease in which the joint cartilage is progressively destroyed until its total breakdown and bones starts to wear out and deform, leading to severe pain and several limitations to the patients in terms of inability to walking, dressing, using the toilet, squatting, etc [12,14,15,18]. On the course of this disease, the water and proteoglycan content in the cartilage decreases, making it more fragile and mechanical disruption is more likely to occur, consequently crack the bone, the biomechanical forces of the joint will be compromised, leading to joint failure [1,17]. Figure 2.4 shows a schematic representation of a normal and osteoarthritic hip joint. Worldwide, 10% and 18% of men and women have OA symptoms, being this disease one of the ten most disabling pathologies in developed countries [20].

Many factors may be involved on osteoarthritis, such as ageing (the cartilage is less resilient), physical activity (sportsmen or patients with extremely frequent and heavy physical activity), hereditary, obesity, and it can be solved, in early stages, by moderate physical activity, weight loss,

therapy and medicine [18,21]. However, when these treatments are no longer enough for guaranteeing the patient's quality of life, hip joint replacement needs to be considered [21].
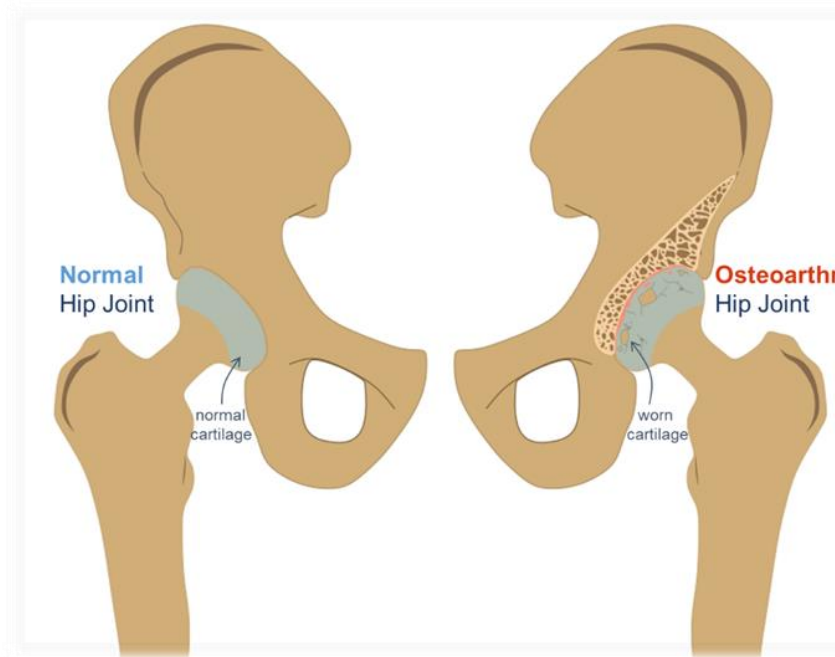
Figure 2.4 - Illustration of normal vs osteoarthritic hip joint.

2.3. Total Hip Arthroplasty

Total Hip Arthroplasty, THA, is a widespread procedure in which the acetabulum, head and proximal neck of the femur are removed and replaced by a prosthesis, to help patients suffering from diseases like osteoarthritis [9,14,18,19]. In fact, according to the 2020 SoFCOT (*Société Française de Chirurgie Orthopédique et Traumatologique*) Total Hip Arthroplasty Register [22], in France, 75.5% of the patients that performed total hip arthroplasties were due to osteoarthritis. In the same year, Swiss annual report registered 84.6% of patients with OA performing hip replacement while England, Wales Northern and the Isle of Man reported 91.5% of the cohort indicated for surgery having osteoarthritis, being the only indication in 88.4% for primary hip replacements [23,24]. The last published Italian report (2019) indicate that from all patients performing hip replacement, 61.1% were indicated to surgery due to OA [25]. International data reveal that, for instance, Australia and New Zealand 2020 reports, 88.5% and 89.2% of the patients that received hip replacement were diagnosed with OA, respectively [26,27] Actually, THA is one of the most successful surgical procedures, even called "the operation of the 20th century", once it improves the qualify of life of the patients by relieving them from pain within a short recovery period and providing hip-joint functionality [9,14,18,21,28].

The earliest recorded attempts for hip replacement were carried out in the year of 1890, in Germany, by Professor Themistocles Gluck in which he proposed an ivory ball and socket joint for femoral head replacement [9,18,21,29,30]. However, the surgery was not successful and it was found that failure occur due to chronic infection [18]. The following experiments were focused on using organic and inorganic substances like skin, *fascia lata*, silver, gold foil, rubber, celluloid and tanned pig bladder to separate joint surfaces [9,29]. Later on, in 1925, the surgeon Marius Smith-Petersen, in USA, developed a glass prosthesis (cup) to allow a smoother surface movement of the femoral head [13,29–31]. However, this material did not withstand the mechanical stresses of this joint and its failure was inevitable [29,30]. Smith-Petersen and Philip Wiles, in 1938, developed the first total hip replacement with a prosthesis made of stainless steel, to replace the femoral head and the acetabulum, but loosening of all prostheses occurred [18,29,30]. A decade later, in 1948, Judet brothers created, in France, an acrylic prosthesis, however, loosening also occurred due to wear debris release [9,15,30,31]. Dr. Austin Moore prosthesis, appeared in 1952, and was based on round head and an intramedullary long stem, a metal on metal (MoM) prosthesis made of a CoCr alloy, that is still used on present days for revision surgeries [13,18,30,31]. An improved design, that was later introduced by Mckee and Farrer, around 1958, was composed by MoM prosthesis also made of a CoCr alloy [9,15,18,29]. The MoM devices were later replaced by metal-on-polyethylene [13,30]. This new concept of a non metallic cup was introduced by Professor John Charnley, in which his design consisted in a femoral component made of stainless steel and a high molecular weight polyethylene acetabular part [9,13,15,18,30]. Charnley's design is currently one of the most commonly used for hip replacements [9,29].

According to the Scientific and Policy Report by the Joint Research Centre of the European Commission [18], the number of performed hip arthroplasties, per year, in the world is around one million, and this number is expected to increase due to the ageing of the population. According to their 2020 annual report [23], England, Wales, Northern Ireland and Isle of Man, from 2017 to 2019, the number of primary hip procedures were 281196, being 59.9% performed in females, in which the mean age at primary operation was 69 years. In 2019, Germany registered a total of 157681 primary arthroplasties, being the majority females (around 60%) while Norway reported a total of 9879 primary hip arthroplasties, a $\approx$ 3 % increase compared with 2018 (9599 hip arthroplasties), being females with an average age of 69.7 years old also the highest sector undergoing this surgery [32,33]. Swiss 2020 annual report recorded an annual growth of more than 2.5% since 2013, performing 134673 THA since the last 7 years in which 52.6% of surgeries

performed in women with an average age of 70.2 years old [24]. Italian average annual increase of all types of hip replacement surgeries (including total, partial, revision surgeries...) since 2001 up to 2018 was registered as 2.6% being 3.2% for total hip arthroplasties [25].

Similarly, international countries also feature an increase in the number of hip replacements. In Australia 2020 registry [26], it was recorded 499439 primary total conventional hip replacements, that corresponds to a percentage increase, since 2003, of 132.9%. As seen in Figure 2.5, this procedure is more common in females (55%) and elderly people, being the mean age of 67.7 years old.
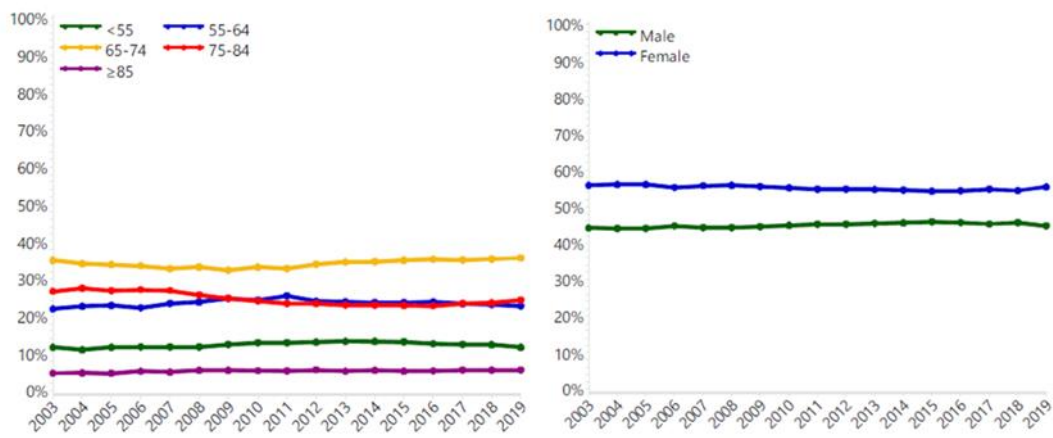
Figure 2.5 - Age and gender and primary diagnosis percentage of hip procedures, in Australia [26].

The number of hip replacements in 2017-2018, in Canada, was about 58492, which corresponds to an increase of 17.4% in a 5 year experiment [34]. It was also recorded that in every 3 patients, 2 have 65 years old or more and, similarly to Australia, more women undergo this surgery compared to men (73.2% in this age over 60% of men) [34].

This trend is observed in countries like the United States of America, in which, according with the projection to 2030, since 2005, the number of primary THA procedures is estimated to grow 174% [35]. Their 2019 annual report recorded, since 2012 up to 2018, a total of 602582 hip arthroplasty surgeries, being the mean age, in 2018, 65.6 years [36]. Regarding age and gender, similarly to the above-mentioned reports, patients older than 60 years were predominantly female, however, in younger patients the opposite occur, being more than half of patient's male (Figure 2.6).
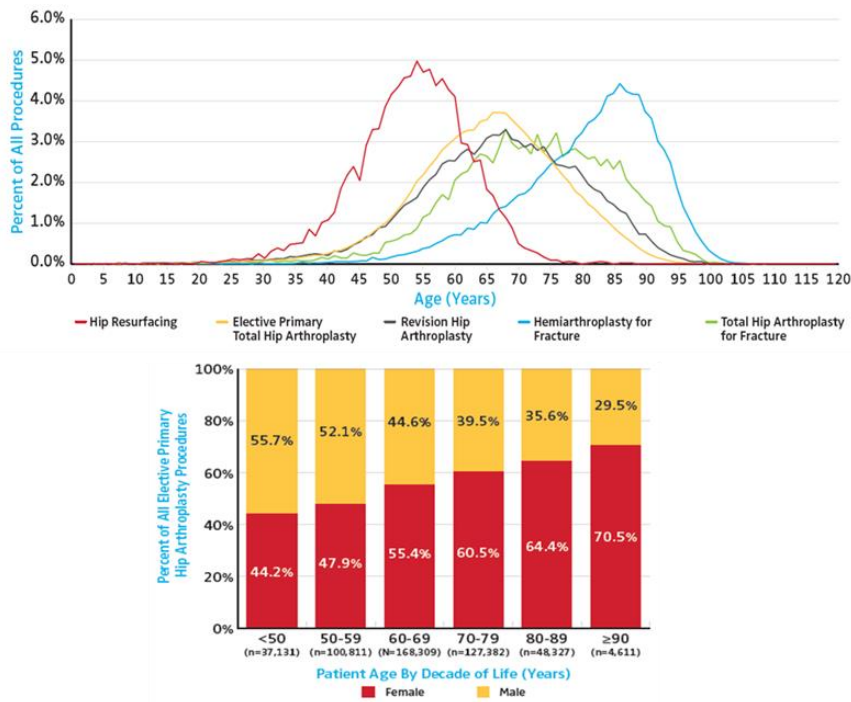
Figure 2.6 - Age and gender and primary diagnosis percentage of hip procedures, in USA (adapted from [36]).

2.3.1. Surgical Procedure

The surgical procedure for a primary hip arthroplasty, as mentioned, involves the removal of the head, neck and acetabulum of the hip joint to replace it by an implant.

Prior to surgical procedure, a pre-operative planning needs to be performed, in which, according with Depuy Synthes [37], with the patient's radiographic images, the size and positioning of the acetabular cup and femur and some other technical measurements are determined, as shown in Figure 2.7.
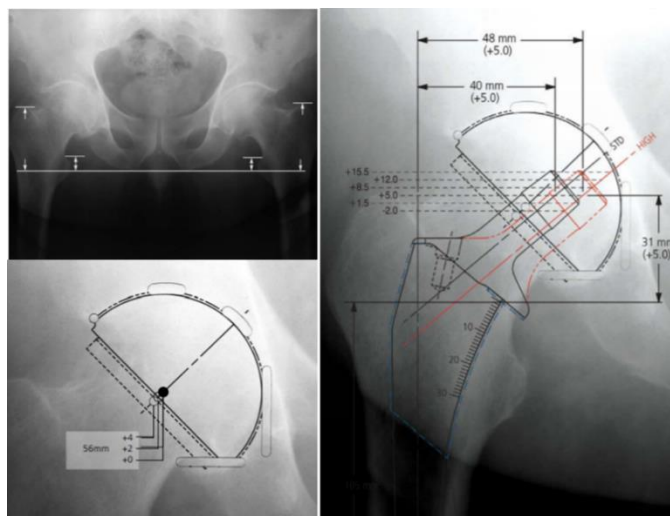
Figure 2.7 - Pre-operative planning of Depuy Synthes for THA of ACTIS™ total hip system (adapted from [37]).

Worldwide, there are several approaches for performing THA, including posterior approach (PA, made from the back), direct lateral (DLA, from the side) and direct anterior (DAA, from the front), as shown in Figure 2.8 [11,38]. In PA, the patient is placed in lateral decubitus position and an incision is made 5 cm distal to the greater trochanter (GT) that continues along the GT curving toward the posterior superior iliac spine for more 5 to 7 cm [9,38–40]. Similarly, DLA is also performed with the patient positioned in the lateral decubitus positions, however, the incision is made 3 to 5 cm proximal and 5 to 8 cm distal to the GT [9,38–40]. Finally, DAA is performed by placing the patient in supine position and a longitudinal incision is performed laterally to the anterior superior iliac spine of the pelvis (2 to 4 cm) and distally towards the fibular head (8 to 12 cm) [9,38–40].
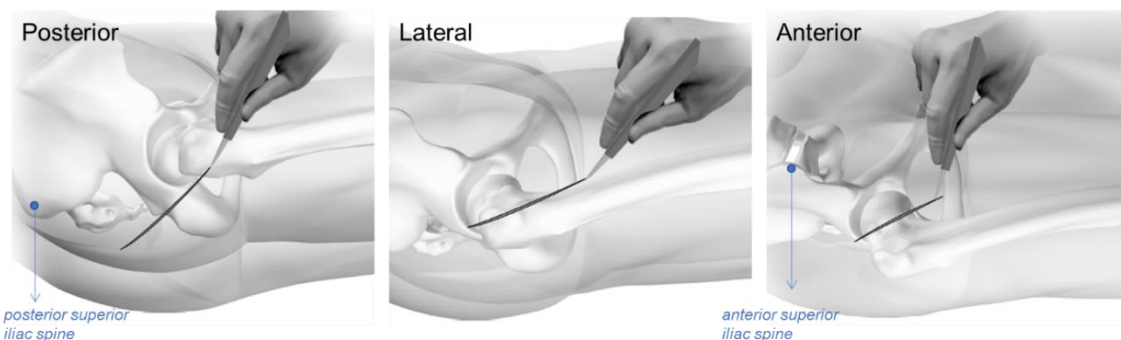
Figure 2.8 - Surgical Procedure approaches for performing total hip arthroplasty: from right to left, posterior lateral and anterior approaches (adapted from [9]).

The following step comprises hip joint access that, depending on the approach, is performed by separating the muscles. It is important to highlight that, in PA, it is essential to detect the sciatic nerve and protect it throughout the surgical procedure since this nerve is the largest peripheral nerve and the major in the lower limb and is responsible for innervating muscles of the thigh (posterior part), leg, ankle, foot and the majority of the skin of the lower limb [1,11]. Once the joint is exposed, a capsulotomy (incision of the joint capsule) is performed, followed by the dislocation of the femoral head through the rotation of the leg [9,11,38–40]. With the exposure of the femoral neck, an osteotomy is performed using a reciprocating saw, i.e., the femoral neck is cut and the femoral head removed (Figure 2.9(1)) [9,11,38–40]. The following step comprises the preparation of the socket by removing the remaining cartilage and removing bone from the surface so that the acetabular component shell of the implant fit in the space [9,11,38–40].

It is important to mention that implant fixation can be performed either with or without cement. In cemented fixation, the femoral stem/acetabular component is fixed to the bone with a

cement (usually made of polymethylmethacrylate – PMMA), while in cementless fixation, this process is performed by press-fitting against the bone [9,11,14,18].

The subsequent step, Figure 2.9(2), includes the femoral channel preparation in which, proper tool named broach handle is used to initiate broaching while maintaining a proper alignment [11,37,39,40]. This is followed by using a sequence of broaches with increased sizes down the femoral canal until achieving a desired axial and rotational stability [37]. Afterwards, trial reduction is performed (Figure 2.9(3)) by placing trial components and testing the new joint through the leg movement in multiple planes to check if the joint works properly [11,37]. The final stem is then press fitted or cemented inside the femoral canal by hand, followed by an inserter (Figure 2.9(4)) and the femoral head is implanted by impact (Figure 2.9(5)) [11,38–40]. Figure 2.10 details the different implant components and postoperative radiographs.
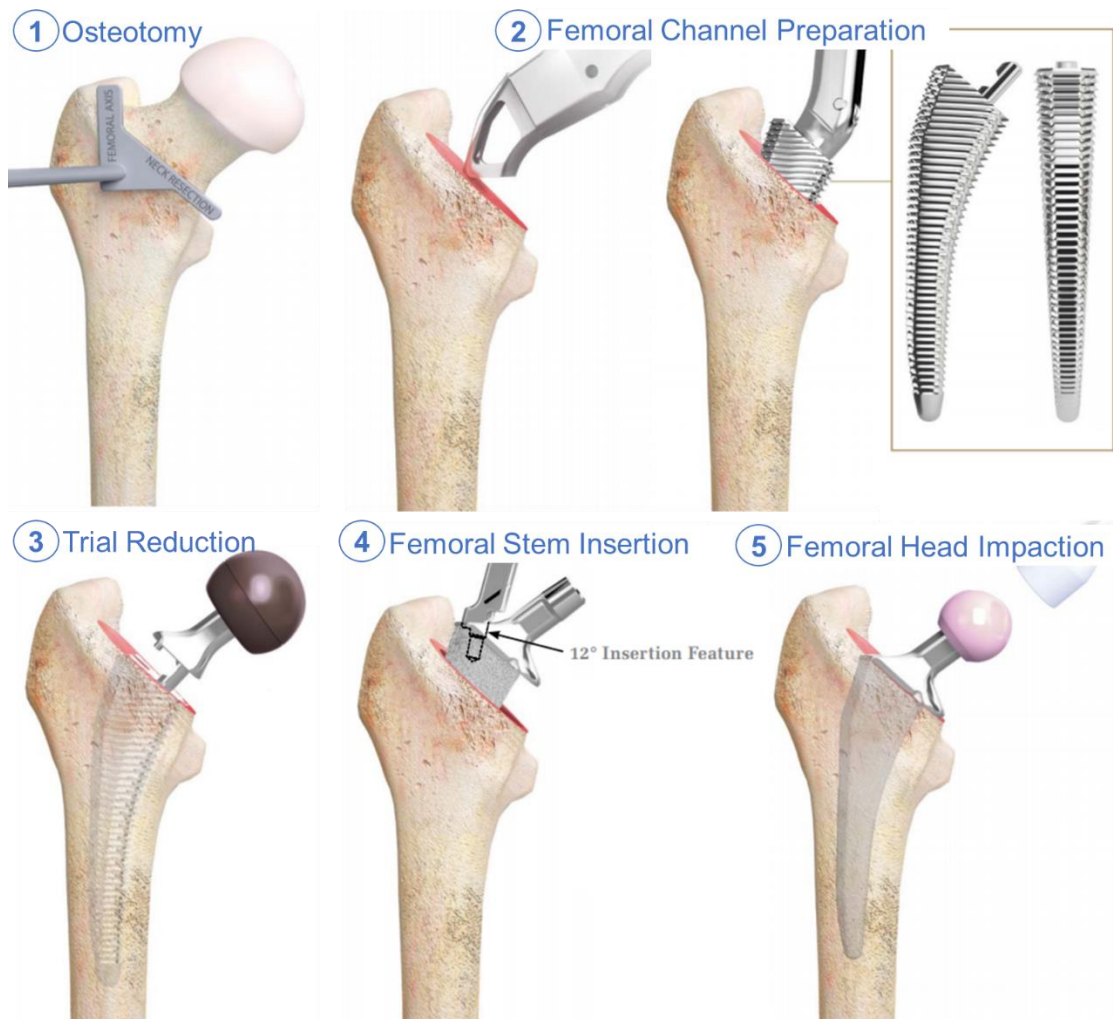
Figure 2.9 - Total hip arthroplasty surgical procedure according with Depuy Synthes of ACTIS™ total hip system (adapted from [37]).
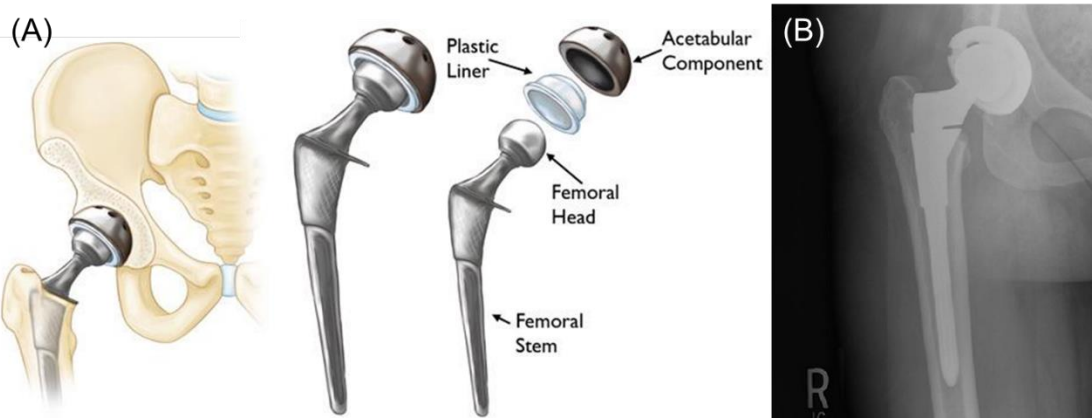
Figure 2.10 - Total Hip Replacement (A) schematic representation of implant position and components (adapted from [41]) and (B) post-operative radiograph (reproduced from [42]).

2.3.2. Bone Formation around the Implant

To guarantee a successful implantation and, thus, ensure a long-term success of the implant, it is extremely important that implant osseointegration is achieved [43,44]. Right after implantation, the implant is mechanically fixed to the bone, achieving the so-called primary stability [44,45]. Formerly, a cascade of biological events occurs on bone-implant interface in order to promote new bone formation, phase that corresponds to the secondary stability [44,45]. This cascade of biological events is characterized by four main phases: hemostasis, inflammatory, proliferative formation and bone remodeling phases [44–47].

During the surgical procedure, bleeding from the rupture of blood vessels occur, being blood the first component to become in contact with the implant surface, triggering the hemostasis phase [44–46]. In fact, seconds after implantation, blood cells like red cells, platelets and inflammatory cells migrate to the injured tissue [44–46,48]. Proteins adhesion and absorption by the implant will form a protein monolayer on its surface, that will further interact with platelets and mesenchymal cells [44]. Then, platelets, also named thrombocytes, become activated by getting in contact with the foreign body and start to adhere to proteins (like fibrinogen and fibronectin) by means of membrane-bound adhesion receptors, followed by its spread and aggregation [44,45]. This will lead to the formation of a blood clot, from the conversion of fibrinogen into fibrin, that will allow osteoinduction by offering the necessary mechanical and biomechanical components [6,44,46]. The resultant fibrin clot will act as a provisional matrix that is adhered to the implant surface and will facilitate cell adherence and proliferation to the implant [6,44]. The platelets starts to release a number of substances that will act as signaling molecules that will be crucial in cell recruitment and differentiation [44]. During the hemostasis process, inflammatory response

17

initiates, hours after the surgery [44,46]. In this stage, cytokines released from the platelets will activate leukocytes (like neutrophils, lymphocytes and macrophages) that will, consequently, migrate and destroy bacteria that remains in the site [44,46,49]. In the proliferative phase, new extracellular matrix is formed via growth factors that were segregated by platelets and macrophages and activate fibroblast migration [44,46]. Mesenchymal cells also migrate towards the implant surface through the preliminary provisional matrix from the fibrin clot and the previously mentioned growth factors induce their differentiation process into osteoblastic lineage [44,46]. Osteoclastic cells start to resorb dead bone in direct contact with the implant, promoting a decay in primary stability of the implant. Afterwards, fully differentiated osteoblastic cells migrate and attach to the implant surface, secrete a collagenous matrix and promote its mineralization thus creating an immature woven bone [44,46]. It is important to mention that, during this procedure, some osteoblasts get trapped into the lacunae and become osteocytes. This woven bone formation will allow the so-called secondary stabilization of the implant [44,46]. During the last remodeling phase, the process begins with the resorption of the woven bone by the osteoclasts, followed by mature bone production by osteoblasts, named lamellar bone [44,45]. The formation of woven bone is very quick and is characterized by collagen fibers randomly organized, whereas, in lamellar bone, these fibers are parallelly aligned in the lamella, making it mechanically stronger than woven bone [44,46,48]. Figure 2.11 displays a schematic representation of the physiology behind bone remodeling process.

As mentioned, primary stability is a result of the friction of the press-fitted implant with the bone with limited micro motion. However, with time, this stability decreases as a result of bone resorption and is replaced by the secondary stability due to new bone formation [43–45]. Figure 2.12 displays the primary and secondary stability in a conventional implant and in a desired implant osseointegration behavior. The delay in the formation of the new bone causes a dip in total stability, thus being important to anticipate the curve of secondary stability, to reduce, as much as possible, this dip formation and, thus, assuring implant stability and long-term success.
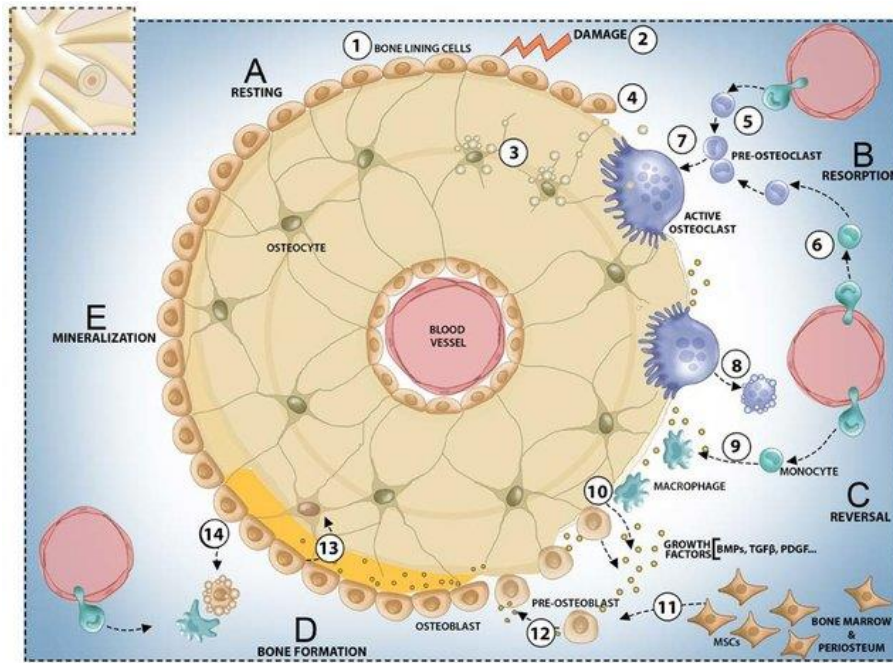
Figure 2.11 - Bone remodeling process (reproduced from [49]).
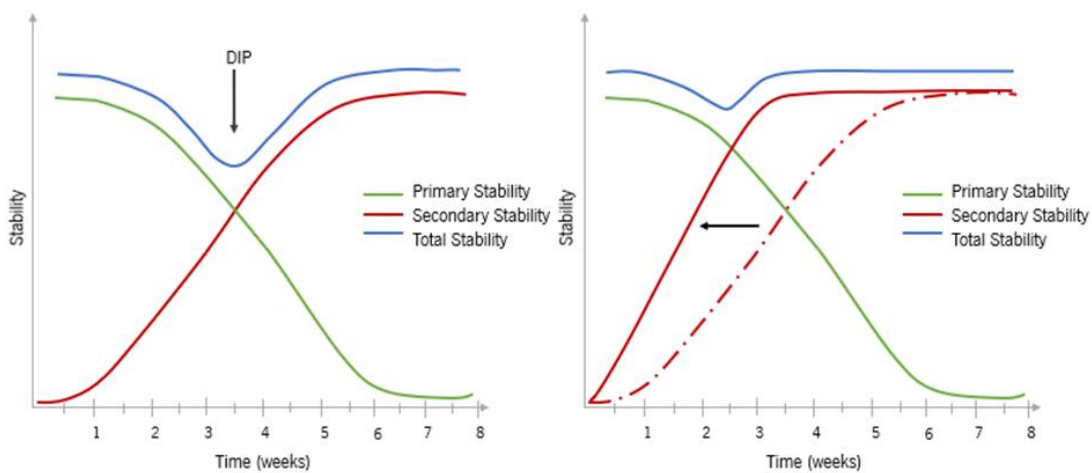
Figure 2.12 - Schematic representation of relation between primary and secondary implant stability in a conventional implant (left-hand side) and a desired behavior (right-hand side).

2.3.3. THA Problems

One year after THA surgery, more than 90% of patients are satisfied and return to normal life [18]. However, despite these good results, THA has limited lifespan, Figure 2.13(A), and many problems can arise to compromise the long-term success of the implant, leading to the need of revision surgery [11,18,21,28]. Although THA is performed mainly on elderly people (patients over 60 years old), the number of younger, more physically active patients is increasing and consequently, they want a solution that do not cause them any limitations or pain [11,18,28]. According with 2020 Australian registry [26], the number of younger patients, under 55 years old, undergoing this procedure is increasing (11.7% in both 2003 and 2019). This means that, the

average age of patients undergoing THA is decreasing and, since life expectancy are increasing, the number of revision surgeries are also growing (Figure 2.13(B)) [18].
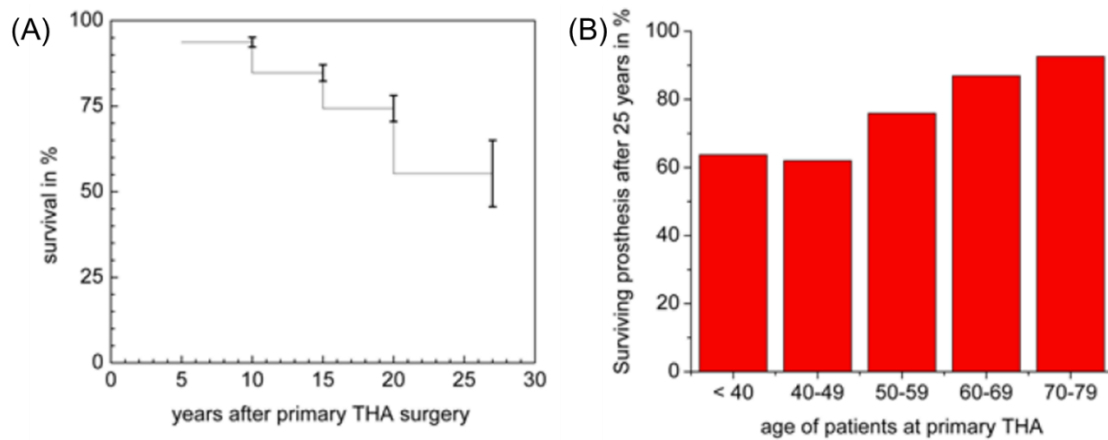
Figure 2.13 - (A) Survival of hip prosthesis, years after primary THA and (B) Prosthesis lifespan after 25 years, according to the age of patients (adapted from [18]).

Bayliss et al. [50] performed an implant survival analysis to determine lifetime risk of revision surgery with age and reported that patients under 60 years old significantly increases their revision surgeries of up to 35%, being this revision performed, in many cases, within 5 years after primary arthroplasty. England, Wales Northern Ireland and Isle of Man 2020 registry reported that when primary surgeries are revised in the first year, 12.69% are re-revised within the next 3 years whereas if primary surgeries can last at least 5 years, this percentage of re-revision decrease for 7.10% [23].

Among all complications that arise after THA that cause revision surgeries inevitable, the major is the loosening of the stem and/or acetabular cup [9,18,51]. France, Germany and Swiss in 2020 reports indicate loosening as the major reason for revision surgeries, representing 45.1%, 27% and 21.7% of all causes, respectively [22,33]. Likewise, England, Wales Northern Ireland and Isle of Man reported that aseptic loosening was the primary reason for revision surgeries, followed by dislocation and particulate debris causing soft tissues reaction [23]. According to Australian Joint Replacement Registry, loosening is the most common reason that leads patients to perform a revision surgery. Moreover, younger patients also are more likely to need revision surgeries in comparison to older patients [26]. In 2017-2018, the revision surgeries in Canada represented 8.2% of all hip replacements, being also aseptic loosening the major reason for this surgeries (24.7%) [34]. This loss of fixation between the implant and bone can be related with poor osseointegration, poor wear and corrosion resistance, high stiffness of current hip implant materials and a non-uniform contact pressure between the implant and bone.

An unsuitable contact between implant and bone can lead to a phenomenon called stress-shielding [18]. Current implants are stiffer when compared with natural bone, i.e., their elasticity modulus is much higher when compared to that of bone leading to an uneven stress distribution [18,21,30,52]. In this sense, when a load is applied to the implant, the stress will not be properly transmitted to the bone, i.e., the stress is transmitted throughout the implant, which means that there is less stress applied to the bone as would naturally happen (Figure 2.14) [12,18,21,30]. As a result, an increased osteoclast activity will resorb the bone and the implant will become loose, leading to its failure [18,21,30,46]. In this sense, an implant with similar elasticity modulus will be desirable to avoid stress-shielding [8].
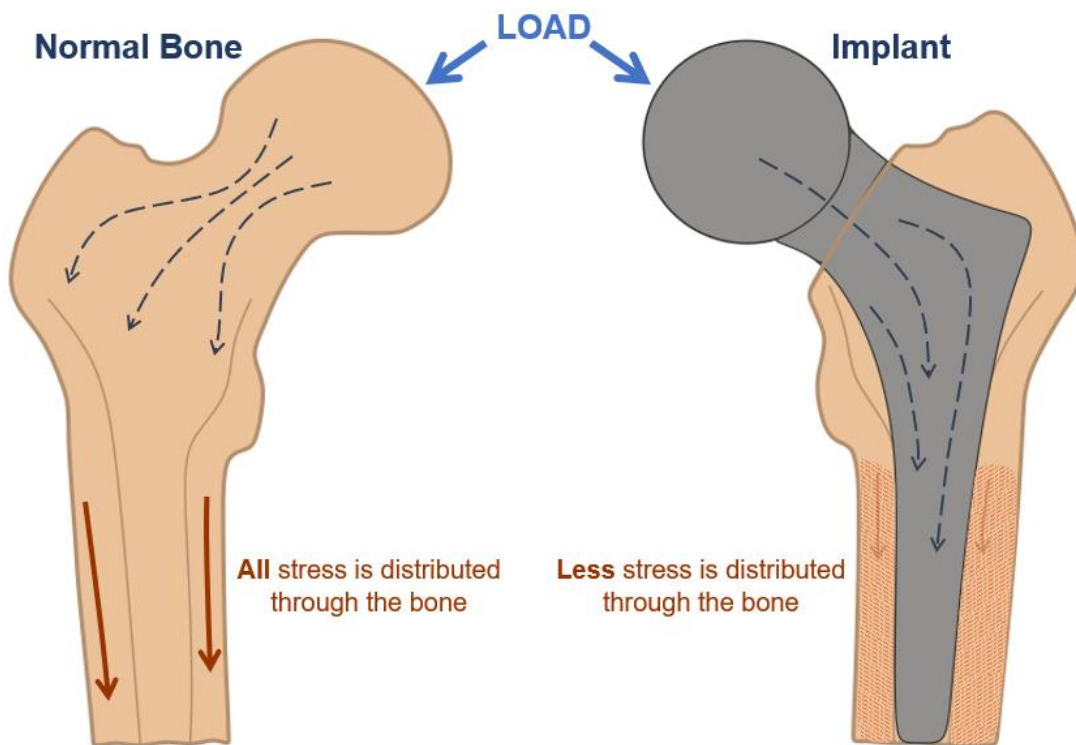
Figure 2.14 - Schematic representation of stress-shielding effect.

Moreover, wear and corrosion are other problems related with aseptic loosening. When implanted into the human body, the implant will be exposed to corrosive body fluids. Together with micro-motions of the implant aggravated by implant loosening, these will contribute to corrosion and degradation of the material [18,53]. Long-term wear of the implant material will lead to the release of metallic ions and debris to the surrounding tissue and consequently induce unwanted side effects like inflammation, allergic and toxic reactions [21,30,54–56]. Biologically, an immune

response will start by recruiting macrophages that will phagocytize this debris, since they recognize them as foreign bodies, and start bone resorption [18,30,55].

Wear, by definition, is "the phenomenon of material removal from a surface due to interaction with a matting surface" [57,58]. Different wear mechanisms can be distinguished, the four major ones schematically represented in Figure 2.15.
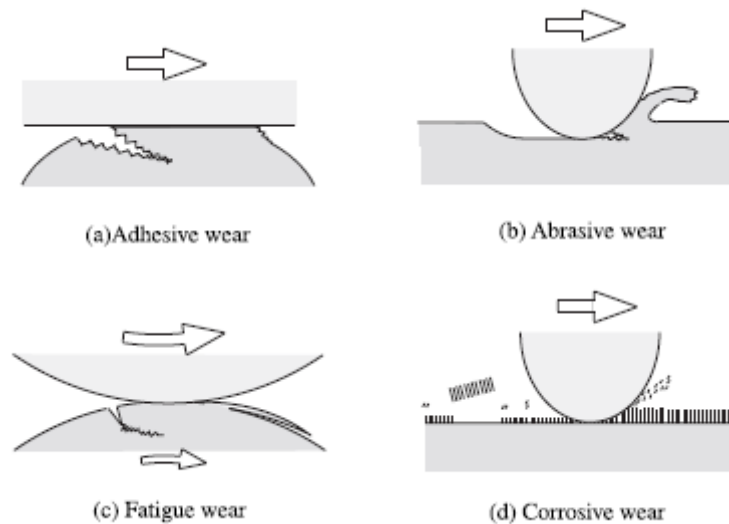
Figure 2.15 - Schematic illustration of common wear mechanisms (reproduced from [57]).

Briefly, adhesive wear is characterized by a plastic deformation of the contact surfaces in small areas in a way that adhesive bond strength can resist sliding [18,57]. In this type of wear, a large plastic deformation occurs, initiating a crack propagation until it reaches the interface between the two surfaces and form a wear particle [57]. On the other hand, abrasive wear consists of material removal from the softer surface forming abrasive grooves. This mechanisms occurs by ploughing through the action of a harder surface over a softer one [18,57,59]. Fatigue wear occurs when repeated cycles of load and unloading weakens the surface due to the formation and propagation of sub-surface or surface cracks, that after a certain number of cycles will induce surface failure [18,57,59]. Finally, corrosive wear (also called tribocorrosion) takes place when sliding happens in corrosive environments, leading to material degradation [18,57,59].

In this sense, to ensure the long-term success of any implant, the material should have high biocompatibility (not causing inflammatory or allergic reactions), good corrosion and wear resistance (withstand corrosive body environment without compromising motion), have suitable mechanical properties (e.g., tailor elastic modulus) while promoting osseointegration (enhanced bone bonding) [18,30,56]. In one hand, some of these requirements may be obtained only by

selecting the appropriate materials while, on the other, they can be achieved by changing the design of the final implant.

2.4. Biocompatible Materials

A biomaterial aims to *"replace a part or a function of the body in a safe, reliable, economic, and physiologically acceptable manner"* [60]. For several years, biomaterials were used within the human body to substitute natural tissues, bones and organs. Ever since, scientists were aware that when a material was placed inside the human body, interactions occurs and that some materials have better tissue response than others [4,61].

It is expected though, that the material that is going to be used as an implant material, do not elicit any toxicity in the human body, i.e., it shouldn't cause any inflammatory or allergic reactions being this, in a rough manner, the definition of biocompatibility [30,56,60]. The well-known definition of biocompatibility appeared in the 1980's, and its was defined as *"the ability of a material to perform with an appropriate host response in a specific application"* [61,62]. This means that the tissue response to the same biomaterial may differ depending on the application [18,61].

In medical devices, the term biocompatibility can be defined as *"the ability of the device to perform its intended function, with the desired degree of incorporation in the host, without eliciting any undesirable local or systemic effects in that host"* [61].

The interaction of a biomaterial with biocompatibility can vary from none to highly interactive, i.e., bioinert or bioactive material, respectively [4,18,56].

2.4.1. Bioinert Materials

A bioinert material exhibits no interaction with the surrounding tissue when implanted and its interaction with the human bone only depends on the tissue integration and regeneration [18,61]. The most commonly used bioinert materials in orthopedic joints are metal alloys like cobalt chromium (CoCr) alloys, stainless steel (SS) and titanium (Ti) alloys due to their high biocompatibility and suitable mechanical properties for such load bearing applications [4,9,30,56,63–65].

In earlier times, SS was the most commonly used material in orthopedic applications, however, its poor fatigue strength, high elastic modulus and relatively low wear and corrosion resistance prove them unsuitable for load-bearing implants [30,61,64]. Later, CoCr alloys appear

as substitutes for SS once this material possess higher wear and corrosion resistance, however, besides having high elastic modulus, they can cause harmful effects to the human body due to Co and Cr toxic ion release [30,56]. In recent days, Ti and its alloys are extensively used in implant applications due to its excellent mechanical properties, good corrosion resistance, high biocompatibility and, when compared with SS and CoCr alloys, its elastic modulus is closer to that of bone [30,56].

2.4.1.1. Ti6Al4V

Ti6Al4V is the most commonly used titanium alloy in orthopedic implants due to its high strength (that is increased by aluminum and vanadium addition), low density (for instance, as compared with steel $\approx$ 8 g/cm³) and corrosion resistance [9,18,30,55,66]. Table 2.1 presents some mechanical properties of Ti6Al4V alloy. Its microstructure consists of α-phase (Hexagonal Closed Packed, HCP) crystal structure, that is stable at room temperature, mixed with β-phase (Body Centered Cubic (BCC) structure, result of a transformation above β transus [30,60,67–69]. As an $\alpha+\beta$ alloy, Ti6Al4V has 6 wt% of aluminum (α-phase stabilizer) and 4 wt.% of vanadium (β - phase stabilizer) [69–71]. When processing this metal, its microstructure can vary, significantly, according with the fabrication process, heat treatment conditions and cooling rates, which will affect its final mechanical properties [30,67].

Table 2.1 - Physical and mechanical Properties of Ti6Al4V and cortical bone.

Property	Ti6Al4V	Cortical Bone
Density (g/cm³)	4.5 [72]	1.5-2 [63]
Elastic Modulus (GPa)	100-110 [30,56]	10-30 [7,30,63]
Yield Strength (MPa)	830-1070 [30,73]	-

Among metals, Ti6Al4V has higher biocompatibility when in contact with body fluids, which is related with its high corrosion resistance [55,74]. High biocompatibility and corrosion resistance are related to Ti6Al4V ability to form an oxide layer on its surface when exposed to atmosphere or to environments that contain oxygen [21,62,74,75]. Briefly, titanium will absorb the oxygen present in the atmosphere and form an oxide layer based on TiO_2 that will act as a barrier against corrosion. Likewise, this layer is also very effective on the attachment and growth of the human cells [62,75].

As mentioned in a previous section, elastic modulus mismatch between implant and bone has been reported as one of the main reasons for stress-shielding [76]. In fact, Ti6Al4V Young's

Modulus (YM) is the closest to bone when compared with the other metal alloys previously mentioned, beneficial to reduce bone resorption [9,21,30,56,61,77]. However, YM of Ti6Al4V ($\approx$ 100-110 GPa) is still quite high when compared to that of bone ($\approx$ 10-30 GPa) which means that the stress is not adequately transferred to the surrounding peri-implant bone and bone starts to resorb leading to implant loosening [61,74,76].

Moreover, it is also important to mention that aluminum and vanadium release in a long-term is pointed as a concern once these ions may be harmful to the human body [21,56,74]. Additionally, being this metal bioinert, this means that its interaction with bone relies only on the tissue integration and regeneration, which may be insufficient to promote a good adhesion between implant and bone [78].

Despite these drawbacks, Ti6Al4V is still an excellent candidate for such applications. In this regard, more research has to be made to overcome the problems that arise with Ti6Al4V. A compromise between suitable mechanical properties, lower YM (closer to that of bone) and enhanced osseointegration has to be found to avoid all the problems previously mentioned that lead to implant loosening.

2.4.1.2. Nickel-Titanium (NiTi)

Nickel-Titanium (NiTi or Nitinol) is one of the most promising titanium alloys for a wide range of applications due to its unique properties [7,56,79–82]. It was at the beginning of the years 1960's, that William Buehler and his coworkers discovered this alloy and named it NiTiNOL (abbreviation for Nickel-Titanium Naval Ordnance Laboratory) [60,79,83,84]. This alloy is a stoichiometric compound of Ni and Ti with approximately 50 at.% of Ni and 50 at.% of Ti [7,85].

NiTi phase diagram is presented in Figure 2.16, showing the three main equilibrium phases of this system: NiTi, Ti_2Ni and Ni_3Ti. NiTi corresponds the equiatomic composition while Ti_2Ni and Ni_3Ti phase can be found around 33 at.% and 75 at.%, respectively. Contrary to NiTi, these phases do not display shape memory effect (SME) however, changes in composition and transformation temperatures may occur due to their formation [86]. Moreover, Ni_4Ti_3, although it is not a stable phase, its formation, due to a decreased solubility of Ni, have a strong effect on transformation temperatures and thus shape memory and strength [86].
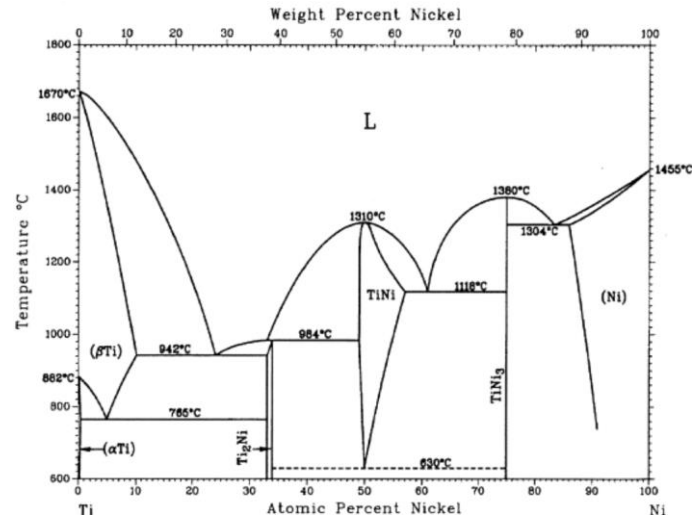
Figure 2.16 - NiTi alloy phase diagram (reproduced from [86]).

NiTi is a shape memory alloy (SMA) known due to its unique properties such as shape memory effect (SME) and superelasticity (SE), also displaying good wear and corrosion resistance, good mechanical properties (Table 2.2) and high biocompatibility, which makes it attractive for medical applications [52,79,80,82,87–91]. Despite that, this set of properties also make this alloy suitable for other industries such as automotive, aerospace and energy applications [56,92,93]. In fact, this alloy has also been widely used in biomedical applications like cardiovascular devices like stents, orthodontic wires and minimal invasive surgical devices [7,52,56,85,94].

Table 2.2 - Physical and mechanical properties of NiTi, compared with Ti6Al4V and cortical bone.

Property	Ti6Al4V	NiTi [30,79,95]	Cortical Bone
Density (g/cm³)	4.5 [72]	6.4-6.5	1.5-2 [63]
Elastic Modulus (GPa)	100-110 [30,56]	Austenite: 75-83 Martensite: 28-41	10-30 [7,30,63]
Yield Strength (MPa)	830-1070 [30,73]	Austenite: 195-690 Martensite: 70-140	-

Table 2.2 displays some NiTi properties, comparing them with those of Ti6Al4V and cortical bone. When compared with Ti6Al4V, although having similar biocompatibility, NiTi elastic modulus is much lower, being closer to that of bone, which will minimize stress shielding effect [79,89,94,96]. In fact, besides lower YM, NiTi displays the abovementioned shape memory effect (that Ti6Al4V do not possess). Also, as shown in Figure 2.17, its high recoverable strain makes this material more comparable to bone under loading/unloading conditions [79].
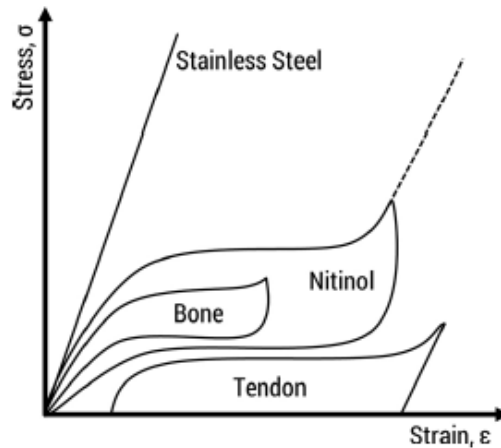
Figure 2.17 - Stress-strain curves for Nitinol compared with Stainless Steel, bone and tendon tissue (reproduced from [79]).

Both SM and SE are related with a solid-solid phase transformation between martensite and austenite phases that allow to recover strains up to 8% by heating and unloading, respectively [7,80,84,85,90,93]. Owing to SME (shape memory effect), the original shape of the material is recovered by raising the temperature above a certain temperature (austenitic finish temperature) whereas in SE this return is achieved without any heating process [90]. In these processes, as mentioned, NiTi crystalline phases are involved. While martensitic phase, has a monoclinic (B19') crystalline structure, stable at room temperature, the austenitic phase is characterized by a body-centered cubic structure (B2) with high-temperature (higher strength) (see Table 2.2) [7,85,87].

During heating or cooling, several transformation temperatures (TTs) are achieved, namely: austenite-start temperature (A_s), austenite-finish temperature (A_f), martensite-start temperature (M_s) and martensite-finish temperature (M_f).

SME is associated with a reversible martensitic transformation, i.e., thermally induce martensite to austenite transformation [85,86,96]. A schematic representation of stress-strain-temperature curve of SME can be seen in Figure 2.18.

By observing this curve, it is visible that, in one-way shape memory, there is a twinned martensite structure below the M_f temperature. In this phase, martensite can be easily deformed by applying a load. SME takes place when NiTi on its martensite phase is deformed and subsequently heated to be transformed into austenite phase, leading to a shape change. After mechanical deformation below M_f temperature (fully martensitic), the crystalline structure starts to convert from martensite to austenite, thus recovering its shape, when the temperature is increased above the A_s temperature, being fully austenitic when the temperature reaches A_f. Afterwards, when decreasing the temperature, austenite is converted into twinned martensite which starts at M_s

temperature until achieving M_f, when the crystalline structure is completely twinned martensite [79,82,85].
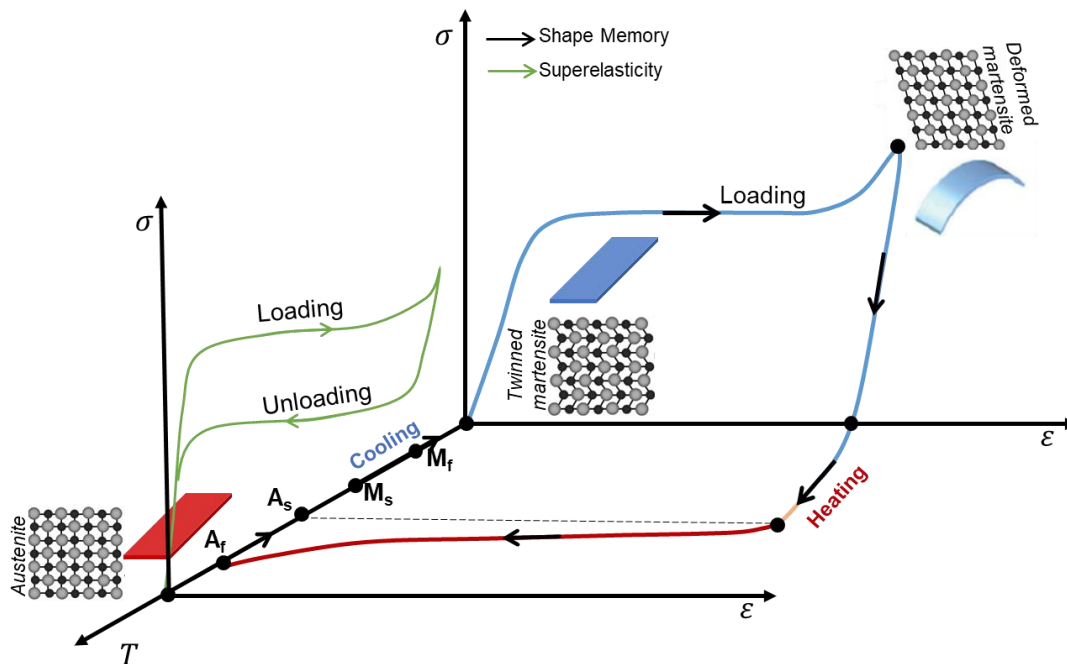
Figure 2.18 - Schematic Representation of stress-strain-temperature curve showing SME and SE (adapted from [82,85,96]).

Above A_f temperature, the material can be loaded and deformed by stress-induced martensitic transformation, reaching strains up to 8%. This so-called superelastic effect will allow to recover the material shape upon unloading, if the deformation did not reach a permanent state [79,82,85]. Studies in literature already proved that the SE significantly affects wear resistance of the material, once it can sustain large deformations without permanent damage, which is also an asset in orthopedic applications where wear, as mentioned, is one of the main concerns of implant failure [84,92,97].

In fact, as seen in Table 2.2, NiTi YM is related with the crystalline phases that are present, with a lower YM displayed by martensite when compared to austenite [96]. As mentioned, although NiTi YM is closer to that of bone, when compared to Ti6Al4V, this value is still high in comparison to cortical bone [98]. This YM mismatch urges the need of finding new solutions to decrease this value without compromising the shape memory effect. Moreover, by using SME, the non-uniform contact between the implant and bone may be improved.

2.4.1.3. Poly-ether-ether-ketone (PEEK)

Besides metals, the use of biocompatible polymers has been growing in the biomedical field due to their biocompatibility, low cost, suitable mechanical and physical properties in addition to being easy to manufacture [60,99,100]. Synthetic polymers are commonly used in orthopedics, dental materials, dressings, drug delivery systems, cardiovascular applications, etc [60,101].

Although metallic implants are extremely used and characterized by its outstanding orthopedic performance in terms of mechanical support, their high elastic modulus are not suitable for such bone applications and improvements needs to be performed [99]. In fact, in orthopedic field, polymers already have been used in articulating bearing surfaces and as cement material for implant-bone fixation [9].

Poly-ether-ether-ketone, also known as PEEK, is a semi-crystalline thermoplastic polymer increasingly employed in aerospace, automotive, dentistry and orthopedic implants like spinal cages and skull plates [102–105].

This polymer is able to resist higher temperatures than other polymers, having a melting point of 343 °C and glass transition temperature of 143 °C [104–109]. Moreover, despite PEEK good chemical and heat resistance, radiolucency and non-toxicity, it also possesses high wear resistance associated with a low coefficient of friction and high corrosion resistance [70,102,104–110]. Besides, it does not elicit any cytotoxicity or unwanted reactions/release of harmful constituents to human body [100].

Compared with metals, PEEK has a significantly lower elastic modulus, ranging from 3 to 4 GPa [55,70,111,112]. However, its elastic modulus is still not desirable, being important to raise it to values closer to that of bone and, this is possible by using reinforcements or developing multi-material approaches [55,112]. Moreover, this polymeric material mechanical properties are not suitable for a mono-material implant, suggesting that its incorporation in a multi-material solution would be needed [113]. Another concern is that PEEK is a bioinert material, displaying poor osseointegration which means that its integration to bone is quite limited [9,55,107,111]. This is related with its low surface energy and hydrophobic nature, that hinders cell adhesion and growth on its surface [100,102,106,110]. In this sense, improvement in elastic modulus mismatch and biocompatibility should be made to further explore the attractive properties of this materials in implantology.

2.4.2. Bioactive Materials

The previously mentioned materials, despite their advantages for orthopedic applications, they are considered bioinert, which means that their ability to interact with the surrounding tissue is very poor [18,98,114–116]. These materials biological bonding to bone can be improved by using bioactive materials, materials that interact with the surrounding tissue in order to enhance bone to implant fixation, in a way that bioinert materials are not able [4,69,117].

The term "bioactive" was defined in 1969 by Larry Hench and his coworkers as a material that "*elicits a specific biological response at the interface of the material which results in the formation of a bond between the tissues and the material*" [4,69,117]. Currently, this concept was expanded and is now defined as a material that has the ability to induce a positive response in a living tissue [4,114,117]. This is achieved by releasing bioactive molecules to promote an active response from the body, to restore and repair a defect while stimulating cell differentiation, proliferation, gene and tissue regeneration [4].

The complex hierarchical organization of bone tissue can be resumed in a simplistic manner by dividing it between trabecular and cortical bone. It is a tissue that possess different bone cells, responsible for different functions: osteoblasts (organic phase of bone matrix production), osteoclasts (bone resorption) and osteocytes (maintenance) [8,69,118]. Moreover, bone matrix is constituted by an organic phase, inorganic/mineral phase and water, as shown in Figure 2.19(A). From this figure, it is also possible to observe that 20% of the bone matrix is organic, which is predominantly type-1 collagen, 70% an inorganic phase mainly composed of calcium phosphates (hydroxyapatite crystals) presented along collagen fibers and other components in minor quantities and the remaining 10% water [69,118].

Taking into account that calcium phosphates (CaP) have a crucial role in bone formation, synthetic CaP are considered the ultimate choice for bone applications due to its high similarity with the natural apatites of bone and their high amounts in the mineral phase of bone matrix, that provides them osteoinductivity [107,119–121]. Figure 2.19(B) illustrates the formation of new bone on a bioactive surface. Upon implantation, the first steps (1,2) of Figure 2.19(B), are characterized by the bioactive surface solubilization due to their contact with body fluids until reaching an equilibrium stage: step (3). Afterwards, proteins and other organic compounds are adsorbed by the surface, step (4), that will allow cell adhesion (step (5)), as explained previously (see section 2.3.2). Cell proliferation will then occur, step (6), and will potentiate new bone formation (steps 7,8) [122,123].
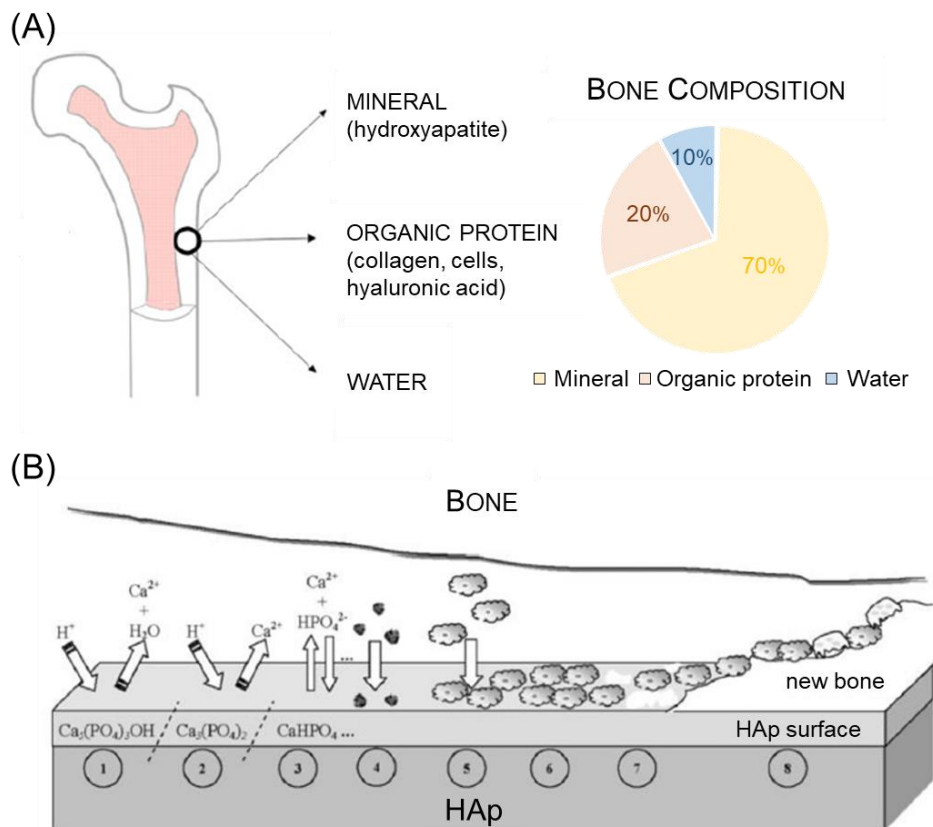
Figure 2.19 - Schematic representation of (A) bone composition (adapted from [118]) and (B) formation of new bone in contact with HAp (adapted from [123]).

In this sense, among physical, chemical, mechanical and biological properties that distinguish these CaP, the Ca to P ratio is one of the main aspects that will highly influence the dissolution rate, and thus osseointegration process [6,107]. The degradation rate increases with the decrease of this ratio, in which, for instance, a ratio too low will lead to a highly acid environment and osteoblast activity may be compromised. In this regard, it was already reported that this value should range between 1 and 2, for biocompatibility to be assured [107]. Among CaP, the most commonly used in orthophedics are hydroxyapatite (HAp) and β-Tricalcium Phosphates (βTCP) [119,124–127].

Hydroxyapatite (HAp) is widely used in implantology once it has a chemical composition similar to the mineral phase of bone. In this regard, it is a material with excellent biocompatibility, bioactivity and osteoconductivity. It has a hexagonal crystalline structure with a stoichiometric formula $Ca_{10}(PO_4)_6(OH)_2$ that corresponds, consequently, to a Ca/P ratio of 1.67 (10:6) which is similar to the natural bone Ca/P ratio [6,107,119,123,128,129].

β-Tricalcium Phosphates (βTCP) is another bioactive material characterized by its excellent biocompatibility, high biodegradability, osteoconductivity and cellular adhesion [120,130–132].

βTCP has a rhombohedral crystalline structure, with a stoichiometric formula of β-$Ca_3(PO_4)_2$, which corresponds to a Ca/P ratio of 1.5 (3:2) [6,107,119,133]. Considering what was previously stated, it can be concluded that βTCP has lower Ca/P ratio, when compared with HAp, which means that its degradation and absorption will be faster when implanted into the human body [6,107,119,134].

Despite their outstanding bioactive properties, HAp and βTCP can experience thermal decomposition during processing. There are ranges of temperature reported in literature for HAp and βTCP decomposition although some controversial exists between authors. Regarding HAp, it undergoes partial decomposition into βTCP, by dehydroxylation, at 900°C/1000°C and its decomposition occurs at temperatures greater than 1350°C [129,135,136]. Moreover, some authors stated that, up to 1125°C, βTCP is stable, while others raise this value to 1185°C/1200°C, in which above this temperature and up to 1430 °C it is converted into αTCP. At temperatures higher that 1430°C, αTCP is decomposed into α'TCP and γTCP [121,132,135].

Another concern regarding these materials is that they are brittle and display low mechanical properties. Its fracture toughness and abrasion resistance its quite poor which means that these materials are not ideal for load-bearing applications [124,128,137]. In this sense, the incorporation of these materials, as coatings, in a mechanically stronger material is a quite explored solution, once it would gather mechanical and bioactive properties of both materials [124,125,128,138]. However, it has been reported that these coatings, upon implantation, may detach from its surface, compromising the desired behavior of the implanted device [124,125,138]. In this sense, other approaches need to be found to avoid delamination to occur.

2.5. Powder Metallurgy

Powder Metallurgy (PM) is a group of manufacturing processes in which a powdered material is converted into shaped objects aiming to produce a near-net-shape component that can be applied in a wide range of applications like automotive, electrical and electronical applications, aesthetic materials and biomedical products like implants [139–141].

These techniques have become extremely attractive, in comparison with conventional routes like casting, machining and hot forging, once they own several advantages [139,140,142]. Unlike many opponents, PM techniques will be able, by using any type of source powder material(s) - metal, polymers, ceramics or composites - to produce components with residual material waste and extremely low energy consumption in a large production volume [139,142]. Additionally,

despite providing final components with good precision and surface finishing, these techniques are indicated when considerable high strength is required (depending on the technique) [139,140].

2.5.1. Press and Sintering

When using Press and Sintering technique (PS), it is possible to manufacture a component by a sequence of steps that comprises the application of pressure on the powder to form a compact, that is then subjected to a sintering step to densify. Briefly, in this process, the powder is placed inside a die and pressure is applied by an upper and lower punch, firstly to accommodate the powder, followed by its deformation and particles bonding. This process is carried out, in the majority of cases, at room temperature and in air, although sometimes other atmospheres may be used. Additionally, this process typically requires a binder, that will provide mechanical strength to the compact formed from the pressure step, commonly referred as green compact, to ease its handling. Afterwards, the green compact is removed from the die and sintered in a sintering furnace in air or under an inert atmosphere (when the material has a binder, it is burned out during this step) [139,140,143]. Figure 2.20 shows a schematic representation of PS process.

Although PS technique offers some advantages in terms of production with low manufacturing cost, it has some disadvantages regarding densification. This process does not allow full densification, which means that the final parts will display some porosity. Densification process is achieved, as mentioned, firstly by accommodating the powder (repacking), neck formation and elimination of pores (bonding) [139,143]. The presence of porosity will dictate the final mechanical properties in a way that higher densification (less pores) lead to higher mechanical properties. Thus, when high performance is required, for instance, in load-bearing implants, an increased porosity could compromise the mechanical properties and, eventually, lead to implant failure. Hence, a decreased porosity can be achieved by applying pressure and temperature simultaneously, to obtain a fully densified component. This process, that will eliminate porosity by collapsing the pores, can be achieved by Hot Pressing technique.
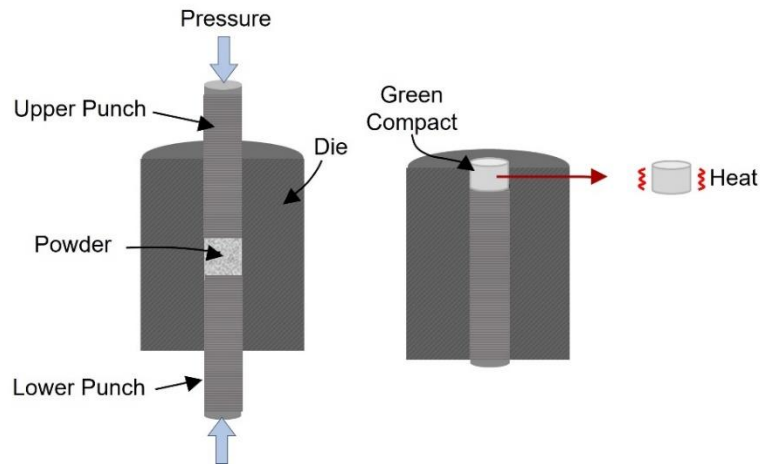
Figure 2.20 - Schematic illustration of press and sintering technique.

2.5.2. Hot Pressing

Hot Pressing (HP) is a pressure-assisted sintering technique, in which unidirectional pressure is applied simultaneously with temperature to obtain a near pore free component [67,70,139,140,142,144].

The experimental details for this technique, schematically represented in Figure 2.21, begin with powder placement inside the die followed by upper and lower punches proper positioning. In this process, the most commonly used die material is graphite, once it enables, under argon, the temperature to rise to values up to 2500°C [139,141,142]. Under air atmospheres, the graphite dies have limited lifespan once, above 500 °C, this material will oxidize [140]. In this sense, using an inert atmosphere or vacuum is recommended, being the latter the most commonly used, due to its advantages in terms of removing air from the environment and thus from the powder [140]. After punches positioning and placement inside a chamber of the HP equipment, and with an inert or vacuum atmosphere, the HP process proceeds with a residual pressure application to accommodate the powder that is further heated by raising the temperature of the die using an external heating source. This external heating source can be either a resistance or, in most cases, by induction, that is characterized by a coil system surrounding the chamber [139,140]. While the powder reaches the desired temperature, it is simultaneously compressed to achieve the desired pressure at the same time it reaches the target temperature. Afterwards, the powder is maintained at that pressure and temperature for a time period (dwell time) till reaching densification. Lastly, temperature and pressure are slowly removed and the part is allowed to cool to room temperature, when it is removed from the die [139,140].

This process, compared with other routes (like PS), offers several advantages once it allows a near full densification of the material with almost no porosity that, as already mentioned, will

enhance the overall mechanical properties of the final component. Moreover, the simultaneous application of temperature and pressure allows to achieve a densification at lower temperatures with lesser pressure application. Despite these advantages, the production rate of this process is low, being a drawback in mass production [139,144].
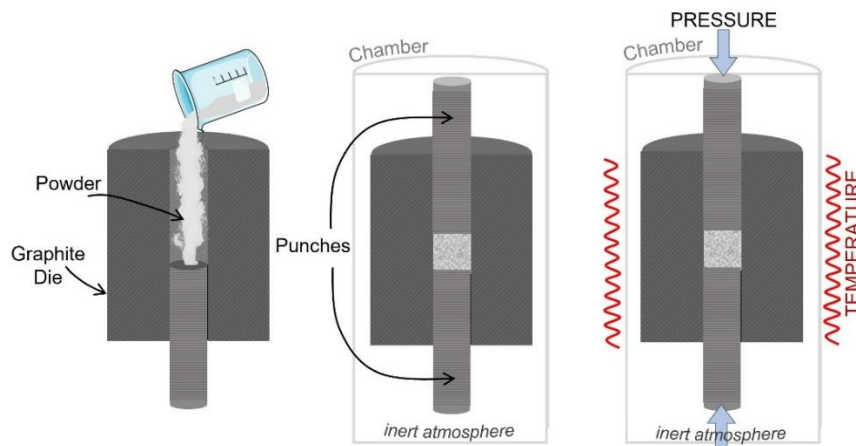
Figure 2.21 - Cross sectional views of steps presented on Hot Pressing process.

2.6. Additive Manufacturing

Additive Manufacturing (AM), also known as 3D printing, comprises a group of technologies that manufactures a 3D product using a layer-by-layer principle. AM is defined, according to the American Society for Testing and Materials (ASTM) F2792 standard, as "*the process of joining materials to make objects from 3-D model data, usually layer upon layer, as opposed to subtractive manufacturing technologies*" [71,74,145,146]. Contrary to conventional routes, that are based on material removal from a block (subtractive manufacturing), AM techniques produce a component by adding material, selectively, which turns the material waste in such techniques extremely low [52,147,148]. In, all the material that was not used to build the final component can be recycled in an eventual succeeding production [147].

Furthermore, the manufacture of complex components by conventional techniques can be difficult, if not almost impossible, once it may requires demanding post-processing machining, however, with AM it is possible to produce parts with high degree of complexity, precision and control, without the need of supplementary steps and, as mentioned, with significantly lower material wastage [65,74,147,149–152]. As a consequence, economically, AM are user friendly once it allows the design of complexity with no cost increase, while in conventional routes, a higher level of customization and/or complexity is translated into higher costs [74,147,151–154]. Besides, its manufacturing speed, reliability, accuracy, allied with the freedom regarding complexity

and customization turns AM technologies highly attractive in a wide range of applications (aerospace, digital art, architectural design, automobile) being the most promising for the biomedical industry [65,153–156]. In the biomedical field, AM can be used not only for soft tissues and vascular structures but also for creating a patient-specific customized implant with high quality and precision, aiming to fit, the best as possible, the patients' anatomy [147,148].

In all AM techniques, the manufacturing process starts with a Computer Aided Design (CAD) model, that is sliced into several thin layers, converted into an .STL file and, consequently, imported to a manufacturing machine that will build the final product, layer upon layer [74,107,149,154,157–159].

AM technologies can be classified, according with ASTM F2792-12a standard [145], in seven different techniques, as displayed in Figure 2.22.
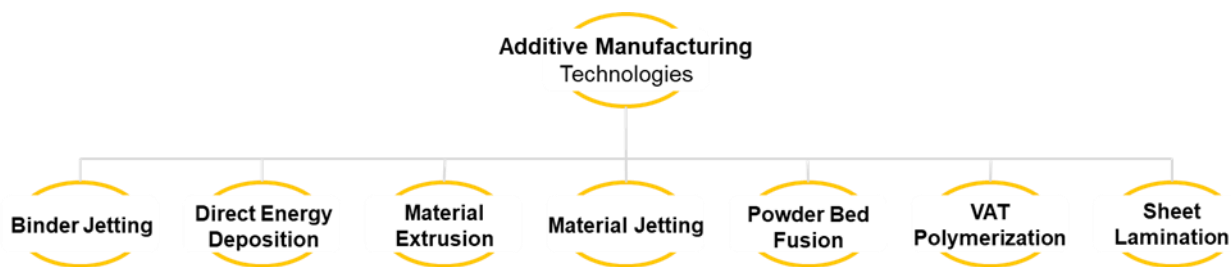
Figure 2.22 - Additive Manufacturing technologies, according to ASTM F2792 standard.

The different technologies differ in terms of materials feedstock, energy source used and application [65,91,151,154,157]. Briefly, binder jetting is a process in which a biding agent (liquid) is distributed selectively on the powder bed, joining powders, to form a predefined component [8,74,107,145,151,159]. On the other hand, in material extrusion, as the name implies, the material is extruded/dispensed, by a nozzle or orifice, in certain areas to create the final component [8,74,107,145,151,159]. Similarly, in material jetting, the object is produced by the deposition of build materials droplets [8,107,145,151,159]. VAT polymerization consists of a vat of a liquid photopolymer resin that is cured after its exposition to a UV light, allowing its polymerization [8,74,107,145,151,159]. Conversely, sheet lamination occurs when sheets of material are bonded together to create a single object [74,145,151]. Figure 2.23 displays schematically the five above-mentioned AM processes.
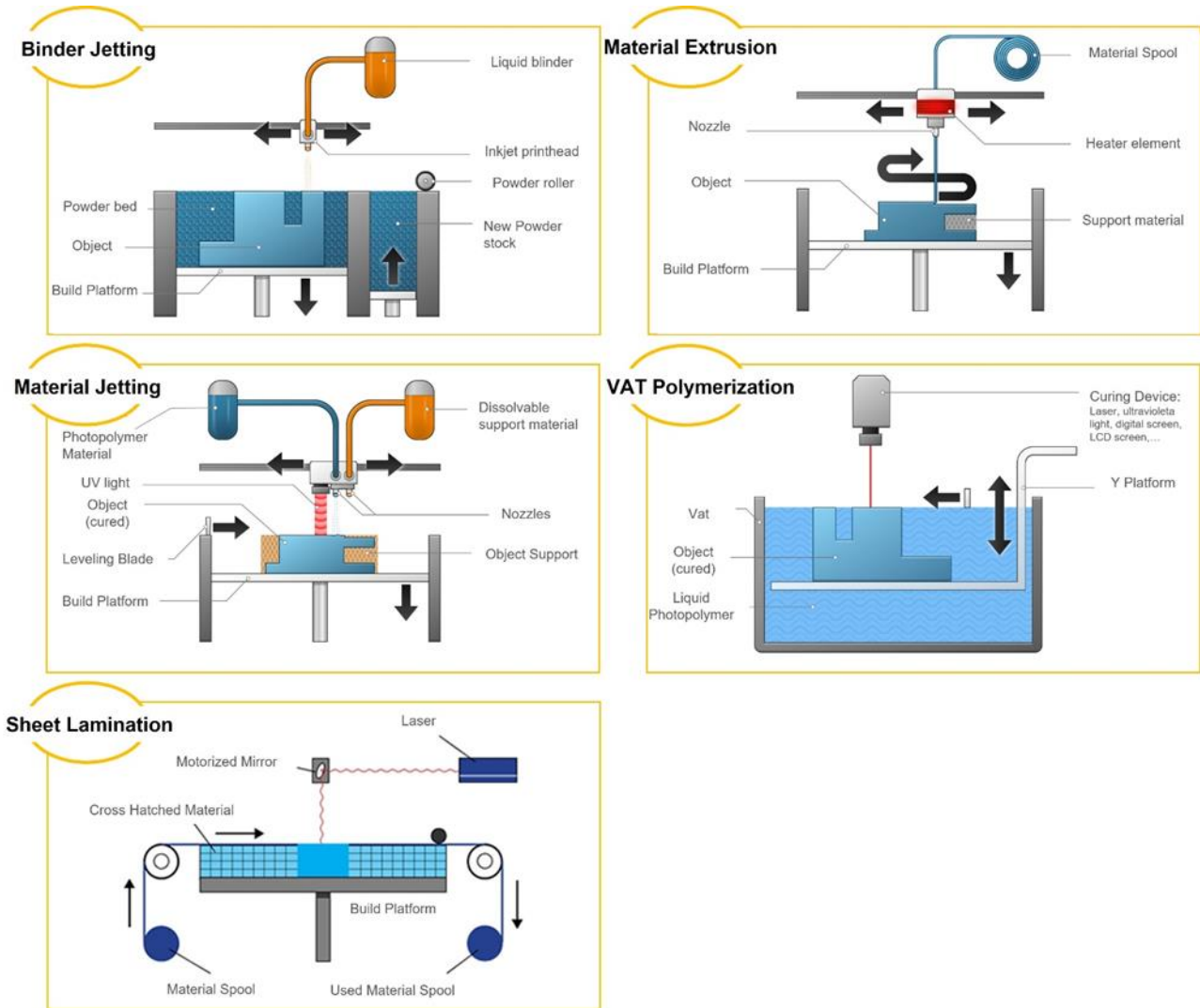
Figure 2.23 - Binder Jetting, Material Extrusion, Material Jetting, Vat Polymerization and Sheet Lamination AM processes (adapted from [160,161]).

Finally, among all AM techniques, both direct energy deposition (DED) and powder bed fusion (PBF), are the most commonly used to produce metal components [154,162]. According to ASTM F2792-12 standard, DED is defined as "*process in which focused thermal energy is used to fuse materials by melting as they are being deposited*" and PBF is a "*process in which thermal energy selectively fuses regions of a powder bed*" [145,151]. Accordingly, in DED, as represented in Figure 2.24, an energy source (electron beam, laser or plasma arc) locally melts the materials (powder, filament or wire) as they are being deposited [65,74,107,146,151]. It is also referred as metal deposition since the process is characterized by material deposition over a substrate that is further scanned by a laser source, according with a predefined design [71,163]. On the other hand, PBF techniques consists of powder fusion in desired areas on a powder bed by using an energy source, which can be either a laser or an electron beam [65,91,107,146,152]. Depending on the

type of energy source, the operating atmosphere will be different, where the use of laser requires an inert environment (usually argon or nitrogen) whereas electron beam sources demands near vacuum atmosphere [146]. In this sense, PBF techniques not only allow the production of complex parts by locally melting certain areas, consequently allowing reusing the remaining powder for other parts, but also allows the use of a wide range of metallic materials [74,152].
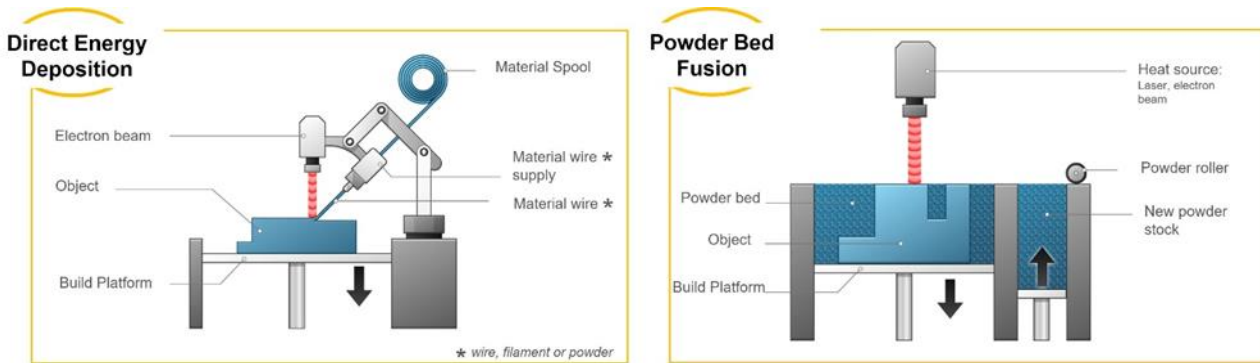
Figure 2.24 - Direct Energy Deposition and Powder Bed Fusion AM processes (adapted from [160]).

2.6.1. Selective Laser Melting

Selective Laser Melting (SLM) is an additive manufacturing technique belonging to PBF group that has been gaining attention in the biomedical field. In fact, many efforts have been made by researchers in order to use this technology to create new implant solutions [65,74,152–154,157,158,164]. Despite all PBF techniques being suitable for producing near net shape metallic components, SLM generally manufactures higher precision parts with better surface finishing [162].

SLM process is characterized by 3D parts production, based on a CAD model data, using a laser to locally melt a powder bed [8,70,157,165]. Firstly, as mentioned, a 3D CAD model is designed according to the desired product and further converted into a .STL file. This CAD model is then sliced into thin successively layers in a software and imported to a SLM equipment [75,162]. Afterwards, the powder is loaded into a tank and, in an inert atmosphere chamber, a build platform is heated (usually up to 200°C) and kept at that temperature for the hole process [74,147]. A layer of powder is then spread on the build platform, and a laser scans this powder bed, melting it in specific areas. Subsequently, the platform descends on the Z-axis at a predefined layer thickness to perform another layer scanning. Again, a new layer of powder is deposited onto the platform and the laser melts the powder bed to the previous layer. A cyclic process of deposition of powder layers and laser scanning will occur (layer-by-layer process) until achieving the final desired product

[71,75,147,158,159,162,166,167]. These sequential steps of SLM process are detailed in Figure 2.25.
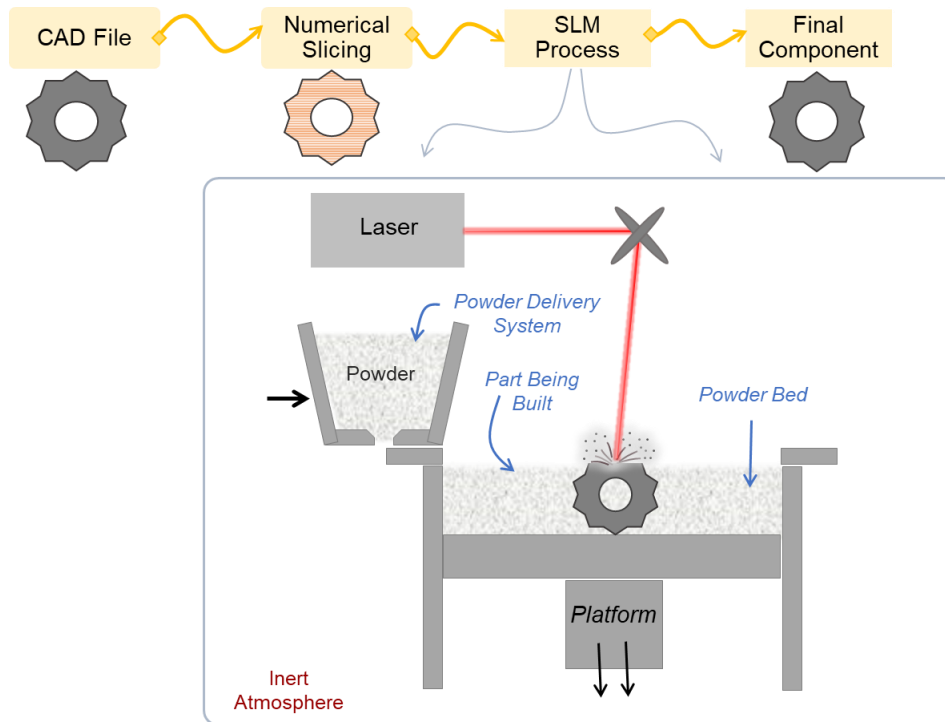
Figure 2.25 - Manufacturing steps of SLM process.

In this regard, SLM processing parameters will highly influence the final properties of the produced component. These parameters (illustrated in Figure 2.26) include laser powder, scan speed, hatch spacing and layer thickness, are translated into energy density, that can be determined by using the following equation (1):

$$E = \frac{P}{v \times h \times t} \tag{1}$$

in which P is the laser power (Watts, W), v the scan speed (mm/s), h the hatch spacing (µm) and t the layer thickness (µm) [162,168]. E is usually expressed in J/mm³, being this a measure of the input energy per volume. Linear and area density energy measures can also be calculated, but the previous is more commonly used. The optimization of the processing parameters is extremely important to obtain products with the desired properties. In fact, many studies have been made in order to understand and optimize the processing parameters for different materials and to evaluate their influence on the final properties of SLM produced parts [68,168–170].
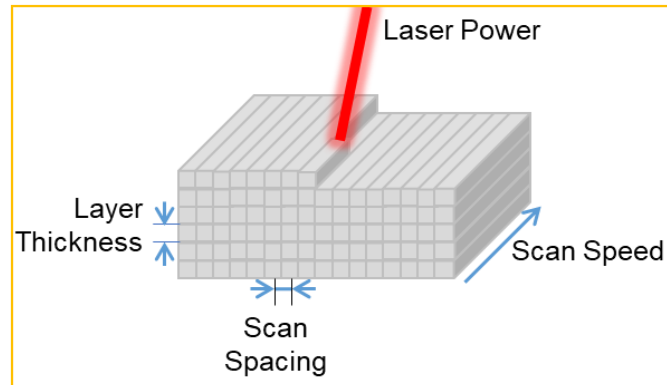
Figure 2.26 - Illustration of SLM key processing parameters.

SLM process displays several advantages in terms of production of components with high accuracy, complexity and low material waste [147]. In fact, when compared with other routes, this technique can be applied in the medical industry and produce implants with adjusted material properties, for instance, matching the stiffness of bone [74,153,155,157].

To sum, in addition to being able to be applied to metals, polymers and ceramics, SLM/AM allows, as mentioned, to tailor properties, thus increasing functionality, in a relatively low cost, low time consumption, with practically no restriction in terms of geometry, without requiring post-processing tooling [7,151,162,171]

2.6.1.1. Porous Structures

In orthopedic implants, as already mentioned, one of the main problems for implant failure is related with elastic modulus mismatch between implant material and host bone. An excellent approach to reduce this mismatch, and tailor elastic properties to values closer to that of bone, is by introducing porosity to the implant. SLM technique can help to solve this problem by allowing the production of components with high degree of complexity and customization. In this sense, it is possible to create a solution that mimic the porosity and permeability of bone by creating cellular structures via SLM. Besides elastic modulus adjustment, these structures aim to enhance vascularization within the pores while allowing bone to growth towards and into the implant (earlier bone osseointegration), all without compromising the necessary mechanical properties [8,52,65,147,153,157].

When designing these structures it is important to consider several aspects, namely, open-cell size, open-cell morphology, orientation, interconnectivity, distance between cells, etc [147,172]. In fact, many studies have been made in order to introduce controlled porosity in metals to tailor the elastic modulus towards similar values of human bone. Yue Du et al. [173] designed

irregular porous Ti6Al4V scaffolds and fabricated them by SLM (Figure 2.27(A)). The produced specimens had porosity ranging from 50 to 85%, resulting in an elastic modulus from 3.97 to 2.13 GPa. Similarly, Ataee et al. [174] manufactured commercially pure titanium gyroid scaffolds with interconnected pores with 2 mm, 2.5 mm and 3 mm pore sizes (Figure 2.27(B)) and the obtained elastic modulus ranged from 2.70 to 1.47 GPa. From both studies, these values are quite low for load-bearing applications, however, considering that the obtained values are close to the modulus of trabecular bone, it can be used in such applications as an inner part, having an outer shell with a higher modulus meeting the cortical bone requirements.
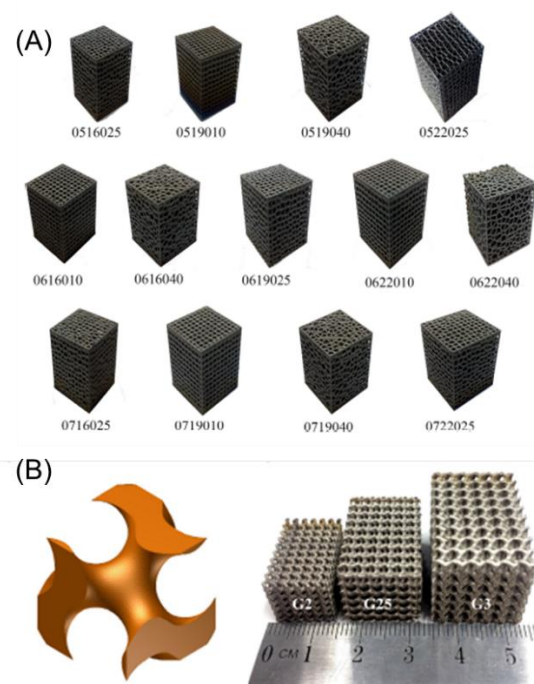
Figure 2.27 - Macroscopic views of (A) irregular porous Ti6Al4V scaffolds (reproduced from [173]) and (B) gyroid cp Ti scaffolds (reproduced from [174]).

Weißmann et al. [175] assessed the influence of the design and dimensions of Ti6Al4V cellular structures on their elastic modulus. The specimens under test had cubic, truncated pyramidal and twisted designs with porosities of 43-73%, 55-67% and 74-80%, respectively (Figure 2.28). Results revealed elastic modulus between 7 and 22 GPa, for the cubic structures, 3 and 7 GPa for the pyramidal design and 17 and 26 GPa for the twisted design.
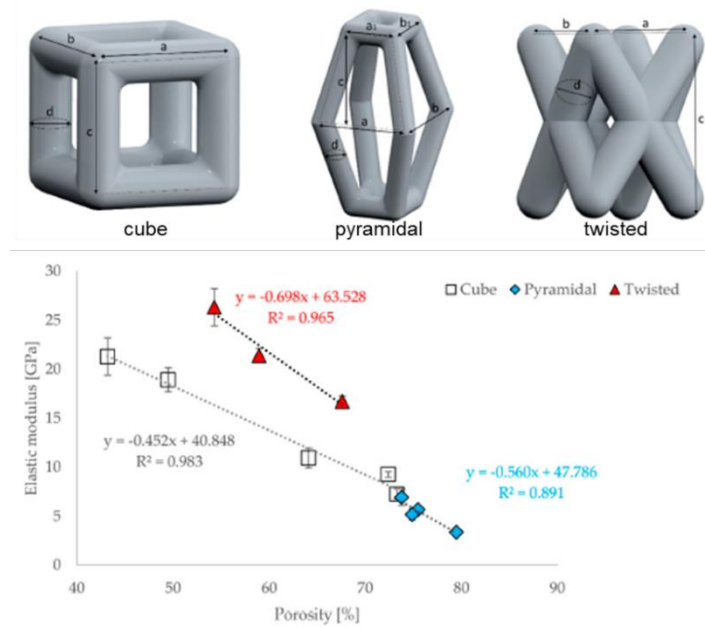
Figure 2.28 - Designs and elastic modulus experimental results obtained in Weißmann work (adapted from [175]).

Andani et al. [176] fabricated a near equiatomic NiTi shape memory alloy through SLM and assessed their mechanical performance. The cellular structures had three different geometries and dimensions, as represented in Figure 2.29, with the cubic geometries having the lower porosity (58, 45 and 32%), followed by the diagonal geometry with the vertical strut inside with 65% and finally the diagonal geometry with 69%. Results from the compressive tests revealed elastic modulus ranging from 16.5 GPa up to 41.2 GPa, allowing to conclude that is possible to significantly reduce this property value by changing the geometry and/or increasing the porosity.

Bartolomeu et al. [172] designed and produced cubic porous Ti6Al4V structures by SLM technique with porosities ranging from 64.3% up to 93.3%, in which SEM images of the lower, intermediate and higher porosities are found in Figure 2.30. From this study, elastic modulus closer or even comparable to that of bone were obtained. In fact, the structures with intermediate porosity (70.3, 80.4 and 87.6%) revealed elastic modulus within the range of those found in literature for bone (10-30 GPa).
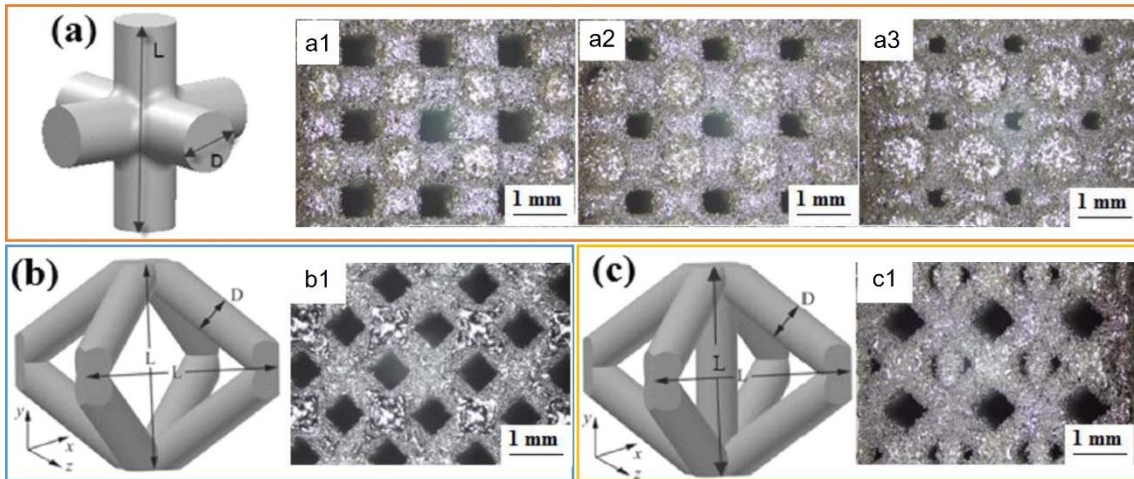
Figure 2.29 - Different unit-cell geometries and optical images of NiTi parts after SLM fabrication of Andani study (adapted from [176]).
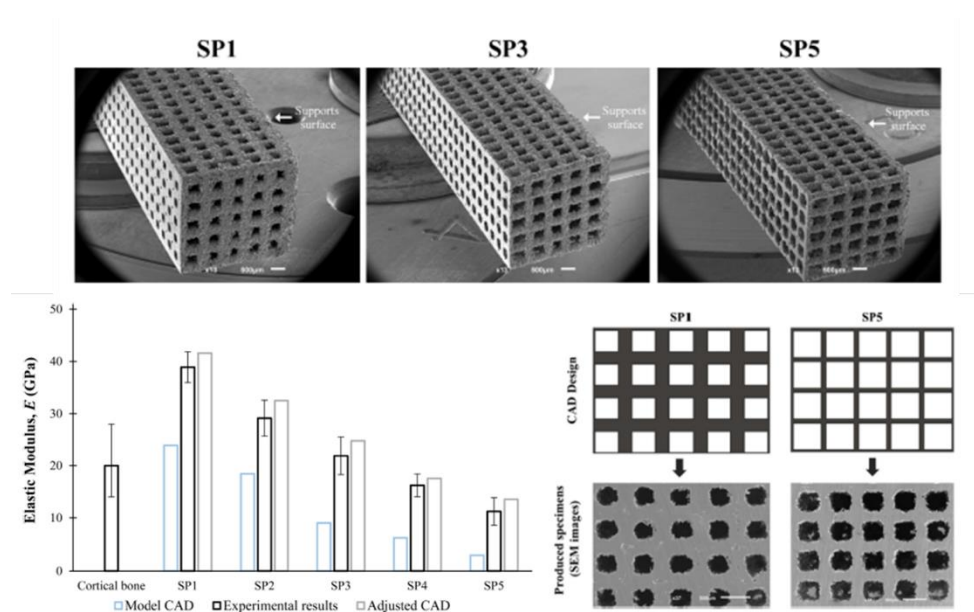
Figure 2.30 - SEM images of produced Ti6Al4V cellular structures (upper images), CAD and Real images deviations and elastic modulus results for all produced specimens (reproduced from[172]).

In another study, Bartolomeu et al. [165] produced cubic mono-material Ti6Al4V cellular structures with porosities ranging from 43.2% to 92.3%, and multi-material Ti6Al4V-PEEK structures with the same dimensions, but with the pores filled with PEEK (Figure 2.31). From this paper, it was possible to obtain models to predict the final properties of the produced components, i.e., through these models, it is possible to know what the input dimensions of the cellular structures would be, to obtain a desired elastic modulus both for the mono and multi-material structures.
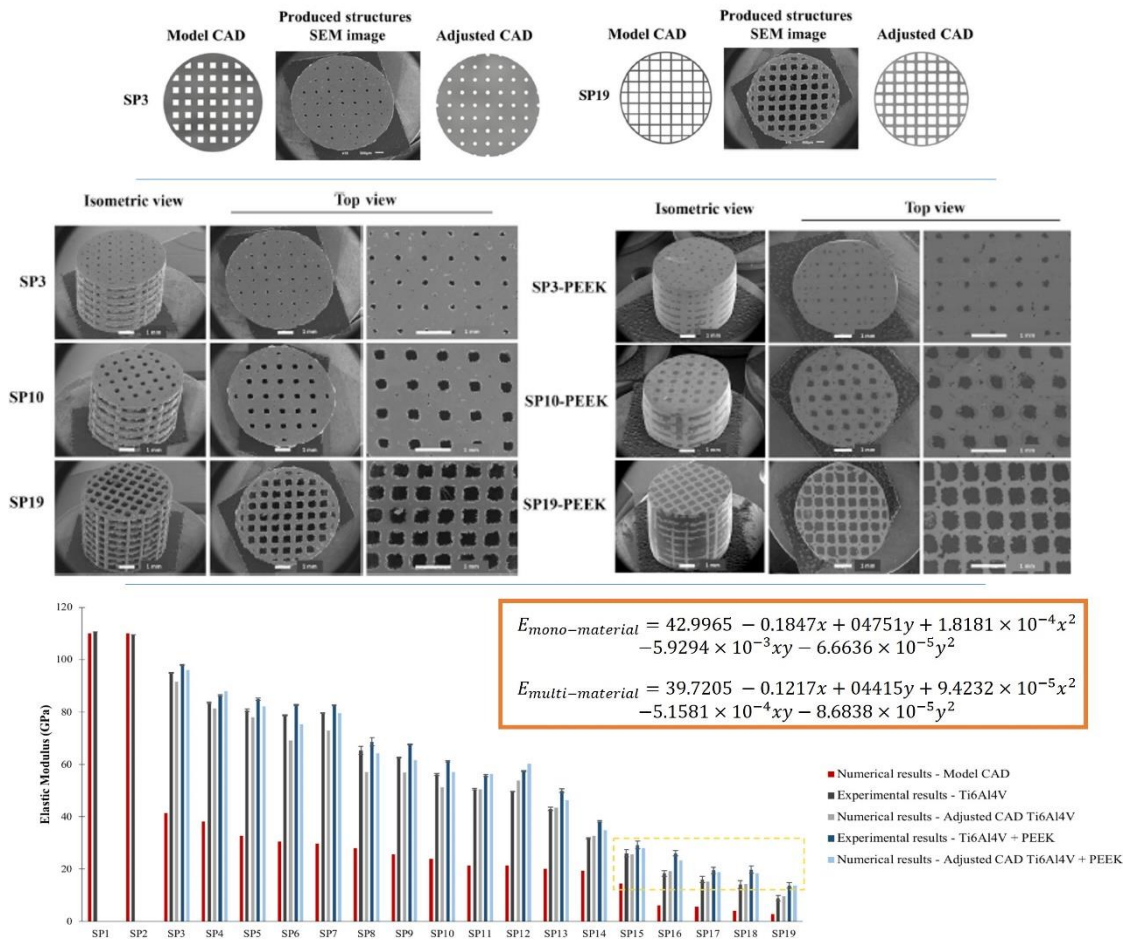
Figure 2.31 - SEM images of produced mono and multi-material structures, final elastic modulus results and predictive model obtained from Bartolomeu study (adapted from [165]).

The basis behind this study from Bartolomeu is related with an inherent aspect of SLM fabrication that, despite not being a drawback, must be considered when designing a certain cellular structure aiming to achieve a desired property [165]. This is related with the differences between the CAD designs and the produced components in terms of dimensions, as observed in Figure 2.30 and Figure 2.31 [165,172]. There are some studies in literature addressing this aspect and even with different equipment's or materials, this phenomenon is still visible [165,172,175,177,178]. This outcome in SLM parts is related to the powder present in the vicinity of the laser melt zone, that partially melts, increasing the final dimensions of the walls, thus decreasing the open-cell sizes [165,172,177]. Thus, when designing a cellular structure to obtain a desired property, like elastic modulus, this aspect is highly important.

Besides the elastic modulus tailoring, when designing cellular structures targeting orthopedic implants, some other key parameters need to be balanced to promote bone ingrowth, such as vascularization and permeability. In one hand, vascularization has a highly important role in bone repair and formation, once this aspect will allow the occurrence of different biological events for

damaged bone resorption and new bone formation [147,179,180]. On the other hand, permeability is also extremely important for cell migration, cellular nutrient transportation and mass transport for improving bone ingrowth [147,180]. These properties can also be enhanced by adding porosity to the materials since higher porosity is associated either by an improved nutrients diffusion and blood vessels growth into the implant [179]. Nevertheless, these factors have to be balanced with the mechanical strength, that can be compromised due to the amount of porosity [147,179].

Literature reports that for an adequate permeability to be achieved the pore size should be within 50 to 800 μm, in which a higher pore size is ideal to provide space for cell growth, proliferation, nutrient and oxygen supply and, thus, vascularization to occur [147]. However, it is reported that, for pore sizes lower than 100 μm, fibrous tissue is more likely to occur whereas pore sizes higher than 200 μm may lead to osteoblast penetration [179,180]. In fact, in smaller pore sizes, despite providing a higher surface area (which favors protein adhesion), it may lead to occlusion of the pores by the cells precluding their ingrowth [6,147,180]. Conversely, a pore size extremely high, is also not desirable, once the cell-to-cell contact ratio decreases, and the mechanical strength of the structure may be compromised [6,8,179].

In a study conducted by Ouyang et al. [181], porous titanium cellular structures with 400, 650, 850 and 1100 μm pore sizes were produced and characterized *in vitro* and *in vivo*. Results revealed that, by increasing pore size, the permeability, flow velocity and inflow also increase, being the structure with a pore size of 650 μm the one that displayed the best bone ingrowth. In other study, Chen et al. [182] assessed the influence of pore size and porosity on cell proliferation, osteogenesis and bone ingrowth. Ti6Al4V cellular structures with pore sizes of 500, 600 and 700 μm and porosities of 60% and 70% were fabricated by SLM and results evidence that a pore size with 500 μm and 60% porosity displayed the best *in vitro* and *in vivo* performance (higher cell proliferation, differentiation and bone ingrowth). However, Bai et al. [183] found that with pore sizes higher than 400 μm, no significant differences on vascularization were observed. Taking into account these varied results, it is important to find a compromise between all these factors. Tan et al. [147] summarize the influence of pore size on bone implantation and, considering the resultant Figure 2.32, concluded that the optimum pore size to achieve bone ingrowth, permeability and vascularization without compromising mechanical strength should be within ≈ 300-600 μm.
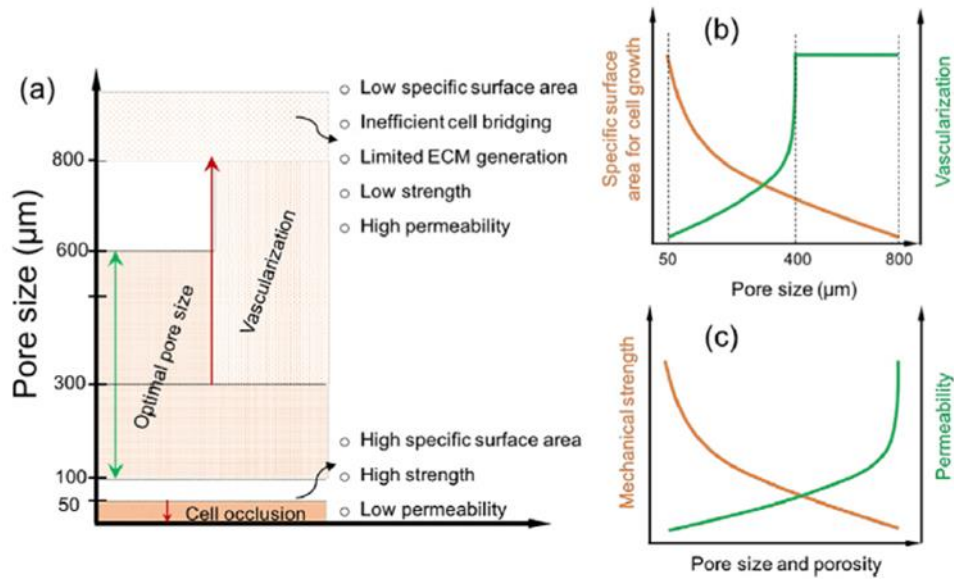
Figure 2.32 - Illustrations of pore size influence on (a) overall biological behavior (b) specific surface area for cell growth and vascularization and (c) mechanical strength and permeability (reproduced from [147]).

2.7. Laser Surface Modification

In SLM fabrication, as already mentioned, the process of 3D manufacturing is carried out by melting powder selectively using laser as an energy source. Laser, or **L**ight **A**mplification by **S**imulated **E**mission of **R**adiation, is a coherent, monochromatic and collimated beam of electromagnetic radiation, i.e., is a device responsible of emitting an amplified optical signal by means of a simulated emission [184–186]. Briefly, this simulated emission is related with the stimulation of atoms in a specific medium in order to emit light in the both same direction and wavelength as the original beam [186]. In this sense, laser is mainly constituted by a gain medium, an energy source (pumping) and a feedback system (optical cavity) [185,186].

For instance, in SLM technique, the machine is equipped with a fiber laser, however many other types of lasers are available for their use in laser systems. In fact, depending on the state or the physical properties of the gain medium, different types of laser can be found, namely, solid state laser (e.g. Nd:YAG, Nd:YVO, fiber lasers), liquid laser (e.g. liquid dyes), gas laser (e.g. CO_2 and excimer) and glass/semiconductor laser (e.g. AlGaAs) [79,184–187]. Moreover, at its operation state, the different types of lasers can function either in a continuous wave (CW), in which the laser beam is emitted continuously, or pulsed mode, where the emission of the beam is performed periodically [187,188]. Considering all these different laser types and operation modes, their selection needs to be performed according to the desired material, i.e., the laser wavelength must match the absorption features of the material that are going to be used [138].

Besides applications like selective laser melting where laser is employed to melt the powder bed to create a 3D final component in a layer-by-layer process, lasers can also be used in using different strategies. When talking about the biomedical field, especially in implantology, it is already widely reported in literature that implant surface features play a crucial role in achieving a good bond and osseointegration and consequently a long-term success of the implant [189–193]. As previously explained, right after implanting surgical procedure, the first biological phenomenon at bone-implant interface consists of protein adhesion and adsorption to the surface, that will consequently lead to cell adherence, proliferation and differentiation for further new bone formation. In this sense, by altering the surface properties of the implant, such as surface topography, energy and roughness, it is possible to promote an earlier osseointegration [189,190,192,194].

Many techniques have been used to perform surface modification such as anodic oxidation, grit blasting, sand blasting, acid etching and coatings [192,195–199]. However, in this type of methods, the surface finish achieved is characterized by a random and uncontrolled surface topography being these methods more prone to leave contaminations on the material surface [195].

Conversely, surface modification by laser is a highly effective and attractive way to improve implant long-term performance once, contrary to conventional routes, it allows to create textures or alter surface chemistry in a controlled, effective and ambient friendly manner [190,200,201]. Moreover, it is important to mention that, by using this strategy, surface features are created without compromising the overall mechanical performance of the material. These surface changes are usually associated with an increased roughness that was already reported in several studies that are preferable over smooth surfaces since it increases implant bone surface contact area and provide a greater bone response [193,194,202,203].

Laser surface texturing (LST) has become one of the most promising solutions to overcome the problems arising from the conventional methods. LST brings several advantages over conventional routes once it is a high-resolution method, that operates considerably fast, at a low cost, with accuracy, precision, reproducibility and control over the process and design, while keeping the bulk properties of the material. Additionally, since it is a technique without direct contact, besides preventing surface contamination, it also avoids tool wear, vibrations and many other unwanted phenomena that occur in conventional routes [188,190,192,204]. Besides that, it has also minimal heat-affected zone, and its flexibility to perform different operations like cutting,

grooving, welding, makes it possible to obtain a final component without the need of additional tooling [187,188,190,192,204]. When regarding biomedical applications, implant surface texturing will not only enhance protein adsorption but also guide cell growth and orientation [192,205].

In general, LST process begins with the application, using laser, of a high energy density on the material surface to promote material ablation, i.e., mass removal of the laser irradiated material [66,195]. Laser ablation process is highly complex and involves a variety of physical and chemical phenomena. When a laser beam is incident on a given material, several physical phenomena can occur according with the material properties, like reflection, absorption, scattering and transmission [188,192]. The absorbed energy is further converted into heat that is further transferred to the material and the environment by conduction, convection and/or radiation. It is important to mention that this temperature distribution is highly dependent not only on the thermophysical properties of the material, but also the laser energy density (i.e. laser processing parameters) [188,192]. After this temperature distribution, different phenomena may be involved to promote material removal [188,192,195]. If the surface temperature reaches the melting point of the material, material removal takes place by melting. As the surface temperature continues to increase until it reaches the boiling point, the material changes from liquid to gas, i.e., vaporization occurs. In some materials, and depending on the laser parameters, sublimation can occur. Moreover, when the material is vaporized, plasma formation may also occur. In fact, if the laser energy density is above a specific threshold, a cloud of vaporized material is formed that will absorb part of the beam energy and, consequently, increase its temperature, until a plasma is formed. In other words, the removed material, in its gas phase forms a plasma plume that is ionized by absorbing the beam energy and form plasma [187,188,206]. These thermal processes will consequently lead to a crater formation on the material surface [190]. Figure 2.33 displays a schematic illustration of the abovementioned process. It is important to mention that these abovementioned phenomena happen considerably fast, which results in a minimal heat-affected zone [79,204].
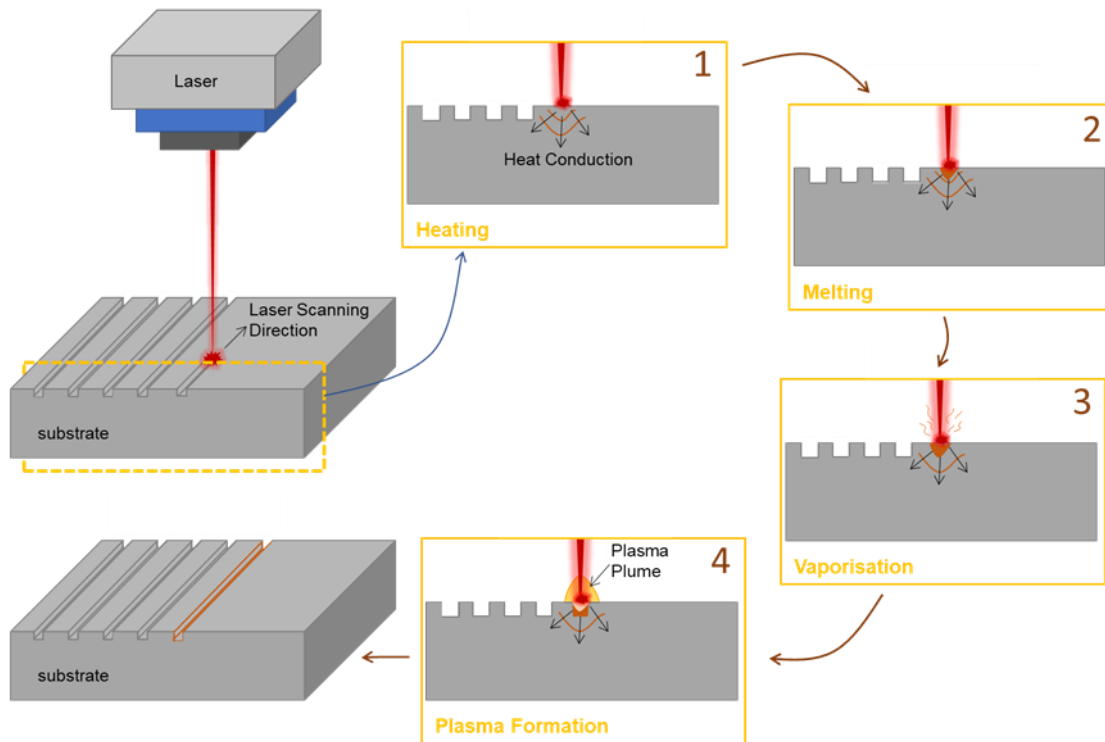
Figure 2.33 - Surface Laser Texturing sequential steps of ablation process.

The creation of a different topography on the surface of the material demands the laser beam motion relative to the substrate. Different textures can be obtained using this technology, by altering the laser processing parameters and design, that can range from the macro-, micro- or to a nanoscale level [190,193,195,207]. These surface geometries vary from holes, grooves, pits, pillars, ridges, etc, being grooves the most common [191,193,195,198,199,203,207,208]. Figure 2.34 shows some of the possible geometries that can be machined by laser.

Generally, these surface topographies will not only increase surface roughness, but also increase the surface area, also altering wettability, increase adhesion to the surface, in addition to having an impact on the cellular behavior [191,204,209]. In literature, several studies reported that the biological behavior is enhanced when using textured surfaces, however, this behavior has been proved to vary according to the texture design [189,198,210,211]. It was already addressed in literature that, these surfaces will improve osseointegration since osteoblastic differentiation and adhesion is also enhanced [203,209].

Mesquita-Guimarães et al. [209] used laser to texture zirconia surfaces according to a square crosslinked configuration, being afterwards coated with bioactive materials that were further sintered also by laser. *In vitro* results using MC3T3-E1 osteoblast-like cells revealed that compared with the non-textured surfaces, cell viability increased about 40% on the textured surfaces and 90% on the textured surfaces with the bioactive coating.
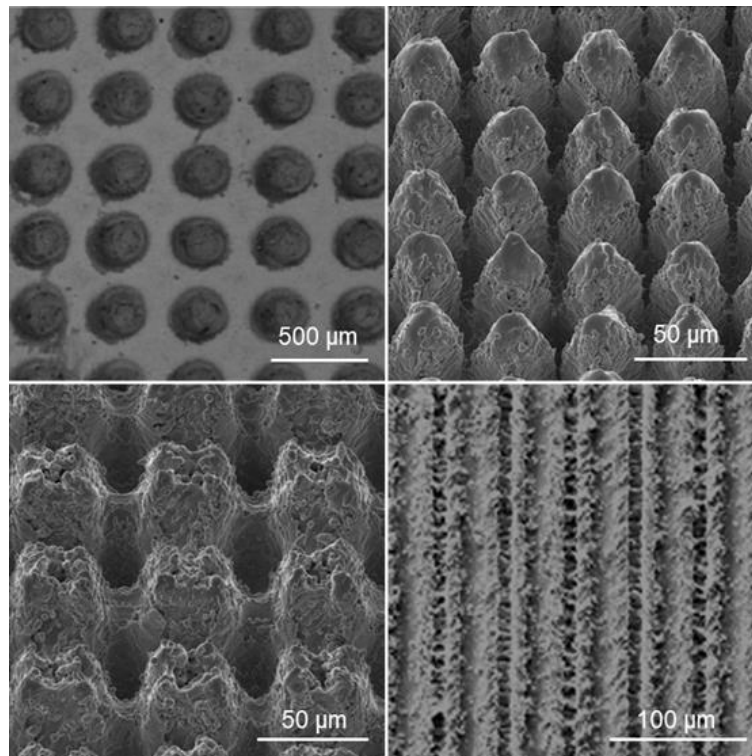
Figure 2.34 - Examples of laser textured surface topographies (adapted from [191,202,212]).

Behera et al. [213] made a micro-dimpled texture on Ti6Al4V surfaces using laser and found that cell adhesion percentage and average cell area were significantly improved in textured surfaces, when compared with non-textured Ti6Al4V surfaces. In the same study, a biphasic calcium phosphate coating was applied on non-textured and textured Ti6Al4V surfaces, being concluded that the coated textured surfaces were the one, among all groups, that displayed the maximum cell spreading and proliferation. Xu and coworkers [207] were inspired on fish scales and micro bulges of shrimp to produce laser textured micro-overlapping structures on Ti6Al4V implants. Cell attachment, proliferation and osteogenic differentiation was improved in these patterns.

Coathup et al. [195] assessed the osseointegration behavior of Ti6Al4V laser-textured implants *in vivo*. In this study, groove textures were performed and implanted in an ovine model for 6 weeks. Results revealed that, compared with machine-finish surface laser textured structures has an increased interfacial strength and bone-implant contact.

In another study, Yu et al. [214] assessed the cell behavior on Ti6Al4V grooved textures and found that these textures improved cell adhesion, having a significant role in cell growth and contact guidance. In fact, regarding these grooved surfaces, in a biological environment, cells tend to align, adhere and spread over this texture [191]. This phenomenon of orientation control of the cells is commonly known as "contact guidance", as the cells are adhered, aligned and elongated according

to this linear channel [191,198,208]. Chen et al. [198] also proved this phenomenon when over 90% of the cells used were aligned with the Ti6Al4V laser microgrooves under study, after 4h. Besides, when this feature has a dimension superior to the cell size, bone ingrowth may also occur, which will enhance the mechanical anchoring [198].

2.8. Multi-material approaches for multi-functionality

Combining different materials to produce a multi-material part will allow to gather properties from two distinct materials and create a multi-functional component, which is difficult or impossible to obtain in mono-material approaches.

Several attempts to produce multi-material components, for a wide range of applications, and their characterization have been reported in literature. In fact, SLM equipment can be extended and adapted to multi-material productions, as demonstrated by Scaramuccia et al. [215] that used an in-house multi-material platform to produce Ti6Al4V-Inconel 718 bimetallic components aiming aerospace applications (turbine blades). In their study, the main focus was to gather low density from Ti6Al4V with Inconel ability to retain its strength in a wide range of temperatures. The experimental procedure went through production of two single materials to obtain optimal processing parameters for both materials, follow by a composite production and finally a graded component. Good results for the composite materials were found, without cracks, below Inconel 718 weight percentages of 20%, whilst the multi-graded components (5, 10, 15 and 20 wt.% gradient) were also successfully achieved without delamination between layers and crack free. In a different study, aiming high temperature and corrosive environment applications (like gas turbines, water reactors, etc), Mei et al. [216] also used Inconel, together with 316L stainless steel to create sandwich SLM-fabricated bimetallic parts being their interfacial characteristics and mechanical properties investigated. Despite a good metallurgical bonding at the interfaces was achieved, some cracks and holes were found close to the interfaces. Chen et al. [217] also manufactured by SLM bimetallic 316L/CuSn10 Tin bronze structures in order to combine steel' strength and corrosion resistance with bronze' high heat conduction and wear resistance for industrial applications. The differences in the physical properties of the two materials led to cracks near to 316L region and fusion zone, although a good metallurgical bonding was achieved at the interface. In another study, Chen and his coworkers produced 316L-CuSn10 parts (for fusion reactors, automobile, aviation industries, etc), and concluded that no interfacial macrocracks were

observed and good interfacial bonding strength obtained, being the ultimate tensile strength higher for multi-material specimens, compared with mono-material CuSn10 ones [218].

Interfacial characterization on AlSi10Mg-C18400 copper alloy multi-material parts produced by SLM was performed by Sing and his coworkers [219]. The high conductivity of cooper with the lower weight and cost of aluminum may create a multi-functional component that can be applied in joints for electrical components, solar collectors, transition pieces for high direct-current bus systems, etc. Results found that a good metallurgical bonding was obtained though the presence of an intermetallic Al_2Cu was detected, that may change the fracture mechanism from ductile to brittle cleavage in this region. In a different study, Demir et al. developed SLM-produced Fe/Al-12Si multi-material components (aiming hybrid or transitional junction elements, like nodes), which consists of pure Fe and Al-12Si on the extremities and an interface made of Fe/Al-12Si composite and reported large crack formation at the composite region due to incompatibilities between these two materials.

Zhang et al. [220] produced bimetallic CuSn-18Ni300 porous structures by SLM to gather CuSn alloy thermal conductivity, ductility and corrosion resistance with 18Ni300 strength. Results indicate that interface microhardness displayed a gradient distribution, decreasing from 18Ni300 to CuSn part, whilst compression behavior followed a sequence of first linear elasticity, first collapse plateau, second linear elasticity, second collapse plateau and final densification behavior. Energy absorption was higher as porosity decreases, being enhanced on bimetallic porous structures.

In a different concept of multi-material bimetallic structures, Ghasri-Khouzani et al. [221] produced 316L SS lattice structures by SLM and, by combining vacuum-assisted melt infiltration casting technique, aluminum alloy was used to fill the 316L cavities. For comparison purposes, SS single lattice structures and monolithic aluminum cast specimens were produced. A continuous gap found at the interface did not allow a change on the tensile properties of the multi-material structure when compared with SS lattice structures, nevertheless compressive properties were considerably higher. Focusing on biomedical applications, like implants, Turalıoglu et al. [222] developed a bimetallic Ti6Al4V/316L parts by SLM with a TiO_2 ceramic coating in order to take advantage of high strength and lightweight of Ti6Al4V with low cost and high load carrying ability of 316L. Wear and corrosion resistance were enhanced on the specimens with anodic oxidation compared with untreated 316L and bimetallic components.

In the biomedical field, combining different material families for meeting specific requirements has also been widely reported. Avila et al. [223] using laser-engineered net shaping

technique effectively produced Ti6Al4V-Hydroxyapatite composites to increase Ti6Al4V biocompatibility and wear resistance. Tribological tests displayed reduced wear rates, when worn against ZrO_2 counter ball in DMEM, whilst *in vivo* results indicate an improved tissue response with push-out tests revealing higher shear modulus. In a different study, also for improving Ti6Al4V tribological performance, Sahasrabudhe and Bandyopadhyay [224] used LENS, in an oxygen free nitrogen-argon environment, to manufacture a Ti6Al4V-calcium phosphate-nitride coating onto a Ti6Al4V plate. Different composites with 0%, 2% and 5 wt% calcium phosphate addition were produced being the coating with 5% CaP the one that showed the highest hardness and lowest wear rate, compared with untreated group. Li et al. [225] successfully fabricated hybrid interconnected porous structures made of Ti6Al4V-βTCP slurry (maximum 10 wt.% βTCP content) by three-dimensional fiber deposition, having compressive strength and young's modulus between trabecular and cortical bone. These structures, in a pilot *in vivo* study (implanted intramuscularly in dogs for 12 weeks), when compared with non or lower amount of βTCP, revealed an enhanced osteoinductive potential. Other study, performed by XiaoHui et al. [226] developed an aliphatic-polycarbonate/hydroxyapatite scaffold by selective laser sintering, showing that composites optimal percentage was 10 wt% of hydroxyapatite with the scaffolds having perfect interconnected porosity, with HAp particles fully or partially embedded in the matrix. An *in vivo* study regarding Ti6Al4V electron beam melting porous structures coated with hydroxyapatite demonstrated enhanced bone formation and osseointegration on these multi-material components [227].

Henriques et al. [228] performed laser surface structuring on Ti6Al4V substrates and then filled the cavities with polymeric PEEK by hot pressing to investigate Ti6Al4V-PEEK bonding strength and, compared with conventional grit-blasting group, shear bond strength was found to be expressively higher. Additionally, focused on artificial cervical disc applications, another study that apply a coating on Ti6Al4V substrates, namely PEEK/5 wt.% ZrO_2, revealed that the tribological performance was significantly improved, in comparison with bare Ti6Al4V [229].

PEEK has also been found in one study along with bioactive hydroxyapatite as composite coating on SS substrate, aiming biomedical applications, reporting that higher amounts of hydroxyapatite on the PEEK-HAp coating enhanced its bioactivity although adhesion strength of the coating was diminished [230]. As stated by Bakar et al. [231] the amount of hydroxyapatite particles in the final composite will influence the final mechanical properties obtained, i.e., the higher the amount of HAp particles, will increase overall composite hardness, but strength and strain to fracture is reduced. In a different study, it was reported that βTCP-PEEK composites allow

to obtained mechanical properties matching the ones found for human bone despite these composites did not have advantageous effect on osteoblast cell proliferation [232].

An *in vitro* and *in vivo* study, performed by Liu et al. [233] developed a 3D-printed PEEK scaffold modified with methacrylated chitosan/polyhedral oligometric silsesquioxane bioactive nanocomposite to improve PEEK bioactive properties. These porous structures together with the modified scaffolds offered not only a suitable environment for cell adhesion, proliferation and osteogenic differentiation from *in vitro* results, but also enabled *in vivo* bone regeneration, when compared with PEEK scaffolds.

To sum, the main focus of the present phD thesis is to produce a hip implant based on multi-functional multi-material designs that increases the lifetime of these solutions for patients undergoing THA.

The weaknesses present in nowadays hip implants, in terms of poor bone to implant contact, inefficient osseointegration and stress shielding effect, may lead to implant failure. The main reasons behind such weaknesses go from the chosen implant material till to its surface morphology. Ideally, an implant should exhibit not only good biocompatibility to avoid undesired biological reactions but also bioactive properties to trigger a biological reaction in terms of bone integration and regeneration. Also, these features should be achieved without compromising the mechanical requirements of the implant, for instance, it should have the elastic modulus similar to that of bone and guarantee body corrosion and wear resistance. A well-defined and controlled structure, especially on its surface, is also an asset for elastic modulus tailoring and promoting bone ingrowth thus guaranteeing mechanical anchoring to the implant.

References

[1]   R.L. Drake, A.W. Vogl, A.W.. Mitchell, Gray's Anatomy for Students, Fourth Edi, Elsevier, 2019.

[2]   E. Varini, Primary stability in cementless total hip replacement: measurement techniques and aided-surgery, Università degli Studi di Bologna, 2007.

[3]   C. Hu, D. Ashok, D.R. Nisbet, V. Gautam, Bioinspired surface modification of orthopedic implants for bone tissue engineering, Biomaterials. 219 (2019) 119366. doi:10.1016/j.biomaterials.2019.119366.

[4]   X. Zhao, J.M. Courtney, H. Qian, Bioactive materials in medicine - Design and applications, Woodhead P, 2011.

[5]   M.M. Stevens, Biomaterials for bone tissue engineering, Materials Today. 11 (2008) 18–

25. doi:10.1016/S1369-7021(08)70086-5.

[6]   G. Zhu, T. Zhang, M. Chen, K. Yao, X. Huang, B. Zhang, Y. Li, J. Liu, Y. Wang, Z. Zhao, Bone physiological microenvironment and healing mechanism: Basis for future bone-tissue engineering scaffolds, Bioactive Materials. 6 (2021) 4110–4140. doi:10.1016/j.bioactmat.2021.03.043.

[7]   X. Wang, S. Xu, S. Zhou, W. Xu, M. Leary, P. Choong, M. Qian, M. Brandt, Y.M. Xie, Topological design and additive manufacturing of porous metals for bone scaffolds and orthopaedic implants: A review, Biomaterials. 83 (2016) 127–141. doi:10.1016/j.biomaterials.2016.01.012.

[8]   S. Kanwar, S. Vijayavenkataraman, Design of 3D printed scaffolds for bone tissue engineering: A review, Bioprinting. 24 (2021) e00167. doi:10.1016/j.bprint.2021.e00167.

[9]   S. Affatato, Perspectives in Total Hip Arthroplasty - Advances in Biomaterials and their Tribological Interactions, Woodhead P, 2014. http://www.sciencedirect.com/science/article/pii/B9781782420316500167.

[10]   L. Molini, M. Precerutti, A. Gervasio, F. Draghi, S. Bianchi, Hip: Anatomy and US technique, Journal of Ultrasound. 14 (2011) 99–108. doi:10.1016/j.jus.2011.03.004.

[11]   S.J.F. MD, 100 Questions & Answers About Hip Replacement, Jones and, 2010.

[12]   D. Shekhawat, A. Singh, A. Patnaik, Tribo-behaviour of biomaterials for hip arthroplasty, Materials Today: Proceedings. 44 (2021) 4809–4815. doi:10.1016/j.matpr.2020.11.420.

[13]   H.S. Sandhu, Journey to total hip arthoplasty, Journal of Arthroscopy and Joint Surgery. 2 (2015) 1–2. doi:10.1016/j.jajs.2014.12.007.

[14]   S.J. Mellon, A.D. Liddle, H. Pandit, Hip replacement: Landmark surgery in modern medical history, Maturitas. 75 (2013) 221–226. doi:10.1016/j.maturitas.2013.04.011.

[15]   S. Pramanik, A.K. Agarwal, K.N. Rai, Chronology of total hip replacement and materials development, Trends in Biomaterials and Artificial Organs. 19 (2005) 15–26.

[16]   A.J. Sophia Fox, A. Bedi, S.A. Rodeo, The basic science of articular cartilage: Structure, composition, and function, Sports Health. 1 (2009) 461–468. doi:10.1177/1941738109350438.

[17]   E.B. Hunziker, Articular cartilage repair: Basic science and clinical progress. A review of the current status and prospects, Osteoarthritis and Cartilage. 10 (2001) 432–463. doi:10.1053/joca.2002.0801.

[18]   U. Holzwarth, G. Cotogno, Total Hip Arthroplasty - State of the Art, Challenges and Prospects, 2012. doi:10.2788/31286.

[19]   S. Salih, A. Hamer, Hip and knee replacement, Surgery. 31 (2013) 482–487. doi:10.1016/j.mpsur.2013.06.005.

[20]   OECD/EU, Health at a Glance: Europe 2016 - State of Health in the EU Cycle, OECD Publishing, Paris, 2016. doi:10.1787/9789264265592-en.

[21]   J. Quinn, R. Mcfadden, C. Chan, L. Carson, Titanium for Orthopedic Applications: An Overview of Surface Modification to Improve Biocompatibility and Prevent Bacterial Biofilm

Formation, ISCIENCE. 23 (2020) 101745. doi:10.1016/j.isci.2020.101745.

[22]   C. Delaunay, C. Brand, SoFCOT Total Hip Arthroplasty Register - Biennial Report 2020, 2020.

[23]   National Joint Registry - 17th Annual Report for England, Wales, Northern Ireland, the Isle of Man and the States of Guernsey, 2020.

[24]   Swiss National Hip & Knee Joint Registry - Report 2020. Annual Report of the SIRIS Registry, Hip & Knee, 2012-2019, 2020.

[25]   I. Urakcheeva, A. Biondi, M. Torre, Italian Arthroplasty Registry. Annual Report 2019 – Addendum. Roma: Il Pensiero Scientifico Editore, 2020. doi:10.3934/math.2020i.

[26]   Autralian Orthopaedic Association National Joint Replacement Registry (AOANJRR). Hip, Knee & Shoulder Arthroplasty: 2020 Annual Report, Adelaide: AOA, 2020.

[27]   The New Zealand Joint Registry. Twenty-one year report (January 1999 to December 2019), 2021.

[28]   L. Zagra, Advances in hip arthroplasty surgery: What is justified?, EFORT Open Reviews. 2 (2017) 171–178. doi:10.1302/2058-5241.2.170008.

[29]   S.R. Knight, R. Aujla, S.P. Biswas, Total Hip Arthroplasty - over 100 Years of Operative History, Orthopaedic Reviews. 3 (2011) 2–4. doi:10.4081/or.2011.16.

[30]   Q. Chen, G.A. Thouas, Metallic implant biomaterials, Materials Science and Engineering R: Reports. 87 (2015) 1–57. doi:10.1016/j.mser.2014.10.001.

[31]   E. Manzi, R. Pezzela, M. Bisaccia, L. Meccariello, G. Rinonapoli, A. Schiavone, C. IbáñezVicente, D. Palmieri, G. Colleluori, P. Ferrara, A. Caraffa, The history of hip replacement and one approach, Canadian Open Orthopaedics and Traumatology Journal. 3 (2016) 50–60.

[32]   Norwegian National Advisory Unit on Arthroplasty and Hip Fractures: Annual Report 2020, 2020.

[33]   A. Grimberg, J. Lützner, O. Melsheimer, M. Morlock, A. Steinbrück, The German Arthroplasty Registry - Annual Report 2020, 2020. doi:10.3934/allergy.2021003.

[34]   Canadian Institute for Health Information, Hip and Knee Replacements in Canada, 2017-2018: Canadian Joint Replacement Registry Annual Report. Ottawa, ON:CIHI, 2019.

[35]   S. Kurtz, K. Ong, E. Lau, F. Mowat, M. Halpern, Projections of primary and revision hip and knee arthroplasty in the United States from 2005 to 2030, Journal of Bone and Joint Surgery - Series A. 89 (2007) 780–785. doi:10.2106/JBJS.F.00222.

[36]   American Joint Replacement Registry, (AJRR): 2019 Annual Report 2019. Rosemont, IL: American Academy of Orthopaedic Surgeons (AAOS), 2019.

[37]   D. Synthes, Surgical Technique: Approach Patients with Confidence, n.d.

[38]   M.R. Angerame, D.A. Dennis, Surgical Approaches for Total Hip Arthroplasty, Annals of Joint (AOJ). 3 (2018) 1–15. doi:10.21037/aoj.2018.04.08.

[39]   V.M. Moretti, Z.D. Post, Surgical Approaches for Total Hip Arthroplasty, Indian Journal of

Orthopaedicsrnal. 51 (2017) 368–376. doi:10.4103/ortho.IJOrtho_317_16.

[40]   S. Petis, J.L. Howard, B.L. Lanting, E.M. Vasarhelyi, Surgical approach in primary total hip arthroplasty: Anatomy, technique and clinical outcomes, Canadian Journal of Surgery. 58 (2015) 128–139. doi:10.1503/cjs.007214.

[41]   J.R.H. Foran, S.J. Fischer, Total Hip Replacement, (2015). https://orthoinfo.aaos.org/en/treatment/total-hip-replacement/ (accessed April 30, 2020).

[42]   M.W. Shrader, Total Hip Arthroplasty and Hip Resurfacing Arthroplasty in the Very Young Patient, Orthopedic Clinics of North America. 43 (2012) 359–367. doi:10.1016/j.ocl.2012.05.005.

[43]   M. Franchi, M. Fini, D. Martini, E. Orsini, L. Leonardi, A. Ruggeri, G. Giavaresi, V. Ottani, Biological fixation of endosseous implants, Micron. 36 (2005) 665–671. doi:10.1016/j.micron.2005.05.010.

[44]   P. Kuzyk, E. Schemitsch, The basic science of peri-implant bone healing, Indian Journal of Orthopaedics. 45 (2011) 108–15. doi:10.4103/0019-5413.77129.

[45]   A.F. Mavrogenis, R. Dimitriou, J. Parvizi, G.C. Babis, Biology of implant osseointegration, Journal of Musculoskeletal Neuronal Interactions. 9 (2009) 61–71.

[46]   R. Tejero, E. Anitua, G. Orive, Toward the biomimetic implant surface: Biopolymers on titanium-based implants for bone regeneration, Progress in Polymer Science. 39 (2014) 1406–1447. doi:10.1016/j.progpolymsci.2014.01.001.

[47]   M.S. Ghiasi, J. Chen, A. Vaziri, E.K. Rodriguez, A. Nazarian, Bone fracture healing in mechanobiological modeling: A review of principles and methods, Bone Reports. 6 (2017) 87–100. doi:10.1016/j.bonr.2017.03.002.

[48]   F. Marco, F. Milena, G. Gianluca, O. Vittoria, Peri-implant osteogenesis in health and osteoporosis, Micron. 36 (2005) 630–644. doi:10.1016/j.micron.2005.07.008.

[49]   M.A. Matsumoto, C.C. Biguetti, A.C. Fonseca, P.P. Saraiva, Bone Tissue Healing Dynamics: From Damage to Reconstruction, Journal of Molecular Signaling Updates. 1 (2016) 33–40.

[50]   L.E. Bayliss, D. Culliford, A.P. Monk, S. Glyn-Jones, D. Prieto-Alhambra, A. Judge, C. Cooper, A.J. Carr, N.K. Arden, D.J. Beard, A.J. Price, The effect of patient age at intervention on risk of implant revision after total replacement of the hip or knee: a population-based cohort study, The Lancet. 389 (2017) 1424–1430. doi:10.1016/S0140-6736(17)30059-4.

[51]   S.D. Ulrich, T.M. Seyler, D. Bennett, R.E. Delanois, K.J. Saleh, I. Thongtrangan, M. Kuskowski, E.Y. Cheng, P.F. Sharkey, J. Parvizi, J.B. Stiehl, M.A. Mont, Total hip arthroplasties: What are the reasons for revision?, International Orthopaedics. 32 (2008) 597–604. doi:10.1007/s00264-007-0364-3.

[52]   G. Liu, X. Zhang, X. Chen, Y. He, L. Cheng, M. Huo, J. Yin, F. Hao, S. Chen, P. Wang, S. Yi, L. Wan, Z. Mao, Z. Chen, X. Wang, Z. Cao, J. Lu, Additive manufacturing of structural materials, Materials Science and Engineering R: Reports. 145 (2021) 100596. doi:10.1016/j.mser.2020.100596.

[53]   M.M. Costa, T.A. Dantas, F. Bartolomeu, N. Alves, F.S. Silva, G. Miranda, F. Toptan, Corrosion behaviour of PEEK or β-TCP-impregnated Ti6Al4V SLM structures targeting biomedical applications, Transactions of Nonferrous Metals Society of China. 29 (2019) 2523–2533. doi:10.1016/S1003-6326(19)65160-5.

[54]   N.S. Manam, W.S.W. Harun, D.N.A. Shri, S.A.C. Ghani, T. Kurniawan, M.H. Ismail, M.H.I. Ibrahim, Study of corrosion in biocompatible metals for implants: A review, Journal of Alloys and Compounds. 701 (2017) 698–715. doi:10.1016/j.jallcom.2017.01.196.

[55]   M. Sampaio, M. Buciumeanu, B. Henriques, F.S. Silva, J.C.M. Souza, J.R. Gomes, Tribocorrosion behavior of veneering biomedical PEEK to Ti6Al4V structures, Journal of the Mechanical Behavior of Biomedical Materials. 54 (2016) 123–130. doi:10.1016/j.jmbbm.2015.09.010.

[56]   M. Geetha, A.K. Singh, R. Asokamani, A.K. Gogia, Ti based biomaterials, the ultimate choice for orthopaedic implants – A review, Progress in Materials Science. 54 (2009) 397–425. doi:10.1016/j.pmatsci.2008.06.004.

[57]   B. Bhushan, Modern Tribology Handbook, Volume One, CRC Press, 2000.

[58]   G.B. Raymond, Mechanical wear fundamentals and testing, Second Edi, Marcel Dekker, 2004. http://scholar.google.com/scholar?hl=en&btnG=Search&q=intitle:Mechanical+Wear+Fundamentals+and+Testing#5.

[59]   B. Bhushan, Principles and Applications of Tribology, Second Edi, John Wiley & Sons, Ltd, 2013. doi:10.1002/9781118403020.

[60]   J.B. Park, J.D. Bronzino, Biomaterials - Principles and Applications, CRC Press, 2003.

[61]   J.-P. Boutrand, Biocompatibility and performance of medical devices, Woodhead P, 2012.

[62]   B.D. Ratner, A.S. Hoffman, F.J. Schoen, J.E. Lemons, Biomaterials Science - An Introduction to Materials in Medicine, Academic P, 1996. doi:10.1016/B978-0-08-087780-8.00148-0.

[63]   J. Čapek, M. Machová, M. Fousová, J. Kubásek, D. Vojtěch, J. Fojt, E. Jablonská, J. Lipov, T. Ruml, Highly porous, low elastic modulus 316L stainless steel scaffold prepared by selective laser melting, Materials Science and Engineering C. 69 (2016) 631–639. doi:10.1016/j.msec.2016.07.027.

[64]   X. Lin, S. Yang, K. Lai, H. Yang, T.J. Webster, L. Yang, Orthopedic implant biomaterials with both osteogenic and anti-infection capacities and associated in vivo evaluation methods, Nanomedicine: Nanotechnology, Biology, and Medicine. 13 (2017) 123–142. doi:10.1016/j.nano.2016.08.003.

[65]   W.S.W. Harun, M.S.I.N. Kamariah, N. Muhamad, S.A.C. Ghani, F. Ahmad, Z. Mohamed, A review of powder additive manufacturing processes for metallic biomaterials, Powder Technology. 327 (2018) 128–151. doi:10.1016/j.powtec.2017.12.058.

[66]   C.G. Moura, O. Carvalho, L.M.V. Gonçalves, M.F. Cerqueira, R. Nascimento, F. Silva, Laser surface texturing of Ti-6Al-4V by nanosecond laser: Surface characterization, Ti-oxide layer analysis and its electrical insulation performance, Materials Science and Engineering C. 104 (2019) 109901. doi:10.1016/j.msec.2019.109901.

[67] F. Bartolomeu, M. Buciumeanu, E. Pinto, N. Alves, F.S. Silva, O. Carvalho, G. Miranda, Wear behavior of Ti6Al4V biomedical alloys processed by selective laser melting, hot pressing and conventional casting, Transactions of Nonferrous Metals Society of China (English Edition). 27 (2017) 829–838. doi:10.1016/S1003-6326(17)60060-8.

[68] F. Bartolomeu, S. Faria, O. Carvalho, E. Pinto, N. Alves, F.S. Silva, G. Miranda, Predictive models for physical and mechanical properties of Ti6Al4V produced by Selective Laser Melting, Materials Science and Engineering A. 663 (2016) 181–192. doi:10.1016/j.msea.2016.03.113.

[69] D. Shi, Introduction to Biomaterials, World Scie, Tsinghua University Press, 2006.

[70] F. Bartolomeu, M. Buciumeanu, M.M. Costa, N. Alves, M. Gasik, F.S. Silva, G. Miranda, Multi-material Ti6Al4V & PEEK cellular structures produced by Selective Laser Melting and Hot Pressing: a tribocorrosion study targeting orthopedic applications, Journal of the Mechanical Behavior of Biomedical Materials. 89 (2019) 54–64. doi:10.1016/j.jmbbm.2018.09.009.

[71] Q. Liu, Y. Wang, H. Zheng, K. Tang, L. Ding, H. Li, S. Gong, Microstructure and mechanical properties of LMD-SLM hybrid forming Ti6Al4V alloy, Materials Science and Engineering A. 660 (2016) 24–33. doi:10.1016/j.msea.2016.02.069.

[72] B. Henriques, Bond strength enhancement of metal-ceramic dental restorations by FGM design, Universidade do Minho, 2012.

[73] ASTM:F136-12a, Standard Specification for Wrought Titanium-6Aluminum-4Vanadium ELI (Extra Low Interstitial) Alloy for Surgical Implant Applications (UNS R56401), 2012. doi:10.1520/F0136-13R21E01.

[74] J.A. Tamayo, M. Riascos, C.A. Vargas, L.M. Baena, Additive manufacturing of Ti6Al4V alloy via electron beam melting for the development of implants for the biomedical industry, Heliyon. 7 (2021) 206892. doi:10.1016/j.heliyon.2021.e06892.

[75] F. Bartolomeu, M. Sampaio, O. Carvalho, E. Pinto, N. Alves, J.R. Gomes, F.S. Silva, G. Miranda, Tribological behavior of Ti6Al4V cellular structures produced by Selective Laser Melting, Journal of the Mechanical Behavior of Biomedical Materials. 69 (2017) 128–134. doi:10.1016/j.jmbbm.2017.01.004.

[76] A. Bandyopadhyay, F. Espana, V.K. Balla, S. Bose, Y. Ohgami, N.M. Davies, Influence of porosity on mechanical properties and in vivo response of Ti6Al4V implants, Acta Biomaterialia. 6 (2010) 1640–1648. doi:10.1016/j.actbio.2009.11.011.

[77] M. Long, H.J. Rack, Titanium alloys in total joint replacement–a materials science perspective., Biomaterials. 19 (1998) 1621–1639. doi:https://doi.org/10.1016/S0142-9612(97)00146-4.

[78] W. Wang, C.K. Poh, Titanium Alloys in Orthopaedics, Titanium Alloys - Advances in Properties Control, Jan Sieniawski and Waldemar Ziaja, IntechOpen, 2013. doi:10.5772/55353.

[79] J.W. Mwangi, L.T. Nguyen, V.D. Bui, T. Berger, H. Zeidler, A. Schubert, Nitinol manufacturing and micromachining: A review of processes and their suitability in processing medical-grade nitinol, Journal of Manufacturing Processes. 38 (2019) 355–

369. doi:10.1016/j.jmapro.2019.01.003.

[80]   N. Shayesteh Moghaddam, S.E. Saghaian, A. Amerinatanzi, H. Ibrahim, P. Li, G.P. Toker, H.E. Karaca, M. Elahinia, Anisotropic tensile and actuation properties of NiTi fabricated with selective laser melting, Materials Science and Engineering A. 724 (2018) 220–230. doi:10.1016/j.msea.2018.03.072.

[81]   S. Saedi, A.S. Turabi, M.T. Andani, C. Haberland, H. Karaca, M. Elahinia, The influence of heat treatment on the thermomechanical response of Ni-rich NiTi alloys manufactured by selective laser melting, Journal of Alloys and Compounds. 677 (2016) 204–210. doi:10.1016/j.jallcom.2016.03.161.

[82]   D. Axinte, Y. Guo, Z. Liao, A.J. Shih, R. M'Saoubi, N. Sugita, Machining of biocompatible materials — Recent advances, CIRP Annals - Manufacturing Technology. 68 (2019) 629–652. doi:10.1016/j.cirp.2019.05.003.

[83]   T. Deepan Bharathi Kannan, P. Sathiya, T. Ramesh, Experimental investigation and characterization of laser welded NiTinol shape memory alloys, Journal of Manufacturing Processes. 25 (2017) 253–261. doi:10.1016/j.jmapro.2016.12.006.

[84]   R. Neupane, Z. Farhat, Wear and dent resistance of superelastic TiNi alloy, Wear. 301 (2013) 682–687. doi:10.1016/j.wear.2012.11.017.

[85]   memry SAES group, Introduction to Nitinol, 2017.

[86]   M. Bram, A. Ahmad-Khanlou, A. Heckmann, B. Fuchs, H.P. Buchkremer, D. Stöver, Powder metallurgical fabrication processes for NiTi shape memory alloy parts, Materials Science and Engineering A. 337 (2002) 254–263. doi:10.1016/S0921-5093(02)00028-X.

[87]   S.K. S, L. Marandi, V.K. Balla, S. Bysakh, D. Piorunek, G. Eggeler, M. Das, I. Sen, Microstructure – Property correlations for additively manufactured NiTi based shape memory alloys, Materialia. 8 (2019) 100456. doi:10.1016/j.mtla.2019.100456.

[88]   M.T. Andani, N. Shayesteh Moghaddam, C. Haberland, D. Dean, M.J. Miller, M. Elahinia, Metals for bone implants. Part 1. Powder metallurgy and implant rendering, Acta Biomaterialia. 10 (2014) 4058–4070. doi:10.1016/j.actbio.2014.06.025.

[89]   X. Ma, H. Wang, H. Xie, J. Qu, X. Chen, F. Chen, Q. Song, H. Yin, Engineering the porosity and superelastic behaviors of NiTi alloys prepared by an electro-assisted powder metallurgical route in molten salts, Journal of Alloys and Compounds. 794 (2019) 455–464. doi:10.1016/j.jallcom.2019.04.166.

[90]   C. Ma, M.T. Andani, H. Qin, N.S. Moghaddam, H. Ibrahim, A. Jahadakbar, A. Amerinatanzi, Z. Ren, H. Zhang, G.L. Doll, Y. Dong, M. Elahinia, C. Ye, Improving surface finish and wear resistance of additive manufactured nickel-titanium by ultrasonic nano-crystal surface modification, Journal of Materials Processing Technology. 249 (2017) 433–440. doi:10.1016/j.jmatprotec.2017.06.038.

[91]   A.N. Alagha, S. Hussain, W. Zaki, Additive manufacturing of shape memory alloys: A review with emphasis on powder bed systems, Materials & Design. 204 (2021) 109654. doi:10.1016/j.matdes.2021.109654.

[92]   R. Neupane, Z. Farhat, Wear mechanisms of nitinol under reciprocating sliding contact, Wear. 315 (2014) 25–30. doi:10.1016/j.wear.2014.02.018.

[93]   M. Elahinia, N. Shayesteh Moghaddam, M. Taheri Andani, A. Amerinatanzi, B.A. Bimber, R.F. Hamilton, Fabrication of NiTi through additive manufacturing: A review, Progress in Materials Science. 83 (2016) 630–663. doi:10.1016/j.pmatsci.2016.08.001.

[94]   M. Mehrpouya, A. Gisario, M. Elahinia, Laser welding of NiTi shape memory alloy: A review, Journal of Manufacturing Processes. 31 (2018) 162–186. doi:10.1016/j.jmapro.2017.11.011.

[95]   Johnson Matthey Medical Components, Nitinol Technical Specifications: Discover the Unique Properties of Nitinol, (2018). http://jmmedical.com/resources/221/Nitinol-Technical-Properties.html (accessed May 6, 2020).

[96]   R. Pfeifer, C.W. Müller, C. Hurschler, S. Kaierle, V. Wesling, H. Haferkamp, Adaptable orthopedic shape memory implants, Procedia CIRP. 5 (2013) 253–258. doi:10.1016/j.procir.2013.01.050.

[97]   N. Levintant-Zayonts, G. Starzynski, M. Kopec, S. Kucharski, Characterization of NiTi SMA in its unusual behaviour in wear tests, Tribology International. 137 (2019) 313–323. doi:10.1016/j.triboint.2019.05.005.

[98]   L. Zhang, Z.Y. He, Y.Q. Zhang, Y.H. Jiang, R. Zhou, Enhanced in vitro bioactivity of porous NiTi-HA composites with interconnected pore characteristics prepared by spark plasma sintering, Materials and Design. 101 (2016) 170–180. doi:10.1016/j.matdes.2016.03.128.

[99]   R. Agarwal, A.J. García, Biomaterial strategies for engineering implants for enhanced osseointegration and bone repair, Advanced Drug Delivery Reviews. 94 (2015) 53–62. doi:10.1016/j.addr.2015.03.013.

[100]   S. Verma, N. Sharma, S. Kango, S. Sharma, Developments of PEEK (Polyetheretherketone) as a biomedical material: A focused review, European Polymer Journal. 147 (2021) 110295. doi:10.1016/j.eurpolymj.2021.110295.

[101]   A. Kurella, N.B. Dahotre, Surface modification for bioimplants: The role of laser surface engineering, 2005. doi:10.1177/0885328205052974.

[102]   A.H.C. Poulsson, D. Eglin, S. Zeiter, K. Camenisch, C. Sprecher, Y. Agarwal, D. Nehrbass, J. Wilson, R.G. Richards, Osseointegration of machined, injection moulded and oxygen plasma modified PEEK implants in a sheep model, Biomaterials. 35 (2014) 3717–3728. doi:10.1016/j.biomaterials.2013.12.056.

[103]   F. Chen, H. Ou, B. Lu, H. Long, A constitutive model of polyether-ether-ketone (PEEK), Journal of the Mechanical Behavior of Biomedical Materials. 53 (2016) 427–433. doi:10.1016/j.jmbbm.2015.08.037.

[104]   A. Haleem, M. Javaid, Polyether ether ketone (PEEK) and its 3D printed implants applications in medical field: An overview, Clinical Epidemiology and Global Health. 7 (2019) 571–577. doi:10.1016/j.cegh.2019.01.003.

[105]   A. Haleem, M. Javaid, Polyether ether ketone (PEEK) and its manufacturing of customised 3D printed dentistry parts using additive manufacturing, Clinical Epidemiology and Global Health. 7 (2019) 654–660. doi:10.1016/j.cegh.2019.03.001.

[106]   M. He, Y. Huang, H. Xu, G. Feng, L. Liu, Y. Li, D. Sun, L. Zhang, Modification of

polyetheretherketone implants: From enhancing bone integration to enabling multi-modal therapeutics, Acta Biomaterialia. 129 (2021) 18–32. doi:10.1016/j.actbio.2021.05.009.

[107] S. Bose, D. Ke, H. Sahasrabudhe, A. Bandyopadhyay, Additive Manufacturing of Biomaterials, Progress in Materials Science. 93 (2018) 45–111. doi:10.1016/j.pmatsci.2017.08.003.

[108] Z. Wang, C. Wang, C. Li, Y. Qin, L. Zhong, B. Chen, Z. Li, H. Liu, F. Chang, J. Wang, Analysis of factors influencing bone ingrowth into three-dimensional printed porous metal scaffolds: A review, Journal of Alloys and Compounds. 717 (2017) 271–285. doi:10.1016/j.jallcom.2017.05.079.

[109] H. Koike, K. Kida, E.C. Santos, J. Rozwadowska, Y. Kashima, K. Kanemasu, Self-lubrication of PEEK polymer bearings in rolling contact fatigue under radial loads, Tribology International. 49 (2012) 30–38. doi:10.1016/j.triboint.2011.12.005.

[110] H. Mahjoubi, E. Buck, P. Manimunda, R. Farivar, R. Chromik, M. Murshed, M. Cerruti, Surface phosphonation enhances hydroxyapatite coating adhesion on polyetheretherketone and its osseointegration potential, Acta Biomaterialia. 47 (2017) 149–158. doi:10.1016/j.actbio.2016.10.004.

[111] C.M. Han, E.J. Lee, H.E. Kim, Y.H. Koh, K.N. Kim, Y. Ha, S.U. Kuh, The electron beam deposition of titanium on polyetheretherketone (PEEK) and the resulting enhanced biological properties, Biomaterials. 31 (2010) 3465–3470. doi:10.1016/j.biomaterials.2009.12.030.

[112] M. Buciumeanu, S. Almeida, F. Bartolomeu, M.M. Costa, N. Alves, F.S. Silva, G. Miranda, Ti6Al4V cellular structures impregnated with biomedical PEEK - New material design for improved tribological behavior, Tribology International. 119 (2018) 157–164. doi:10.1016/j.triboint.2017.10.038.

[113] N. Sheiko, P. Kékicheff, P. Marie, M. Schmutz, L. Jacomine, F. Perrin-Schmitt, PEEK (polyether-ether-ketone)-coated nitinol wire: Film stability for biocompatibility applications, Applied Surface Science. 389 (2016) 651–665. doi:10.1016/j.apsusc.2016.07.159.

[114] R.A. Horowitz, Z. Mazor, C. Foitzik, H. Prasad, M. Rohrer, A. Palti, ß-Tricalcium Phosphate as Bone Substitute Material : Properties and Clinical Applications, The International Journal Of Dental Implants and Biomaterials. 1 (2009) 2–11.

[115] C. Aparicio, A. Padrós, F.J. Gil, In vivo evaluation of micro-rough and bioactive titanium dental implants using histometry and pull-out tests, Journal of the Mechanical Behavior of Biomedical Materials. 4 (2011) 1672–1682. doi:10.1016/j.jmbbm.2011.05.005.

[116] B.L. Pereira, P. Tummler, C.E.B. Marino, P.C. Soares, N.K. Kuromoto, Titanium bioactivity surfaces obtained by chemical/electrochemical treatments, Revista Materia. 19 (2014) 16–23. doi:10.1590/S1517-70762014000100004.

[117] M. Santin, G. Philips, Biomimetic, Bioresponsive, and Bioactive Materials - An Introduction to Integrating Materials with Tissues, Wiley, John Wiley & Sons, 2012.

[118] E. Brett, J. Flacco, C. Blackshear, M.T. Longaker, D.C. Wan, Biomimetics of Bone Implants: The Regenerative Road, BioResearch Open Access. 6 (2017) 1–6. doi:10.1089/biores.2016.0044.

[119] W. Wang, K.W.K. Yeung, Bone grafts and biomaterials substitutes for bone defect repair: A review, Bioactive Materials. 2 (2017) 224–247. doi:10.1016/j.bioactmat.2017.05.007.

[120] B. Li, Z. Liu, J. Yang, Z. Yi, W. Xiao, X. Liu, X. Yang, W. Xu, X. Liao, Preparation of bioactive β-tricalcium phosphate microspheres as bone graft substitute materials, Materials Science and Engineering C. 70 (2017) 1200–1205. doi:10.1016/j.msec.2016.03.040.

[121] D. Brazete, P.M.C. Torres, J.C.C. Abrantes, J.M.F. Ferreira, Influence of the Ca/P ratio and cooling rate on the allotropic α↔β-tricalcium phosphate phase transformations, Ceramics International. 44 (2018) 8249–8256. doi:10.1016/j.ceramint.2018.02.005.

[122] S. V. Dorozhkin, Calcium orthophosphate bioceramics, Ceramics International. 41 (2015) 13913–13966. doi:10.1016/j.ceramint.2015.08.004.

[123] M.Z. Ibrahim, A.A.D. Sarhan, F. Yusuf, M. Hamdi, Biomedical materials and techniques to improve the tribological, mechanical and biomedical properties of orthopedic implants – A review article, Journal of Alloys and Compounds. 714 (2017) 636–667. doi:10.1016/j.jallcom.2017.04.231.

[124] M. Buciumeanu, D. Faria, J. Mesquita-guimarães, F.S. Silva, Tribological characterization of bioactive zirconia composite layers on zirconia structures, Ceramics International. 44 (2018) 18663–18671. doi:10.1016/j.ceramint.2018.07.094.

[125] T.A. Dantas, C.S. Abreu, M.M. Costa, G. Miranda, F.S. Silva, N. Dourado, J.R. Gomes, Bioactive materials driven primary stability on titanium biocomposites, Materials Science and Engineering C. 77 (2017) 1104–1110. doi:10.1016/j.msec.2017.04.014.

[126] A.K. Khanra, H.C. Jung, K.S. Hong, K.S. Shin, Comparative property study on extruded Mg-HAP and ZM61-HAP composites, Materials Science and Engineering A. 527 (2010) 6283–6288. doi:10.1016/j.msea.2010.06.031.

[127] R. Ghosh, R. Sarkar, Synthesis and characterization of sintered beta-tricalcium phosphate: A comparative study on the effect of preparation route, Materials Science and Engineering C. 67 (2016) 345–352. doi:10.1016/j.msec.2016.05.029.

[128] E. Yılmaz, B. Çakıroğlu, A. Gökçe, F. Findik, H.O. Gulsoy, N. Gulsoy, Ö. Mutlu, M. Özacar, Novel Hydroxyapatite/Graphene Oxide/Collagen Bioactive Composite coating on Ti16Nb Alloys by Electrodeposition, Materials Science and Engineering C. 101 (2019) 292–305. doi:10.1016/j.msec.2019.03.078.

[129] S.L. Bee, Z.A.A. Hamid, Hydroxyapatite derived from food industry bio-wastes: Syntheses, properties and its potential multifunctional applications, Ceramics International. 46 (2020) 17149–17175. doi:10.1016/j.ceramint.2020.04.103.

[130] D.H. Lee, N. Tripathy, J.H. Shin, J.E. Song, J.G. Cha, K.D. Min, C.H. Park, G. Khang, Enhanced osteogenesis of β-tricalcium phosphate reinforced silk fibroin scaffold for bone tissue biofabrication, International Journal of Biological Macromolecules. 95 (2017) 14–23. doi:10.1016/j.ijbiomac.2016.11.002.

[131] T.A. Dantas, M.M. Costa, G. Miranda, F.S. Silva, C.S. Abreu, J.R. Gomes, Effect of HAp and β-TCP incorporation on the tribological response of Ti6Al4V biocomposites for implant parts, Journal of Biomedical Materials Research - Part B Applied Biomaterials. 106 (2017) 1010–1016. doi:10.1002/jbm.b.33908.

[132] L. Xie, H. Yu, Y. Deng, W. Yang, L. Liao, Q. Long, Preparation, characterization and in vitro dissolution behavior of porous biphasic α/β-tricalcium phosphate bioceramics, Materials Science and Engineering C. 59 (2016) 1007–1015. doi:10.1016/j.msec.2015.11.040.

[133] M. Yashima, A. Sakai, T. Kamiyama, A. Hoshikawa, Crystal structure analysis of β-tricalcium phosphate Ca3(PO4)2 by neutron powder diffraction, Journal of Solid State Chemistry. 175 (2003) 272–277. doi:10.1016/S0022-4596(03)00279-2.

[134] Y. Su, I. Cockerill, Y. Zheng, L. Tang, Y.X. Qin, D. Zhu, Biofunctionalization of metallic implants by calcium phosphate coatings, Bioactive Materials. 4 (2019) 196–206. doi:10.1016/j.bioactmat.2019.05.001.

[135] A. Arifin, A.B. Sulong, N. Muhamad, J. Syarif, M.I. Ramli, Material processing of hydroxyapatite and titanium alloy (HA/Ti) composite as implant materials using powder metallurgy: A review, Materials and Design. 55 (2014) 165–175. doi:10.1016/j.matdes.2013.09.045.

[136] C.F. Koch, S. Johnson, D. Kumar, M. Jelinek, D.B. Chrisey, A. Doraiswamy, C. Jin, R.J. Narayan, I.N. Mihailescu, Pulsed laser deposition of hydroxyapatite thin films, Materials Science and Engineering C. 27 (2007) 484–494. doi:10.1016/j.msec.2006.05.025.

[137] N. Horandghadim, J. Khalil-Allafi, M. Urgen, Influence of tantalum pentoxide secondary phase on surface features and mechanical properties of hydroxyapatite coating on NiTi alloy produced by electrophoretic deposition, Surface and Coatings Technology. 386 (2020) 125458. doi:10.1016/j.surfcoat.2020.125458.

[138] D. Faria, C.S. Abreu, M. Buciumeanu, N. Dourado, O. Carvalho, F.S. Silva, G. Miranda, Ti6Al4V laser surface preparation and functionalization using hydroxyapatite for biomedical applications, Journal of Biomedical Materials Research - Part B Applied Biomaterials. 106B (2018) 1534–1545. doi:10.1002/jbm.b.33964.

[139] R.M. German, Powder Metallurgy & Particulate Materials Processing, Metal Powder Industry Federation, 2005.

[140] G.S. Upadhyaya, Powder Metallurgy Technology, Cambridge International Science Publishing, 2002. https://books.google.com/books?id=04IT–Sbxb4C&pgis=1.

[141] F. Thummler, R. Oberacker, An Introduction to Powder Metallurgy, CRC Press, 1994. doi:10.1016/1044-5803(95)80037-9.

[142] I. Chang, Y. Zhao, Advances in powder metallurgy: Properties, processing and applications, First Edit, Woodhead Publishing, 2013.

[143] S. Madeira, M. Buciumeanu, O. Carvalho, F.S. Silva, Influence of sintering pressure on the microstructure and tribological properties of low temperature fast sintered hot-pressed Y-TZP, Ceramics International. 45 (2019) 5883–5893. doi:10.1016/j.ceramint.2018.12.055.

[144] G. Miranda, A. Araújo, F. Bartolomeu, M. Buciumeanu, O. Carvalho, J.C.M. Souza, F.S. Silva, B. Henriques, Design of Ti6Al4V-HA composites produced by hot pressing for biomedical applications, Materials & Design. 108 (2016) 488–493. doi:10.1016/j.matdes.2016.07.023.

[145] A. Standard, Standard terminology for additive manufacturing technologies, ASTM Standard

F2792-12a, ASTM International. (2012).

[146] S.K. Everton, M. Hirsch, P. Stravroulakis, R.K. Leach, A.T. Clare, Review of in-situ process monitoring and in-situ metrology for metal additive manufacturing, Materials and Design. 95 (2016) 431–445. doi:10.1016/j.matdes.2016.01.099.

[147] X.P. Tan, Y.J. Tan, C.S.L. Chow, S.B. Tor, W.Y. Yeong, Metallic powder-bed based 3D printing of cellular scaffolds for orthopaedic implants: A state-of-the-art review on manufacturing, topological design, mechanical properties and biocompatibility, Materials Science and Engineering: C. 76 (2017) 1328–1343. doi:10.1016/J.MSEC.2017.02.094.

[148] M. Javaid, A. Haleem, Additive manufacturing applications in medical cases: A literature based review, Alexandria Journal of Medicine. 54 (2018) 411–422. doi:10.1016/j.ajme.2017.09.003.

[149] D. Greitemeier, F. Palm, F. Syassen, T. Melz, Fatigue performance of additive manufactured TiAl6V4 using electron and laser beam melting, International Journal of Fatigue. 94 (2017) 211–217. doi:10.1016/j.ijfatigue.2016.05.001.

[150] M. Galati, L. Iuliano, A literature review of powder-based electron beam melting focusing on numerical simulations, Additive Manufacturing. 19 (2018) 1–20. doi:10.1016/j.addma.2017.11.001.

[151] A. Busachi, J. Erkoyuncu, P. Colegrove, F. Martina, C. Watts, R. Drake, A review of Additive Manufacturing technology and Cost Estimation techniques for the defence sector, CIRP Journal of Manufacturing Science and Technology. 19 (2017) 117–128. doi:10.1016/j.cirpj.2017.07.001.

[152] G. Nicoletto, Anisotropic high cycle fatigue behavior of Ti–6Al–4V obtained by powder bed laser fusion, International Journal of Fatigue. 94 (2017) 255–262. doi:10.1016/j.ijfatigue.2016.04.032.

[153] Q. Yan, H. Dong, J. Su, J. Han, B. Song, Q. Wei, Y. Shi, A Review of 3D Printing Technology for Medical Applications, Engineering. 4 (2018) 729–742. doi:10.1016/j.eng.2018.07.021.

[154] A. Bandyopadhyay, Y. Zhang, S. Bose, Recent developments in metal additive manufacturing, Current Opinion in Chemical Engineering. 28 (2020) 96–104. doi:10.1016/j.coche.2020.03.001.

[155] M. Javaid, A. Haleem, Additive manufacturing applications in orthopaedics: A review, Journal of Clinical Orthopaedics and Trauma. 9 (2018) 202–206. doi:10.1016/j.jcot.2018.04.008.

[156] P. Parandoush, D. Lin, A review on additive manufacturing of polymer-fiber composites, Composite Structures. 182 (2017) 36–53. doi:10.1016/j.compstruct.2017.08.088.

[157] N. Li, S. Huang, G. Zhang, R. Qin, W. Liu, H. Xiong, G. Shi, J. Blackburn, Progress in additive manufacturing on new materials: A review, Journal of Materials Science and Technology. 35 (2019) 242–269. doi:10.1016/j.jmst.2018.09.002.

[158] A.T. Sidambe, Biocompatibility of advanced manufactured titanium implants-A review, Materials. 7 (2014) 8168–8188. doi:10.3390/ma7128168.

[159] B. Yilmaz, A. Al Rashid, Y.A. Mou, Z. Evis, M. Koç, Bioprinting: A review of processes, materials and applications, Bioprinting. 23 (2021) e00148. doi:10.1016/j.bprint.2021.e00148.

[160] D. Systèmes, 3D printing - Additive - Introduction to 3D printing - additive processes, 3DEXPERIENCE Marketplace. (2018). https://make.3dexperience.3ds.com/processes/3D-printing (accessed May 13, 2020).

[161] A.M.R. Group, About Additive Manufacturing - VAT Photopolymerisation, Loughborough University. (n.d.). https://www.lboro.ac.uk/research/amrg/about/the7categoriesofadditivemanufacturing/vatphotopolymerisation/ (accessed May 13, 2020).

[162] J.H. Tan, W.L.E. Wong, K.W. Dalgarno, An overview of powder granulometry on feedstock and part performance in the selective laser melting process, Additive Manufacturing. 18 (2017) 228–255. doi:10.1016/j.addma.2017.10.011.

[163] W. Li, L. Yan, S. Karnati, F. Liou, J. Newkirk, K.M.B. Taminger, W.J. Seufzer, Ti-Fe intermetallics analysis and control in joining titanium alloy and stainless steel by Laser Metal Deposition, Journal of Materials Processing Technology. 242 (2017) 39–48. doi:10.1016/j.jmatprotec.2016.11.010.

[164] W.S.W. Harun, N.S. Manam, M.S.I.N. Kamariah, S. Sharif, A.H. Zulkifly, I. Ahmad, H. Miura, A review of powdered additive manufacturing techniques for Ti-6al-4v biomedical applications, Powder Technology. 331 (2018) 74–97. doi:10.1016/j.powtec.2018.03.010.

[165] F. Bartolomeu, J. Fonseca, N. Peixinho, N. Alves, M. Gasik, F.S. Silva, G. Miranda, Predicting the output dimensions, porosity and elastic modulus of additive manufactured biomaterial structures targeting orthopedic implants, Journal of the Mechanical Behavior of Biomedical Materials. 99 (2019) 104–117. doi:10.1016/j.jmbbm.2019.07.023.

[166] H. Zhang, H. Zhu, T. Qi, Z. Hu, X. Zeng, Selective laser melting of high strength Al-Cu-Mg alloys: Processing, microstructure and mechanical properties, Materials Science and Engineering A. 656 (2016) 47–54. doi:10.1016/j.msea.2015.12.101.

[167] B. Van Hooreweder, Y. Apers, K. Lietaert, J.P. Kruth, Improving the fatigue performance of porous metallic biomaterials produced by Selective Laser Melting, Acta Biomaterialia. 47 (2017) 193–202. doi:10.1016/j.actbio.2016.10.005.

[168] S. Saedi, N. Shayesteh Moghaddam, A. Amerinatanzi, M. Elahinia, H.E. Karaca, On the effects of selective laser melting process parameters on microstructure and thermomechanical response of Ni-rich NiTi, Acta Materialia. 144 (2018) 552–560. doi:10.1016/j.actamat.2017.10.072.

[169] G. Miranda, S. Faria, F. Bartolomeu, E. Pinto, S. Madeira, A. Mateus, P. Carreira, N. Alves, F.S. Silva, O. Carvalho, Predictive models for physical and mechanical properties of 316L stainless steel produced by selective laser melting, Materials Science & Engineering A. 657 (2016) 43–56. doi:10.1016/j.msea.2016.01.028.

[170] G. Kasperovich, J. Haubrich, J. Gussone, G. Requena, Correlation between porosity and processing parameters in TiAl6V4 produced by selective laser melting, Materials and Design. 105 (2016) 160–170. doi:10.1016/j.matdes.2016.05.070.

[171] P.K. Gokuldoss, S. Kolla, J. Eckert, Additive manufacturing processes: Selective laser melting, electron beam melting and binder jetting-selection guidelines, Materials. 10 (2017) 1–12. doi:10.3390/ma10060672.

[172] F. Bartolomeu, N. Dourado, F. Pereira, N. Alves, G. Miranda, F.S. Silva, Additive manufactured porous biomaterials targeting orthopedic implants: A suitable combination of mechanical, physical and topological properties, Materials Science and Engineering C. 107 (2020) 110342. doi:10.1016/j.msec.2019.110342.

[173] Y. Du, H. Liang, D. Xie, N. Mao, J. Zhao, Z. Tian, C. Wang, L. Shen, Design and statistical analysis of irregular porous scaffolds for orthopedic reconstruction based on voronoi tessellation and fabricated via selective laser melting (SLM), Materials Chemistry and Physics. 239 (2020) 121968. doi:10.1016/j.matchemphys.2019.121968.

[174] A. Ataee, Y. Li, M. Brandt, C. Wen, Ultrahigh-strength titanium gyroid scaffolds manufactured by selective laser melting (SLM) for bone implant applications, Acta Materialia. 158 (2018) 354–368. doi:10.1016/j.actamat.2018.08.005.

[175] V. Weißmann, J. Wieding, H. Hansmann, N. Laufer, A. Wolf, R. Bader, Specific yielding of selective laser-melted Ti6Al4V open-porous scaffolds as a function of unit cell design and dimensions, Metals. 6 (2016) 1–20. doi:10.3390/met6070166.

[176] M.T. Andani, S. Saedi, A.S. Turabi, M.R. Karamooz, C. Haberland, H.E. Karaca, M. Elahinia, Mechanical and shape memory properties of porous Ni50.1Ti49.9 alloys manufactured by selective laser melting, Journal of the Mechanical Behavior of Biomedical Materials. 68 (2017) 224–231. doi:10.1016/j.jmbbm.2017.01.047.

[177] Q. Ran, W. Yang, Y. Hu, X. Shen, Y. Yu, Y. Xiang, K. Cai, Osteogenesis of 3D printed porous Ti6Al4V implants with different pore sizes, Journal of the Mechanical Behavior of Biomedical Materials. 84 (2018) 1–11. doi:10.1016/j.jmbbm.2018.04.010.

[178] S. Arabnejad, R. Burnett Johnston, J.A. Pura, B. Singh, M. Tanzer, D. Pasini, High-strength porous biomaterials for bone replacement: A strategy to assess the interplay between cell morphology, mechanical properties, bone ingrowth and manufacturing constraints, Acta Biomaterialia. 30 (2016) 345–356. doi:10.1016/j.actbio.2015.10.048.

[179] A. Marrella, T.Y. Lee, D.H. Lee, S. Karuthedom, D. Syla, A. Chawla, A. Khademhosseini, H.L. Jang, Engineering vascularized and innervated bone biomaterials for improved skeletal tissue regeneration, Materials Today. 21 (2018) 362–376. doi:10.1016/j.mattod.2017.10.005.

[180] N. Abbasi, S. Hamlet, R.M. Love, N.T. Nguyen, Porous scaffolds for bone regeneration, Journal of Science: Advanced Materials and Devices. 5 (2020) 1–9. doi:10.1016/j.jsamd.2020.01.007.

[181] P. Ouyang, H. Dong, X. He, X. Cai, Y. Wang, J. Li, H. Li, Z. Jin, Hydromechanical mechanism behind the effect of pore size of porous titanium scaffolds on osteoblast response and bone ingrowth, Materials and Design. 183 (2019) 108151. doi:10.1016/j.matdes.2019.108151.

[182] Z. Chen, X. Yan, S. Yin, L. Liu, X. Liu, G. Zhao, W. Ma, W. Qi, Z. Ren, H. Liao, M. Liu, D. Cai, H. Fang, Influence of the pore size and porosity of selective laser melted Ti6Al4V ELI porous scaffold on cell proliferation, osteogenesis and bone ingrowth, Materials Science

and Engineering C. 106 (2020) 110289. doi:10.1016/j.msec.2019.110289.

[183] F. Bai, Z. Wang, J. Lu, J. Liu, G. Chen, R. Lv, J. Wang, K. Lin, J. Zhang, X. Huang, The correlation between the internal structure and vascularization of controllable porous bioceramic materials in vivo: A quantitative study, Tissue Engineering - Part A. 16 (2010) 3791–3803. doi:10.1089/ten.tea.2010.0148.

[184] J. Dutta Majumdar, I. Manna, Laser material processing, International Materials Reviews. 56 (2011) 341–388. doi:10.1179/1743280411Y.0000000003.

[185] A.K. Dubey, V. Yadava, Laser beam machining-A review, International Journal of Machine Tools and Manufacture. 48 (2008) 609–628. doi:10.1016/j.ijmachtools.2007.10.017.

[186] M.S.J. Hashmi, Comprehensive Materials Processing - Thirteen Volume Set, Elsevier, 2014.

[187] G. Chryssolouris, Laser Machining Theory and Practice, Springer-Verlag New York, 1991. doi:https://doi.org/10.1007/978-1-4757-4084-4.

[188] A.N. Samant, N.B. Dahotre, Laser machining of structural ceramics-A review, Journal of the European Ceramic Society. 29 (2009) 969–993. doi:10.1016/j.jeurceramsoc.2008.11.010.

[189] N. Mirhosseini, P.L. Crouse, M.J.J. Schmidth, L. Li, D. Garrod, Laser surface micro-texturing of Ti-6Al-4V substrates for improved cell integration, Applied Surface Science. 253 (2007) 7738–7743. doi:10.1016/j.apsusc.2007.02.168.

[190] P. Pou, A. Riveiro, J. del Val, R. Comesaña, J. Penide, F. Arias-González, R. Soto, F. Lusquiños, J. Pou, Laser surface texturing of Titanium for bioengineering applications, Procedia Manufacturing. 13 (2017) 694–701. doi:10.1016/j.promfg.2017.09.102.

[191] L. Tiainen, P. Abreu, M. Buciumeanu, F. Silva, M. Gasik, R. Serna Guerrero, O. Carvalho, Novel laser surface texturing for improved primary stability of titanium implants, Journal of the Mechanical Behavior of Biomedical Materials. 98 (2019) 26–39. doi:10.1016/j.jmbbm.2019.04.052.

[192] O. Carvalho, F. Sousa, S. Madeira, F.S. Silva, G. Miranda, HAp-functionalized zirconia surfaces via hybrid laser process for dental applications, Optics and Laser Technology. 106 (2018) 157–167. doi:10.1016/j.optlastec.2018.03.017.

[193] R. Zhang, Y. Wan, X. Ai, B. Men, T. Wang, Z. Liu, D. Zhang, Fabrication of micro/nano-textured titanium alloy implant surface and its influence on hydroxyapatite coatings, Journal of Wuhan University of Technology, Materials Science Edition. 31 (2016) 440–445. doi:10.1007/s11595-016-1389-5.

[194] Y. Zheng, C. Xiong, Z. Wang, X. Li, L. Zhang, A combination of CO2 laser and plasma surface modification of poly(etheretherketone) to enhance osteoblast response, Applied Surface Science. 344 (2015) 79–88. doi:10.1016/j.apsusc.2015.03.113.

[195] M.J. Coathup, G.W. Blunn, N. Mirhosseini, K. Erskine, Z. Liu, D.R. Garrod, L. Li, Controlled laser texturing of titanium results in reliable osteointegration, Journal of Orthopaedic Research. 35 (2017) 820–828. doi:10.1002/jor.23340.

[196] C. Wedemeyer, H. Jablonski, A. Mumdzic-Zverotic, H. Fietzek, T. Mertens, G. Hilken, C. Krüger, A. Wissmann, H. Heep, R. Schlepper, M.D. Kauther, Laser-induced nanostructures

on titanium surfaces ensure osseointegration of implants in rabbit femora, Materialia. 6 (2019) 100266. doi:10.1016/j.mtla.2019.100266.

[197] L. Salou, A. Hoornaert, G. Louarn, P. Layrolle, Enhanced osseointegration of titanium implants with nanostructured surfaces: An experimental study in rabbits, Acta Biomaterialia. 11 (2015) 494–502. doi:10.1016/j.actbio.2014.10.017.

[198] S. Mukherjee, S. Dhara, P. Saha, Enhancing the biocompatibility of Ti6Al4V implants by laser surface microtexturing: an in vitro study, International Journal of Advanced Manufacturing Technology. 76 (2015) 5–15. doi:10.1007/s00170-013-5277-2.

[199] J. Frostevarg, R. Olsson, J. Powell, A. Palmquist, R. Brånemark, Formation mechanisms of surfaces for osseointegration on titanium using pulsed laser spattering, Applied Surface Science. 485 (2019) 158–169. doi:10.1016/j.apsusc.2019.04.187.

[200] J.C.M. Souza, M.B. Sordi, M. Kanazawa, S. Ravindran, B. Henriques, F.S. Silva, C. Aparicio, L.F. Cooper, Nano-scale modification of titanium implant surfaces to enhance osseointegration, Acta Biomaterialia. 94 (2019) 112–131. doi:10.1016/j.actbio.2019.05.045.

[201] S. Li, Z. Cui, W. Zhang, Y. Li, L. Li, D. Gong, Biocompatibility of micro/nanostructures nitinol surface via nanosecond laser circularly scanning, Materials Letters. 255 (2019) 126591. doi:10.1016/j.matlet.2019.126591.

[202] M. Sadeghi, M. Kharaziha, H.R. Salimijazi, E. Tabesh, Role of micro-dimple array geometry on the biological and tribological performance of Ti6Al4V for biomedical applications, Surface and Coatings Technology. 362 (2019) 282–292. doi:10.1016/j.surfcoat.2019.01.113.

[203] B.E.J. Lee, H. Exir, A. Weck, K. Grandfield, Characterization and evaluation of femtosecond laser-induced sub-micron periodic structures generated on titanium to improve osseointegration of implants, Applied Surface Science. 441 (2018) 1034–1042. doi:10.1016/j.apsusc.2018.02.119.

[204] R. A, M. Das, V.K. Balla, D. D, D. Sen, G. Manivasagam, Surface engineering of LENS-Ti-6Al-4V to obtain nano- and micro-surface topography for orthopedic application, Nanomedicine: Nanotechnology, Biology, and Medicine. 18 (2019) 157–168. doi:10.1016/j.nano.2019.02.010.

[205] K. Sugioka, M. Meunier, A. Piqué, Laser Precision Microfabrication, Springer, 2010. doi:10.1007/978-3-642-10523-4.

[206] J. Min, H. Wan, B.E. Carlson, J. Lin, C. Sun, Application of laser ablation in adhesive bonding of metallic materials: A review, Optics and Laser Technology. 128 (2020) 106188. doi:10.1016/j.optlastec.2020.106188.

[207] Y. Xu, W. Liu, G. Zhang, Z. Li, H. Hu, C. Wang, X. Zeng, S. Zhao, Y. Zhang, T. Ren, Friction stability and cellular behaviors on laser textured Ti–6Al–4V alloy implants with bioinspired micro-overlapping structures, Journal of the Mechanical Behavior of Biomedical Materials. 109 (2020) 103823. doi:10.1016/j.jmbbm.2020.103823.

[208] G. Menci, A.G. Demir, D.G. Waugh, J. Lawrence, B. Previtali, Laser surface texturing of β-Ti alloy for orthopaedics: Effect of different wavelengths and pulse durations, Applied

Surface Science. 489 (2019) 175–186. doi:10.1016/j.apsusc.2019.05.111.

[209] J. Mesquita-Guimarães, R. Detsch, A.C. Souza, B. Henriques, F.S. Silva, A.R. Boccaccini, O. Carvalho, Cell adhesion evaluation of laser-sintered HAp and 45S5 bioactive glass coatings on micro-textured zirconia surfaces using MC3T3-E1 osteoblast-like cells, Materials Science and Engineering C. 109 (2020) 110492. doi:10.1016/j.msec.2019.110492.

[210] J. Li, H. Liao, B. Fartash, L. Hermansson, T. Johnsson, Surface-dimpled commercially pure titanium implant and bone ingrowth, Biomaterials. 18 (1997) 691–696. doi:10.1016/S0142-9612(96)00185-8.

[211] S. Çelen, C. Efeoğlu, H. Özden, Pulsed laser-induced micro-pits: As bone stabilizers, Physics Procedia. 12 (2011) 245–251. doi:10.1016/j.phpro.2011.03.130.

[212] Y. Jiao, E. Brousseau, X. Shen, X. Wang, Q. Han, H. Zhu, S. Bigot, W. He, Investigations in the fabrication of surface patterns for wettability modification on a Zr-based bulk metallic glass by nanosecond laser surface texturing, Journal of Materials Processing Technology. 283 (2020) 116714. doi:10.1016/j.jmatprotec.2020.116714.

[213] R.R. Behera, A. Das, A. Hasan, D. Pamu, L.M. Pandey, M.R. Sankar, Deposition of biphasic calcium phosphate film on laser surface textured Ti-6Al-4V and its effect on different biological properties for orthopedic applications, Journal of Alloys and Compounds. 842 (2020) 155683. doi:10.1016/j.jallcom.2020.155683.

[214] Z. Yu, G. Yang, W. Zhang, J. Hu, Investigating the effect of picosecond laser texturing on microstructure and biofunctionalization of titanium alloy, Journal of Materials Processing Technology. 255 (2018) 129–136. doi:10.1016/j.jmatprotec.2017.12.009.

[215] M.G. Scaramuccia, A.G. Demir, L. Caprio, O. Tassa, B. Previtali, Development of processing strategies for multigraded selective laser melting of Ti6Al4V and IN718, Powder Technology. 367 (2020) 376–389. doi:10.1016/j.powtec.2020.04.010.

[216] X. Mei, X. Wang, Y. Peng, H. Gu, G. Zhong, S. Yang, Interfacial characterization and mechanical properties of 316L stainless steel/inconel 718 manufactured by selective laser melting, Materials Science and Engineering A. 758 (2019) 185–191. doi:10.1016/j.msea.2019.05.011.

[217] J. Chen, Y. Yang, C. Song, M. Zhang, S. Wu, D. Wang, Interfacial microstructure and mechanical properties of 316L / CuSn10 multi-material bimetallic structure fabricated by selective laser melting, Materials Science & Engineering A. 752 (2019) 75–85. doi:10.1016/j.msea.2019.02.097.

[218] K. Chen, C. Wang, Q. Hong, S. Wen, Y. Zhou, C. Yan, Y. Shi, Selective laser melting 316L/CuSn10 multi-materials: Processing optimization, interfacial characterization and mechanical property, Journal of Materials Processing Tech. 283 (2020) 116701. doi:10.1016/j.jmatprotec.2020.116701.

[219] S.L. Sing, L.P. Lam, D.Q. Zhang, Z.H. Liu, C.K. Chua, Interfacial characterization of SLM parts in multi-material processing: Intermetallic phase formation between AlSi10Mg and C18400 copper alloy, Materials Characterization. 107 (2015) 220–227. doi:10.1016/j.matchar.2015.07.007.

[220] M. Zhang, Y. Yang, D. Wang, C. Song, J. Chen, Microstructure and mechanical properties

of CuSn/18Ni300 bimetallic porous structures manufactured by selective laser melting, Materials and Design. 165 (2019) 107583. doi:10.1016/j.matdes.2019.107583.

[221] M. Ghasri-Khouzani, X. Li, A.A. Bogno, Z. Chen, J. Liu, H. Henein, A.J. Qureshi, Fabrication of aluminum/stainless steel bimetallic composites through a combination of additive manufacturing and vacuum-assisted melt infiltration casting, Journal of Manufacturing Processes. 69 (2021) 320–330. doi:10.1016/j.jmapro.2021.07.047.

[222] K. Turalıoğlu, M. Taftalı, H. Tekdir, O. Çomaklı, M. Yazıcı, T. Yetim, A.F. Yetim, The tribological and corrosion properties of anodized Ti6Al4V/316L bimetallic structures manufactured by additive manufacturing, Surface and Coatings Technology. 405 (2021) 126635. doi:10.1016/j.surfcoat.2020.126635.

[223] J.D. Avila, K. Stenberg, S. Bose, A. Bandyopadhyay, Hydroxyapatite reinforced Ti6Al4V composites for load-bearing implants, Acta Biomaterialia. 123 (2021) 379–392. doi:10.1016/j.actbio.2020.12.060.

[224] H. Sahasrabudhe, A. Bandyopadhyay, In situ reactive multi-material Ti6Al4V-calcium phosphate-nitride coatings for bio-tribological applications, Journal of the Mechanical Behavior of Biomedical Materials. 85 (2018) 1–11. doi:10.1016/j.jmbbm.2018.05.020.

[225] J. Li, H. Yuan, A. Chandrakar, L. Moroni, P. Habibovic, 3D porous Ti6Al4V-beta-tricalcium phosphate scaffolds directly fabricated by additive manufacturing, Acta Biomaterialia. 126 (2021) 496–510. doi:10.1016/j.actbio.2021.03.021.

[226] S. Xiaohui, L. Wei, S. Pinghui, S. Qingyong, W. Qingsong, S. Yusheng, L. Kai, L. WenGuang, Selective laser sintering of aliphatic-polycarbonate/hydroxyapatite composite scaffolds for medical applications, The International Journal of Advanced Manufacturing Technology. 81 (2015) 15–25. doi:10.1007/s00170-015-7135-x.

[227] H. Huang, P. Lan, Y. Zhang, X. Li, X. Zhang, C. Yuan, X. Zheng, Z. Guo, Surface characterization and in vivo performance of plasma-sprayed hydroxyapatite-coated porous Ti6Al4V implants generated by electron beam melting, Surface & Coatings Technology. 283 (2015) 80–88. doi:10.1016/j.surfcoat.2015.10.047.

[228] B. Henriques, M. Sampaio, M. Buciumeanu, J.C.M. Souza, J.R. Gomes, F. Silva, O. Carvalho, Laser surface structuring of Ti6Al4V substrates for adhesion enhancement in Ti6Al4V-PEEK joints, Materials Science and Engineering C. 79 (2017) 177–184. doi:10.1016/j.msec.2017.04.157.

[229] J. Song, Y. Liu, Z. Liao, S. Wang, R. Tyagi, W. Liu, Wear studies on ZrO2-filled PEEK as coating bearing materials for artificial cervical discs of Ti6Al4V, Materials Science and Engineering C. 69 (2016) 985–994. doi:10.1016/j.msec.2016.08.007.

[230] F.E. Bastan, M.A. Ur Rehman, Y.Y. Acvu, E. Avcu, F. Üstel, A.R. Boccaccini, Electrophoretic co-deposition of PEEK-hydroxyapatite composite coatings for biomedical applications, Colloids and Surfaces B: Biointerfaces. 169 (2018) 176–182. doi:10.1016/j.colsurfb.2018.05.005.

[231] M.S.A. Bakar, P. Cheang, K.A. Khor, Tensile properties and microstructural analysis of spheroidized hydroxyapatite-poly (etheretherketone) biocomposites, Materials Science and Engineering A. 345 (2003) 55–63. doi:https://doi.org/10.1016/S0921-5093(02)00289-7.

[232] L. Petrovic, D. Pohle, H. Munstedt, T. Rechtenwald, K.A. Schlegel, S. Rupprecht, Effect of βTCP filled polyetheretherketone on osteoblast cell proliferation in vitro, Journal of Biomedical Science. 13 (2006) 41–46. doi:10.1007/s11373-005-9032-z.

[233] Z. Liu, M. Zhang, Z. Wang, Y. Wang, W. Dong, W. Ma, S. Zhao, D. Sun, 3D-printed porous PEEK scaffold combined with CSMA/POSS bioactive surface: A strategy for enhancing osseointegration of PEEK implants, Composites Part B: Engineering. 230 (2022) 109512. doi:10.1016/j.compositesb.2021.109512.

CHAPTER 3

Development of β-TCP-Ti6Al4V structures: Driving cellular response by modulating physical and chemical properties

M.M. Costa[a*], R. Lima[c,d], F. Melo-Fonseca[a,b], F. Bartolomeu[a], N. Alves[e], A. Miranda[c,d], M. Gasik[f], F.S. Silva[a], N.A. Silva[c,d], G. Miranda[a]

[a]Center for MicroElectroMechanical Systems (CMEMS-UMinho), University of Minho, Campus de Azurém, 4800-058 Guimarães – Portugal

[b]MIT Portugal Program, School of Engineering, University of Minho, Guimarães, Portugal

[c]Life and Health Sciences Research Institute (ICVS), School of Medicine, University of Minho, Campus de Gualtar, 4710-057 Braga, Portugal

[d]ICVS/3B's - PT Government Associate Laboratory, Braga/Guimarães, Portugal

[e]Center for Rapid and Sustainable Product Development (CDRSP), Polytechnic Institute of Leiria, Rua General Norton de Matos, Apartado 4133, 2411-901 Leiria, Portugal

[f]Department of Chemical and Metallurgical Engineering, School of Chemical Engineering, Aalto University Foundation, 00076 Aalto, Espoo, Finland

Abstract

Load-bearing implants success is strongly dependent on several physical and chemical properties that are known to drive cellular response. In this work, multi-material β-TCP-Ti6Al4V cellular structures were designed to combine Ti6Al4V mechanical properties and β-Tricalcium Phosphate bioactivity, in order to promote bone ingrowth as the bioactive material is being absorbed and replaced by newly formed bone.

In this sense, the produced structures were characterized regarding roughness, wettability, β-TCP quantity and quality inside the structures after fabrication and the pH measured during cell culture (as consequence of β-TCP dissolution) and those aspects were correlated with cellular viability, distribution, morphology and proliferation.

These structures displayed a hydrophilic behavior and results showed that the addition of β-TCP to these cellular structures led to an alkalization of the medium, aspect that significantly influences the cellular response. Higher impregnation ratios were found more adequate for lowering the media pH and toxicity, and thus enhance cell adhesion and proliferation.

Keywords: Multi-material cellular structures; Selective Laser Melting; Press and Sintering; Ti6Al4V; β-Tricalcium Phosphate

3.1. Introduction

Hip Implants are currently used for restoring mobility in patients suffering from osteoarthritis or trauma, being implanted worldwide, per year, in one million people [1]. Currently hip implants are commonly made of Ti6Al4V alloy, due to this material excellent biocompatibility when in contact with body fluids, high strength (related with the addition of vanadium and aluminum) and corrosion resistance (due to the formation of an oxide layer) [2–6].

Typically, after 10 to 20 years of total hip arthroplasty surgery, revision surgeries are needed due to implant loosening [1,7]. The loss of the implant-bone fixation has been related to the stiffness mismatch existing between cortical bone and currently used hip implant materials [1,8]. In fact, current solutions are Ti6Al4V dense implants with an excessively high Young's modulus (≈ 110 GPa [2,9]) when compared to bone (≈10–30 GPa [2,9]). This mismatch causes a reduction on the stress that is transferred from the implant to the cortical bone (stress-shielding effect), thus leading bone to resorb [1,2,8,10].

Although biocompatible, Ti6Al4V implants are bioinert, thus non-eliciting an enhanced biological interaction with the human body [11]. Ideally, for bone tissue repair it is important to find a nontoxic, biocompatible, bioactive solution owing suitable mechanical properties (stiffness and strength), that allow a free flow of nutrients to promote cell growth, proliferation and differentiation and consequently new tissue formation [12–14].

When scanning the available literature, different strategies are found, spanning different materials, combinations and structures. (i) Biomaterials like hydrogels are widely used for bone tissue repair once they promote a suitable environment highly similar to the extracellular matrix (ECM) for cell migration, adhesion, proliferation and adhesion. However, many challenges remain due to unsuitable mechanical and bioactive properties in natural and synthetic hydrogels, respectively [13]. (ii) Bioactive ceramics (hydroxyapatite, β-Tricalcium Phosphate (β-TCP), bioactive glass [12,14]) are vastly studied for bone tissue repair due to its chemical composition highly similar to natural apatites of bone, however, its brittle nature make them not suitable for load bearing applications [12,14–17]. Many researchers overcome the lower mechanical properties of bioactive materials by introducing a second phase material. (iii) Low-dimensional nanomaterials (LDN), such as carbon nanotubes, graphene or boron nitride nanotubes are very promising reinforcements due to their ability to enhance these bioactive materials mechanical properties [14,18,19], especially suitable for fabricating scaffolds [18]. However, the use of LDN is still challenging once it is difficult to achieve their homogeneous dispersion, besides their low oxidation temperature, easily achieved when sintering the bioactive material [14,18,19]. (iv) Recent studies show the potential of using polymeric scaffolds with incorporation of bioactive ceramics or antibacterial agents [19,20], however their mechanical properties are still below these implants loading requirements [12]. (v) Regarding metallic alloys, there are some studies on bioactive reinforced composites for load-bearing applications with faster and enhanced osseointegration [3,17,21,22] while many studies address bioactive coatings for Ti6Al4V implants [9,23,24]. However, some problems arise when using coatings, especially the detachment of the coating layer, that may compromise the bioactive properties of the final implant and lead to local inflammatory reactions [21,22].

Considering the abovementioned strategies, a multi-material solution that gathers different materials appears as a promising solution towards the improvement of conventional hip implants by promoting multifunctionality. This study proposes a multi-material solution (Ti6Al4V and β-TCP) based on cellular structures that simultaneously lowers implant Young's modulus, add bioactivity,

allow a flow of nutrients and waste while assuring bone ingrowth and vascularization [10,25]. Vascularization is extremely important in implants, especially after implantation, once it will potentiate a cascade of biological events that will resorb the damaged bone and replace it by newly formed bone [12,26].

This multifunctionality can be achieved by fabricating Ti6Al4V cellular structures impregnated with β-TCP bioactive ceramic that will be absorbed and replaced by newly formed bone. Selective Laser Melting (SLM) is an Additive Manufacturing technique that melts successive layers of metallic powders for building a final part [5,10,27,28] which allows an enormous freedom for designing cellular structures within the optimum pore size to enhance bone vascularization and ensuing bone ingrowth [25,29–31], reported between 100 and 400 μm [12,26,32].
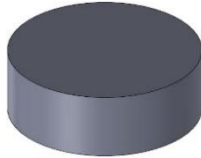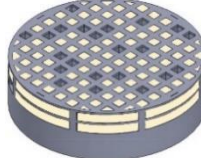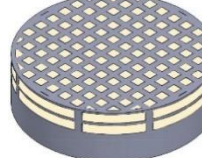
Targeting hip implants, the present work shows the influence of these structures design on physical and chemical aspects that drive cellular response. The quantity and quality of the β-TCP inside the structures and the cell culture pH were evaluated and correlated with cellular viability, cellular distribution, morphology and proliferation on the surface and inside these structures.

3.2. Materials and Methods

3.2.1. Specimens Production

In this study, four different Ti6Al4V-based specimens were studied, being their details presented in Table 3.1.

Table 3.1 - Groups detailed description.

Representation				
Group Number	G1	G2	G3	G4
Description	Ti6Al4V Cast SLA treated	Ti6Al4V SLM	Ti6Al4V SLM β-TCP impregnated (1.58 wt.%)	Ti6Al4V SLM β-TCP impregnated (2.98 wt.%)

The first group (G1) intends to replicate the material/surface condition usually found in several commercially available endosseous implants (hip, dental) [33,34] and in this sense will act as a control group. A Ti6Al4V casted/forged commercial rod with 6mm diameter, purchased from Titanium Products (United Kingdom), was cut to obtain G1 specimens having 3mm thickness.

These specimens were then subjected to a sandblast-acid etching process (SLA) to achieve a microroughness of 2–4 µm (Ra), the most frequent value used in these implants [33]. This process begins by sand blasting the Ti6Al4V specimens using spherical alumina particles (with a granulometric range between 106 and 150 µm) for 30 s followed by a 5 min acid-etching process (with 32% HCl, 96% H_2SO_4 and H_2O (2,1,1)) at 65 ± 3 °C. After etching the specimens were ultrasonically cleaned with isopropanol for 5 min.

The specimens from G2, G3 and G4 groups all start from Ti6Al4V cellular structure made by an additive manufacturing technology – Selective Laser Melting (SLM). The selection of this technology was due to its several advantages over conventional methods, in terms of cost, material waste, speed, reliability and accuracy [27,29,35]. These cellular structures were produced in a SLM equipment from SLM Solutions, model 125 HL. The powder used in the production was purchased from the equipment manufacturer (SLM Solutions GmbH, Germany). The processing parameters used for these structures fabrication were based in previous studies [5,36] being the laser power set as 90 W, a layer thickness of 30 µm and a scan speed and spacing of 600 mm/s and 80 µm, respectively. These cubic-like Ti6Al4V scaffolds have holes interconnected superiorly and also laterally and were designed to have an open-cell (pore) size of 400 µm and a wall thickness of 300 µm, having after production an average pore and wall sizes of 293 and 400 µm, respectively.

While G2 group represents the cellular structures obtained by SLM, G3 and G4 specimens incorporate β-TCP in these cellular structures, using different percentages of this bioactive (Table 3.1). The choice of alternative processes to AM to impregnate the bioactive material into these cellular structures is due to the fact that direct AM techniques of ceramic materials like β-TCP still pose some limitations due to the high temperatures involved in laser processing, leading to chemical degradation of the β-TCP, thus diminishing its bioactivity [37–39].

The specimens from G3 were prepared by immersing the cellular structures inside a viscous solution of β-TCP powder (Trans-Tech, Inc) and acetone (≈15% (w/v)) being then ultrasonically stirred. This solution was then heated under mechanical stirring to promote acetone evaporation. The β-TCP-Ti6Al4V scaffolds were then sintered, in a tubular furnace at 1100 °C for 2 h, under high vacuum, with a heating and cooling rate of 5 °C/min.

The fourth group of specimens (G4) was obtained using a powder metallurgy technique (Press and Sintering) for impregnating and afterwards sinter β-TCP inside the structures. After positioning the structures inside a steel mold, these were immersed in a β-TCP powder and acetone

solution (≈63% (w/v)) and pressure was applied for 10 min using a hydraulic press, for injecting the bioactive to the open cells of the Ti6Al4V structures. These specimens were then removed from the mold and sintered in a tubular furnace at 1100 °C for 2 h, under high vacuum, with a heating and cooling rate of 5 °C/min.

The β-TCP percentage inside G3 and G4 specimens (named bioactive percentage) was obtained by weighting each sample before and after the impregnation process. This bioactive percentage was obtained dividing the mass of bioactive (determined by the mass difference before and after impregnation) by the final weight of the specimen. G3 group exhibited a bioactive percentage of 1.58 wt% while G4 exhibited 2.98 wt%.

Besides this "bioactive percentage", an "impregnation ratio" was also determined by dividing the weighted mass of β-TCP inside the structures by the β-TCP mass that would totally fill the pores of the structures. The impregnation ratio of G3 and G4 was, therefore, 12.52% and 23.89%, respectively.

After production, G2, G3 and G4 specimens were polished using abrasive silicon carbide papers from mesh P120 till P4000 being afterwards ultrasonically cleaned with isopropanol for 5 min.

3.2.2. Specimens Characterization

The produced specimens from the four groups were analyzed using Scanning Electron Microscopy (SEM) equipment (NanoSEM - FEI Nova 200 (FEG/SEM)). X-rays diffraction (XRD) analysis was conducted on cast Ti6Al4V (G1), Ti6Al4V cellular structures fabricated by SLM (G2) and Ti6Al4V cellular structures impregnated with β-TCP (G3 and G4). XRD's were collected using a 2θ from 10 to 80° with a step size of 0.02 at 1 s per step, using a Bruker AXS D8 Discover equipment.

3.2.3. Surface Roughness

The surface roughness of the specimens was assessed by using a contact profilometer (Surftest SJ 201from Mitutoyo, Tokyo, Japan). The test was conducted on the metallic walls of the structures using λ_c=0.8 μm, λ_s=2.5 μm, at 0.25 mm/s, according to ISO 4287-1997 [40]. From this test the average roughness (Ra), the peak-to-valley roughness (Rz) and the root-mean-square roughness of the departures of the profile from the mean line (Rq) were taken. For each sample, five measurements were performed to calculate average results. Surface roughness differences

between the four groups were assessed by performing one-way ANOVA with post hoc Bonferroni multiple comparison test, where $p_{value} < 0.05$ was defined as statistical significant (GraphPad Prism v, GraphPad Software, La Jolla, California, USA).

3.2.4. Contact Angle Measurements

In order to determine the wettability properties of the metallic scaffolds, contact angle measurements for each group were performed by sessile drop technique using water and phosphate-buffered saline (PBS) as a probe liquid. The contact angle system OCA 15 plus (Dataphysics) was used to measure the angle formed by the droplets. Five droplets were measured for each group and the average was taken from these results. To assess the statistical difference between groups and among the two different solutions, two-way ANOVA and *post hoc* Bonferroni multiple comparison test was used (GraphPad Prism v, GraphPad Software, La Jolla, California, USA). For both statistical tests $p_{value} < 0.05$ was defined as statistical significant.

3.2.5. Cytotoxicity Assessment

Short-term cytotoxicity tests were performed on the produced specimens following the protocol described by Silva et al. [41]. The scaffolds were incubated with minimum essential culture medium (MEM) and after each time-point (24 h, 7, 14, 21 and 28 days) the medium was extracted and filtered using a 0.45mm pore-size filter. In all MEM tests, the material weight-to-extract fluid rate was constant at a rate of 0.2 g/ml. For this analysis, latex extracts with the same extraction protocol were used as positive controls for cell death and culture medium as negative control.

3.2.5.1. Cell Culture

Rat lung fibroblasts L929 cell line from European Collection of Cell Cultures were cultured in 24-well plates (n=3, 5×10^3 cells/well), and incubated in a humidified atmosphere with 5% CO_2 at 37 °C for 24 h. These cells were cultured in a Dulbecco's modified Eagle's culture medium (DMEM) supplemented with 10% fetal bovine serum (Gibco, Barcelona, Spain) and 1% antibiotic-antimycotic mixture (Sigma).

3.2.5.2. MEM Extraction Test

Cell culture medium was discarded from the wells 24 h after cell seeding. Subsequently, the MEM extraction fluid was added to the L929 cells. These cells were then incubated for another 72

h at 37 °C. The incubation was placed in a humidified atmosphere with 5% CO_2. Live/death assay was conducted by staining live cells with calcein-AM (1 mg/ml; Molecular Probes, Eugene, OR) and nonviable cells with propidium iodide (0.1 mg/ml; Molecular Probes). After staining, cultures were then observed under a fluorescence microscope (BX-61; Olympus, Hamburg, Germany).

Statistical analysis was performed by using one-way ANOVA using post-hoc Bonferroni to assess the statistical significant differences on live/death results between all the produced specimens under study (p_{value} < 0.05 was defined as statistical significance).

Additionally, pH values of the medium of each group were also determine by means of inoLab pH 720 (WTW, Germany) pH meter to assess its variance on the specimens leachables.

3.2.6. Direct Contact Assay

Direct contact assay was used to assess *in vitro* biocompatibility of the scaffolds by evaluating cell attachment and proliferation of human mesenchymal stem cells (hMSCs) [42]. These hMSCs were derived from human bone marrow, purchased on Lonza (Switzerland) and were cultured as monolayers in Alpha MEM medium supplemented, in sterile T175 tissue culture flasks, with 10% FBS and 1% antibiotic-antimycotic mixture.

Moreover, the same protocol was used to assess cell seeding [43]. Briefly, the P6 hMSCs were trypsinized, centrifuged and resuspended in α-MEM medium. Subsequently, 50 μl of medium containing 1×10^5 cells were seeded during one hour on top of the scaffold. After seeding, 750 μl of culture medium was added to each well and cell-scaffolds were incubated in a humidified atmosphere at 37 °C, containing 5% CO_2, for 3 and 7 days, with medium changes every 3 days.

3.2.6.1. Cell Distribution, Morphology and Proliferation

After each timepoint (3 and 7 days), hMSCs distribution and morphology were assessed through a *phalloidin/DAPI* staining [44], in which the phalloidin and *DAPI* (4′,6-diamidino-2-phenylindole) stained cytoskeleton (red) and nucleus (blue), respectively. Cells were fixed with paraformaldehyde 4% for 30 min at room temperature and, subsequently, the cell-scaffold structure was washed and sliced to evaluate cell maintenance and migration throughout the scaffold. The top and the cross-section images of the scaffold were incubated with 0.1 μg/ml of *phalloidin* (Sigma) and 1 μg/ml of *DAPI* for 30 min. Lastly, the cell-scaffolds structures were washed with PBS and observed using a confocal microscope (Fluoview FV 1000; Olympus, Hamburg, Germany).

3.3. Results and Discussion

3.3.1. Microstructural Characterization

SEM micrographs of the produced specimens (G1–G4) can be observed in Figure 3.1. Group G1 was included as control group, once it represents the typical surface topography present in the majority of commercial hip implants. This topography results from the SLA process, as previously mentioned in the experimental section.

The micrographs from G2, G3 and G4 depicted in Figure 3.1 prove that the production by SLM of these Ti6Al4V cubic-like cellular structures was successfully accomplished. As seen in Figure 3.1 it is possible to observe the scaffold structure (holes and walls) evidencing a high densification of the material, proving that SLM process is suitable for the fabrication of these structures.

Additionally, the micrographs of G3 and G4 structures show that G4 attained a higher impregnation ratio than G3. These evidences are in accordance with the calculated bioactive percentages, of 1.58 wt% for G3 and 2.98 wt% for G4.
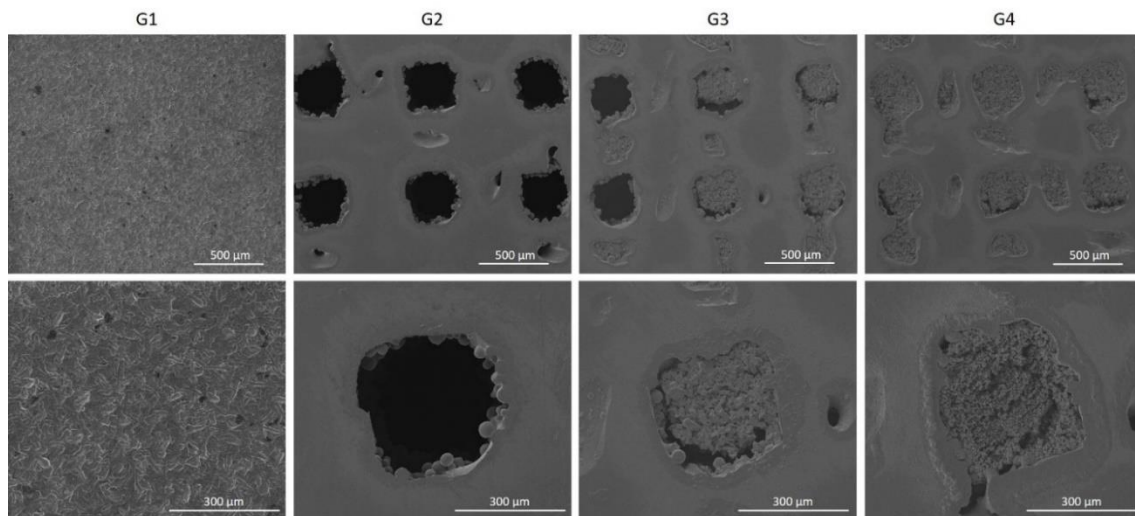
Figure 3.1 - SEM micrographs of commercial Ti6Al4V sample (G1), SLM processed Ti6Al4V structures (G2), and Ti6Al4V SLM structures impregnated with β-TCP with a bioactive percentage of 1.58 wt% (G3) and 2.98 wt% (G4).

XRD analysis was performed in specimens from all the groups to assess the influence of the production process on the crystalline structure of the alloy (Ti6Al4V) and on the condition of the bioactive material inside the cellular structure.

Figure 3.2 presents a XRD spectrum for each group, with the respective microstructures being displayed in Figure 3.3. It is possible to detect from all spectra the hexagonal close-packed (HCP) and body-centered cubic (BCC) crystalline structures of titanium. By comparing G1 and G2

XRD patterns, no significant differences were found. From Figure 3.3, it is possible to observe the microstructure of G1 which corresponds to Ti6Al4V cast material, being visible the α grains at light gray and β phase in dark gray. This microstructure is commonly found reported in literature for Ti6Al4V specimens produced by casting [45,46].
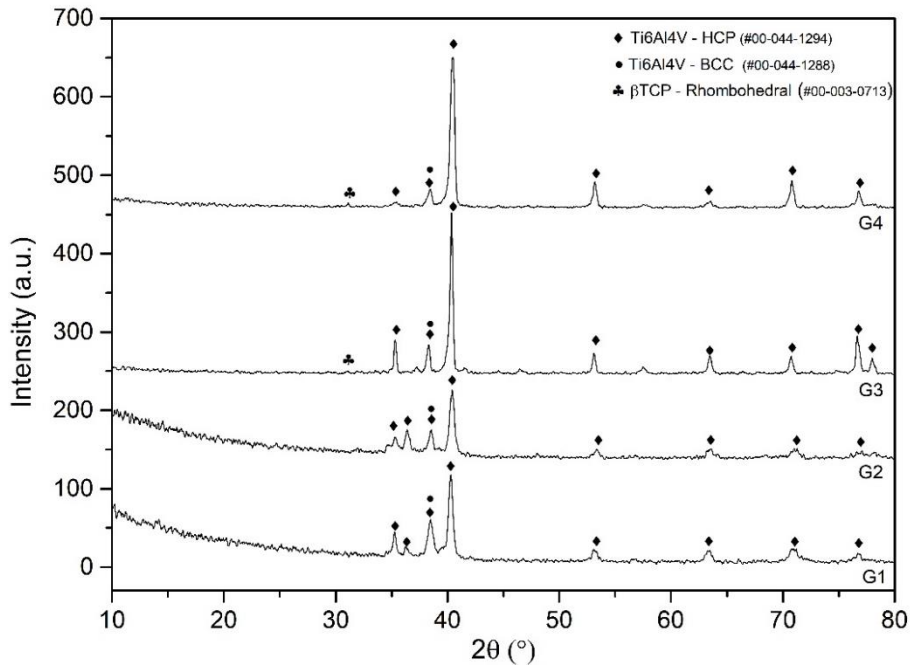
Figure 3.2 - XRD patterns of commercial Ti6Al4V sample (G1), SLM processed Ti6Al4V structures (G2) and Ti6Al4V SLM structures impregnated with β-TCP with a bioactive percentage of 1.58 wt% (G3) and 2.98 wt% (G4).
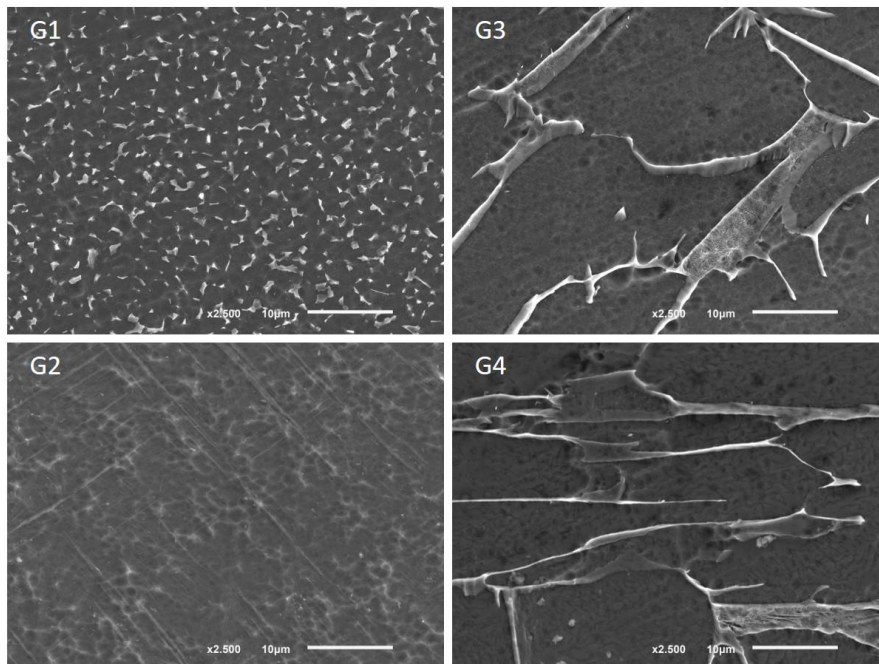
Figure 3.3 - Ti6Al4V microstructure for the produced groups (G1-G4) after acid etching, acquired by SEM.

Some studies already reported that Ti6Al4V produced by SLM present some microstructural differences from the cast alloy [6,45]. SLM process is characterized by a fast cooling rate, which will influence the microstructure of Ti6Al4V by increasing the needle-shape β phase [47]. In fact, SLM fast cooling rate will promote a transformation from β-phase to martensitic α′ phase [36]. From the XRD pattern of G2 (SLM Ti6Al4V cellular structure) it is not possible to distinguish the α′ from the α phase once both are characterized by the same hexagonal close packed crystalline structure [45,48]. However, from Figure 3.3, G2 microstructure evidences the presence of martensitic α′ phase, as also proven in other studies [45,47].

The addition of β-TCP to the scaffolds (G3 and G4) led to the presence of a new peak near 30–35° on the XRD pattern, corresponding to β-TCP phase. G3 and G4 microstructure (Figure 3.3) suggests that the sintering process of β-TCP could act as a heat treatment for Ti6Al4V once the temperatures involved in this process are quite high. This phenomenon, according to literature, will lead to the formation of β-phase that results from the decomposition of martensite phase at high temperatures (above β transus) [49], which is in accordance with the typical β-phase microstructure found on G3 and G4 (Figure 3.3).

3.3.2. Roughness

Despite the high number of parameters conditioning cell adhesion and proliferation, surface energy appears to be a dominant factor [50]. The surface energy depends on the surface charge, microstructural topography and chemical composition [51]. Surface roughness can modulate the activity of cells interacting with an implant [52] and therefore strongly disturb the relationship between surface energy and cell proliferation [50]. In this sense, the surface of an implant significantly affects the implant-cell interactions [50].

Surface roughness values (Ra, Rz and Rq) of all groups are presented in Table 3.2, being the results for Ra statistically analyzed in Figure 3.4.

Table 3.2 - Roughness measurements of the four groups.

Group	Ra (μm)	Rz (μm)	Rq (μm)
G1	1.90 ± 0.10	14.17 ± 0.99	2.38 ± 0.09
G2	0.18 ± 0.04	2.13 ± 1.22	0.29 ± 0.13
G3	0.14 ± 0.06	1.24 ± 0.6	0.21 ± 0.12
G4	0.10 ± 0.03	0.67 ± 0.14	0.12 ± 0.04

As seen in Table 3.2, G1 that corresponds to cast Ti6Al4V SLA treated presents a roughness value of 1.90 ± 0.10 μm. This value is very similar to those found in literature for this treatment on this material [53]. Furthermore, studies reveal that in acid etched specimens a hydrogen desorption occurs, consequently leading to the formation of a titanium hydride (TiH_2) that will also lead to increased roughness [54]. The roughness promoted on this group represents the commercial solution found in implants. According to the statistical analysis presented on Figure 3.4, G2, G3 and G4 groups are statistically different comparing to G1 group (representing the commercial solution).
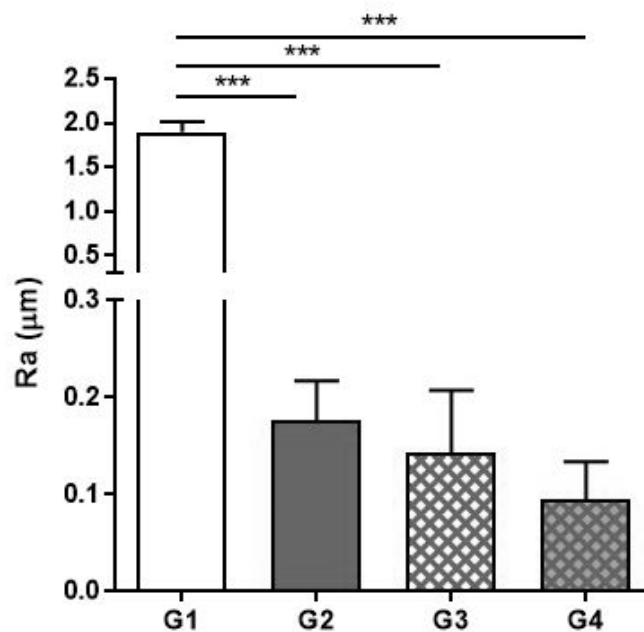
Figure 3.4 - Surface roughness values (Ra) for all groups. Data are presented as average ± SD (n=5). Symbol *** denote statistically significant differences (p<0.001) in comparison with G1.

The Ti6Al4V cellular structures, as-produced by SLM, present a typical rough surface due to the partial melting of powders on the vicinity of the laser path [5,11]. The as-produced cellular structures produced in this study revealed a roughness of 19.75 ± 1.50 μm (Ra). Those values are aligned with literature, where Ti6Al4V specimens produced by SLM display an as-produced roughness (before polishing) of 17.60 ± 3.70 μm [55]. Ponsonnet et al. [50] reported that a roughness value lower than 1 μm favors cell proliferation, regardless of the wettability of the specimens. For this reason, as mentioned in the experimental section, G2, G3 and G4 were polished to reduce this as-produced roughness. The SLM Ti6Al4V cellular structures (G2) displayed an Ra of 0.18 ± 0.04 μm, while G3 and G4 groups present a slight tendency to display lower values

when compared with G2. This could be explained by the presence of surface defects, inherent of the SLM process, which as clearly seen in Figure 3.5, will contribute to a higher roughness on the metallic walls (especially on G2). However, the impregnation process will promote a filling of those defects with bioactive materials (see G3 and G4 in Figure 3.5), which will, consequently, diminish the roughness.
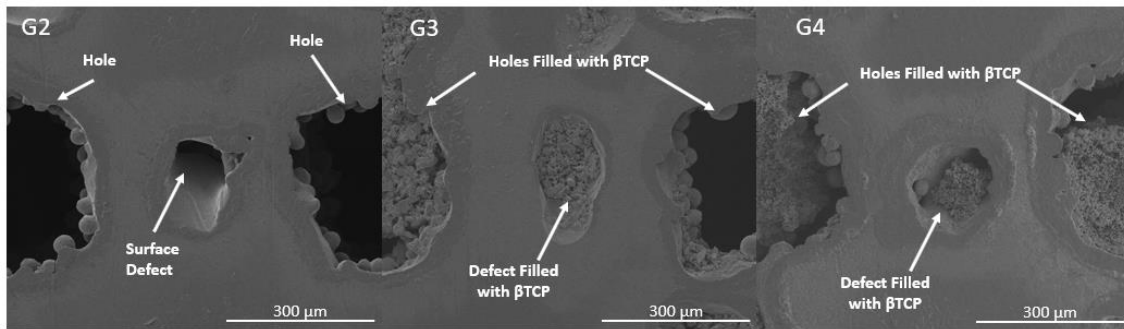
Figure 3.5 - SLM structures surface defects.

3.3.3. Wettability

Wettability was assessed for all the produced specimens in order to understand its influence on cell adhesion. It is known that the surface chemical composition and charge affect the wettability of the material and therefore influence the interaction between tissue and implant and consequently osseointegration [50,56,57] When interacting with biological fluids, highly hydrophilic surfaces are preferred rather than hydrophobic ones, once, when implanted in bone, hydrophilicity surfaces lead to an increased bone formation [56,57]. A surface is considered hydrophilic when the contact angle is approximate or lower than 65° [58].

The wettability of each scaffold was assessed by measuring the contact angle at the moment the drop touched the surface.

The as-produced Ti6Al4V SLM-fabricated scaffolds (having a Ra of 19.75 ± 1.50 μm) displayed water and PBS contact angles of 129.46 ± 5.00° and 120.78 ± 2.81°, respectively, thus being considered non-suitable for cell interaction, once their surface is highly hydrophobic. This aspect reinforced the need to polish the cellular structures (either impregnated or not) from groups G2, G3 and G4.

Two different fluids were used for these wettability tests: water in order to be comparable with results found in literature for similar specimens and PBS once it is more representative of a biological fluid. The water and PBS contact angles that were measured are presented on Table 3.3

and Figure 3.6 depicts the statistical results regarding the impregnated groups, G3 and G4, in water and PBS.

Table 3.3 - Water and PBS contact angles (mean ⬜ SD) of Ti6Al4V Cast, Ti6Al4V SLM structures, and Ti6Al4V impregnated structures with 1.58 wt.% and 2.98 wt. of β-TCP.

Group	Contact Angle (Average ± SD (°))	
	Water	PBS
G1	97.76 ± 3.02	92.90 ± 4.09
G2	Undetectable	Undetectable
G3	46.04 ± 6.45	46.80 ± 3.86
G4	20.92 ± 2.23	18.50 ± 2.52
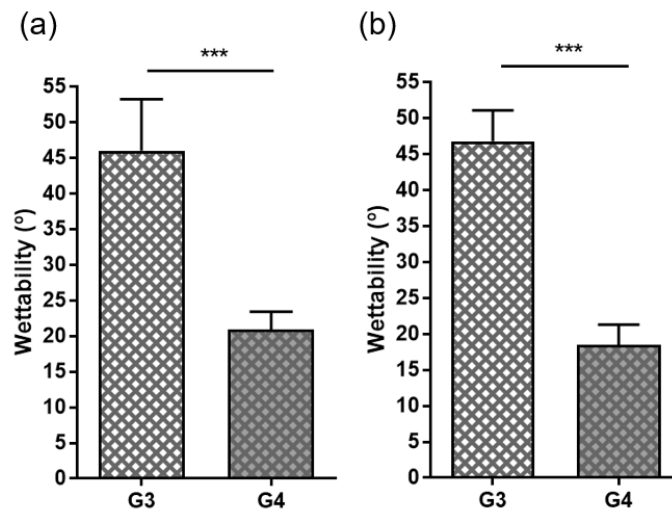
Figure 3.6 - Differences between G3 and G4 for (a) water and (b) PBS contact angles. Data are presented as average ± SD (n=5). Symbol *** denotes statistically significant differences (p<0.001) between both groups

From Table 3.3 it is possible to conclude that from all the produced groups, G1 is the one that displays the most hydrophobic behavior (recalling that this group corresponds to SLA cast Ti6Al4V). These contact angles are in good agreement with available values found in literature [53]. In fact, this hydrophobic behavior has been reported as a consequence of forming TiH_2 on the material's surface, due to hydrogen desorption [54], as proven in several studies regarding SLA-treated specimens where this titanium hydride was found [54,59]. Furthermore, wetting properties are influenced by roughness, and according to Wenzel model [60], surface roughness will enhance liquid repellence when the contact angle is higher than 90° while surface roughness will promote liquid spreading for contact angle below 90° [60]. The former situation (contact angle higher than 90°) occurs in specimens from group G1, where the highest roughness is found.

All the SLM produced specimens presented hydrophilic surfaces since the measured contact angles are lower than 65° [58]. When comparing the results obtained using water and those using PBS, no significant differences regarding the contact angle were found. In porous structures such as Ti6Al4V SLM-cellular structures from G2, if the pressure is enough, the water will pass through the pores [60]. In this group of specimens, it is not possible to measure a static contact angle right after the drop gets in contact with the specimen, as seen in the frame sequence presented in Figure 3.7. The design of this specimen, i.e. the open cell geometry together with the low surface roughness contribute to this super hydrophilic behavior once both water and PBS drops spread very quickly on its surface and throughout the specimens' porosity.

Another model that correlates surface roughness with wetting properties is Cassie-Baxter model [61]. In this model, air bubbles trapped between the liquid drop and the surface are also a factor that affects wettability [61]. In G2 group the interconnected pores will increase the contact area between the liquid and the solid and, consequently, the capillary forces. When the pressure of the air bubbles trapped inside the pores is overcame by these capillary forces, the capillary-pressure balance for these structures is disrupted and will eliminate this air pressure effect [62]. This behavior was clearly seen in G2 group, with water and PBS spreading inside the structure.

According to literature, hydrophilicity is preferable over hydrophobicity once it allows protein adsorption at an implant surface and consequently lead to an enhanced interaction between cells and the surface [56,57].

Groups G3 and G4 also display a hydrophilic behavior, with higher contact angles than that of G2. For G3 and G4, statistical results (two-way ANOVA) revealed no significant differences on wettability when regarding the solution (water *versus* PBS). On the other hand, significant statistical differences between G3 and G4 wettability were found, either for water and PBS solution (Figure 3.6), with lower contact angles being consistently measured for G4.

G4 lower average contact angle when compared with G3, could be related with the higher impregnation ratio in G4. Being β-TCP a hydrophilic material [63], the higher the quantity of this bioactive material, the higher the hydrophilicity of the specimen. Additionally, it is important to highlight that the effect of the capillary forces described for G2, also applies to the structures from G3 and G4 groups, once for both groups a full impregnation is not promoted.
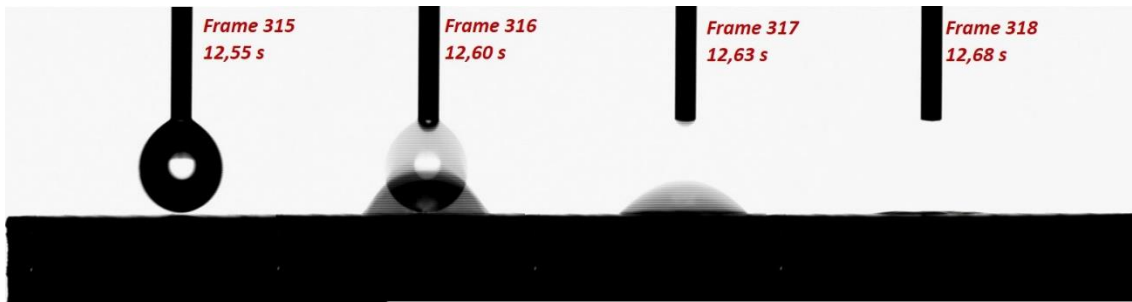
Figure 3.7 - Hydrophilic behavior of Ti6Al4V SLM cellular structures (G2).

3.3.4. pH

The biodegradation of biomaterials like calcium phosphates is a combination of physical, chemical and biological factors [64]. The dissolution of β-TCP leads to an increase on the concentration of Ca^{2+} and $PO4^{3-}$ in the medium, as shown in the following Eq. (1) [65]:

$$Ca_3(PO4)_2 \rightarrow Ca^{2+} + PO_4^{3-} \tag{1}$$

$$PO_4^{3-} + H^+ \rightarrow HPO_4^{2-} \tag{2}$$

Subsequently, PO_4^{3-} ions will react with H^+ ions, according to Eq. (2), leading to an alkalization of the medium [65,66]. This outcome has been reported in several studies found in literature [65]. Although cellular and phagocytic activities and also cell mediated factors tend to decrease the pH of the surrounding medium [64], this acidification is not enough to compensate pH increase induced by the dissolution of β-TCP. This alkalization has a profound impact in hMSC's proliferation and consequent osteogenic differentiation [67]. Moreover, the extended release of calcium ions into the medium promotes the inflow of calcium ions in osteoblasts, which slightly hyperpolarizes the plasma membrane and thus stimulates osteoblast ATP (adenosine triphosphate) production [68].

Figure 3.8 depicts the effect of the specimens' leachables in the pH measured at two different culture timepoints: 24 h and 7 days. These results show that G3 group was the one that displayed the higher pH, for both timepoints, corresponding to the leachables with a more alkaline media. On the other hand, the group that displays a more acidic solution is the commercial solution (group G1), with similar pH being found for both timepoints.

For G3 and G4 specimens, the porosity filled with β-TCP will hamper the free flow of the solution throughout the interconnected holes and, therefore, increase the pH inside the structures (Figure 3.8). This pH increase is more pronounced in G3 group, due to G3 lower impregnation ratio (when compared to G4). Due to this lower impregnation, G3 specimens have a higher contact area between the bioactive material and the medium. As a consequence, a higher dissolution rate occurs, thus increasing the pH.
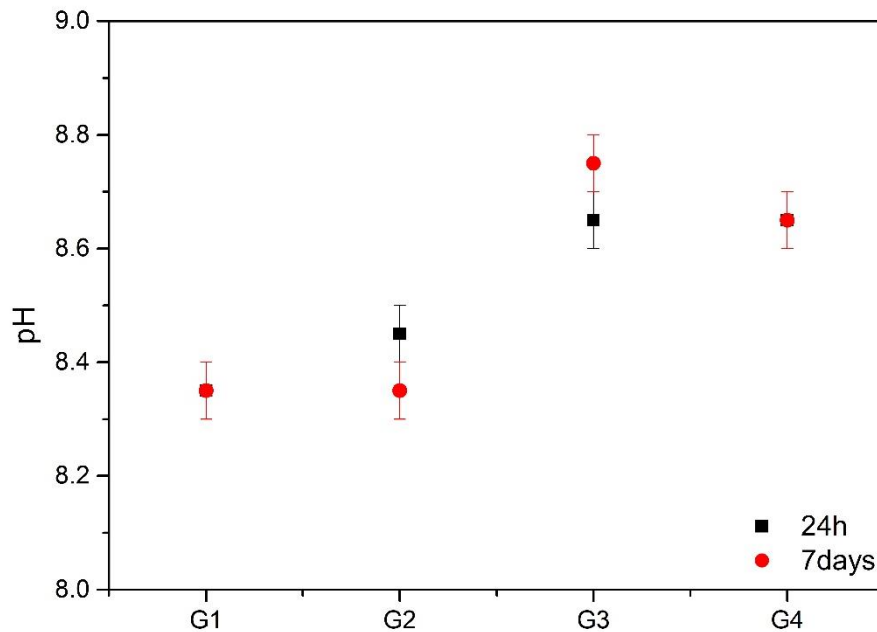
Figure 3.8 - pH results for all the groups after 24h and 7 days.

3.3.5. Cell Viability

The cytotoxicity of the produced specimens was assessed in order to ascertain the toxic effect of the products released from the metallic scaffolds during incubation with MEM. Figure 3.9 shows the viability results for the four groups in five different timepoints. Moreover, a statistical analysis was performed to compare these results. No significant differences were observed between groups, even for the higher timepoint of MEM extraction (28 days). Overall, we can assume that all constructs were not releasing toxic substances to the medium, proving that these specimens assure a suitable environment for cells to proliferate and attach. However, at the 14 days extraction, the medium of G3 scaffolds seems to indicate some levels of toxicity, that can be related to the lack of medium renewal inside the pores. Nonetheless, this effect is not found on the ensuing timepoints.
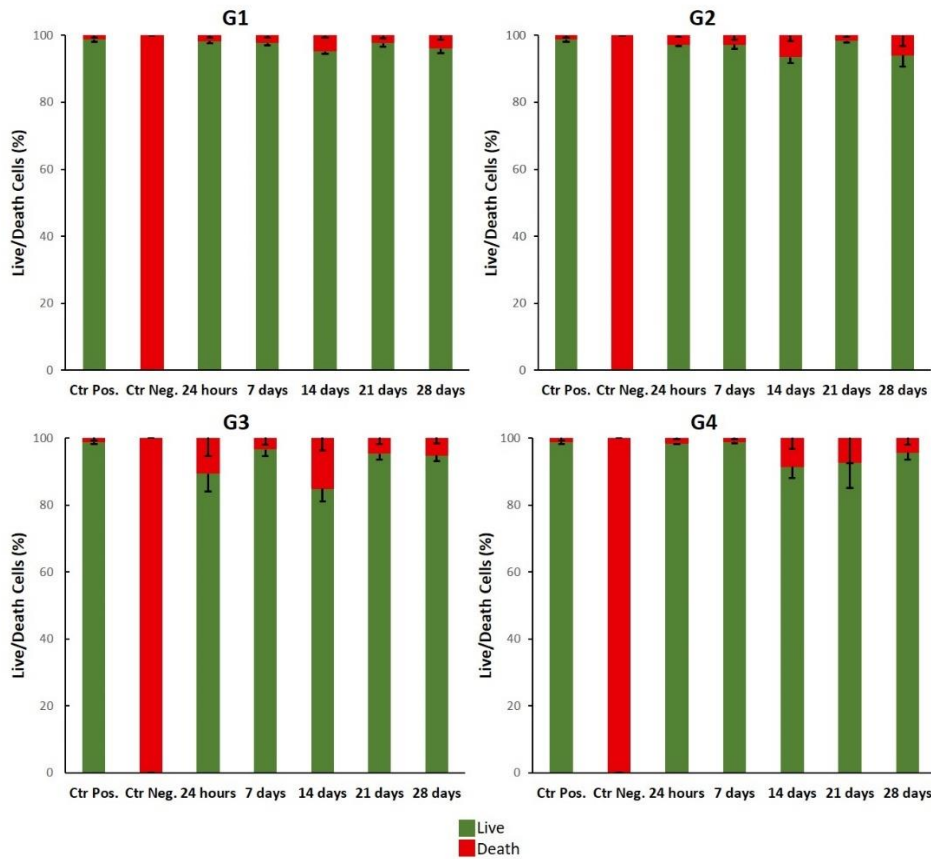
Figure 3.9 - Cell Viability of L929 cells after culturing with the four groups of scaffolds for 24 hours, 7, 14, 21 and 28 days.

3.3.6. Cell Adhesion

One of the factors that influence cell adhesion is the surface energy, which depends on the chemical composition, charge and microstructural topography of the surface [15]. On metallic materials, cell adhesion increases linearly with surface hydrophilicity and thus surface energy has a direct effect on the cellular adhesion strength [51]. Figure 3.10 shows the cell adhesion on the surface (top images) and inside the Ti6Al4V-based structures (bottom images), after an incubation of 7 days. Both G1 and G2 groups show a densely and uniform cell distribution on the surface and, in the case of G2, cells seem to easily penetrate the scaffold. After an incubation of 7 days, the cell adhesion on the surface of the cellular structures impregnated with β-TCP (G3 and G4) is lower, compared with the one without bioactive material (G2), although being possible to identify cells inside the G3 and G4 scaffolds. For these two groups, cells have a spindle shape and, while on the constructs with lower impregnation ratio (G3) DAPI stained cell nucleus are observed on the bioactive location, this stain is not abundantly present on G4 scaffolds (with higher impregnation ratio).
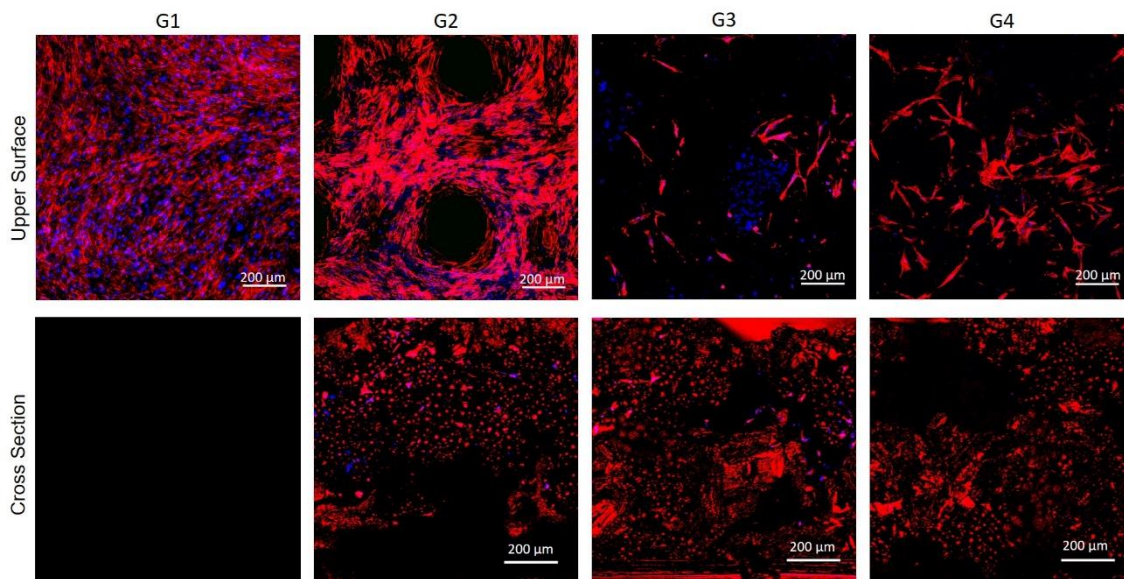
Figure 3.10 - Fluorescence microscopy images of hMSC cultured for 7 days on commercial Ti6Al4V (G1), SLM Ti6Al4V structures (G2), and Ti6Al4V SLM structures impregnated with β-TCP with a bioactive percentage of 1.58wt.% (G3) and 2.98wt.% (G4). hMSCs were stained with *DAPI* (nucleus at blue) and with *phalloidin* (actin cytoskeleton at red). Images on the top are from the top surface whereas cross section images are on the bottom. (For interpretation of the references to color in this figure legend, the reader is referred to the web version of this article.)

The morphology of hMSC after incubation for 7 days was assessed by SEM (Figure 3.11 and Figure 3.12). Generally, all the groups exhibited cell protrusions and the formation of extracellular matrix (ECM) after 7 days of incubation. Figure 3.11 shows that cells are well distributed on the surface of specimens from G1 group, proving that G1 sandblasted and acid-etched (SLA) surface is effective for superficial cell growth. On the other hand, scaffolds allow the ingrowth of cells, to enable future osseointegration of metallic implants owing this structure. The cellular structures produced by SLM (G2) show that this topography and roughness are adequate for cell culture, once several cells protrusions are observed in Figure 3.11 (surface) and Figure 3.12 (cross-section). For β-TCP impregnated scaffolds (G3 and G4), cells display a flattened morphology, with protrusions being less visible, when compared to the SLM constructs without bioactive (G2), for both surface and cross section.

These results show that the presence of β-TCP inside these cellular structures influences the pH of the medium, that in turn will affect cell viability. In this sense, a higher impregnation ratio is preferable, once it will lead to a lower pH and toxicity and, consequently, enhanced cell adhesion and proliferation.
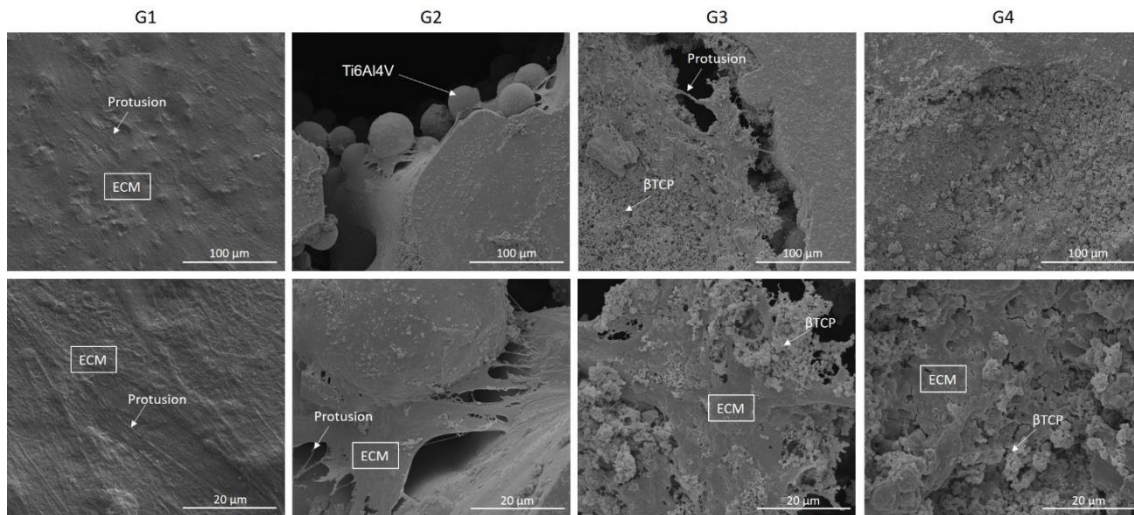
Figure 3.11 - SEM micrographs of hMSC, after an incubation of 7 days, cultured on commercial Ti6Al4V sample (G1), SLM processed Ti6Al4V structures (G2), and Ti6Al4V SLM structures impregnated with β-TCP with a bioactive percentage of 1.58 wt.% (G3) and 2.98 wt.% (G4).
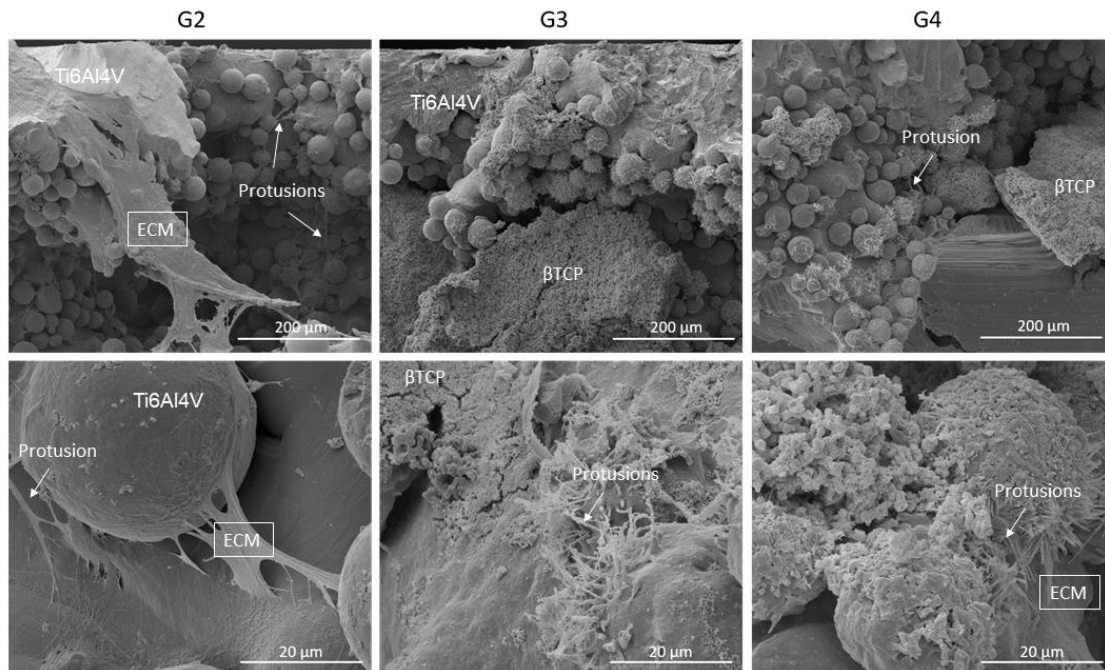
Figure 3.12 - SEM cross section micrographs of hMSC, after 7 days of incubation, SLM processed Ti6Al4V structures (G2), and Ti6Al4V SLM structures impregnated with β-TCP with a bioactive percentage of 1.58 wt.% (G3) and 2.98 wt.% (G4).

3.4. Conclusions

This study proposes a solution for load-bearing implants by designing a multi-material Ti6Al4V cellular structure impregnated with β-TCP. This multi-material structures were designed to be the outer layer of a hip implant that assures no bioactive detachment upon implantation and allow cell adhesion and proliferation not only on implant surface but also inside the structure. The processing route used for manufacturing these multi-material structures (combining an additive manufacturing technique (SLM) with Press and Sintering) allowed the fabrication of a load-bearing

interconnected structure that allows bone ingrowth, vascularization and flow of nutrients, and on the other hand assured the bioactive retention and non-degradation within the Ti6Al4V cellular structure. The influence of the design on some of the physical and chemical properties was evaluated. All the produced cellular structures revealed a hydrophilic behavior when compared with the commercial solution due to its interconnected porosity. Results revealed that when adding β-TCP to these structures, although nontoxic, the medium becomes more alkaline. Furthermore, the β-TCP quantity inside the structures had a direct influence on the pH of the medium, affecting significantly cells behavior. In this context higher impregnation ratios were found more adequate in these structures, for lowering the medium pH and promoting cell adhesion and proliferation. This solution can also be used to incorporate drugs into metallic cellular structures and therefore create a drug delivery system to treat, for instance, local infections.

Acknowledgments

Cofinanciado por:

References

[1] U. Holzwarth, G. Cotogno, Total hip arthroplasty - state of the art, Chall. Prospects (2012), https://doi.org/10.2788/31286.

[2] Q. Chen, G.A. Thouas, Metallic implant biomaterials, Mater. Sci. Eng. R. Rep. 87 (2015) 1–57, https://doi.org/10.1016/j.mser.2014.10.001.

[3] T.A. Dantas, C.S. Abreu, M.M. Costa, G. Miranda, F.S. Silva, N. Dourado, J.R. Gomes, Bioactive materials driven primary stability on titanium biocomposites, Mater. Sci. Eng. C 77 (2017) 1104–1110, https://doi.org/10.1016/j.msec.2017.04.014.

[4] S. Bruschi, R. Bertolini, A. Ghiotti, Coupling machining and heat treatment to enhance the wear behaviour of an additive manufactured Ti6Al4V titanium alloy, Tribol. Int. 116 (2017) 58–68, https://doi.org/10.1016/j.triboint.2017.07.004.

[5] F. Bartolomeu, M. Sampaio, O. Carvalho, E. Pinto, N. Alves, J.R. Gomes, F.S. Silva, G. Miranda, Tribological behavior of Ti6Al4V cellular structures produced by Selective laser melting, J. Mech. Behav. Biomed. Mater. 69 (2017) 128–134, https://doi.org/10.1016/j.jmbbm.2017.01.004.

[6] F. Bartolomeu, M. Buciumeanu, M.M. Costa, M. Gasik, F.S. Silva, G. Miranda, Multi-material Ti6Al4V & PEEK cellular structures produced by selective laser melting and hot pressing: a tribocorrosion study targeting orthopedic applications, J. Mech. Behav. Biomed. Mater. 89 (2018) 54–64, https://doi.org/10.1016/j.jmbbm.2018.09.009.

[7] F. Bartolomeu, C.S. Abreu, C.G. Moura, M.M. Costa, N. Alves, F.S. Silva, G. Miranda, Ti6Al4V-PEEK multi-material structures – design, fabrication and tribological characterization focused on orthopedic implants, Tribol. Int. 131 (2018) 672–678, https://doi.org/10.1016/j.triboint.2018.11.017.

[8] S. Affatato, Perspectives in Total Hip Arthroplasty - Advances in Biomaterials and Their Tribological Interactions, Woodhead P, 2014, https://doi.org/10.1016/B978-1-78242-031-6.50016-7.

[9] D. Apostu, O. Lucaciu, C. Berce, D. Lucaciu, D. Cosma, Current methods of preventing aseptic loosening and improving osseointegration of titanium implants in cementless total hip arthroplasty: a review, J. Int. Med. Res. (2017), https://doi.org/10.1177/0300060517732697 (030006051773269).

[10] X.P. Tan, Y.J. Tan, C.S.L. Chow, S.B. Tor, W.Y. Yeong, Metallic powder-bed based 3D printing of cellular scaffolds for orthopaedic implants: a state-of-the-art review on manufacturing, topological design, mechanical properties and biocompatibility, Mater. Sci. Eng. C 76 (2017) 1328–1343, https://doi.org/10.1016/J.MSEC.2017.02.094.

[11] N. Taniguchi, S. Fujibayashi, M. Takemoto, K. Sasaki, B. Otsuki, T. Nakamura, T. Matsushita, T. Kokubo, S. Matsuda, Effect of pore size on bone ingrowth into porous titanium implants fabricated by additive manufacturing: an in vivo experiment, Mater. Sci. Eng. C 59 (2016) 690–701, https://doi.org/10.1016/j.msec.2015.10.069.

[12] C. Gao, S. Peng, P. Feng, C. Shuai, Bone biomaterials and interactions with stem cells, Bone Res. 5 (2017) 1–33, https://doi.org/10.1038/boneres.2017.59.

[13] M. Liu, X. Zeng, C. Ma, H. Yi, Z. Ali, X. Mou, S. Li, Y. Deng, N. He, Injectable hydrogels for cartilage and bone tissue engineering, Bone Res. 5 (2017) 1–25, https://doi.org/10.1016/j.actbio.2017.01.036.

[14] C. Gao, P. Feng, S. Peng, C. Shuai, Carbon nanotube, graphene and boron nitride nanotube reinforced bioactive ceramics for bone repair, Acta Biomater. 61 (2017) 1–20, https://doi.org/10.1016/j.actbio.2017.05.020.

[15] D.H. Lee, N. Tripathy, J.H. Shin, J.E. Song, J.G. Cha, K.D. Min, C.H. Park, G. Khang, Enhanced osteogenesis of β-tricalcium phosphate reinforced silk fibroin scaffold for bone tissue biofabrication, Int. J. Biol. Macromol. 95 (2017) 14–23, https://doi.org/10.1016/j.ijbiomac.2016.11.002.

[16] B. Li, Z. Liu, J. Yang, Z. Yi, W. Xiao, X. Liu, X. Yang, W. Xu, X. Liao, Preparation of bioactive β-tricalcium phosphate microspheres as bone graft substitute materials, Mater. Sci. Eng. C 70 (2017) 1200–1205, https://doi.org/10.1016/j.msec.2016.03.040.

[17] T.A. Dantas, M.M. Costa, G. Miranda, F.S. Silva, C.S. Abreu, J.R. Gomes, Effect of HAp and β-TCP incorporation on the tribological response of Ti6Al4V biocomposites for implant parts, J. Biomed. Mater. Res. - Part B Appl. Biomater. (2017) 1–7, https://doi.org/10.1002/jbm.b.33908.

[18] C. Shuai, P. Feng, P. Wu, Y. Liu, X. Liu, D. Lai, C. Gao, S. Peng, A combined nanostructure constructed by graphene and boron nitride nanotubes reinforces ceramic scaffolds, Chem. Eng. J. 313 (2017) 487–497, https://doi.org/10.1016/j.cej.2016.11.095.

[19] C. Shuai, W. Guo, P. Wu, W. Yang, S. Hu, Y. Xia, P. Feng, A graphene oxide-Ag co-dispersing nanosystem: dual synergistic effects on antibacterial activities and mechanical properties of polymer scaffolds, Chem. Eng. J. 347 (2018) 322–333, https://doi.org/10.1016/j.cej.2018.04.092.

[20] P. Feng, P. Wu, C. Gao, Y. Yang, W. Guo, W. Yang, C. Shuai, A Multimaterial Scaffold, With tunable properties: toward bone tissue repair, Adv. Sci. 5 (2018) 1–15, https://doi.org/10.1002/advs.201700817.

[21] G. Miranda, A. Araújo, F. Bartolomeu, M. Buciumeanu, O. Carvalho, J.C.M. Souza, F.S. Silva, B. Henriques, Design of Ti6Al4V-HA composites produced by hot pressing for biomedical applications, Mater. Des. 108 (2016) 488–493, https://doi.org/10.1016/j.matdes.2016.07.023.

[22] G.M. Peñarrieta-Juanito, M. Costa, M. Cruz, G. Miranda, B. Henriques, J. Marques, R. Magini, A. Mata, J. Caramês, F. Silva, J.C.M. Souza, Bioactivity of novel functionally structured titanium-ceramic composites in contact with human osteoblasts, J. Biomed. Mater. Res. - Part A. 106 (2018) 1923–1931, https://doi.org/10.1002/jbm.a.36394.

[23] Y. Zhang, X. Liu, Z. Li, S. Zhu, X. Yuan, Z. Cui, X. Yang, P.K. Chu, S. Wu, Nano Ag/ZnO-incorporated hydroxyapatite composite coatings: highly effective infection prevention and excellent osteointegration, Appl. Mater. Interfaces 10 (2018) 1266–1277, https://doi.org/10.1021/acsami.7b17351.

[24] J. Shen, Y. Qi, B. Jin, X. Wang, Y. Hu, Q. Jiang, Control of hydroxyapatite coating by self-assembled monolayers on titanium and improvement of osteoblast adhesion, J. Biomed. Mater. Res. - Part B Appl. Biomater. 105 (2017) 124–135, https://doi.org/10.1002/jbm.b.33539.

[25] G. Li, L. Wang, W. Pan, F. Yang, W. Jiang, X. Wu, X. Kong, K. Dai, Y. Hao, In vitro and in vivo study of additive manufactured porous Ti6Al4V scaffolds for repairing bone defects, Sci. Rep. 6 (2016) 34072, https://doi.org/10.1038/srep34072.

[26] A. Kumar, S. Mandal, S. Barui, R. Vasireddi, U. Gbureck, M. Gelinsky, B. Basu, Low temperature additive manufacturing of three dimensional scaffolds for bone-tissue engineering applications: processing related challenges and property assessment, Mater. Sci. Eng. R. Rep. 103 (2016) 1–39, https://doi.org/10.1016/j.mser.2016.01.001.

[27] Q. Liu, Y. Wang, H. Zheng, K. Tang, L. Ding, H. Li, S. Gong, Microstructure and mechanical properties of LMD-SLM hybrid forming Ti6Al4V alloy, Mater. Sci. Eng. A 660 (2016) 24–33, https://doi.org/10.1016/j.msea.2016.02.069.

[28] B. Van Hooreweder, Y. Apers, K. Lietaert, J.P. Kruth, Improving the fatigue performance of porous metallic biomaterials produced by selective laser melting, Acta Biomater. 47 (2017) 193–202, https://doi.org/10.1016/j.actbio.2016.10.005.

[29] D. Greitemeier, F. Palm, F. Syassen, T. Melz, Fatigue performance of additive manufactured TiAl6V4 using electron and laser beam melting, Int. J. Fatigue 94 (2017) 211–217, https://doi.org/10.1016/j.ijfatigue.2016.05.001.

[30] M. Elahinia, N. Shayesteh Moghaddam, M. Taheri Andani, A. Amerinatanzi, B.A. Bimber, R.F. Hamilton, Fabrication of NiTi through additive manufacturing: a review, Prog. Mater. Sci. 83 (2016) 630–663, https://doi.org/10.1016/j.pmatsci.2016.08.001.

[31] S. Bose, D. Ke, H. Sahasrabudhe, A. Bandyopadhyay, Additive manufacturing of biomaterials, Prog. Mater. Sci. 93 (2018) 45–111, https://doi.org/10.1016/j.pmatsci.2017.08.003.

[32] R.A. Perez, G. Mestres, Role of pore size and morphology in musculo-skeletal tissue regeneration, Mater. Sci. Eng. C 61 (2016) 922–939, https://doi.org/10.1016/j.msec.2015.12.087.

[33] Straumann, Straumann SLA, Sci. Evid, First ed., 2011 (2011), pp. 1–36.

[34] P. Ming, S. Shao, J. Qiu, J. Yang, Y. Yu, J. Chen, W. Zhu, C. Tang, Superiority of calcium-containing nanowires modified titanium surface compared with SLA titanium surface in biological behavior of osteoblasts: a pilot study, Appl. Surf. Sci. 416 (2017) 790–797, https://doi.org/10.1016/j.apsusc.2017.04.152.

[35] M. Javaid, A. Haleem, Additive manufacturing applications in medical cases: a literature based review, Alex. J. Med. (2017), https://doi.org/10.1016/j.ajme.2017.09.003.

[36] F. Bartolomeu, S. Faria, O. Carvalho, E. Pinto, N. Alves, F.S. Silva, G. Miranda, Predictive models for physical and mechanical properties of Ti6Al4V produced by selective laser melting, Mater. Sci. Eng. A 663 (2016) 181–192, https://doi.org/10.1016/j.msea.2016.03.113.

[37] R.W.N. Nilen, P.W. Richter, The thermal stability of hydroxyapatite in biphasic calcium phosphate ceramics, J. Mater. Sci. Mater. Med. 19 (2008) 1693–1702, https://doi.org/10.1007/s10856-007-3252-x.

[38] C. Wang, R. Quan, H. Wang, X. Wei, Z. Zhao, Investigation on high-temperature decomposition characteristic of hydroxyapatite, 2009 IEEE 3rd Int. Conf. Nano/Molecular Med. Eng. NANOMED, 2009 2009, pp. 65–70, https://doi.org/10.1109/NANOMED.2009.5559116.

[39] G. Muralithran, S. Ramesh, The effects of sintering temperature on the properties of hydroxyapatite, Ceram. Int. 26 (2000) 221–230 (doi:S0272-8842(99)00046-2).

[40] ISO 4287:1997, Geometrical product specifications (GPS) – surface texture: profile method – terms, definitions and surface texture parameters, Int. Organ. Stand, https://www.iso.org/standard/10132.html, (1997).

[41] N.A. Silva, A.J. Salgado, R.A. Sousa, J.T. Oliveira, A.J. Pedro, H. Leite-Almeida, R. Cerqueira, A. Almeida, F. Mastronardi, J.F. Mano, N.M. Neves, N. Sousa, R.L. Reis, Development and characterization of a novel hybrid tissue engineering–based scaffold for spinal cord injury repair, Tissue Eng. Part A 16 (2010) 45–54, https://doi.org/10.1089/ten.tea.2008.0559.

[42] S. Ribeiro-Samy, N.A. Silva, V.M. Correlo, J.S. Fraga, L. Pinto, A. Teixeira-Castro, H. Leite-Almeida, A. Almeida, J.M. Gimble, N. Sousa, A.J. Salgado, R.L. Reis, Development and characterization of a PHBHV- based 3D scaffold for a tissue Engineering and cell-therapy combinatorial approach for spinal cord injury regeneration, Macromol. Biosci. 13 (2013) 1576–1592, https://doi.org/10.1002/mabi.201300178.

[43] A. Canha-Gouveia, A. Rita Costa-Pinto, A.M. Martins, N.A. Silva, S. Faria, R.A. Sousa, A.J. Salgado, N. Sousa, R.L. Reis, N.M. Neves, Hierarchical scaffolds enhance osteogenic differentiation of human Wharton's jelly derived stem cells, Biofabrication 7 (2015) 35009, https://doi.org/10.1088/1758-5090/7/3/035009.

[44] R. Silva, H. Ferreira, A.C. Carvalho, A.C. Gomes, A. Cavaco-Paulo, Protein microspheres as suitable devices for piroxicam release, Colloids Surf. B Biointerfaces 92 (2012) 277–285, https://doi.org/10.1016/j.colsurfb.2011.11.050.

[45] F. Bartolomeu, M. Buciumeanu, E. Pinto, N. Alves, F.S. Silva, O. Carvalho, G. Miranda, Wear behavior of Ti6Al4V biomedical alloys processed by Selective laser melting, hot pressing and conventional casting, Trans. Nonferrous Metals Soc. China (2017) 829–838, https://doi.org/10.1016/S1003-6326(17)60060-8 (English ed. 27).

[46] M. Buciumeanu, A. Bagheri, N. Shamsaei, S.M. Thompson, F.S. Silva, B. Henriques, Tribocorrosion behavior of additive manufactured Ti-6Al-4V biomedical alloy, Tribol. Int. 119 (2018) 381–388, https://doi.org/10.1016/j.triboint.2017.11.032.

[47] S. Zhang, Q. Wei, L. Cheng, S. Li, Y. Shi, Effects of scan line spacing on pore characteristics and mechanical properties of porous Ti6Al4V implants fabricated by selective laser melting, Mater. Des. 63 (2014) 185–193, https://doi.org/10.1016/j.matdes.2014.05.021.

[48] A. Bandyopadhyay, F. Espana, V.K. Balla, S. Bose, Y. Ohgami, N.M. Davies, Influence of porosity on mechanical properties and in vivo response of Ti6Al4V implants, Acta Biomater. 6 (2010) 1640–1648, https://doi.org/10.1016/j.actbio.2009.11.011.

[49] B. Vrancken, L. Thijs, J.-P. Kruth, J. Van Humbeeck, Heat treatment of Ti6Al4V produced by selective laser melting: microstructure and mechanical properties, J. Alloys Compd. 541 (2012) 177–185, https://doi.org/10.1016/j.jallcom.2012.07.022.

[50] L. Ponsonnet, K. Reybier, N. Jaffrezic, V. Comte, C. Lagneau, M. Lissac, C. Martelet, Relationship between surface properties (roughness, wettability) of titanium and titanium alloys and cell behaviour, Mater. Sci. Eng. C 23 (2003) 551–560, https:// doi.org/10.1016/S0928-4931(03)00033-X.

[51] N.J. Hallab, K.J. Bundy, K. O'Connor, R.L. Moses, J.J. Jacobs, Evaluation of metallic and polymeric biomaterial surface energy and surface roughness characteristics for directed cell adhesion, Tissue Eng. 7 (2001) 55–71, https://doi.org/10.1089/107632700300003297.

[52] L. Ponsonnet, V. Comte, A. Othmane, C. Lagneau, M. Charbonnier, M. Lissac, N. Jaffrezic, Effect of surface topography and chemistry on adhesion, orientation and growth of fibroblasts on nickel-titanium substrates, Mater. Sci. Eng. C 21 (2002) 157–165, https://doi.org/10.1016/S0928-4931(02)00097-8.

[53] C.-J. Chen, S.-J. Ding, C.-C. Chen, Effects of surface conditions of titanium dental implants on bacterial adhesion, Photomed. Laser Surg. 34 (2016), https://doi.org/10.1089/pho.2016.4103.

[54] M. Taborelli, M. Jobin, P. François, P. Vaudaux, M. Tonetti, S. Szmukler-Moncler, J. Simpson, P. Descouts, Influence of surface treatments developed for oral implants on the physical and biological properties of titanium. Surface characterization, Clin. Implant. Dent. Relat. Res. 8 (1997) 208–216.

[55] J. Vaithilingam, S. Kilsby, R.D. Goodridge, S.D.R. Christie, S. Edmondson, R.J.M. Hague, Functionalisation of Ti6Al4V components fabricated using selective laser melting with a bioactive compound, Mater. Sci. Eng. C 46 (2015) 52–61, https://doi.org/10.1016/j.msec.2014.10.015.

[56] G. Zhao, Z. Schwartz, M. Wieland, F. Rupp, J. Geis-Gerstorfer, D.L. Cochran, B.D. Boyan, High surface energy enhances cell response to titanium substrate microstructure, J. Biomed. Mater. Res. - Part A. 74 (2005) 49–58, https://doi.org/10.1002/jbm.a.30320.

[57] L. Le Guéhennec, A. Soueidan, P. Layrolle, Y. Amouriq, Surface treatments of titanium dental implants for rapid osseointegration, Dent. Mater. 23 (2007) 844–854, https://doi.org/10.1016/J.DENTAL.2006.06.025.

[58] E.A. Vogler, Structure and reactivity of water at biomaterial surfaces, Adv. Colloid Interf. Sci. 74 (1998) 69–117, https://doi.org/10.1016/S0001-8686(97)00040-7.

[59] R.A. Gittens, T. McLachlan, Y. Cai, S. Berner, R. Tannenbaum, Z. Schwartz, K.H. Sandhage, B.D. Boyan, The effects of combined micron-/submicron-scale surface roughness and nanoscale features on cell proliferation and differentiation, Biomaterials 32 (2011) 3395–3403, https://doi.org/10.1016/j.biomaterials.2011.01.029.The.

[60] R.N. Wenzel, Resistance of solid surfaces to wetting by water, Ind. Eng. Chem. 28 (1936) 988–994, https://doi.org/10.1021/ie50320a024.

[61] A.B.D. Cassie, S. Baxter, Wettability of porous surfaces, Trans. Faraday Soc. 40 (1944) 546–551, https://doi.org/10.1039/TF9444000546.

[62] S.P. Rodrigues, C.F.A. Alves, A. Cavaleiro, S. Carvalho, Water and oil wettability of anodized 6016 aluminum alloy surface, Appl. Surf. Sci. 422 (2017) 430–442, https://doi.org/10.1016/j.apsusc.2017.05.204.

[63] T. Motohiro, K. Yukari, S. Takahiro, Y. Yoshiyuki, N. Kaori, N. Fukue, Wettability of calcium phosphate ceramics by water, J. Ceram. Soc. Jpn. 103 (1995) 46–49.

[64] J. Lu, M. Descamps, J. Dejou, G. Koubi, P. Hardouin, J. Lemaitre, J.P. Proust, The biodegradation mechanism of calcium phosphate biomaterials in bone, J. Biomed. Mater. Res. 63 (2002) 408–412, https://doi.org/10.1002/jbm.10259.

[65] K.A. Shariff, K. Tsuru, K. Ishikawa, Fabrication of dicalcium phosphate dihydrate-coated β-TCP granules and evaluation of their osteoconductivity using experimental rats, Mater. Sci. Eng. C 75 (2017) 1411–1419, https://doi.org/10.1016/j.msec.2017.03.004.

[66] F.L. Yen, W.J. Shih, M.H. Hon, H.T. Chen, I.M. Hung, H.H. Ko, M.C. Wang, Understanding the biocompatibility of sintered calcium phosphate with ratio of [Ca]/[P]=1.50, J. Nanomater. 2012 (2012), https://doi.org/10.1155/2012/325605.

[67] L.-E. Monfoulet, P. Becquart, D. Marchat, K. Vandamme, M. Bourguignon, E. Pacard, V. Viateau, H. Petite, D. Logeart-Avramoglou, The pH in the microenvironment of human mesenchymal stem cells is a critical factor for optimal osteogenesis in tissue-engineered constructs, Tissue Eng. Part A 20 (2014) 1827–1840, https://doi.org/10.1089/ten.tea.2013.0500.

[68] I.A. Silver, J. Deas, M. Erecińska, Interactions of bioactive glasses with osteoblasts in vitro: effects of 45S5 Bioglass(®), and 58S and 77S bioactive glasses on metabolism, intracellular ion concentrations and cell viability, Biomaterials 22 (2001) 175–185, https://doi.org/10.1016/S0142-9612(00)00173-3.

CHAPTER 4

Corrosion Behaviour of PEEK or β-TCP-impregnated Ti6Al4V SLM Structures Targeting Biomedical Applications

M.M. Costa[a], T.A. Dantas[a,b*], F. Bartolomeu[a], N. Alves[c], F.S. Silva[a], G. Miranda[a], F. Toptan[a,d]

[a]Center for MicroElectroMechanical Systems (CMEMS-UMinho), University of Minho, Campus de Azurém, 4800-058 Guimarães – Portugal

[b]MIT Portugal Program, School of Engineering, University of Minho, Guimarães, Portugal;

[c]Centre for Rapid and Sustainable Product Development Polytechnic Institute of Leiria, Rua General Norton de Matos, Apartado 4133, Leiria, Portugal;

[d]IBTN/Br – Brazilian Branch of the Institute of Biomaterials, Tribocorrosion and Nanomedicine, UNESP, Campus de Bauru, Av. Eng. Luiz Edmundo Carrijo Coube, 14-01, 17033-360, Bauru, SP, Brazil

Abstract

Ti6Al4V cellular structures were produced by selective laser melting (SLM) and then filled either with beta-tricalcium phosphate (β-TCP) or PEEK (poly-ether-ether-ketone) through powder metallurgy techniques, to improve osteoconductivity and wear resistance. The corrosion behavior of these structures was explored considering its importance for the long-term performance of implants. Results revealed that the incorporation of open cellular pores induced higher electrochemical kinetics when being compared with dense structures. The impregnation of β-TCP and PEEK led to the creation of voids or gaps between the metallic matrix and the impregnated material which also influenced the corrosion behavior of the cellular structures.

4.1. Introduction

Ti6Al4V is one of the most used Ti alloys in biomedical applications, such as orthopedic implants, due to its good mechanical properties. It is a lightweight metal, having high strength, good fracture toughness, low thermal expansion and lower elastic modulus (among metallic biomaterials) [1,2]. Additionally, it presents high biocompatibility and excellent capacity to resist corrosion, associated with the formation of a stable and compact oxide layer on its surface that is created spontaneously when exposed to oxygenated environments [3–6]. However, as other Ti alloys, this material presents no bioactivity which is required to reduce implant-tissue osseointegration time and, subsequently, to promote shorter healing time. Hence, several functionalization techniques are being studied to improve bioactivity [7]. Beta-tricalcium phosphate (β-TCP, $Ca_3(PO_4)_2$), a bioactive material highly similar to the mineral phase of bone, has been applied to overcoming the lack of bioactivity [8–10]. The addition of this ceramic to a Ti matrix is expected to induce a natural bone tissue growth, and consequently promote a faster bone-tissue osseointegration [11,12]. On the other hand, Ti6Al4V also presents poor wear resistance and tends to release metallic ions and wear debris to the surrounding medium [13–15]. To overcome these issues, Poly-ether-ether-ketone (PEEK) and PEEK-based materials have been applied due to their excellent thermal and chemical stability and higher wear resistance, comparing to Ti and its alloys [16,17]. Furthermore, PEEK has excellent mechanical properties, such as low elastic modulus and relatively low manufacturing cost [18].

Selective laser melting (SLM) is an additive manufacturing technique that allows the production of customized and complex 3D parts from CAD data by using laser energy to melt metallic powders in a layer-by-layer process [19–23]. Among all the advantages, the SLM technique allows the production of parts without the need for using additional steps [24,25]. Briefly, in this process, 3D CAD data are imported to an SLM software that slices the part into successive layers with a given layer thickness. The metallic powder is spread across the SLM platform and a laser beam scans the powder in predefined sites to melt it and, layer-by-layer, to produce the desired 3D part [20,22,24,26]. The processing parameters like laser power, scan speed, and scan spacing have a huge impact on the SLM components final properties. Many studies have been made to assess the influence of the processing parameters on the final properties of SLM components, in terms of physical, mechanical and microstructural properties [26–29]. Bartolomeu et al [26] have investigated the effect of SLM processing parameters on the final properties of Ti6Al4V samples such as density, hardness and shear strength and reported the optimal parameters for this technology on this material. Zhao et al [30] produced Ti6Al4V alloy by electron beam melting (EBM) and SLM, compared their corrosion behavior in simulated body fluid and reported good corrosion resistance for the samples produced by EBM and SLM that were regarded by authors as suitable for implantation in vivo. However, some authors reported poorer corrosion resistance for the SLM-produced Ti6Al4V alloy due to a large amount of acicular α' and less β-Ti phase in the microstructure [31,32].

Many studies have been made on the production of porous structures, by SLM, to promote bone growth towards the implant, ensuring a good mechanical interlocking between implant and bone [33–35]. However, since these structures will be surrounded by corrosive body fluids, it is essential to assess their corrosion performance. Studies performed on highly-porous Ti [36] and Ti alloy [37] structures showed that increased porosity resulted in the formation of a less protective oxide film on the pore surfaces due to difficulties or delays on the electrolyte penetration through the innermost pores.

Targeting biomedical applications, the present study aimed to evaluate the effect of porosity and the incorporation of β-TCP or PEEK on the corrosion behavior of Ti6Al4V-SLM structures. Ti6Al4V cellular structures were designed and produced by SLM in a way to obtain near-net-shape structures according to the predefined CAD model. Using these multifunctional structures, it can be possible to reduce the elastic modulus, to promote the bone ingrowth, as well, to improve the bioactivity and wear resistance by impregnating β-TCP and PEEK, respectively, into the open cells.

4.2. Experimental

4.2.1. Starting materials

The Ti6Al4V starting powders used to produce the SLM samples were supplied from SLM solutions (Germany). Table 4.1 and Figure 4.1(a) show the composition and particle size, respectively, according to the manufacturers.

Table 4.1 - Composition of Ti6Al4V powders (wt.%).

Al	V	C	Fe	O	N	H	Ti
6.4	3.8	0.01	0.23	0.12	0.02	0.0074	Bal.

After producing the Ti6Al4V cellular structures, two approaches were evaluated: bioactive impregnation of β-TCP and polymer impregnation of PEEK. The bioactive impregnation using β-TCP was carried out by using press and sintering technique. β-TCP powder was supplied from Trans-Tech, Inc, with a particle size distribution as presented in Figure 4.1(b). The polymer impregnation using PEEK was carried out by using hot pressing. PEEK powder was supplied from Evonik Industries, with the particle size distribution presented in Figure 4.1(c).
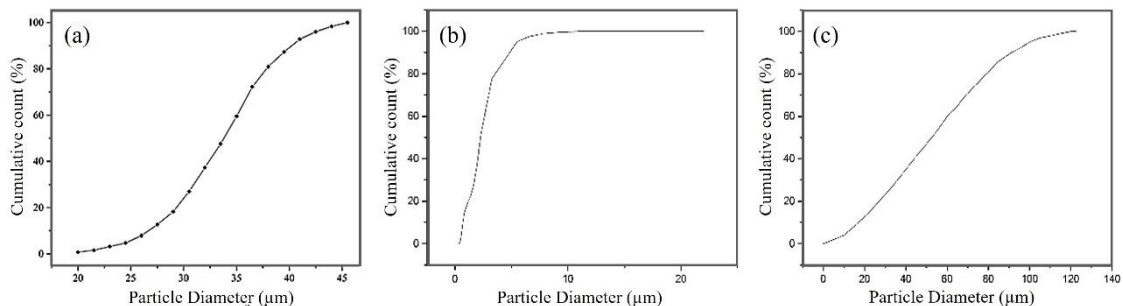
Figure 4.1 - Powder size distributions of Ti6Al4V (a), β-TCP (b) and PEEK (c).

4.2.2. Processing

To fabricate dense and cellular structured Ti6Al4V samples, a commercial SLM equipment (SLM solutions, model 125HL) was used. The main characteristics of the equipment are shown in Table 4.2. Briefly, this equipment has an Yb-faser-laser, a focus beam diameter of 87 μm and a maximum laser power of 100 W. The process occurs under an Ar/N$_2$ atmosphere keeping the temperature of the building platform at 200 °C. The present study used SLM processing parameters, a laser power of 90 W, a scan speed of 600 mm/s, a scan spacing of 80 μm and a layer thickness of 30 μm.

Table 4.2 - SLM equipment (model 125 HL) characteristics.

Laser type	Effective build volume/ mm³	Laser power/ W	Scanning speed/ (mm.s⁻¹)	Layer thickness/ μm	Distance between scanning lines/ mm	Laser spot/ μm	Iner gas (Ar/N₂) flow during production/ (L.min⁻¹)	Iner gas (Ar/N₂) flow during filling of chamber/ (L.min⁻¹)
Yb-faser-laser	125×125×125	40-100	100-200	20-40	0.07-0.15	87	0.5	10

Four different types of Ti6Al4V or Ti6Al4V-based samples were produced and investigated. Table 4.3 gives the component type and processing technique for each group of samples.

Table 4.3 - Testing samples.

Sample No.	Ti6Al4V component type	Processing Technique
SP1	Dense	SLM
SP2	Cellular structured	SLM
SP3	Cellular structured impregnated with β-TCP	SLM + press and sintering
SP4	Cellular structured impregnated with PEEK	SLM + hot pressing

After producing the cellular structured parts (SP2), β-TCP (SP3) and PEEK (SP4) were introduced into the available open cells (Figure 4.2). On SP3 samples, β-TCP impregnation was performed through a press and sintering process. In this process, the cellular structures were placed in a steel mold. Thereafter, a solution of β-TCP powder and acetone was prepared and introduced into a steel mold where the cellular structure was already properly positioned. Then, using an upper punch, the pressure was slowly applied by a hydraulic press to force this solution to occupy the open cells. After 10 min under pressure, the samples were removed from the mold. To sinter the β-TCP powders, a subsequent sintering step was performed in a tubular furnace at 1100 °C for 2 h under a high vacuum (10^{-3} Pa), with heating and cooling rates of 5 °C/min.

On SP4 samples, hot pressing was used to impregnate PEEK by applying simultaneously pressure and temperature. The cellular structures were inserted inside a steel mold, followed by the introduction of PEEK powder. After placing and positioning the mold inside the chamber, a residual pressure was applied to compressing the powder. Posteriorly, the mold was heated until 380 °C (above PEEK melting point of 345 °C). Finally, the induction heating was turned off to decrease the temperature down to 300 °C and PEEK was pressed under 25 MPa for 5 s, to force it to fill the available space inside the open cells.
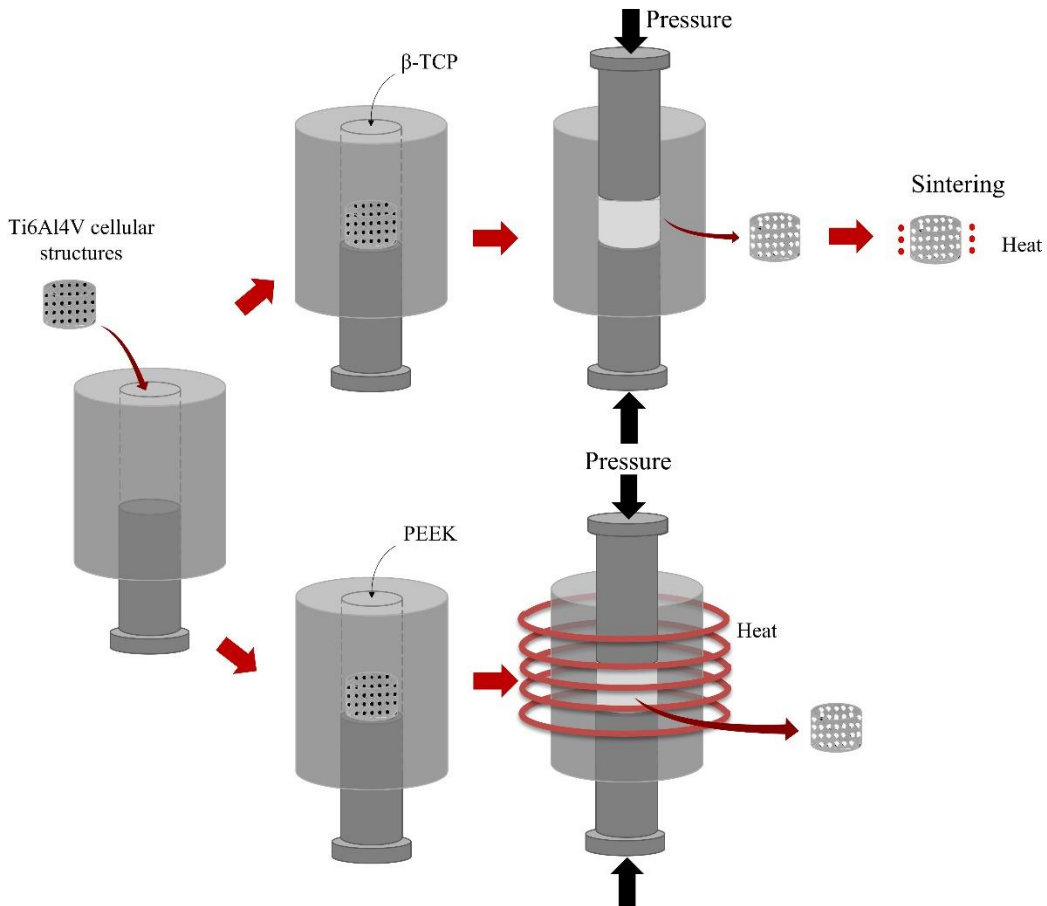
Figure 4.2 - Fabrication details of Ti6Al4V cellular structures impregnated with β-TCP or PEEK.

4.2.3. Microstructural analysis

Field emission gun scanning electron microscopy (FEG SEM, FEI Nova 200, USA) was used to characterize the surfaces before and after testing. The effect of the impregnation method on the microstructure of Ti6Al4V was evaluated on the surfaces etched with Kroll's reagent (5% HNO_3, 10% HF and 85% distilled water) and analyzed by SEM. Before corrosion tests, crystalline structures were characterized with X-ray diffraction using Bruker AXS D8 Discover equipment. Diffraction data were collected from 10° to 80° of 2θ, with a step size of 0.02° and counting time of 1 s/step.

4.2.4. Corrosion tests

Before testing, all samples were polished with different abrasive silicon carbide papers, ranging from 0.125 to 0.0374 mm grit size. After grinding, samples were ultrasonically cleaned with propanol for 30 min in the case of SP2 and 10 min in the other three conditions. Regarding the cellular structure (SP2), due to its complex geometry, cleaning was done in a net positioned upside down, to avoid the accumulation of debris coming from grinding.

A three-electrode cell assembly comprising the sample as the working electrode, a platinum electrode as the counter electrode, a saturated calomel electrode as the reference electrode, and 40 mL of NaCl (9 g/L) solution as the electrolyte was used for the electrochemical tests. Open-circuit potential (OCP) and cyclic polarization were carried out using a Gamry Potentiostat/Galvanostat/ZRA (Reference 600) equipment on samples having a geometric exposed area of 0.36 cm^2 that was also used for normalizing the electrochemical results for SP1 samples. The exposed areas of SP2 and SP3 were calculated from the CAD model whereas only the metallic exposed area was considered for SP4 samples. Before cyclic polarization, OCP values were monitored until stabilization (the values of potential did not vary more than 40 mV in 1 h). Cyclic polarization curves were acquired using a scan rate of 1 mV/s, starting at −0.2 V (vs OCP), and the sweep direction was reversed at 1 V (vs SCE).

4.3. Results and discussion

4.3.1. Microstructural characterization

Figure 4.3 shows the representative morphologies of the raw powders. Figure 4.3(a), (b) and (c) correspond to the Ti6Al4V, β-TCP and PEEK powders, respectively. From these figures, it is possible to observe that Ti6Al4V had a spherical shape, β-TCP powder was characterized by an aggregate of spherical particles and PEEK powder had an irregular shape.
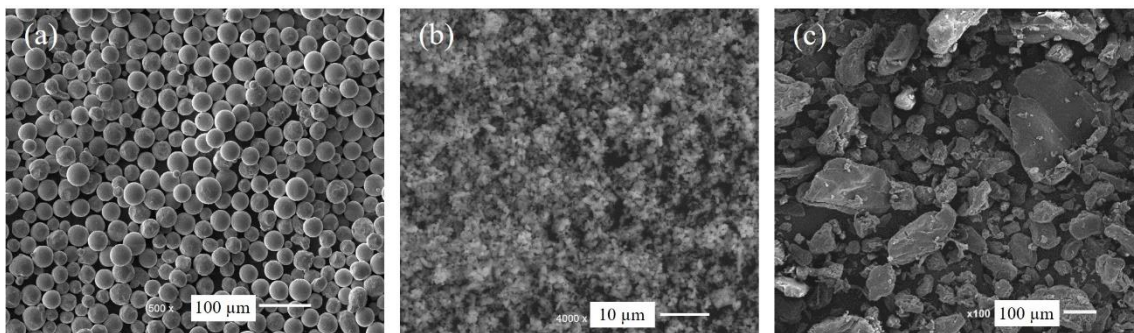
Figure 4.3 - SEM images of raw powders: (a) Ti6Al4V; (b) β-TCP; (c) PEEK.

3D parts, produced by SLM based on the CAD data, are presented in Figure 4.4. It is possible to verify from the images that the samples were successfully produced by this technique, once the geometry of the CAD model and the SLM processed sample was very similar.
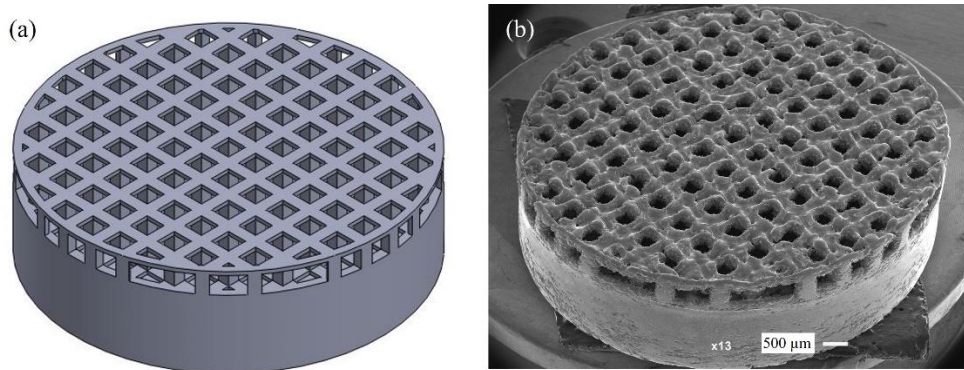
Figure 4.4 - SLM structure of CAD model (a) and as-built sample (b).

Figure 4.5 presents the samples before corrosion testing. Regarding SP1 (dense) samples (Figure 4.5(a)), no evidence of pronounced porosity was observed, suggesting that the processing technique was efficient to promote the densification of the samples. The open cellular structures can be seen in Figure 4.5(b) showing the viability of SLM to produce such geometries. On the other hand, Figure 4.5(c) and (d) show the Ti6Al4V cellular structures impregnated with β-TCP and PEEK, respectively. It was possible to observe that the impregnation process of β-TCP was not as efficient as PEEK, once the holes were not totally filled with the ceramic material.
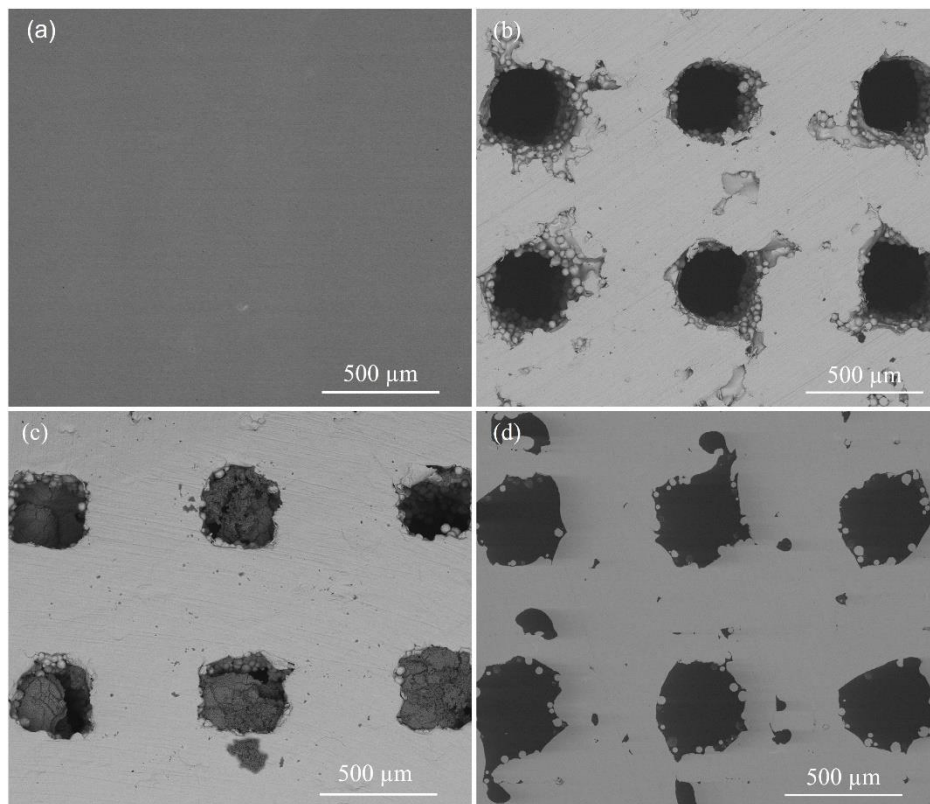
Figure 4.5 - SEM images of SLM-produced samples: (a) SP1; (b) SP2; (c) SP3; (d) SP4.

Figure 4.6 presents the XRD patterns of each sample. Regarding SP1 and SP2 samples, no significant differences were detected in the XRD pattern where hexagonal close-packed (HCP) and body-centered cubic (BCC) crystalline structures of Ti were detected. On the other hand, by adding β-TCP to the cellular structure (SP3), it was possible to observe a new peak (≈31°) that corresponds to the β-TCP phase. Analyzing the SP4 pattern, new peaks were observed corresponding to the PEEK pattern, which is in accordance with the XRD patterns for this material [38–40].

The acid etched microstructures of the metallic matrix of SP1, SP2, SP3, and SP4 are given in Figure 4.7. Ti6Al4V alloy is known for its structure composed of α phase (HCP) and β phase (BCC). SEM images revealed the presence of acicular α′ martensite, that is hard to observe on the XRD spectra since α and α′ phases have HCP structure with very close lattice parameters [32]. The XRD results of SP3 together with the microstructure presented in Figure 4.7(c) suggested that the martensite phase was decomposed into α and β phases when subjected to high temperatures (temperatures above the β transus) [41].
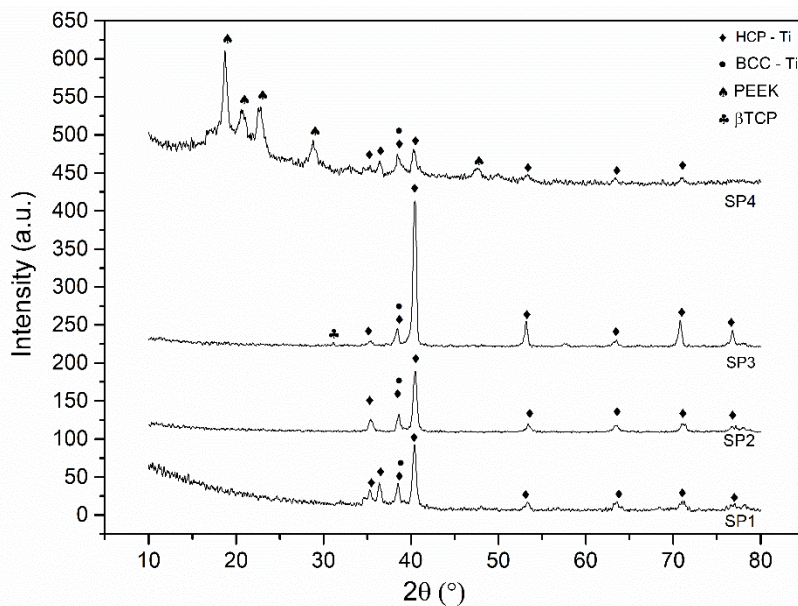
Figure 4.6 - XRD patterns of tested samples showing distinctive phase constituents.
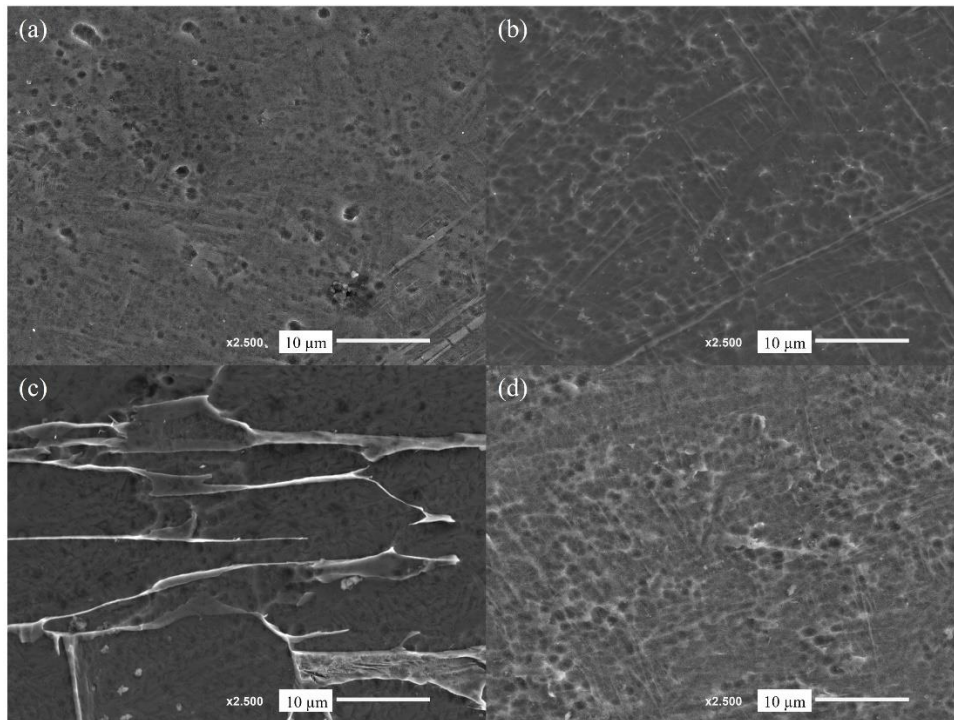
Figure 4.7 - SEM images of acid etched samples: (a) SP1; (b) SP2; (c) SP3; (d) SP4.

4.3.2. Corrosion behavior

In order to normalize the electrochemical data, the electrolyte exposed area of 1.92 cm^2 for the SP2 calculated from the CAD model by considering the following areas is shown in Figure 4.8, where A_1 is the area of the pore walls (green) that are presented both on top and bottom of the sample, A_2 corresponds to the area of the interconnecting walls between pores, A_3 represents the superficial area (blue) of the sample, A_4 is the bottom area (orange) and A_5 represents the top walls (red).
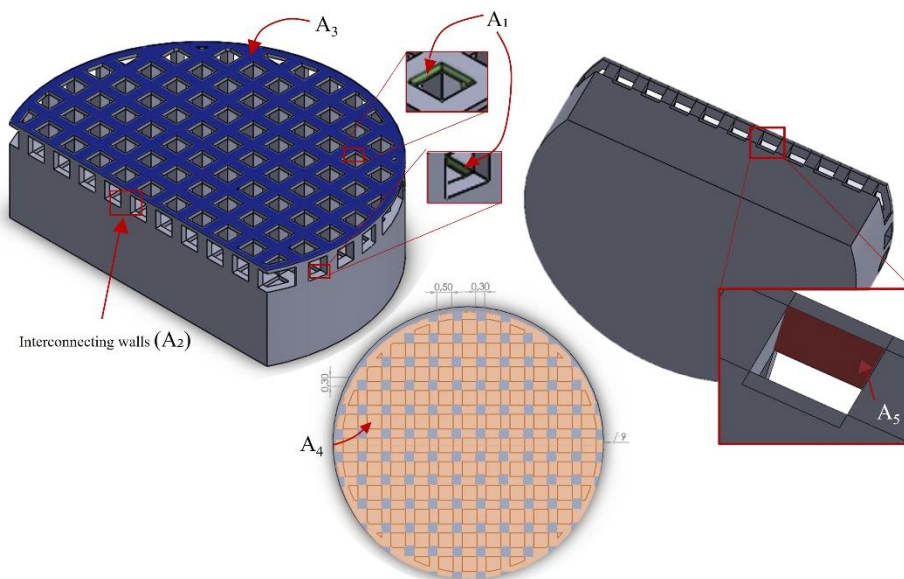
Figure 4.8 - Schematic representation of total area in contact with electrolyte for cellular structures (unit: mm).

As it is shown in Figure 4.5(c), the β-TCP impregnation was not fully achieved on SP3. In this sense, the exposed area was determined on the CAD model (Figure 4.9) by considering the areas shown by arrows in Figure 4.9 (top areas of A_1, A_2, A_3, and A_5). According to this assumption, the exposed area is calculated as 1.23 cm². Nevertheless, it is worthy to stress that these area calculations are approximations and particularly on SP3, the irregularity inside the open cells made it difficult to obtain accurate calculations. Therefore, future works on the optimized samples should use more accurate techniques, such as micro-CT, to calculate the exposed area more precisely. For the SP4 sample, since the impregnation was almost fully achieved, only the metallic area was considered (0.26 cm²).
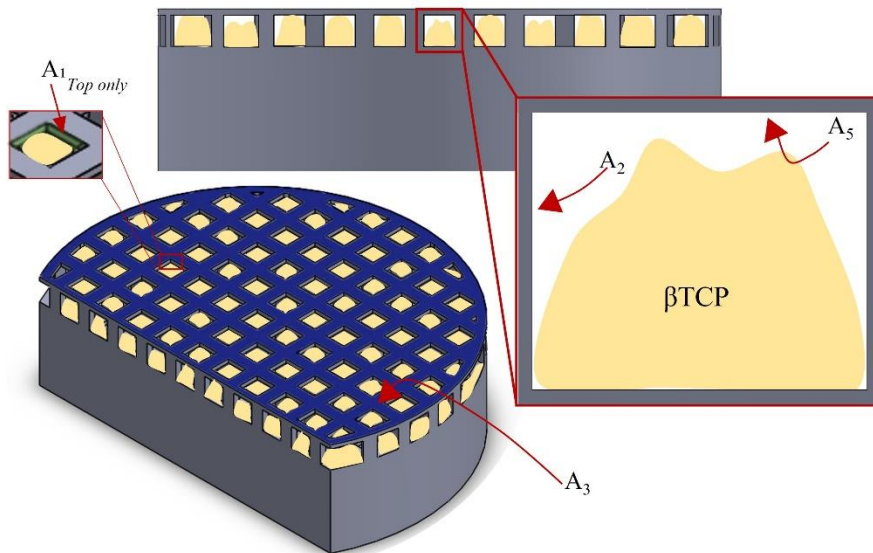
Figure 4.9 - Schematic representation of total area in contact with electrolyte for SP3 sample.

The cyclic polarization curves of the different tested materials are presented in Figure 4.10. Average values of the last 10 minutes of φ_{OCP}, corrosion potential ($\varphi_{(i=0)}$) and corrosion current density (J_{corr}) (obtained by Tafel extrapolation), and J_{pass} values (derived from the curves) are given in Table 4.4. As it is very well known [3,42], Ti has a strong affinity to oxygen which leads to its ability to create a stable passive film in any environment that contains oxygen, characterized by a well-defined passivation plateau. The reverse curves of all tested materials evolved on the left-hand side of the forward curves, i.e., for the same potential the current density on the backward scan presented lower values, indicating their ability to resist to localized corrosion [43].
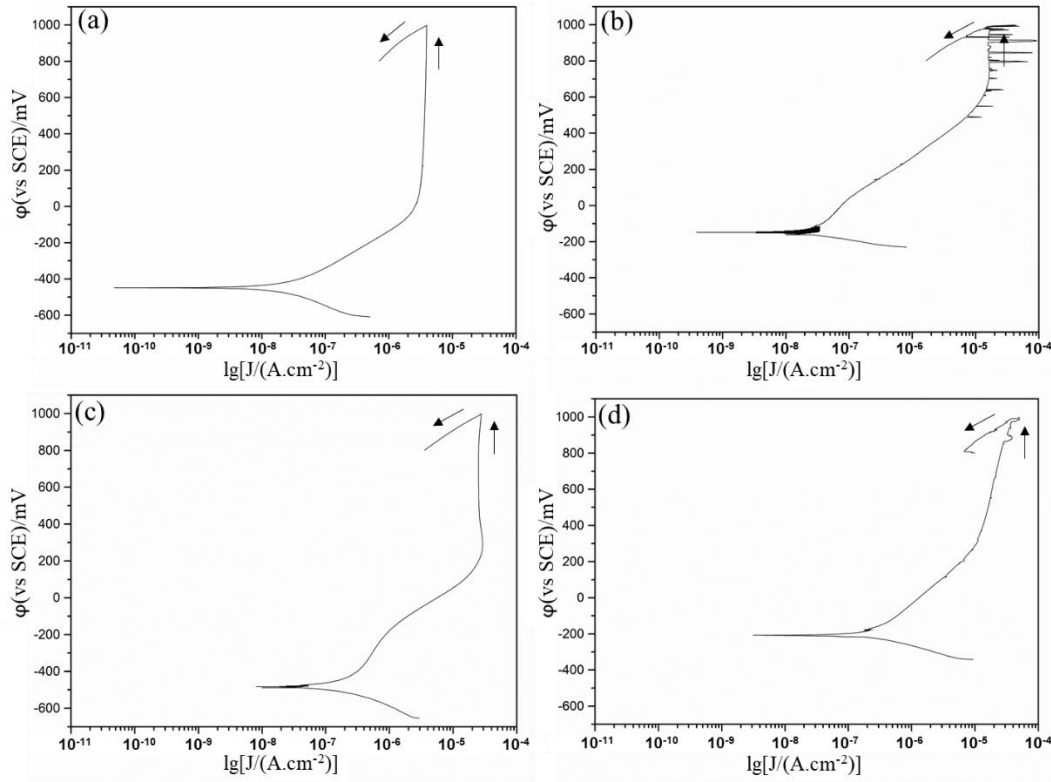
Figure 4.10 - Cyclic polarization curves of tested materials: (a) SP1; (b) SP2; (c) SP3; (d) SP4.

Table 4.4 - Electrochemical data derived from cyclic polarization curves for tested materials.

Sample	φ_{OCP}	$\varphi_{(i=0)}$ (mV)	J_{corr} ($\times 10^{-7}$ A.cm^{-2})	J_{pass} ($\times 10^{-5}$ A.cm^{-2})
SP1	-386 ± 23	-423 ± 25	-	0.39 ± 0.04
SP2	-59 ± 53	-141 ± 59	-	1.53 ± 0.07
SP3	-459 ± 22	-492 ± 18	-	2.51 ± 0.02
SP4	-153 ± 10	-209 ± 22	5.03 ± 0.49	-

A clear passivation plateau was observed on the cyclic polarization curve of SP1 (Figure 4.10(a)) at $(0.39 \pm 0.04) \times 10^{-5}$ A/cm^2 (J_{pass}). On the other hand, the transition from cathodic to anodic domain was characterized by a $\varphi_{(i=0)}$ of (-423 ± 25) mV (Table 4.4). The representative evaluation of the cyclic polarization curve of the cellular structures (SP2) is presented in Figure 4.10(b). The forward scan was characterized by a $\varphi_{(i=0)}$ of (-141 ± 59) mV (Table 4.4) with a passivation current density (J_{pass}) of $(1.53 \pm 0.07) \times 10^{-5}$ A/cm^2. The passivation plateau observed on SP2 shifted to higher current density values and presented some local increments on the current. These samples were characterized by the existence of interconnected holes that may allow a delay in electrolyte flow, that eventually may result in creation of less protective oxide film on the inner cell surface, which may be responsible for the increased J_{pass} values, as already reported for Ti [36] and Ti–Nb based [37] highly-porous structures. Nevertheless, since the exposed area was calculated over a CAD

110

model, and since as-built samples presented rough cell surfaces (Figure 4.5), the real exposed area may be increased, which may have an influence on obtaining increased J_{pass} values.

Figure 4.10(c) represents the cyclic polarization curve of SP3. Despite having lower corrosion potential compared with SP2, $\varphi_{(i=0)}=(-492\pm18)$ mV, it has the capability of forming a stable passive film evidenced by a well-marked passivation plateau. Furthermore, comparing SP1 and SP3 polarization curves, the corrosion potentials of both plots were very similar ($\varphi_{(i=0)}=(-423\pm25)$ mV vs $\varphi_{(i=0)}=(-492\pm18)$ mV). However, J_{pass} of SP3 was higher than that of SP1 ($(2.51\pm0.02)\times10^{-5}$ A/cm^2). As also mentioned above, although a model was followed to calculate the exposed area on SP3 sample, this model may have some deviations since it is very difficult to simulate the impregnation process with β-TCP, that eventually may lead to a deviation on the J_{pass} values, in addition to the possible heterogeneities on the passive film due to the delays on the electrolyte penetration.

Figure 4.10(d) shows the cyclic polarization curves of samples impregnated with PEEK (SP4). The corrosion potential of this material was (-209 ± 22) mV and J_{corr} was $(5.03\pm0.49)\times10^{-7}$ A/cm^2. It was possible to observe that for these samples that there was a deviation on the passivation plateau, which can be related with the presence of some narrow gaps between the polymeric and metallic transition that might act as active zones that, consequently, promoted some discontinuities on the passive film [44].

Therefore, although the presence of β-TCP and PEEK was not expected to influence directly the corrosion behavior of Ti6Al4V, the impregnation process led to some interfacial voids or gaps between the impregnated material and the metallic matrix that eventually influenced the corrosion behavior of these structures.

Figure 4.11 shows the SEM micrographs of the surfaces after corrosion testing. There were no visible changes in the surface morphology on none of the samples when compared with the as-processed ones. However, further analysis of the impregnated samples (Figure 4.11(c) and (d)) may explain the different results obtained on the electrochemical tests. As already mentioned, and as can be seen in Figure 4.11(c), the impregnation process was not fully accomplished on SP3, which led to increased exposed area and possibly led to some difficulties on electrolyte penetration that apparently influenced the corrosion behavior. Moreover, in the case of SP4 (Figure 4.11(d)), the impregnation process was fully achieved; however, some gaps were visible on the material surface that apparently affected the corrosion behavior. Therefore, these results showed that further work should be performed to optimize the impregnation process to avoid discontinuities at the interface between the impregnated material and the metallic matrix. After optimization, further

electrochemical analysis such as electrochemical impedance spectroscopy should be carried out to better understand the corrosion mechanisms.
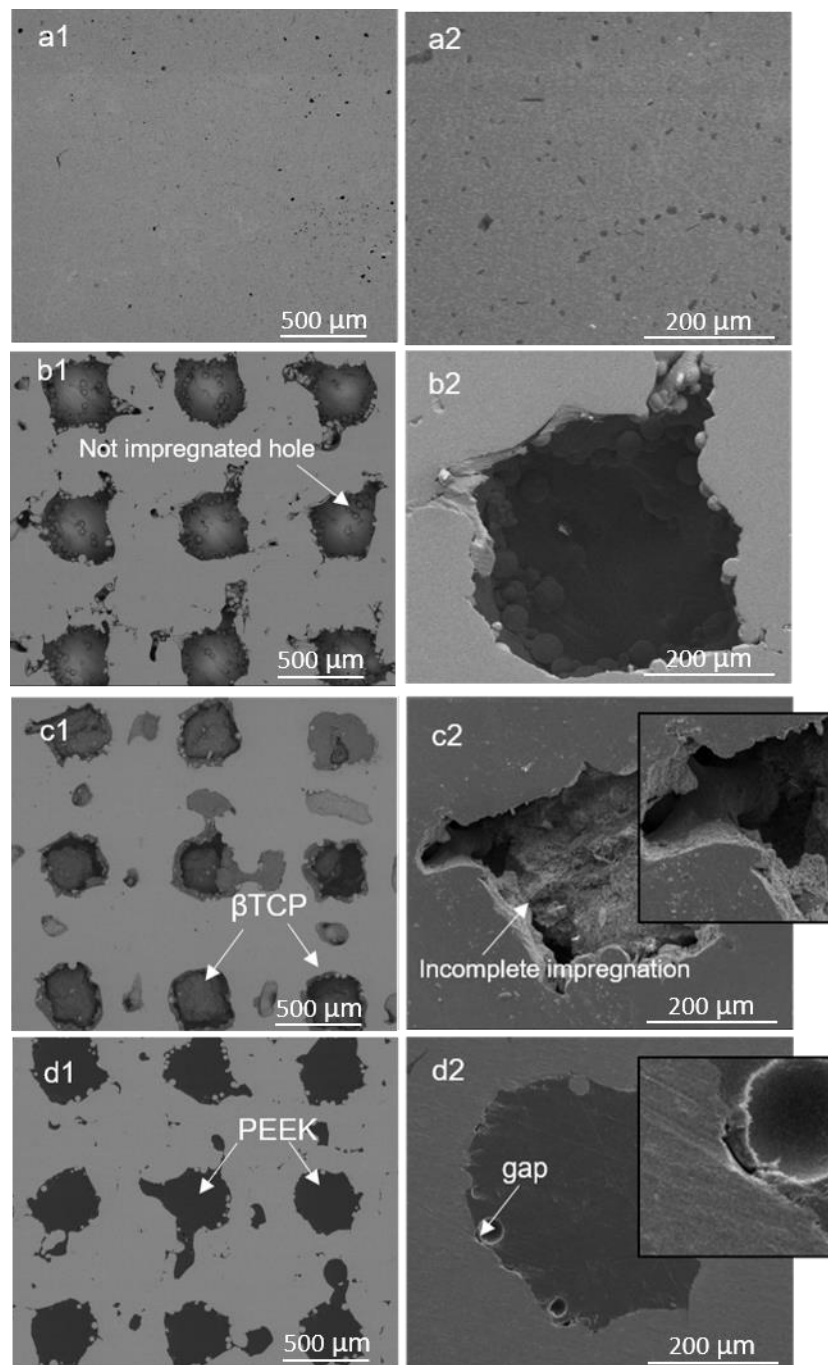
Figure 4.11 - Lower and higher magnification SEM micrographs of surfaces after corrosion tests: (a) SP1; (b) SP2; (c) SP3; (d) SP4.

4.4. Conclusions

(1) Processing of Ti6Al4V alloy by SLM led to the formation of acicular α′ martensite, along with α and β phases. Further sintering process applied for β-TCP resulted in the decomposition of the martensite phase into α and β phases.

(2) Corrosion studies revealed that the introduction of open cellular porosity on Ti6Al4V or uncompleted impregnation process could influence the corrosion behavior through the presence of interconnected pores or gaps between the metal and the impregnated material leading to the difficulties or delays on the electrolyte penetration that may create heterogeneities on the passive film.

(3) No evidence of localized corrosion was observed on the polarization curves neither for the cellular structures nor for the β-TCP or PEEK impregnated structures; however, some narrow gaps between the impregnated PEEK and the Ti6Al4V matrix probably acted as active zones and promoted some discontinuities on the passive film.

Acknowledgments

References

[1] Niinomi M. Biologically and mechanically biocompatible titanium alloys Ti−6Al−4V ELI [J]. Materials Transactions, 2008, 49:2170−2178.

[2] Kahraman N, Gulenc B, Findik F. Corrosion and mechanical-microstructural aspects of dissimilar joints of Ti−6Al−4V and Al plates [J]. International Journal of Impact Engineering, 2007,34: 1423−1432.

[3] Licausi M P, Igual Muñoz A, Borrás V A. Tribocorrosion mechanisms of Ti6Al4 V biomedical alloys in artificial saliva with different pHs [J]. Journal of Physics D: Applied Physics, 2013, 46:404003.

[4] Souza J C M, Barbosa S L, Ariza E, Celis J P, Rocha L A. Simultaneous degradation by corrosion and wear of titanium in artificial saliva containing fluorides [J]. Wear, 2012, 292−293:82−88.

[5] Ratner B D, Hoffman A, Schoen F, Lemons J. Biomaterials science: An introduction to materials in medicine [M]. Third ed. USA: Elsevier, 2013.

[6] Costa M M, Bartolomeu F, Alves N, Silva F S, Miranda G. Tribological behavior of bioactive multi-material structures targeting orthopedic applications [J]. Journal of the Mechanical Behavior of Biomedical Materials, 2019, 94: 193−200.

[7] Yilmaz E, Çakiroğlu B, Gökçe A, Findik F, Gulsoy H O, Gulsoy N, Mutlu Ö, Özacar M. Novel hydroxyapatite/graphene oxide/collagen bioactive composite coating on Ti16Nb alloys by electrodeposition [J]. Materials Science and Engineering C, 2019, 101: 292–305.

[8] Ogose A, Hotta T, Kawashima H, Kondo N, Gu W, Kamura T, Endo N. Comparison of hydroxyapatite and beta tricalcium phosphate as bone substitutes after excision of bone tumors [J]. Journal of Biomedical Materials Research, Part B:Applied Biomaterials, 2004, 72B: 94–101.

[9] Dantas T A, Abreu C S, Costa M M, Miranda G, Silva F S, Dourado N, Gomes J R. Bioactive materials driven primary stability on titanium biocomposites [J]. Materials Science and Engineering C, 2017, 77: 1104–1110.

[10] Costa M M, Lima R, Melo-Fonseca F, Bartolomeu F, Alves N, Miranda A, Gasik M, Silva F S, Silva N A, Miranda G. Development of β-TCP–Ti6Al4V structures: Driving cellular response by modulating physical and chemical properties [J]. Materials Science and Engineering C, 2019, 98: 705–716.

[11] Zhang S, Xianting Z, Yongsheng W, Kui C, Wenjian, W. Adhesion strength of sol–gel derived fluoridated hydroxyapatite coatings [J]. Surface and Coatings Technology, 2006, 200:6350–6354.

[12] Mohseni E, Zalnezhad E, Bushroa A R. Comparative investigation on the adhesion of hydroxyapatite coating on Ti–6Al–4V implant: A review paper [J]. International Journal of Adhesion and Adhesives, 2014, 48: 238–257.

[13] Cintia S, Milani M. Evaluation of the stress distribution in CFR-PEEK dental implants by the three-dimensional finite element method [J]. Journal of Materials Science: Materials in Medicine, 2010, 21: 2079–2085.

[14] Meenen N M, Lehmann W. Response of primary fibroblasts and osteoblasts to plasma treated polyetheretherketone (PEEK) surfaces [J]. Journal of Materials Science: Materials in Medicin, 2005, 6:671–677.

[15] Dantas T A, Costa M M, Miranda G, Silva F S, Abreu C S, Gomes J R. Effect of HAp and β-TCP incorporation on the tribological response of Ti6Al4V biocomposites for implant parts [J]. Journal of Biomedical Materials Research, Part B: Applied Biomaterials, 2018, 106: 1010–1016.

[16] Chen F, Ou H, Lu B, Long H. A constitutive model of polyether-ether-ketone [J]. Journal of the Mechanical Behavior of Biomedical Materials, 2016, 53: 427–433.

[17] Zhou L, Qian Y, Zhu Y, Liu H, Gan K, Guo J. The effect of different surface treatments on the bond strength of PEEK composite materials [J]. Dental Materials, 2014, 30: 209–215.

[18] Garcia-Gonzalez D, Rodriguez-Millan M, Rusinek A, Arias A. Low temperature effect on impact energy absorption capability of PEEK composites [J]. Composite Structures, 2015, 134:440–449.

[19] Takezawa A, Kobashi M, Koizumi Y, Kitamura M. Porous metal produced by selective laser melting with effective isotropic thermal conductivity close to the Hashin-Shtrikman bound [J]. International Journal of Heat and Mass Transfer, 2017, 105:564–572.

[20] Spierings A B, Dawson K, Heeling T, Uggowitzer P J, Schäublin R, Palm F, Wegener K. Microstructural features of Sc- and Zr-modified Al–Mg alloys processed by selective laser melting [J]. Materials & Design, 2017, 115: 52–63.

[21] Milton S, Morandeau A, Chalon F, Leroy R. Influence of finish machining on the surface integrity of Ti6Al4V produced by selective laser melting [C]//3rd CIRP Conference on Surface Integrity (CIRP CSI). Charlotte, North Carolina, UAS: Elsevier, 2016:127–130.

[22] Boschetto A, Bottini L, Veniali F. Roughness modeling of AlSi10Mg parts fabricated by selective laser melting [J]. Journal of Materials Processing Technology, 2017, 241: 154–163.

[23] Sun J, Yang Y, Wang D. Parametric optimization of selective laser melting for forming Ti6Al4V samples by Taguchi method [J]. Optics & Laser Technology, 2013, 49: 118–124.

[24] Yadroitsev I, Bertrand P, Smurov I. Parametric analysis of the selective laser melting process [J]. Applied Surface Science, 2007, 253: 8064–8069.

[25] Bartolomeu F, Buciumeanu M, Pinto E, Alves N, Silva F S, Carvalho O, Miranda G. Wear behavior of Ti6Al4V biomedical alloys processed by selective laser melting, hot pressing and conventional casting [J]. Transactions of Nonferrous Metals Society of China, 2017, 27:829–838.

[26] Bartolomeu F, Faria S, Carvalho O, Pinto E, Alves N, Silva F S, Miranda G. Predictive models for physical and mechanical properties of Ti6Al4V produced by selective laser melting [J]. Materials Science and Engineering A, 2016, 663: 181–192.

[27] Zhang H, Zhu H, Qi T, Hu Z, Zeng X. Selective laser melting of high strength Al–Cu–Mg alloys: Processing, microstructure and mechanical properties [J]. Materials Science and Engineering A, 2016, 656: 47–54.

[28] Hao L, Dadbakhsh S, Seaman O, Felstead M. Selective laser melting of a stainless steel and hydroxyapatite composite for load-bearing implant development [J]. Journal of Materials Processing Technology, 2009, 209: 5793–5801.

[29] Bordin A, Sartori S, Bruschi S, Ghiotti A. Experimental investigation on the feasibility of dry and cryogenic machining as sustainable strategies when turning Ti6Al4V produced by Additive Manufacturing [J]. Journal of Cleaner Production, 2017, 142:4142–4151.

[30] Zhao B, Wang H, Qiao N, Wang C, Hu M. Corrosion resistance characteristics of a Ti-6Al-4V alloy scaffold that is fabricated by electron beam melting and selective laser melting for implantation in vivo [J]. Materials Science and Engineering C, 2017, 70: 832–841.

[31] DAI Nian-Wei, ZHANG Lai-Chang, ZHANG Jun-Xi, CHEN Qi-Meng, WU Mao-Liang. Corrosion behaviour of selective laser melted Ti–6Al–4V alloy in NaCl solution [J]. Corrosion Science, 2016, 102:484–489.

[32] Toptan F, Alves A C, Carvalho O, Bartolomeu F, Pinto A M, Silva F S, Miranda G. Corrosion and tribocorrosion behavior of Ti6Al4V produced by selective laser melting and hot pressing in comparison with the commercial alloy [J]. Journal of Materials Processing Technology, 2019, 266: 239–245.

[33] Arabnejad S, Burnett Johnston R, Pura J A, Singh B, Tanzer M, Pasini D. High-strength porous biomaterials for bone replacement: A strategy to assess the interplay between cell morphology, mechanical properties, bone ingrowth and manufacturing constraints [J]. Acta Biomaterialia, 2016, 30:345–356.

[34] Bartolomeu F, Sampaio M, Carvalho O, Pinto E, Alves N, Gomes J R, Silva F S, Miranda G. Tribological behavior of Ti6Al4V cellular structures produced by Selective Laser Melting [J]. Journal of the Mechanical Behavior of Biomedical Materials, 2017, 69: 128–134.

[35] Taniguchi N, Fujibayashi S, Takemoto M, Sasaki K, Otsuki B, Nakamura T, Matsushita T, Kokubo T, Matsuda S. Effect of pore size on bone ingrowth into porous titanium implants fabricated by additive manufacturing: An in vivo experiment [J]. Materials Science and Engineering C, 2016, 59:690–701.

[36] Alves A, Ariza E, Toptan F, Ponthiaux P, Pinto A M. Corrosion behaviour of porous Ti intended for biomedical applications [J]. Journal of Porous Materials, 2016, 23: 1261–1268.

[37] Yilmaz E, Gökçe A, Findik F, Gulsoy H O, İyibilgin O. Mechanical properties and electrochemical behavior of porous Ti–Nb biomaterials [J]. Journal of the Mechanical Behavior of Biomedical Materials, 2018, 87: 59–67.

[38] Wang N, Yang Z, Thummavichai K, Xu F, Hu C, Chen H, Xia Y, Zhu Y. Novel graphitic carbon coated IF-WS 2 reinforced poly(ether ether ketone) nanocomposites [J]. Royal Society of Chemistry Advances, 2017, 7: 35265–35273.

[39] Díez-Pascual A M, Xu C, Luque R. Development and characterization of novel poly(ether ether ketone)/ZnO bionanocomposites [J]. Journal of Materials Chemistry B, 2014, 2:3065–3078.

[40] Han C M, Lee E J, Kim H E, Koh Y H, Kim K N, Ha Y, Kuh S U. The electron beam deposition of titanium on polyetheretherketone (PEEK) and the resulting enhanced biological properties [J]. Biomaterials, 2010, 31: 3465–3470.

[41] Vrancken B, Thijs L, Kruth J P, Van Humbeeck J. Heat treatment of Ti6Al4V produced by selective laser melting: Microstructure and mechanical properties [J] Journal of Alloys and Compounds, 2012, 541: 177–185.

[42] Jackson M J, Ahmed W. Surface engineered surgical tools and medical devices [M]. USA: Springer, 2007.

[43] Bhola R, Bhola S M, Mishra B, Olson D L. Electrochemical behavior of titanium and its alloys as dental implants in normal saline [J]. Research Letters in Physical Chemistry, 2009, 2009: 1–4.

[44] Ribeiro A M, Alves A C, Silva F S, Toptan F. Electrochemical characterization of hot pressed CoCrMo-HAP biocomposite in a physiological solution [J]. Materials and Corrosion, 2015, 66: 790–795.

CHAPTER 5

Tribological Behavior of Bioactive Multi-Material Structures Targeting Orthopedic Applications

M.M. Costa[a]*, F. Bartolomeu[a], N. Alves[b], F.S. Silva[a], G. Miranda[a]

[a]Center for MicroElectroMechanical Systems (CMEMS-UMinho), University of Minho, Campus de Azurém, 4800-058 Guimarães – Portugal

[b]Centre for Rapid and Sustainable Product Development Polytechnic Institute of Leiria, Rua General Norton de Matos, Apartado 4133, 2411-901 Leiria – Portugal

Abstract

The following study proposes a multi-material solution in which Ti6Al4V cellular structures produced by Selective Laser Melting are impregnated with bioactive materials (hydroxyapatite or β-tricalcium phosphate) using press and sintering technique. To assess the tribological response of these structures, an alumina plate was used as a counterpart in a flat-on-flat reciprocating sliding test. Ti6Al4V cellular structures impregnated with bioactive materials displayed the highest wear resistance when compared with the unreinforced structures.

Among the bioactive structures, Ti6Al4V cellular structures impregnated with βTCP were the ones with higher wear resistance, having the lowest weight loss. Hence, these structures are promising multifunctional solutions for load-bearing applications by gathering suitable mechanical properties (strength and stiffness); bioactive properties and in addition an improved wear performance.

Keywords: Multi-material structures, Ti6Al4V, Hydroxyapatite, β-tricalcium phosphate, Selective Laser Melting, Press and sintering

5.1. Introduction

Metallic materials, specially titanium and its alloys, are the first choice of materials for load-bearing orthopedic applications, such as hip or dental implants due to their high mechanical properties (Dantas et al., 2017b, 2017a; Taniguchi et al., 2016).

Among titanium alloys, Ti6Al4V is the most frequently used alloy in orthopedics due to its high strength, biocompatibility, corrosion resistance and lower density among metals (Bartolomeu et al., 2017; Bruschi et al., 2017; Dantas et al., 2017a; Sahoo et al., 2014; Sampaio et al., 2016). In fact, this alloy biocompatibility and corrosion resistance are related with its ability to form an oxide layer on its surface when in contact with atmosphere or an environment with oxygen (Buciumeanu et al., 2018; Massaro et al., 2002; Ratner et al., 1996; Sampaio et al., 2016; Sidambe, 2014). This layer protects the material against corrosion but also promotes an effective cell attachment and growth (Sampaio et al., 2016; Sidambe, 2014). However, despite all its advantages, Ti6Al4V bioinertness can be a drawback to such applications once the adhesion between implant and bone can be quite poor and could lead to implant failure (Aparicio et al., 2011; Horowitz et al., 2009; Pereira et al., 2014; Taniguchi et al., 2016). This bioinertess means that the integration between implant and bone only depends on the tissue integration and

regeneration and not the implant itself, which turns interesting the addition of a material that promotes a biological response and improves implant osseointegration (Aparicio et al., 2011; Ducheyne and Qiu, 1999; Horowitz et al., 2009; Lee et al., 2017; Pereira et al., 2014; Santin and Philips, 2012; Zhang et al., 2016; Zhao et al.,2011).

Bioactive materials like hydroxyapatite (HAp) and β-tricalcium phosphate (βTCP) are materials very similar to the natural apatites of bone, characterized by their excellent biocompatibility, osteoconductivity and cell adhesion and, therefore, interacts with the biological environment, enhancing bone tissue formation and a strong bonding between implant and bone (Dantas et al., 2017a; Ducheyne and Qiu, 1999; Horowitz et al., 2009; Lee et al., 2017; Zhang et al., 2016).

Zhang et. al studied the effect of a bioactive inclusion on porous HAp-Ti alloy composites, regarding mechanical properties and in vitro bioactivity. Results revealed that, besides good mechanical properties, the addition of HAp improves significantly the bioactivity of the material due to the formation of a complete apatite layer formed in these composites (Zhang et al., 2016). Melo-Fonseca et. al, evaluated the influence of multi-material Ti6Al4V cellular structures impregnated with a bioactive bioglass on physical and chemical aspects that drive cellular response, stressing the importance of controlling pH for obtaining a suitable environment for cell growth (Melo-Fonseca et al.,2018). Dantas et al. evaluated the frictional response and surface damage of Ti6Al4V-HAp and Ti6Al4V- βTCP composites, in order to optimize primary stability on prosthesis implantation. In this study, it was concluded that polished bioactive composites promoted an enhanced primary stability when compared with common rough surfaces (Dantas et al., 2017a).

Nowadays Ti6Al4V implants are dense parts, however some endeavors have been made by industry and some research groups to introduce bioactive materials on these implants (Blind et al., 2005; Evis and Doremus, 2007; Karamian et al., 2014; Khandelwal et al., 2013; Ning and Zhou, 2002; Queiroz et al., 2004). Bioactive materials brittle nature makes them not suitable for load bearing applications (Blind et al., 2005; Buciumeanu et al., 2017; Hu et al., 2010; Khandelwal et al., 2013; Ning and Zhou, 2002), in this sense, bioactive coatings are being proposed/developed for Ti6Al4V surfaces (Blind et al., 2005; Evis and Doremus, 2007; Karamian et al., 2014; Khandelwal et al., 2013; Ning and Zhou, 2002; Queiroz et al., 2004), once they allow to combine the titanium alloy suitable mechanical properties and bioactive materials bioactivity. However, upon implantation, coating detachment can occur due to the shear stresses involved on prosthesis insertion, which compromises their function (Miranda et al., 2016; Ryan et al., 2006). Moreover,

dense Ti6Al4V implants are not an optimal solution due to its high Young's modulus ($\approx$ 110 GPa (Apostu et al., 2017)), that despite being the lower among metals used in implants, is still much higher than that of bone ($\approx$ 10–30 GPa (Bandyopadhyay et al., 2010)).

Considering the abovementioned, urge the need to find new solutions that effectively approximate the stiffness of the implant to that of bone, by altering implants design.

In this sense, it would be interesting to tailor these implants Young's modulus, to reduce the mismatch between implant and bone. This is possible by introducing controlled porosity, by designing open cellular structures made of Ti6Al4V. These structures, besides decreasing the Young's modulus, are also capable of promoting bone ingrowth, once these structures allow nutrients flow and vascularization to occur (Arabnejad et al., 2016; Tan et al., 2017; Taniguchi et al., 2016). This vascularization will trigger a cascade of biological events that promote new bone formation. In this regard, many studies address the effect of pore size on bone vascularization, concluding that the optimum pore size should range from 100 to 400 µm (Bobyn et al., 1980; Kumar et al., 2016). Moreover, by this approach it is possible to impregnate bioactive materials into the open cells, preventing the bioactive detachment to occur once these materials are imprisoned inside the Ti6Al4V structure by a mechanical interlocking.

Additive manufacturing techniques like selective laser melting (SLM) allows the production of these cellular structures once this technique allows the fabrication of parts with complex geometries that were previously designed in a CAD software. In this process, the CAD data is imported to the SLM machine that will produce the final part in a layer-by-layer process by melting successive layers of powder that are scanned by a laser source (Bartolomeu et al., 2017; Sidambe, 2014; Van Hooreweder et al., 2017). To introduce the bioactive materials into these structures, press and sintering is a suitable powder metallurgy technique once it forces the bioactive powders to impregnate the open cells, being afterwards sintered.

The present study proposes a novel solution targeting load-bearing applications that allows obtaining the necessary strength and adequate stiffness while introducing bioactivity to enhance implant performance. However, implants performance also depends on the tribological behavior of the final component, which, in fact, is quite poor for Ti6Al4V alloy (Bruschi et al., 2017; Buciumeanu et al., 2018; Dantas et al., 2017b). The corrosive medium present in the human body allied to the poor wear resistance of this material can potentiate corrosion which will destroy the passive layer formed on its surface and lead to successive formation of new oxide layers. This process leads to the formation of wear debris that can be resorbed by the organism and lead to

undesired outcomes (Buciumeanu et al., 2018; Runa et al., 2013). Therefore, several studies have been made to improve the tribological response of this material, by applying coatings (Fu et al., 1998; Lee, 2012), performing surface treatments (Dong and Bell, 2000), developing composites (Buciumeanu et al., 2017; Dantas et al., 2017b), etc. In fact, some studies already stated that the addition of these bioactive materials (HAp and βTCP) will enhance the overall microhardness of the component and therefore their wear resistance (Buciumeanu et al., 2017; Dantas et al., 2017b).

In this sense, the present work aims to evaluate the tribological behavior of Ti6Al4V cellular structures impregnated either with HAp and βTCP against an alumina (Al_2O_3) plate and understand its potential for improving the tribological performance of load-bearing implants.

5.2. Experimental details

5.2.1. Specimens fabrication

For the present work, Ti6Al4V cellular structures impregnated with bioactive materials (βTCP and HAp) were produced and evaluated.

Ti6Al4V powder purchased from SLM solutions (Germany), with a particle size (d50) of 34 μm, was used to produce Ti6Al4V cellular structures by using SLM technique, with further details on this fabrication being given below. The bioactive materials: βTCP (d50=2.26 μm) and HAp (d50=10 μm), that were used to impregnate the cellular structures were purchased from Trans-Tech, Inc. and Fluidinova S.A. (nanoXim. Hap203®), respectively. Figure 5.1 displays SEM micrographs of Ti6Al4V, βTCP and HAp powders.
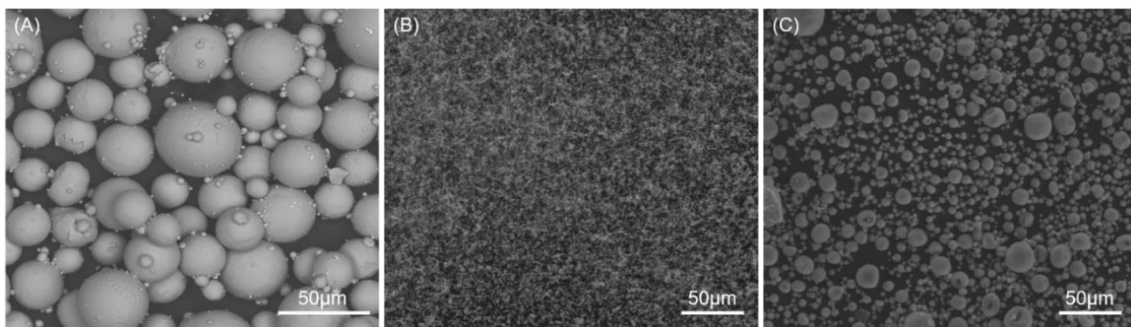
Figure 5.1 – SEM micrographs of (A) Ti6Al4V, (B) βTCP and (C) HAp powders.

As presented in Table 5.1, the three groups of specimens tested in this study are based in SLM-produced cellular structures. These structures were previously designed on a CAD software and fabricated on a Selective Laser Melting equipment from *SLM Solutions* (model 125HL). Briefly,

the CAD data were imported to the SLM software that slices the part in successive layers that will be further scanned by a laser and, layer-by-layer, produce the final component. Based on previous optimization studies for this alloy (Bartolomeu et al., 2017, 2016), the specimens were produced by SLM using the following processing parameters: laser power: 90 W; scan speed: 600 mm/s; scan spacing: 80 μm; layer thickness: 30 μm.

These structures were designed to have a pore size and wall thickness of 400 μm, with interconnected porosity. The produced scaffolds displayed an average thickness of 2.5 mm and 6 mm in diameter.

Table 5.1 - Ti6Al4V-based specimens' schematic representation, group number, description and fabrication method.

Representation	Group Number	Description	Fabrication Method
	G1	Ti6Al4V cellular structure	Selective Laser Melting
	G2	Ti6Al4V cellular Structure impregnated w/βTCP	Selective Laser Melting + press and sintering
	G3	Ti6Al4V cellular structure impregnated w/HAp	Selective Laser Melting + press and sintering

The non-reinforced scaffolds were tested, being referred along this study as G1.

For producing G2 and G3 groups, a batch of samples produced in the same way as G1 were used to impregnate the bioactive materials. The impregnation process begins by preparing a viscous solution that contains either βTCP or HAp and acetone. Afterwards, the cellular structures were positioned inside a steel mold with 10mm diameter where the introduction of the bioactive solution is then made by applying pressure using a hydraulic press for 10 min. Finally, the samples were removed from the steel mold and sintered in an induction heated chamber under vacuum at 1100 °C and kept at this temperature for 2 h. Figure 5.2 displays a schematic representation of the specimens' production from its SLM process until the impregnation of the bioactive materials.

Finally, after their production, the samples from all the three groups were polished using abrasive silicon carbide papers from P120 until P4000 and ultrasonically cleaned with isopropanol.
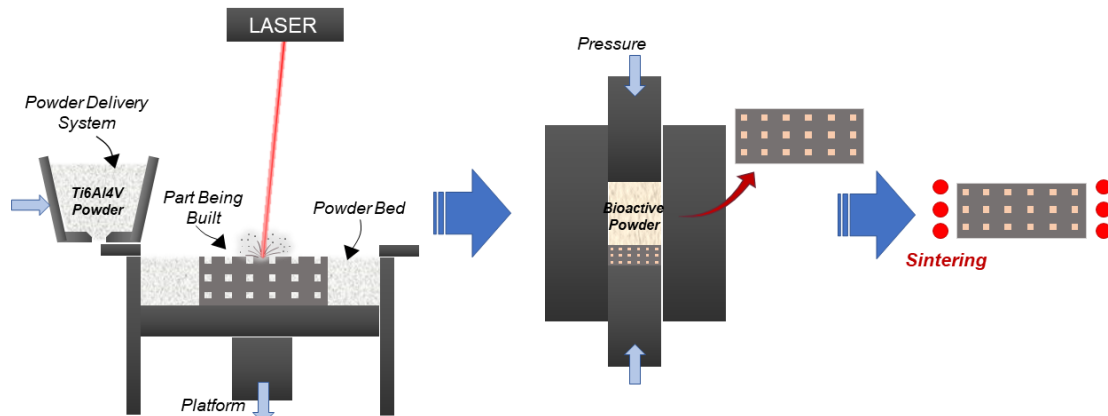
Figure 5.2 - Schematic representation of the specimens' production.

5.2.2. Tribological tests

Once prepared, the specimens from the three groups were subjected to flat-on-flat (FOF) reciprocating sliding tests, in which the counterpart was an alumina (Al_2O_3) plate (50×25×5 mm), performed in a Bruker-UMT-2 (USA) tribometer (Fig. 3(B)). The whole apparatus of the tests performed in this study is schematically represented in Figure 5.3.
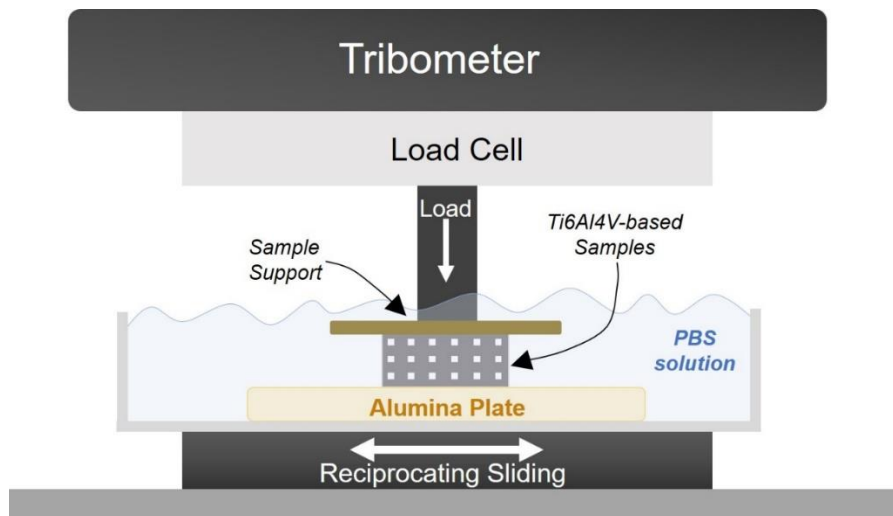
Figure 5.3 - Schematic representation of tribological test.

The alumina plate was polished with resin bonded diamond grinding discs (*MD-Piano 120 and 220*), displaying an Ra of 0.869 ± 0.024 μm.

The specimens were placed in a metallic support that in turn is attached to the load cell. On the other hand, the alumina plate was fixed to an acrylic container that is also fixed to the oscillatory plate of the tribometer. To obtain an approximation of the physiological conditions, the whole apparatus is immersed in a phosphate buffer saline (PBS) solution and an oscillating frequency of 1 Hz was selected.

Taylor et al. (1995) reported that compressive radial stresses starting from 2 MPa can be generated in the bone during the press-fit. To replicate these conditions, in the experimental tests performed in this study, Ti6Al4V specimens having a diameter of 6mm (surface area $\approx$ 28 mm^2) were used against alumina plate under a normal load of 50 N, thus corresponding to a stress of approximately 2 MPa.

Each test was performed in four iterations, that were named in this paper as static initial (Si), implantation (I), final static (Sf) and tribological performance (Tp).

The first three iterations aim to mimic the moment of implantation/insertion of an implant, while the last one aims to evaluate the tribological performance in terms of mass loss of the specimens (Tp test).

In other words, during the implantation, for instance of hip implants, the ill femoral head, neck and acetabulum is removed from the patient and replaced by the prosthesis. Afterwards, at the time of the prosthesis implantation, there is an initial opposing force to the movement of the implant (frictional force) – this phenomenon was reproduced by the so called static initial (Si) test.

When the surgeon inserts the implant into the bone cavity, an interaction between implant and bone will occur, being this aspect assessed by the implantation (I) test. This test was performed for a stroke length of 3 mm and a total sliding distance of 51.6 mm.

After the implant reaches its final position, there is a final opposing force which dictates the final stability of the implant relative to the bone (commonly referred in literature as primary stability (Affatato, 2014; Dantas et al., 2017a; Moura et al., 2017)) which will be assessed by the third test, named final static (Sf).

Tp test, a reciprocating sliding test, that aims to evaluate the mass loss of each specimen, was performed for a stroke length of 3 mm and a total sliding distance of 5400 mm, with a maximum speed of 9,42 mm/s, for a total test time of 30 min.

Each test was performed, as mentioned, under a load of 50 N at 1 Hz in which the stroke length was 3 mm that in turn corresponds to a total sliding distance for I and Tp of 51.6 mm and 5400 mm, respectively. It is important to highlight that for each group, in average three specimens were analyzed, being the results displayed as the average of those repetitions.

5.2.3. Specimens characterization: Weight loss calculation, roughness measurement and SEM/EDS analysis

The specimens' roughness before the tribological tests was measured on *Mitutoyo Surftest SJ-210* series roughness equipment.

Before and after the tribological tests, three measurements of the mass of each sample were made in a *Mettler AE 240* balance (sensitivity of 40 g at a readability of 0.01 mg), to obtain a mean of the weight loss of each group.

The microstructure of the produced specimens' surface after and before the tribological tests and also the morphology of the worn surfaces was assessed by means of Scanning Electron Microscopy (SEM).

Additionally, the alumina plate was also analyzed in order to assess the material transfer to the counterpart during sliding. In this sense, chemical characterization on the alumina plate and some sites of the cellular structures worn surfaces was made by Energy-dispersive X-ray spectroscopy analysis (EDS).

5.3. Results and discussion

5.3.1. Specimens characterization

In the present study, Ti6Al4V cellular structures were produced by SLM and impregnated with bioactive materials by using press and sintering technique. Figure 5.4 displays the morphology of the Ti6Al4V-based specimens (G1, G2 and G3) before the tribological tests. These specimens contacting surfaces have been polished and the average roughness of the metallic walls was measured. No statistically significant differences were found between all the groups (e.g. the measured Ra for G1 (non-reinforced specimens) was 0.176 ± 0.036 µm and for G2 was 0.095 ± 0.035 µm).
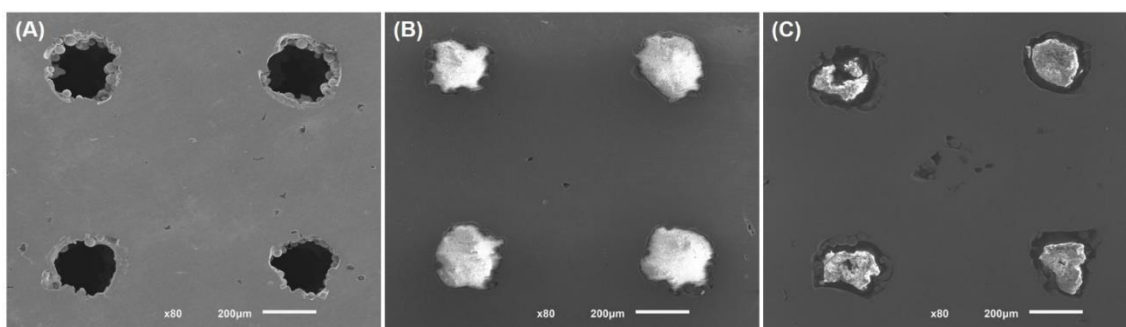
Figure 5.4 - SEM micrographs of the surfaces of the produced Ti6Al4V-based specimens (A) G1, (B) G2 and (C) G3.

125

From Figure 5.4 it is possible to observe that all the groups exhibit similar surface morphology. Moreover, it is notable that the pore size of the manufactured specimens is smaller than the CAD designed dimension, an inherent aspect of this additive manufacturing technology, abundantly reported by other authors (Bartolomeu et al., 2017; Taniguchi et al., 2016), mainly due to powder related aspects (size distribution) and to the over melting beyond the laser path (related with thermal conductivity).

By analyzing Figure 5.4(B) and (C) it is possible to validate the impregnation process of the bioactive materials. By comparing these two images (Figure 5.4(B) and (C)), βTCP-impregnated specimens (G2) seem to present a higher filling of the pores than HAp-impregnated ones (G3). This fact may be related with the particle size of HAp, that is higher (d50=10 μm) than βTCP (d50=2.26 μm). In fact, it is reported in literature that the packing density is highly dependent on particle size distribution in which a smaller particle size of the powder will lead to a smoother surface finishing with lower porosity and, therefore, a higher densification (German, 2005; Pease III and West, 2002). Therefore, the impregnation process is more difficult to achieve when using a higher particle size.

5.3.2. Tribological behavior

5.3.2.1. Tribological performance (Tp) test

The evolution of the coefficient of friction on the Ti6Al4V-based structures during tribological performance (Tp) test is displayed in Figure 5.5. For the three groups tested, coefficient of friction curves follows a typical evolution once this value quickly increases in the beginning (more pronounced on G1), before reaching a steady-state regime. This steady-state regime presents some oscillations, more evident on G1, attributable to the material transfer from Ti6Al4V to the alumina plate and to the third body effect phenomenon.
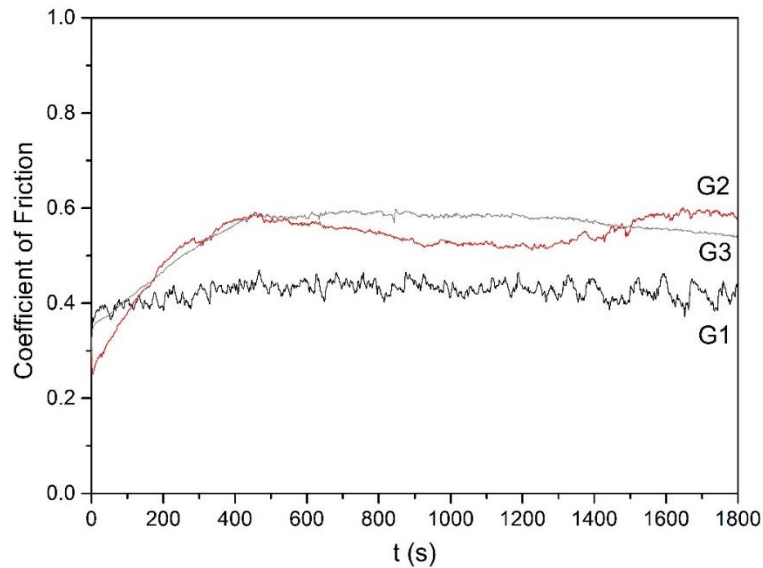
Figure 5.5 - Coefficient of friction evolution for the tested Ti6Al4V-based specimens against alumina plate.

By analyzing the average coefficient of friction values (Table 5.2) it is possible to observe that the presence of these harder bioactive materials (6.1 GPa (Boilet et al., 2013) for HAp and 4.9 GPa (Boilet et al., 2013) for βTCP) led to a coefficient of friction increase, when compared to unreinforced Ti6Al4V (≈ 3.8 GPa) (Bartolomeu et al., 2016)), as reported in other studies (Buciumeanu et al., 2017; Dantas et al., 2017b).

As seen in Figure 5.6, after sliding against the alumina plate (Tp test) it is noticeable the detachment of bioactive material (either βTCP or HAp) from the pores of the structure. Then these harder materials are transferred to the metallic walls, where they remain adhered. Due to this fact, the sliding between the bioactive (either βTCP or HAp) and the alumina plate will have a predominant contribution to the coefficient of friction. In literature, the coefficient of friction between βTCP and alumina is commonly reported around 0.90 (Elghazel et al., 2018; Trabelsi et al., 2019), while the coefficient of friction between HAp and alumina is reported in the range 0.70–0.85 (Kalin et al., 2002). Both of these values are substantially above the coefficient of friction between Ti6Al4V and alumina (measured result of 0.441). Despite the higher hardness of these bioactive materials, these facts can explain the higher coefficient of friction found for G2 group, followed by G3, when compared with G1 (see Table 5.2).

Table 5.2 - Coefficient of friction values obtained for Tp (Tribological performance) test.

Material	Coefficient of friction	
	Average	SD
G1	0.441	0.015
G2	0.561	0.030
G3	0.477	0.052

By analyzing the different weight losses obtained by the different groups (Table 5.3) some differences between them are found, with G1 displaying the higher weight loss and, therefore, the worst wear resistance, while G2 displayed the lower weight loss.

Table 5.3 - Weight loss obtained for G1, G2 and G3 against alumina plate.

Material	Weight Loss (mg)	
	Average	SD
G1	0.921	0.088
G2	0.668	0.122
G3	0.732	0.174

In fact, among these groups, G1 displayed the worse performance (higher weight loss), fact that could be related with the higher contact pressure involved during the test, once for G1 the same load is applied in a smaller area, when compared with the other groups in which the cells are filled with bioactive materials.

When comparing Ti6Al4V cellular structures impregnated with hydroxyapatite (G3) with the non-impregnated structures (G1), a 20.5 % decrease on weight loss was found. Following the same trend, Ti6Al4V cellular structures impregnated with βTCP (G2) displayed an even higher reduction on their weight loss, in the order of 27.4 %, when compared to G1.

The wear surfaces after Tp tribological performance tests against alumina plate are visible in Figure 5.6 while SEM micrographs of the alumina plate can be seen in Figure 5.7. Regarding the wear mechanisms, by analyzing Figure 5.6, it is possible to observe in all the Ti6Al4V-based specimens the presence of abrasive grooves which are aligned with the sliding direction. In the images at higher magnification (Figure 5.6A2, B2 and B3) the presence of worn areas indicating plastic deformation resulting from the rubbing movements are visible, as well as the release of wear debris.

In G1 specimens (Figure 5.6A) the abrasion is more pronounced that on specimens from other groups (Figure 5.6B and C) once, as mentioned, the bioactive material will protect the

metallic surface from wear. Moreover, delamination is clearly seen due to the formation of plate-like metallic fragments during sliding (Sahoo et al., 2014; Singh and Alpas, 1996). Delamination wear mechanism occurs when large local strains are generated at layers adjacent to the contact surface and wear proceeds by mechanisms such as subsurface delamination (Singh and Alpas, 1996). Also for G1 group, by analyzing the counterpart SEM micrographs (Figure 5.7(A)) and EDS results (Table 5.4), it is also possible to observe adhesion mechanism, once Ti6Al4V was transferred to the alumina plate.

G2 and G3 specimens wear surfaces are shown in Figure 5.6(B) and (C) respectively, both having a similar appearance, with a smoother wear track than that of G1. This topographical difference and also the weight loss decrease found for the bioactive- impregnated structures – G2 and G3 (Table 5.3 - Weight loss obtained for G1, G2 and G3 against alumina plate.Table 5.3), can be justified by these harder particles protecting role to the softer material (Ti6Al4V), by supporting the load during sliding (see Figure 5.6) (Buciumeanu et al., 2017).

From G3 micrographs at higher magnification (Figure 5.6(C3)) it is possible to detect HAp dragged from the open-cells to the Ti6Al4V surface (walls). This is proven by the atomic contrast differences and EDS analysis made on this dragged material (in wt%, 43.9 O; 38.4 Ti; 5.8 Al; 3.9 V; 3.0 P; 0.5 Ca; 4.6 other) and by its brittle nature proven by the presence of cracks (Figure 5.6(C2)).

G2 displayed a similar outcome, with βTCP being dragged to Ti6Al4V walls, as proven by the atomic contrast (Figure 5.6(B3)), although undetected by EDS analysis, probably due to the lower amount of βTCP transferred to Ti6Al4V walls when compared with HAp specimens.

When looking at Figure 5.7(B) and (C) it is possible to identify an expressive material transfer from the specimens to the alumina plates (adhesion wear mechanism), for both G2 and G3 groups. From these images and Table 5.3 results it is possible to conclude that besides titanium alloy transfer, also bioactive material was found adhered to the plate. This phenomenon is more evident in G3 than G2, once a higher amount of transfer material was generally found for the previous, displaying several cracks, suggesting the brittle nature of this transferred tribolayer (Kalin et al., 2002).
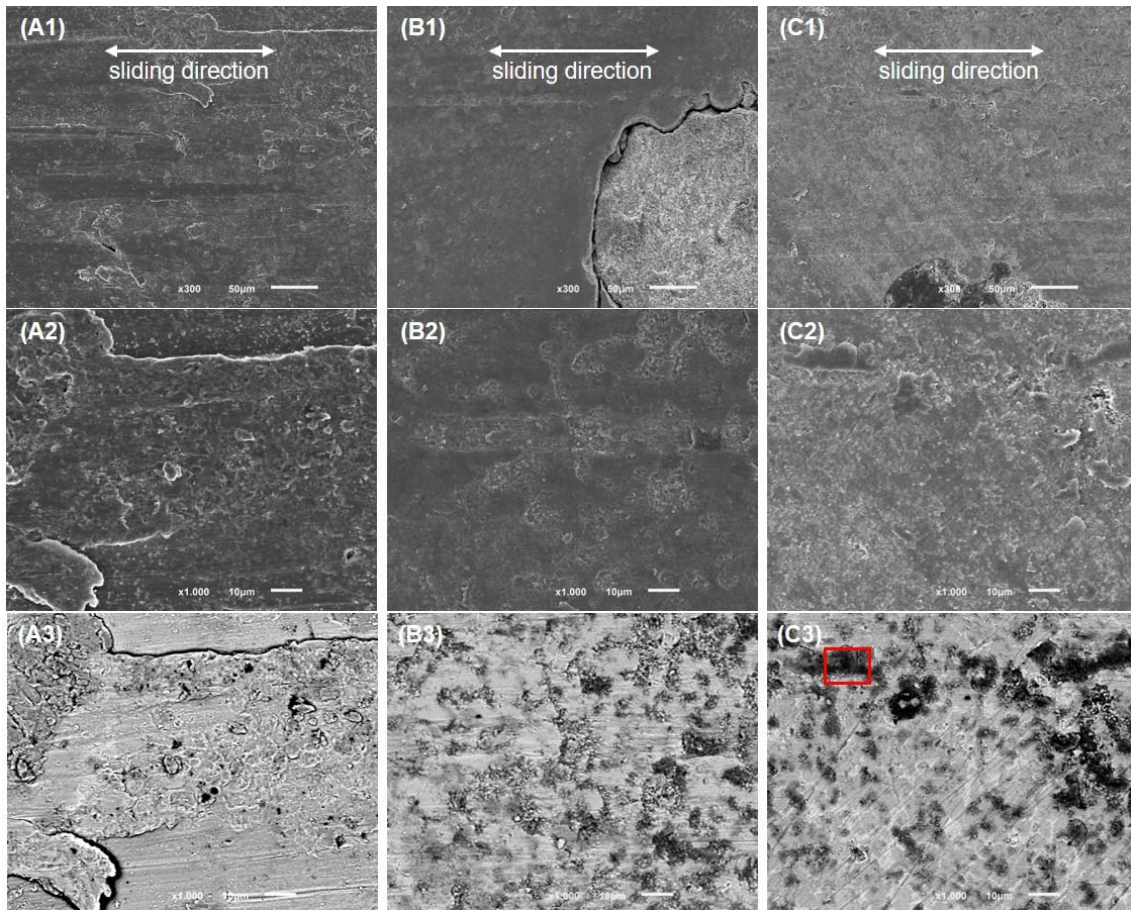
Figure 5.6 - SEM micrographs of the worn Ti6Al4V-based specimens against alumina: (A), (B) and (C) are G1, G2 and G3 in which 1, 2 and 3 are micrographs at higher magnification, lower and backscattered mode, respectively, with marked area where EDS analysis was performed.
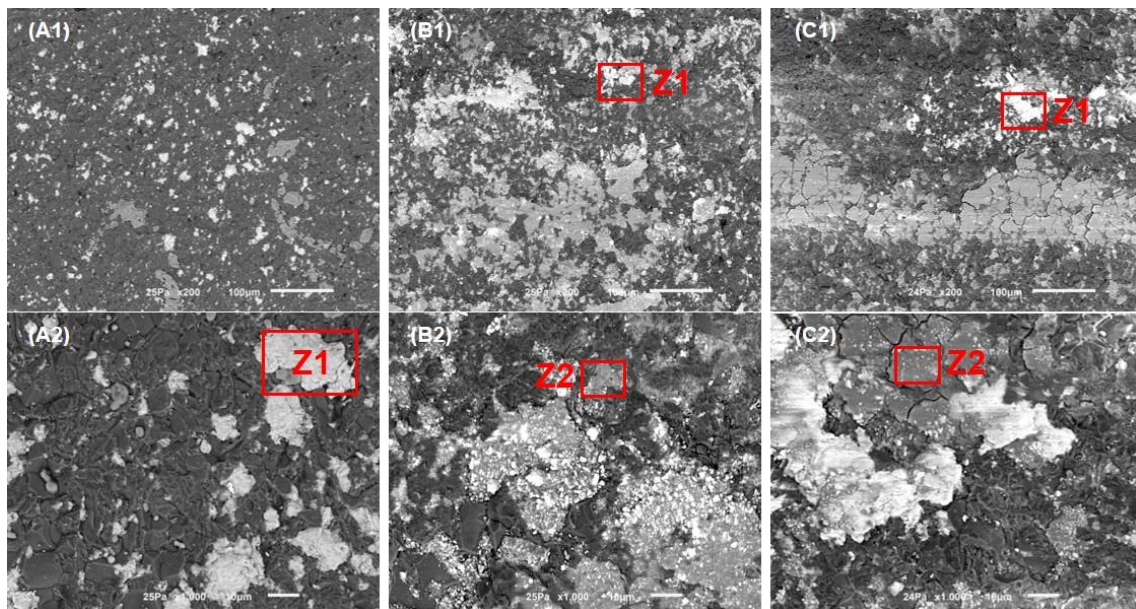
Figure 5.7 - SEM micrographs of the counterpart (Al_3O_2 plate) worn surface subjected to tribological tests against (A) G1, (B) G2 and (C) G3. Each marked zone corresponds to the different material transferred to the Al_3O_2.

Table 5.4 - Chemical composition (in wt%) of the material transfer zones in Al_2O_2 plate.

Composition, wt.%	G1	G2		G3	
	Z1	Z1	Z2	Z1	Z2
Ti	52.3	50.2	30.7	41.0	20.9
Al	12.1	13.4	12.5	10.7	9.8
V	1.7	2.8	1.1	1.7	1.0
Ca	-	0.2	1.5	-	0.7
P	0.7	0.7	4.2	1.9	7.9
O	29.0	27.4	42.6	37.1	52.8
Na	0.7	0.3	1.3	0.8	2.9
K	-	-	0.8	0.4	2.0
C	2.8	5.0	5.0	6.2	1.7
Cl	0.6	-	0.2	0.1	0.3

5.3.2.2. Initial and final static coefficient and implantation tests

Figure 5.8 presents the average coefficient of friction of the first three tribological tests performed for the three groups.
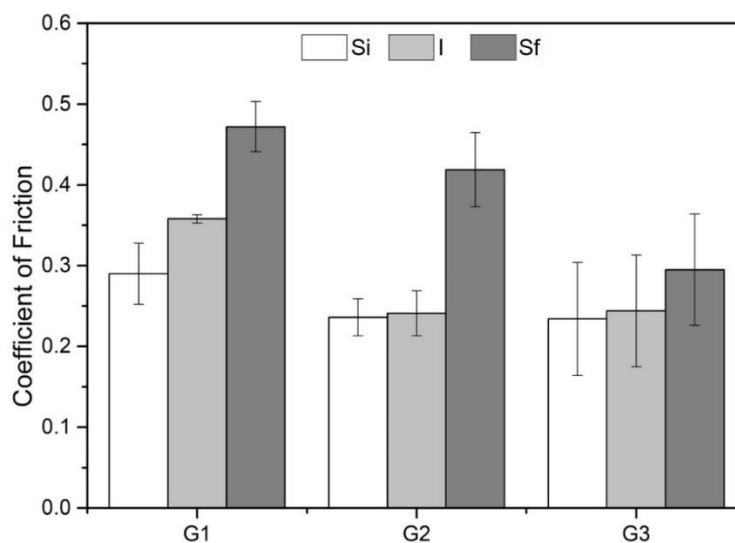
Figure 5.8 - Mean values of coefficient of friction obtained on the tested Ti6Al4V-based specimens.

The first test (Si), as previously mentioned, corresponds to the initial opposing force to the movement of the implant. The results for this test showed very similar static coefficient of friction, for all the groups (Figure 5.8). This outcome seems to indicate that during these first seconds (that encompass the Si test) no detachment of the bioactive occurred due to its mechanical interlocking inside these structures open-cells. Furthermore, these results may indicate that for G2 and G3, the

metal is dictating the initial opposing force to motion, since Ti6Al4V area is expressively higher than that of the bioactives.

The second test (I) intends to reproduce the insertion course of the implant into the bone cavity. Comparing the static initial coefficient (Si) and the dynamic coefficient (I), no significant differences were observed between them (Figure 5.8), which is in accordance with literature that states that the static coefficient of friction values are higher or equal to the kinetic coefficient of friction (Bhushan, 2013; Moura et al., 2017). Regarding the comparison between the final coefficient of friction (Sf) and the dynamic coefficient (I), greater values were found for the previous, again in line with literature (Bhushan, 2013; Moura et al., 2017).

The final static coefficient (Sf) is extremely important to assess the primary stability of bone, once a higher coefficient of friction will guarantee that, after implantation, there is a good adhesion between bone and the implant material. The results obtained in this study show that G2, that displayed the highest wear resistance (Tribological performance test) revealed one of the highest static coefficient of friction (Sf) (Figure 5.8), making this material a good option for improved primary stability.

When talking about friction, and according to Bowden and Tabor theory, the total frictional force is a sum of the adhesion force between two surfaces and the deformation force of the same surfaces (Bhushan, 2013; Bowden and Tabor, 1964). The performed tests show that Sf test coefficient of friction values are much higher than those of Si, for all groups, being this difference associated with the adhesion component of friction that is more pronounced in Sf tests. These results indicate that there is a good adhesion between these specimens and the alumina plate.

5.4. Conclusions

Ti6Al4V cellular structures impregnated with βTCP or HAp were designed and produced by using an Additive Manufacturing technique (SLM) combined with press and sintering. These multi-material structures assure no detachment of the bioactive material by using a mechanical interlocking strategy. These multi-functional structures will enhance the interaction between bone and implant, by promoting bone ingrowth into the structures open-cells as the bioactive material is being absorbed and replaced by newly formed bone.

The introduction of bioactive materials inside these SLM-fabricated Ti6Al4V structures led to an increased wear performance, with a weight loss decrease of 27.4 % for βTCP- Ti6Al4V structures and 20.5 % for HAp-Ti6Al4V structures, when compared to unreinforced structures.

The proposed solution is a promising approach by gathering suitable mechanical properties (strength and stiffness) for load-bearing implants, assured by the metallic structure; bioactive properties, assured by the bioactive materials and in addition an improved wear performance by introducing these bioactive materials.

Acknowledgments

References

Affatato, S., 2014. Perspectives in total hip arthroplasty - advances in biomaterials and their tribological interactions. Biomaterials. https://doi.org/10.1016/B978-1-78242-031-6.50016-7.

Aparicio, C., Padrós, A., Gil, F.J., 2011. In vivo evaluation of micro-rough and bioactive titanium dental implants using histometry and pull-out tests. J. Mech. Behav. Biomed. Mater. 4, 1672–1682. https://doi.org/10.1016/j.jmbbm.2011.05.005.

Apostu, D., Lucaciu, O., Berce, C., Lucaciu, D., Cosma, D., 2017. Current methods of preventing aseptic loosening and improving osseointegration of titanium implants in cementless total hip arthroplasty: a review. J. Int. Med. Res. 0. https://doi.org/10.1177/0300060517732697.

Arabnejad, S., Burnett Johnston, R., Pura, J.A., Singh, B., Tanzer, M., Pasini, D., 2016. High-strength porous biomaterials for bone replacement: a strategy to assess the interplay between cell morphology, mechanical properties, bone ingrowth and manufacturing constraints. Acta Biomater. 30, 345–356. https://doi.org/10.1016/j.actbio.2015.10.048.

Bandyopadhyay, A., Espana, F., Balla, V.K., Bose, S., Ohgami, Y., Davies, N.M., 2010. Influence of porosity on mechanical properties and in vivo response of Ti6Al4V implants. Acta Biomater. 6, 1640–1648. https://doi.org/10.1016/j.actbio.2009.11.011.

Bartolomeu, F., Faria, S., Carvalho, O., Pinto, E., Alves, N., Silva, F.S., Miranda, G., 2016. Predictive models for physical and mechanical properties of Ti6Al4V produced by selective laser melting. Mater. Sci. Eng. A 663, 181–192. https://doi.org/10.1016/j.msea.2016.03.113.

Bartolomeu, F., Sampaio, M., Carvalho, O., Pinto, E., Alves, N., Gomes, J.R., Silva, F.S., Miranda, G., 2017. Tribological behavior of Ti6Al4V cellular structures produced by selective laser melting. J. Mech. Behav. Biomed. Mater. 69, 128–134. https://doi.org/10.1016/j.jmbbm.2017.01.004.

Bhushan, B., 2013. Principles and Applications of Tribology, 2nd ed. John Wiley & Sons, Ltd., USA. https://doi.org/10.1002/9781118403020.

Blind, O., Klein, L.H., Dailey, B., Jordan, L., 2005. Characterization of hydroxyapatite films obtained by pulsed-laser deposition on Ti and Ti-6AL-4v substrates. Dent. Mater. 21, 1017–1024. https://doi.org/10.1016/j.dental.2004.12.003.

Bobyn, J.D., Pilliar, R.M., Cameron, H.U., Weatherly, G.C., 1980. The optimum pore size for the fixation of porous-surfaced metal implants by the ingrowth of bone. Clin. Orthop. Relat. Res. 263–270.

Boilet, L., Descamps, M., Rguiti, E., Tricoteaux, A., Lu, J., Petit, F., Lardot, V., Cambier, F., Leriche, A., 2013. Processing and properties of transparent hydroxyapatite and βtricalcium phosphate obtained by HIP process. Ceram. Int. 39, 283–288. https://doi.org/10.1016/j.ceramint.2012.06.023.

Bowden, F.P., Tabor, D., 1964. The Friction and Lubrication of Solids. Clarendon Press, Oxford, UK.

Bruschi, S., Bertolini, R., Ghiotti, A., 2017. Coupling machining and heat treatment to enhance the wear behaviour of an Additive Manufactured Ti6Al4V titanium alloy. Tribol. Int. 116, 58–68. https://doi.org/10.1016/j.triboint.2017.07.004.

Buciumeanu, M., Almeida, S., Bartolomeu, F., Costa, M.M., Alves, N., Silva, F.S., Miranda, G., 2018. Ti6Al4V cellular structures impregnated with biomedical PEEK - new material design for improved tribological behavior. Tribol. Int. 119. https://doi.org/10.1016/j.triboint.2017.10.038.

Buciumeanu, M., Araujo, A., Carvalho, O., Miranda, G., Souza, J.C.M., Silva, F.S., 2017. Study of the tribocorrosion behaviour of Ti6Al4V – HA biocomposites. Tribiol. Int. 107, 77–84. https://doi.org/10.1016/j.triboint.2016.11.029.

Dantas, T.A., Abreu, C.S., Costa, M.M., Miranda, G., Silva, F.S., Dourado, N., Gomes, J.R., 2017a. Bioactive materials driven primary stability on titanium biocomposites. Mater. Sci. Eng. C 77, 1104–1110. https://doi.org/10.1016/j.msec.2017.04.014.

Dantas, T.A., Costa, M.M., Miranda, G., Silva, F.S., Abreu, C.S., Gomes, J.R., 2017b. Effect of HAp and β-TCP incorporation on the tribological response of Ti6Al4V biocomposites for implant parts. J. Biomed. Mater. Res. Part B Appl. Biomater. 1–7. https://doi.org/10.1002/jbm.b.33908.

Dong, H., Bell, T., 2000. Enhanced wear resistance of titanium surfaces by a new thermal oxidation treatment. Wear 238, 131–137. https://doi.org/10.1016/S0043-1648(99)00359-2.

Ducheyne, P., Qiu, Q., 1999. Bioactive ceramics: the effect of surface reactivity on bone formation and bone cell function. Biomaterials 20, 2287–2303. https://doi.org/10.1016/S0142-9612(99)00181-7.

Elghazel, A., Taktak, R., Elleuch, K., Bouaziz, J., 2018. Mechanical and tribological properties of tricalcium phosphate reinforced with fluorapatite as coating for orthopedic implant. Mater. Lett. 215, 53–57. https://doi.org/10.1016/j.matlet.2017.12.044.

Evis, Z., Doremus, R.H., 2007. Hot-pressed hydroxylapatite/monoclinic zirconia composites with improved mechanical properties. J. Mater. Sci. 42, 2426–2431. https://doi.org/10.1007/s10853-006-1299-6.

Fu, Y., Batchelor, A.W., Wang, Y., Khor, K.A., 1998. Fretting wear behaviors of thermal sprayed hydroxyapatite (HA) coating under unlubricated conditions. Wear 217, 132–139. https://doi.org/10.1016/S0043-1648(98)00142-2.

German, R.M., 2005. Powder Metallurgy & Particulate Materials Processing, Metal Powd. ed. Princeton.

Horowitz, R. a., Ziv, D.D.S., Dmd, M., Foitzik, C., Prasad, H., Rohrer, M.D.T.M., Palti, M.S.A., 2009. ß-tricalcium phosphate as bone substitute material: properties and clinical applications. Int. J. Dent. Implant. Biomater. 1, 2–11.

Hu, J., Wang, Z., Guan, T., Gao, Y., Lv, X., Lin, X., Tang, C. yin, Gao, B., 2010. In situ synthesis and fabrication of tricalcium phosphate bioceramic coating on commercially pure titanium by laser rapid forming. Surf. Coat. Technol. 204, 3833–3837. https://doi.org/10.1016/j.surfcoat.2010.04.062.

Kalin, M., Jahanmir, S., Ives, L.K., 2002. Effect of counterface roughness on abrasive wear of hydroxyapatite. Wear 252, 679–685. https://doi.org/10.1016/S0043-1648(02)00028-5.

Karamian, E., Khandan, A., Kalantar Motamedi, M.R., Mirmohammadi, H., 2014. Surface characteristics and bioactivity of a novel natural HA/zircon nanocomposite coated on dental implants. Biomed. Res. Int. 2014. https://doi.org/10.1155/2014/410627.

Khandelwal, H., Singh, G., Agrawal, K., Prakash, S., Agarwal, R.D., 2013. Characterization of hydroxyapatite coating by pulse laser deposition technique on stainless steel 316 L by varying laser energy. Appl. Surf. Sci. 265, 30–35. https://doi.org/10.1016/j.apsusc.2012.10.072.

Kumar, A., Mandal, S., Barui, S., Vasireddi, R., Gbureck, U., Gelinsky, M., Basu, B., 2016. Low temperature additive manufacturing of three dimensional scaffolds for bone-tissue engineering applications: processing related challenges and property assessment. Mater. Sci. Eng. R Rep. 103, 1–39. https://doi.org/10.1016/j.mser.2016.01.001.

Lee, C.-K., 2012. Fabrication, characterization and wear corrosion testing of bioactive hydroxyapatite/nano-TiO2 composite coatings on anodic Ti–6Al–4V substrate for biomedical applications. Mater. Sci. Eng. B 177, 810–818. https://doi.org/10.1016/J.MSEB.2012.03.034.

Lee, D.H., Tripathy, N., Shin, J.H., Song, J.E., Cha, J.G., Min, K.D., Park, C.H., Khang, G., 2017. Enhanced osteogenesis of β-tricalcium phosphate reinforced silk fibroin scaffold for bone tissue biofabrication. Int. J. Biol. Macromol. 95, 14–23. https://doi.org/10.1016/j.ijbiomac.2016.11.002.

Massaro, C., Rotolo, P., De Riccardis, F., Milella, E., Napoli, a., Wieland, M., Textor, M., Spencer, N.D., Brunette, D.M., 2002. Comparative investigation of the surface properties of commercial titanium dental implants. Part I: chemical composition. J. Mater. Sci. Mater. Med. 13, 535–548. https://doi.org/10.1023/A:1015170625506.

Melo-Fonseca, F., Lima, R., Costa, M.M., Bartolomeu, F., Alves, N., Miranda, A., Gasik, M., Silva, F.S., Silva, N.A., Miranda, G., 2018. 45S5 BAG-Ti6Al4V structures: the influence of the design on some of the physical and chemical interactions that drive cellular response. Mater. Des. 160, 95–105. https://doi.org/10.1016/J.MATDES.2018.08.056.

Miranda, G., Araújo, A., Bartolomeu, F., Buciumeanu, M., Carvalho, O., Souza, J.C.M., Silva, F.S., Henriques, B., 2016. Design of Ti6Al4V-HA composites produced by hot pressing for biomedical applications. Mater. Des. 108, 488–493. https://doi.org/10.1016/j.matdes.2016.07.023.

Moura, C.G., Pereira, R., Buciumeanu, M., Carvalho, O., Bartolomeu, F., Nascimento, R., Silva, F.S., 2017. Effect of laser surface texturing on primary stability and surface properties of zirconia implants. Ceram. Int. 43, 15227–15236. https://doi.org/10.1016/j.ceramint.2017.08.058.

Ning, C.Q., Zhou, Y., 2002. In vitro bioactivity of a biocomposite fabricated from HA and Ti powders by powder metallurgy method. Biomaterials 23, 2909–2915. https://doi.org/10.1016/S0142-9612(01)00419-7.

Pease III, L.F., West, W.G., 2002. Fundamentals of Powder Metallurgy. Metal Powder Industry, USA.

Pereira, B.L., Tummler, P., Marino, C.E.B., Soares, P.C., Kuromoto, N.K., 2014. Titanium bioactivity surfaces obtained by chemical/electrochemical treatments. Rev. Mater. 19, 16–23. https://doi.org/10.1590/S1517-70762014000100004.

Queiroz, A.C., Santos, J.D., Vilar, R., Eugénio, S., Monteiro, F.J., 2004. Laser surface modification of hydroxyapatite and glass-reinforced hydroxyapatite. Biomaterials 25, 4607–4614. https://doi.org/10.1016/j.biomaterials.2003.11.054.

Ratner, B.D., Hoffman, A.S., Schoen, F.J., Lemons, J.E., 1996. Biomaterials Science – an introduction to materials in medicine. Biomater. Sci. Introd. Mater. Med. https://doi.org/10.1016/B978-0-08-087780-8.00148-0.

Runa, M.J., Mathew, M.T., Rocha, L.A., 2013. Tribocorrosion response of the Ti6Al4V alloys commonly used in femoral stems. Tribol. Int. 68, 85–93. https://doi.org/10.1016/j.triboint.2013.09.022.

Ryan, G., Pandit, A., Apatsidis, D.P., 2006. Fabrication methods of porous metals for use in orthopaedic applications. Biomaterials 27, 2651–2670. https://doi.org/10.1016/j.biomaterials.2005.12.002.

Sahoo, R., Jha, B.B., Sahoo, T.K., 2014. Dry sliding wear behaviour of Ti-6Al-4V alloy consisting of bimodal microstructure. Trans. Indian Inst. Met. 67, 239–245. https://doi.org/10.1007/s12666-013-0343-x.

Sampaio, M., Buciumeanu, M., Henriques, B., Silva, F.S., Souza, J.C.M., Gomes, J.R., 2016. Tribocorrosion behavior of veneering biomedical PEEK to Ti6Al4V structures. J. Mech. Behav. Biomed. Mater. 54, 123–130. https://doi.org/10.1016/j.jmbbm.2015.09.010.

Santin, M., Philips, G., 2012. Biomimetic, Bioresponsive, and Bioactive Materials – An Introduction to Integrating Materials with Tissues. John Wiley & Sons, USA.

Sidambe, A.T., 2014. Biocompatibility of advanced manufactured titanium implants-a review. Materials 7, 8168–8188. https://doi.org/10.3390/ma7128168.

Singh, J., Alpas, A.T., 1996. High-temperature wear and deformation processes in metal matrix composites. Metall. Mater. Trans. A Phys. Metall. Mater. Sci. 27, 3135–3148.https://doi.org/10.1007/BF02663864.

Tan, X.P., Tan, Y.J., Chow, C.S.L., Tor, S.B., Yeong, W.Y., 2017. Metallic powder-bed based 3D printing of cellular scaffolds for orthopaedic implants: a state-of-the-art review on manufacturing, topological design, mechanical properties and biocompatibility. Mater. Sci. Eng. C 76, 1328–1343. https://doi.org/10.1016/J.MSEC.2017.02.094.

Taniguchi, N., Fujibayashi, S., Takemoto, M., Sasaki, K., Otsuki, B., Nakamura, T., Matsushita, T., Kokubo, T., Matsuda, S., 2016. Effect of pore size on bone ingrowth into porous titanium implants fabricated by additive manufacturing: an in vivo experiment. Mater. Sci. Eng. C 59, 690–701. https://doi.org/10.1016/j.msec.2015.10.069.

Taylor, M., Tanner, K.E., Freeman, M.A.R., Yettram, A.L., 1995. Cancellous bone stresses surrounding the femoral component of a hip prosthesis: an elastic-plastic finite element analysis. Med. Eng. Phys. 17, 544–550. https://doi.org/10.1016/1350-4533(95)00018-I.

Trabelsi, M., AlShahrani, I., Algarni, H., Ben Ayed, F., Yousef, E.S., 2019. Mechanical and tribological properties of the tricalcium phosphate - magnesium oxide composites. Mater. Sci. Eng. C 96, 716–729. https://doi.org/10.1016/j.msec.2018.11.070.

Van Hooreweder, B., Apers, Y., Lietaert, K., Kruth, J.P., 2017. Improving the fatigue performance of porous metallic biomaterials produced by selective laser melting. Acta Biomater. 47, 193–202. https://doi.org/10.1016/j.actbio.2016.10.005.

Zhang, L., He, Z.Y., Zhang, Y.Q., Jiang, Y.H., Zhou, R., 2016. Enhanced in vitro bioactivity of porous NiTi-HA composites with interconnected pore characteristics prepared by spark plasma sintering. Mater. Des. 101, 170–180. https://doi.org/10.1016/j.matdes.2016.03.128.

Zhao, X., Courtney, J.M., Qian, H., 2011. Bioactive materials in medicine - design and applications. Bioact. Mater. Med. Des. Appl. https://doi.org/10.1533/9780857092939.1.

CHAPTER 6

Multi-material NiTi-PEEK hybrid cellular structures by Selective Laser Melting and Hot Pressing: Tribological characterization

M.M. Costa[a], F. Bartolomeu[a], J. Palmeiro[a], B. Guimarães[a], N. Alves[b], G. Miranda[c], F.S. Silva[a],

[a]Center for MicroElectroMechanical Systems (CMEMS-UMinho), University of Minho, Campus de Azurém, 4800-058 Guimarães – Portugal

[b]Centre for Rapid and Sustainable Product Development Polytechnic Institute of Leiria, Rua General Norton de Matos, Apartado 4133, Leiria, Portugal;

[c]CICECO, Aveiro Institute of Materials, Department of Materials and Ceramic Engineering, University of Aveiro, 3810-193, Aveiro, Portugal

Abstract

In this study, a multi-material NiTi-PEEK cellular structured solution was designed, produced and characterized targeting orthopedic applications. For that purpose, Selective Laser Melting (SLM) technique was used to produce NiTi cellular structures with different open-cell sizes and wall thicknesses. Hot Pressing (HP) technique was used to introduce PEEK in the open-cells of NiTi structures to obtain multi-material components. Morphological characterization showed that the selected SLM processing parameters were suited to achieve high-quality parts without significant defects. Tribological characterization proved an enhanced wear resistance to the multi-material specimens when compared with the mono-material NiTi structures. These multi-material structures are a promising solution for providing a customized stiffness and superior wear resistance to NiTi structures to be integrated in innovative orthopedic designs.

Keywords: Multi-Material structures; NiTi-PEEK; Selective Laser Melting; Hot Pressing

6.1. Introduction

The selection of a biomaterial for fabricating an implant is of utmost importance for its success, once it should be able to (i) allow bone regeneration not being harmful to the host, thus, displaying high biocompatibility; (ii) have suitable mechanical properties, by displaying adequate stiffness and strength, high corrosion and wear resistance [1–5].

Metals, such as Ti6Al4V, have been historically used as orthopedic implant materials, once they meet satisfactorily with some of these requirements in terms of mechanical strength, high corrosion resistance and biocompatibility [1,5–8]. However, improvements are still needed to enhance their overall performance once implant loosening often occurs, consequently leading to revision surgeries [4,9–11]. The high elastic modulus and poor wear resistance of Ti6Al4V, besides a non-uniform contact between implant and bone are the three main factors accountable for implants failure [7,9,10].

Nickel–Titanium (NiTi) shape memory alloy owes attractive properties for biomedical applications of different areas like cardiology (e.g. stents), neurology and orthodontics [1,3,12,13]. NiTi shape memory effect (SME) and superelasticity (SE) together with its high strength, fatigue wear and corrosion resistance, and high biocompatibility [13–16] make this alloy also a good candidate for orthopaedic implants [4,17]. Compared with Ti6Al4V, besides the addition of SME and SE, NiTi displays higher wear resistance and lower elastic modulus [13].

The control of an implant porosity allows to tailor its elastic modulus, desirably to values closest to that of bone in order to avoid the stress-shielding effect [4,12,18,19]. NiTi elastic modulus (≈ 40–75 GPa [13]) is still high when compared to that of bone (≈ 10–30 GPa [2,13]), thus the creation of engineered porous NiTi structures can allow to lower this value. Additionally, in an open-cell structured implant, the porosity will allow nutrient flow and vascularization for osteoblasts and mesenchymal cells to adhere and proliferate and, consequently, for bone to growth into the implant pores and create a strong implant-bone bond [4,12,18,19]. In literature, the adequate pore or open-cell size to promote bone ingrowth ranges between 100 and 600 μm [4,12]. Finally, another advantage of NiTi as implant material is its shape memory effect, that can be used to promote an implant expansion once implanted, promoting an uniform contact pressure within the bone, increasing implant fixation [18].

Machining and processing NiTi presents some challenges due to its high ductility, adhesion, work hardening and reactivity to titanium content [14–16,20–22]. Furthermore, conventional manufacturing technologies limit the fabrication of complex NiTi parts. Recently, the emergence of Additive Manufacturing (AM) technologies allow to overcome some of these conventional technologies issues and produce complex parts, layer by layer, directly from CAD data [17,19]. Among AM techniques, Selective Laser Melting (SLM) is commonly used for the production of NiTi complex parts [16,20,21,23]. Specially regarding orthopedic applications, this technique makes possible to manufacture customized implants for a specific patient anatomy [20].

Poly-ether-ether ketone (PEEK) is a biocompatible polymer, extremely attractive for the medical field, especially for orthopedic implants, due to its high chemical stability, excellent wear and corrosion resistance [4,24–26]. PEEK elastic modulus (≈ 3.6 GPa [27,28]) is much lower than that of bone and despite its advantageous properties, its mechanical strength is inadequate for load-bearing applications as orthopedic implants [25,27]. The combination of PEEK and NiTi in an engineered structure allows tackling this last problem.

In physiological conditions, micromovements at the implant-bone interface occur and may result in metallic debris release to the interface, which was already found in literature that, besides promoting bone resorption, can cause allergic and toxic reactions to the tissue [29–31]. Literature on the improvement of Ti6Al4V poor wear resistance is quite vast, by applying coatings, creating multi-material solutions and so on [6,10,32], however, besides being promising solutions, NiTi high wear resistance allied with its unique properties make it an outstanding biomaterial implant substitute. It is already reported in literature that, contrary to conventional materials, NiTi wear

performance is not only dependent on its mechanical properties (e.g. hardness, work-hardening, etc), but also its superelastic effect [33–35]. In this sense, the tribological response of NiTi cellular structures should be investigated to assess its applicability in implant solutions. It is important to highlight that, to the authors best knowledge, the present study is the pioneer regarding tribological characterization of NiTi cellular structures by SLM technique.

In this study, mono-material NiTi cellular structures were produced by SLM and multi-material NiTi-PEEK structures were obtained by SLM and HP for PEEK impregnation, being tribologically characterized.

6.2. Experimental details

6.2.1. Specimens fabrication

NiTi cellular structures were designed and manufactured by SLM using an equipment from SLM solutions (model 125HL) equipped with a 400 W Ytterbium-fiber laser. For that purpose, a $Ni_{50.8}Ti_{49.2}$ (at. %) ingot (*SAES Smart Materials, USA*) was atomized at *TLS technique GmbH (Germany)* through an electrode induction melting gas atomization (EIGA) technique. The NiTi powder with spherical morphology, displaying a particle size diameter (D50) of 47.5 µm. Multi-material NiTi-PEEK structures were fabricated using PEEK powder, obtained from *Evonik Industries (Germany)*, which presents an irregular shape and a particle size (D50) of 50 µm.

Table 6.1 displays the processing parameters used to produce NiTi cellular structures, that were selected based on previous optimization studies [36,37].

Table 6.1 - Selective Laser Melting parameters used for NiTi cellular structures production.

Laser Power	Scan Speed	Scan Spacing	Layer Thickness	Energy Density
90 W	600 mm/s	90 µm	30 µm	55.6 J/mm³

Briefly, SLM process starts with the design of the structures using a CAD software, being the file then imported to a SLM equipment that will produce the part, layer by layer, by melting, via laser, the powder bed in specific sites (Figure 6.1(A)). SLM process was conducted under argon atmosphere using a Ti6Al4V platform at 200 ºC.

The specimens produced in this study displayed an average height and diameter of approximately 2.66 ± 0.34 mm and 6.08 ± 0.04 mm, respectively. The architecture of these specimens consists in a cubic-like structure with interconnecting porosity that differs in terms of

open-cell sizes (500 or 600 μm) and wall thicknesses (100, 150 and 350 μm). After the SLM production, these cellular structures were impregnated with PEEK by means of a pressure-assisted technique, Hot Pressing (HP). In this technique, pressure and temperature are applied, simultaneously, to melt the polymer and force it to fill the open-cells of the NiTi structure, thus creating a multi-material NiTi-PEEK structure. The impregnation process, depicted in Figure 6.1(B), starts with the placement of the NiTi specimens on top of the lower punch, followed by the positioning of the die and PEEK powder insertion. With the positioning of the upper punch, the system is placed inside a chamber under vacuum atmosphere (10^2 mbar). Firstly, to accommodate the powder, a residual pressure is applied before beginning the thermal cycle. Afterwards, the system is heated using an induction coil until the temperature reaches 380 °C, above PEEK melting point (345 °C). Then the temperature is decreased until 300 °C and, to force PEEK to fill the open cells, a small pressure of approximately 10 MPa was applied and kept for 5 s. This cycle was repeated two times and then the sample was allowed to cool inside the chamber till room temperature.
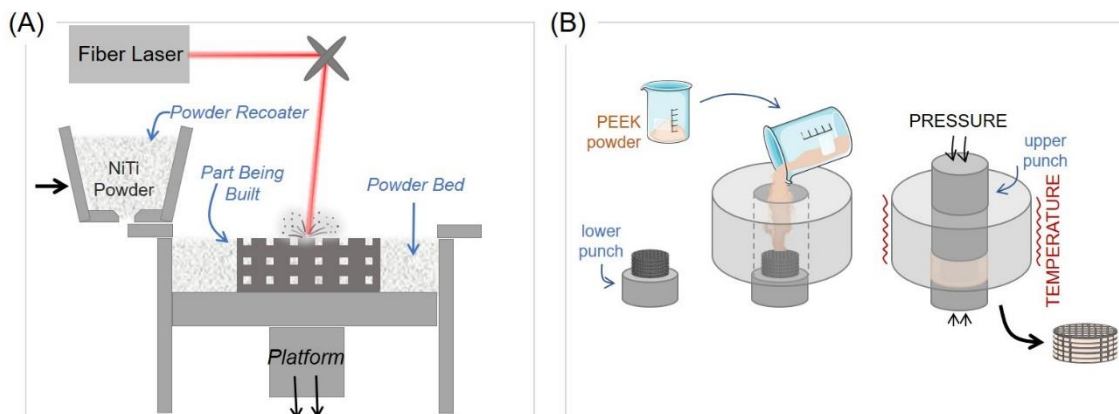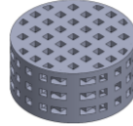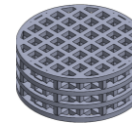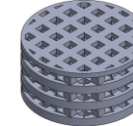
Figure 6.1 - Schematic representation of (A) SLM building and (B) PEEK impregnation processes.

Following these fabrication strategies (SLM and SLM + HP), a total of twelve groups were manufactured for the present study, where six of them are NiTi cellular structures and the other six NiTi-PEEK multi-material cellular structures. Table 6.2 resumes the main features of these groups of specimens, namely, CAD model design and open-cell, wall sizes and porosity of CAD design and SLM-produced specimens. Porosity was determined for all specimens by determining their mass and volume and considering the theoretical density of NiTi.

Table 6.2 - CAD model design and SLM.Produced details (P denoting specimens with PEEK).

Group		500-100 / 500-100P	500-150 / 500-150P	500-350 / 500-350P	600-100 / 600-100P	600-150 / 600-150P	600-350 / 600-350P
CAD design	Open-cell (µm)	500	500	500	600	600	600
	Wall (µm)	100	150	350	100	150	350
	Porosity (%)	90.7	83.3	61.7	92.3	87.0	66.7
	CAD model design						
SLM-Produced	Open-cell (µm)	387.2 ± 7.3	387.8 ± 7.3	381.4 ± 15.3	491.8 ± 9.7	495.0 ± 4.6	478.7 ± 21.2
	Wall (µm)	208.3 ± 12.2	247.7 ± 9.2	466.5 ± 24.5	205.8 ± 7.6	251.8 ± 9.6	450.5 ±14.5
	Porosity (%)	73.9 ± 0.3	68.4 ± 0.5	46.1 ± 0.1	78.1 ± 0.4	72.7 ± 0.6	52.2 ± 2

6.2.2. Tribological Tests

After fabrication, NiTi cellular structures were prepared for tribological testing by polishing down to 4000 mesh by using SiC abrasive paper and subsequent ultrasonic cleaning for 5 min in isopropanol. Afterwards, the specimens were placed inside an acrylic device fixed to a tribometer (*Bruker-UMT-2, USA*), where ball-on-plate reciprocating sliding tests were performed using a 10 mm alumina (Al_2O_3) ball, from *Ceratec, NL*, as counterpart and the specimens as plates. Figure 6.2 shows a schematic representation of the tribological tests carried out in the present study. The tests were conducted with the specimens immersed in phosphate buffered solution (PBS) at 37 ± 2 °C, under a 6 N normal load, at a frequency of 1 Hz, for 30 min. For each group, an average ranging from 3 to 6 repetitions were performed, being the results presented as the average ± standard deviation. The values for the coefficient of friction (COF) were obtained directly from the tribometer and the results were determined by the average of the COF values, when the steady state regime of each specimen was achieved.

After the tribological tests, the specimens were cleaned in isopropanol to remove loose wear debris and an optical microscope from *Leica Microsystems (Leica DM 2500, Germany)* was used for wear track observation. The width and length of the wear tracks were measured using *Image J* software, to further calculate the total volume loss. Since NiTi cellular structures are not dense, it was necessary to develop a methodology for estimating the volume loss, taking into consideration the empty spaces of the wear track. The methodology adopted for volume loss determination using a CAD software will be thoroughly described as follows:
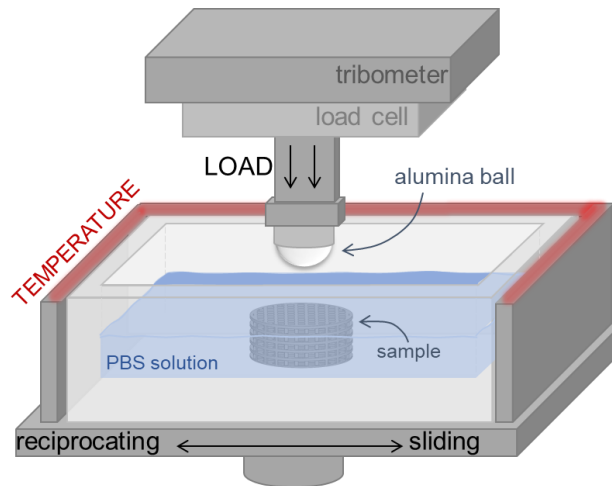
Figure 6.2 - Schematic illustration of the tribological apparatus.

Firstly, it is important to highlight that adjusted CAD designs were modeled for each group by substituting the designed dimensions by the real dimensions (open-cell and thickness) that were measured after SLM fabrication. More details on these differences between CAD design and SLM fabricated parts can be found in literature [38–42]. From the "adjusted CAD model" of each group, the initial volume of the specimen was taken from the software and, subsequently, the wear track that was previously designed in 3D (considering the collected width and length of the track) was imported. Then, optical microscope images of each specimen track were imported and properly positioned and rescaled taking into account the known measurements. Finally, the 3D wear track was matched together with the image and subtracted from the final specimen, to determine its final volume, without the track. The total volume loss was, then calculated, by the difference between the initial and final volume of the specimen. For NiTi-PEEK multi-material structures, it was not necessary to apply such strategy since the holes are now filled with PEEK. In this regard, the total volume loss was obtained by drawing the 3D wear track using the width and length measurements, assuming that these tracks result of the sliding of a perfect alumina ball geometry.

With all volume losses calculated for the twelve groups, the specific wear rate was determined according to Archard's model, as follows:

$$k = \frac{\Delta V}{F \times S} \tag{1}$$

where k is the specific wear rate (mm³/Nm), ΔV the total volume loss of the wear track (mm³), F the normal applied load (N) and S the total sliding distance (m).

6.2.3. Scanning Electron Microscopy (SEM) and X-ray diffraction (XRD) analysis

Surface morphology and microstructure of the specimens from the different groups, before and after tribological tests, were analyzed by Scanning Electron Microscopy (SEM). Additionally, after SLM fabrication and PEEK impregnation, X-ray diffraction analysis (XRD) was also performed, being the data collected in a *Bruker AXS D8 Discover (USA)* equipment from 10 to 90º, with a step size and counting time of 0.02º and 1 s, respectively. Finally, after the tribological tests, Energy-dispersive X-Ray spectroscopy analysis (EDS) was used in some specific sites of the specimens for chemical characterization, being the alumina ball observed by SEM and EDS to assess eventual material transfer.

6.3. Results and discussion

6.3.1. Morphological, crystallographic and mechanical characterization

In the present study, NiTi mono-material and NiTi-PEEK multi-material cellular structures with different open-cell sizes and wall thicknesses were developed and studied. Figure 6.3 resumes top views SEM micrographs of all twelve different structures produced.

Few studies in literature report high-quality SLM-produced NiTi cellular structures. This study was able to, by using adequate materials and processing parameters to produce such structures successfully.

By analyzing mono-material cellular structures some deviations between the real dimensions obtained for open-cell sizes and wall thicknesses and the ones designed in the CAD model are observed, with these structures displaying lower open-cell sizes and higher wall thicknesses. This phenomenon, already reported in literature, is typical of SLM process and is related with powder related aspects and partial melting of powder particles near the laser melted zones [6,39,41,43,44].

To the author's best knowledge, this study is the first reporting a multi-material component gathering NiTi and PEEK within a cubic-like cellular architecture. By observing the multi-material specimens, it can be concluded that the impregnation of PEEK into the open cells was successfully achieved, with an effective mechanical interlocking. Figure 6.4 displays the cross-section view of mono- and multi-material 500-100 specimens as an example of the microstructure found for the produced specimens. By analyzing these SEM micrographs it is possible to observe that, in one hand, SLM technique allowed to produce high-quality NiTi cellular structures with good densification and, on the other hand, the adopted strategy to impregnate PEEK into the cellular

structures was successfully validated, once an effective impregnation with mechanical interlocking is observed inside the produced specimens.
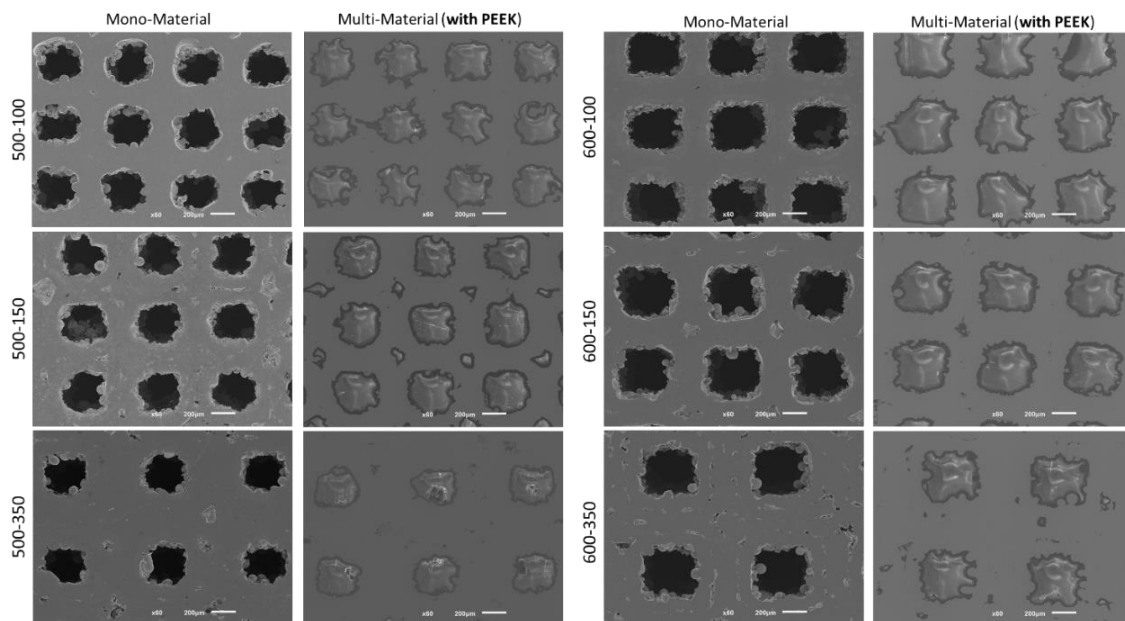
Figure 6.3 - SEM micrographs of the NiTi cellular structures produced by SLM.
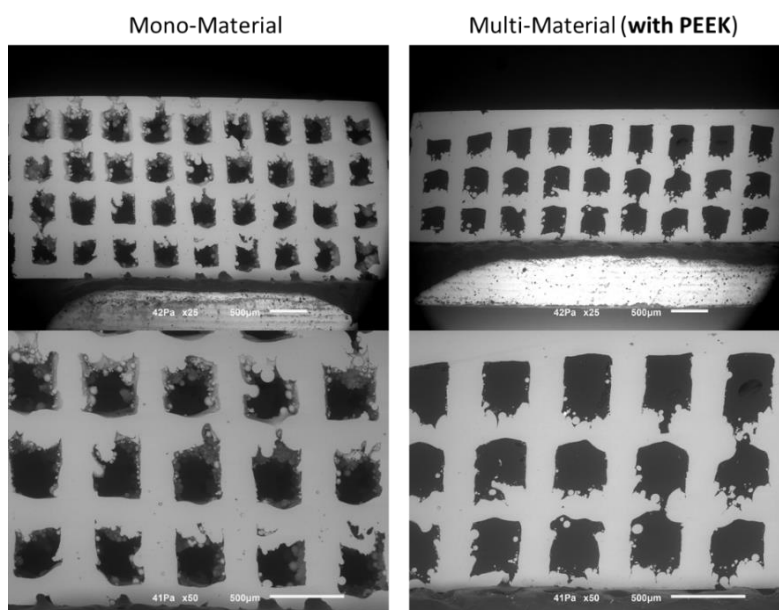
Figure 6.4 - Cross-section view of SEM micrographs of 500–100 mono-material and multi-material specimens.

To determine the existing phases in the mono- and multi-material specimens, XRD analyses were performed and the resulting spectra are shown in Figure 6.5. Both spectra evidence the main peaks matching to the austenite phase (cubic B2 phase) of NiTi that, according to reference pattern number 03-065-5746, present major peaks at 42.436°, 77.637° and 61.571°. NiTi martensitic phase (B19' monoclinic) has four main peaks at 41.365°, 44.927°, 39.223° and 43.917°

(reference pattern number 00-035-1281). And although the XRD spectrum for the multi-material (Figure 6.5) show no clear indication of these peaks, that may be undetectable, a work by Saedi et al. [45] show that changes in transformation temperatures of NiTi specimens are observed after thermal treatments performed from as low as 350 ºC, when compared to as produced parts by SLM. No other Ni–Ti intermetallic phases are detected in these spectra. Finally, several additional peaks were detected in the multi-material XRD spectrum, attributable to PEEK, in agreement with some PEEK patterns found in literature [7,27].
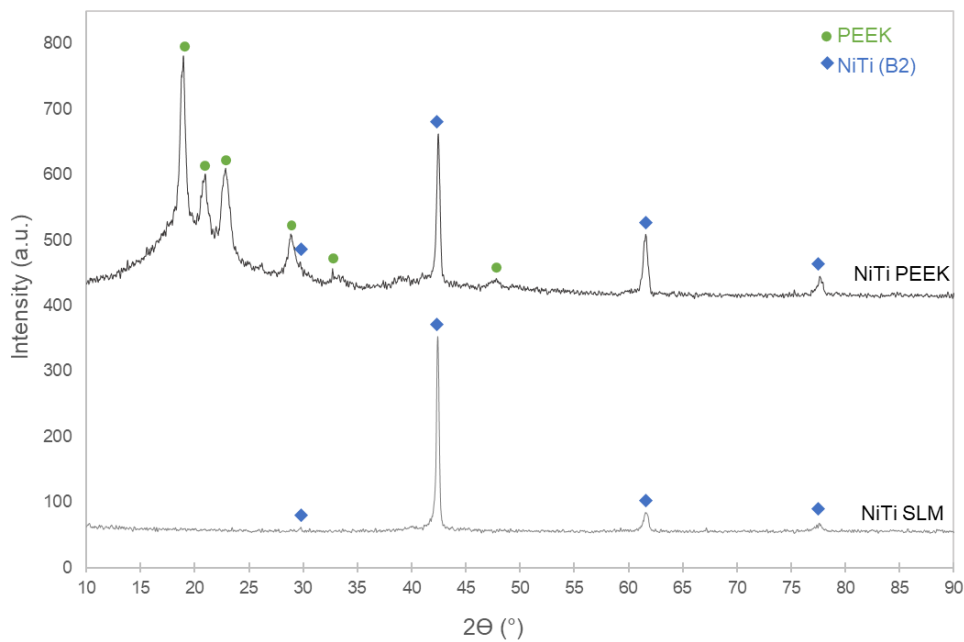
Figure 6.5 - X-ray diffraction patterns of NiTi-SLM specimens before and after PEEK impregnation.

6.3.2. Tribological analysis

The tribological results regarding specific wear rate and coefficient of friction (COF) are shown Figure 6.6 and Figure 6.7, respectively.

It is important to highlight that, in conventional materials, wear resistance highly depend on their mechanical properties such as hardness, strength, toughness, ductility, work hardening and crystallographic texture [34,35,46,47]. However, in shape memory alloys, like NiTi, these properties are insufficient to comprehend their tribological behavior. Many studies in literature reported that the high wear resistance of NiTi alloy is also attributed to its superelastic behavior, which means that it also depends of the stress-induced martensitic transformation and reorientation of martensitic phase under stress [33,35,46,48]. In one hand, the reorientation of martensite phase may hinder crack propagation, once it can accommodate the deformation strain

147

and, on the other hand, superelastic behavior decreases the sliding stress by increasing the elastic contact area [34,46,48,49].
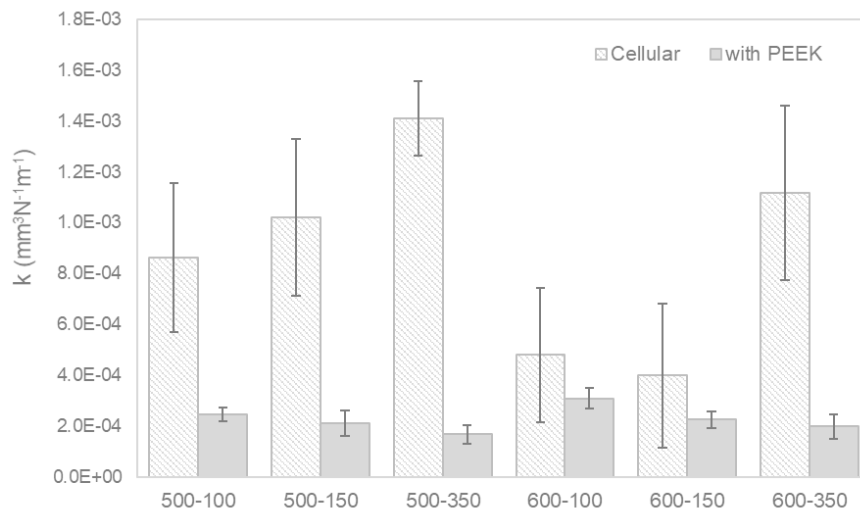
Figure 6.6 - Specific wear rate for all the tested specimens, against alumina ball.
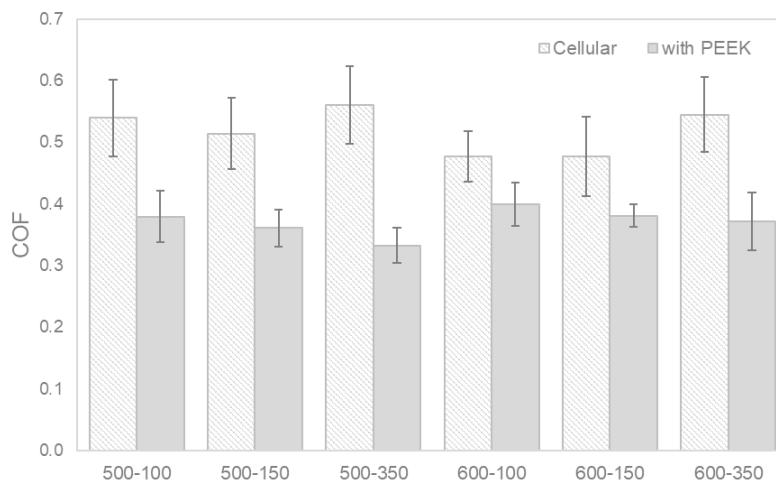
Figure 6.7 - Average coefficient of friction for all the tested specimens, against alumina ball.

The wear testing conditions is another factor that influences NiTi wear performance once the superelastic behavior may be compromised. It is clear that, for all materials, the testing conditions influence wear resistance, however, in NiTi, during wear tests, the load and thermal cycles may lead to microstructural changes that will influence wear performance and superelasticity [35].

In the present study, under the defined tribology conditions (6 N, 1 Hz and 37 °C), superelasticity may be a factor influencing wear resistance. Some authors report that under high loads the superelastic property is not completely functional and deformation started to occur,

contrary to what happens when tested at lower loads [34,35]. Neupane et al. [35] studied the superelastic behavior of NiTi under reciprocating sliding contact with different loads and frequencies. At lower frequencies and normal loads, the main factor influencing wear is the hardening of NiTi and stress-induced austenite to martensite with temperature.

Results show that the introduction of PEEK in these metallic structures led to an increase in their wear resistance, once significantly lower specific wear rates were observed for the multi-material solution (when PEEK is present) when compared to the corresponding unreinforced structures (see Figure 6.6). This reduction was similar for all groups: 72% decrease for 500-100 group, 79% for 500–150, 88% for 500–350, 36% for 600–100, 43% for 600–150 and 600–350, leading to an overall average decrease of 82%. This outcome is attributed to PEEK self-lubrication ability, high heat resistance, low coefficient of friction, excellent wear and corrosion resistance and favorable mechanical strength [4,24–26].

In respect to the COF results (Figure 6.7), a similar tendency is observed as the average COF values obtained for all the multi-material NiTi-PEEK cellular structures are lower than those for the mono-material NiTi structures. Literature reports a COF value around 0.1 for bulk PEEK against alumina [28]. Consequently, it would be expected that the overall COF of the multi-material specimens lowers. In fact, an average decrease of 30% was observed for 500–100 and 500-150 groups, 41% for 500–350, 16% for 600–100, 20% for 600–150 and 32% for 600-350 group, when considering the impregnation of PEEK. These results are aligned with some studies found in literature where the introduction of PEEK in Ti alloys metallic cellular structures lead to an increased wear resistance and lower values of coefficient of friction [26–28,32]. PEEK self-lubrication ability and superior wear resistance [28,32,50] can explain these results.

When analyzing the wear results of NiTi mono-material it can be observed that specimens with lower porosity (lower number of open-cells on a given area) show a higher specific wear rate and thus a lower wear resistance. Theoretically, under the same wear conditions, higher porosity (more open-cells) would lead to higher specific wear rates due to a higher contact pressure. However, in the present work, this was not observed, indicating that for these NiTi architectures under these specific conditions, other phenomenon is controlling the tribological interaction. The fact that structures with higher open-cell sizes or more open-cells may be able to collect a superior amount of wear debris in these holes can explain these results, by reducing the third body wear mechanism in structures having higher porosity. By this mean, these work-hardened particles that

severely contribute to abrasion wear are pushed out from the sliding area, thus reducing the overall wear on these structures.

The specific wear rate for NiTi mono-material structures ranges from 4.0×10^{-4} to 1.4×10^{-3} $mm^3N^{-1}m^{-1}$, approximately. Stainless steel and Ti6Al4V titanium alloy are some materials used in the implantology field, being the later the most commonly used, as already mentioned. Bartolomeu et al. [51] reported a specific wear rate for stainless steel of, approximately, 3 to 5×10^{-5} $mm^3N^{-1}m^{-1}$ for Cast, Hot-Pressed and SLM dense specimens and, in another study [52], it was reported a specific wear rate for Ti6Al4V of around 6 to 8×10^{-4} $mm^3N^{-1}m^{-1}$ for Cast, Hot-Pressed and SLM dense specimens. When compared with these implant materials, the specific wear rate for the NiTi mono-materials structures present in this study is slightly higher than SS and similar than Ti6Al4V. Similarly, when searching in literature for the tribological behavior of NiTi specimens, the results are scarce. Nevertheless, Neupane et al. [35] reported an average specific wear rate of 7.5×10^{-5} $mm^3N^{-1}m^{-1}$. However, it is important to highlight that these values reported in literature are for dense structures, being the slightly higher value of the specific wear rate in this study explained by the presence of the open-cells. When compared with multi-material structures, this value decreases significantly, to values ranging from around 1.7 to 3.1×10^{-4} $mm^3N^{-1}m^{-1}$, which are higher than the ones reported in the Ti6Al4V study already mentioned and near to the ones reported for NiTi dense specimens, being these results explained by the addition of PEEK material to the structures, as already stated.

Figure 6.8 shows SEM images of all the mono-material NiTi and multi-material NiTi-PEEK structures after the tribological tests against alumina ball.

By analyzing this figure, it is possible to observe the damaged features of the tribological interaction related to the prevailing wear mechanisms. All the specimens displayed abrasive wear by exhibiting a series of grooves parallelly aligned with the sliding direction, scratch marks and some wear debris. These abrasion grooves are created by the alumina hard asperities, resulting in a two-body abrasive wear mode that leads to surface damage and loss of material. Similar worn scars were found in literature for NiTi specimens against hard materials (WC and Si_3N_4 balls) [35,53]. Plastic deformation of the wear debris (in lower amounts) and subsequent clustering to form tribolayers are also visible. Also, EDS analysis on the red rectangles drawn on Figure 6.7 detected aluminum element on the specimens, meaning that adhesion wear also occur.
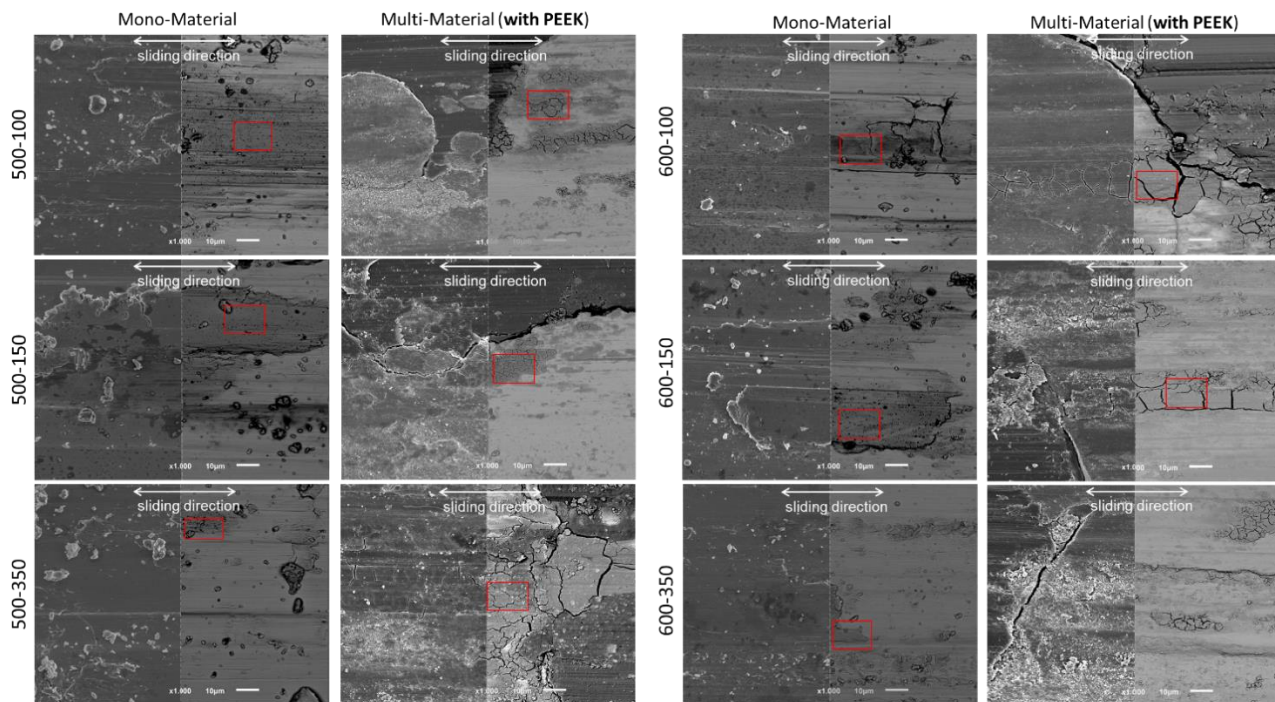
Figure 6.8 - SEM micrographs of the worn NiTi cellular structure specimens against Al_2O_3 ball.

Comparing the worn surfaces of mono- and multi-material specimens, it seems that multi-material specimens present smoother wear tracks, with less evident grooves and less wear debris. These smoother scars found on multi-material specimens may be explained by the presence of PEEK, that is protecting the NiTi surface from wear. These results are in accordance with the lower coefficient of friction values found for multi-material specimens, when compared with the mono-material ones.

SEM micrographs of the worn Al_2O_3 balls and corresponding EDS analysis were performed and results are displayed in Figure 6.9 and Figure 6.10 and Table 6.3, respectively.

Results from SEM and EDS analyses clearly evidence adhesion wear, once in all Al_2O_3 balls Ni and Ti elements were detected, proving the metal adherence to the ball surface. Moreover, the micrographs of the balls that slide against to the mono-material specimens shows a much more damaged and fractured surface when compared to the surfaces of the balls corresponding to the multi-material specimens. This phenomenon suggests that in the multi-material specimens, the PEEK seems to reduce the abrasive wear. This can be clearly seen at the SEM images at lower magnifications (Figure 6.10), where the mono-material specimens demonstrate a severity in the ball-specimen contact which led to a higher wear of the counterball, when compared with the multi-material.
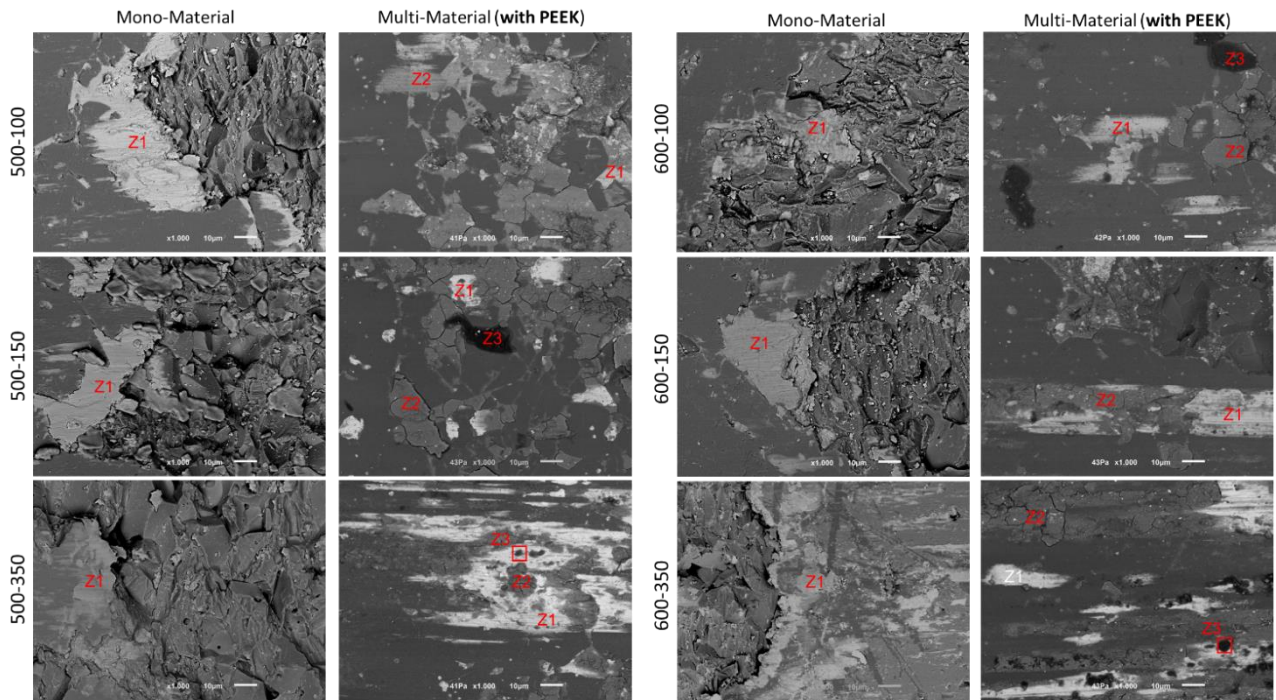
Figure 6.9 - SEM micrographs of the Al_3O_2 balls after wear tests against NiTi cellular structure specimens.
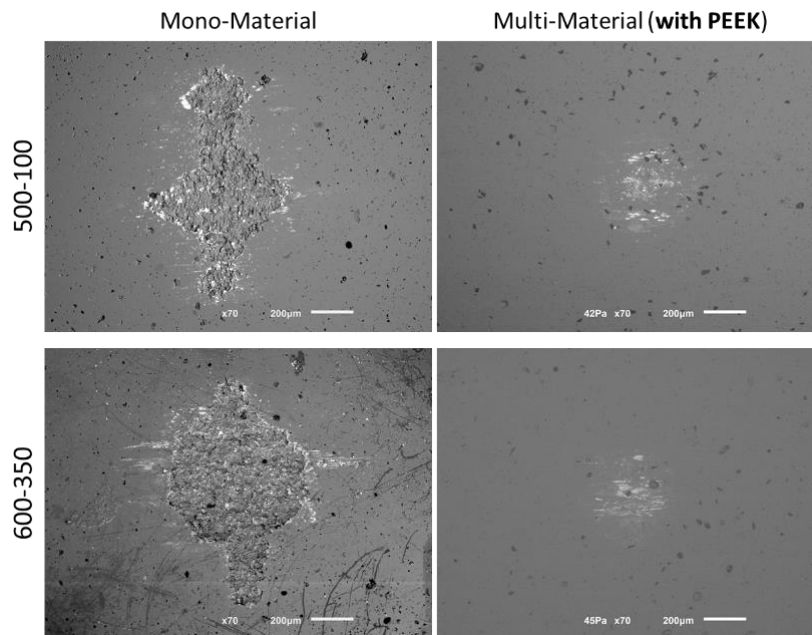
Figure 6.10 - SEM micrographs of the Al_3O_2 balls after wear tests, at lower magnification, for 500–100 and 600-350 specimens.

This phenomenon can be clearly seen in the images at the lowest magnification, where the mono-material samples demonstrate a severity in the contact and consequently, a greater wear of the ball, when compared with the multi-material samples. It is important to note, that this phenomenon is verified in all samples.

Table 6.3 - Chemical composition (in wt. %) of the material transfer zones in Al3O2 balls.

Composition (wt.%)		Ni	Ti	Al	O	C	P	Na	Cl	others
500100	Z1	32.7	32.0	2.5	30.7	-	2.1	-	-	-
500150	Z1	37.4	36.8	1.1	23.0	-	1.6	-	-	-
500350	Z1	43.5	25.3	14.3	4.6	12.3	-	-	-	-
500100P	Z1	20.8	20.1	19.2	33.8	4.6	1.5	-	-	-
	Z2	17.9	9.6	31.2	35.5	4.7	1.0	-	-	-
500150P	Z1	20.3	13.9	20.6	34.9	8.6	1.7	-	-	-
	Z2	5.2	6.5	20.4	49.0	7.9	6.8	2.9	0.5	0.8
	Z3	-	-	22.8	37.0	36.6	1.0	1.3	1.3	-
500350P	Z1	24.3	22.8	17.2	28.3	6.2	1.1	-	-	-
	Z2	20.8	3.4	17.3	38.1	15.1	0.9	3.1	1.3	-
	Z3	6.8	8.5	16.9	33.4	32.2	0.9	1.4	-	-
600100	Z1	18.5	20.5	12.9	41.1	-	3.6	3.0	-	0.4
600150	Z1	38	31	4.8	16.2	9.0	1.0	-	-	-
600350	Z1	42.2	33.5	2.7	19.4	-	1.4	1.0	-	-
600100P	Z1	19.4	16.6	21.6	34.1	6.4	0.8	1.0	-	-
	Z2	7.3	9.3	18.5	44.9	10	6.2	2.3	-	1.5
	Z3	-	0.8	15.5	29.4	45.7	-	3.2	3.7	1.3
600150P	Z1	20	21.7	16.9	31.3	7.5	1.5	1.1	-	-
	Z2	11.8	11.5	18.6	41.8	7.9	5.8	2.6	-	-
600350P	Z1	18.9	23.7	15.9	33.2	5.4	1.7	1.2	-	-
	Z2	8.6	11.3	17.2	43.1	10.3	5.8	3.1	0.7	-
	Z3	2.9	2.2	14.9	33.6	40.9	0.8	2.3	2.6	-

Overall, based on these findings, multi-material specimens show a superior wear resistance when compared to the mono-material ones. This means that the proposed solution based on NiTi cellular structures production by SLM, followed by PEEK open-cells filling with Hot Pressing is a promising strategy to improve current implant mono-material solutions. Additionally, these structures allow to tailor the elastic modulus to values that are within the range of values found for bone.

6.4. Conclusions

In the present study, NiTi mono-material cellular structures were effectively designed and produced by Selective Laser Melting. SEM images, besides proving the effectiveness of the process to produce NiTi cellular structures also demonstrate the effectiveness of the impregnation process to produce multi-material NiTi-PEEK structures. XRD patterns allowed concluding that both mono and multi-material specimens presented austenite as the main phase, with no evidence of other intermetallics. The tribological characterization showed that all the multi-material NiTi-PEEK structures exhibit a higher wear resistance (lower specific wear rate) and lower COF when

compared to the mono-material NiTi structures. These results indicate that the developed solution, i.e., the addition of PEEK to NiTi structures produced by SLM, can provide an improved solution for medical applications when compared with fully metal solutions commercially available.

Acknowledgments

References

[1] Li J, Cui X, Hooper GJ, Lim KS, Woodfield TBF. Rational design, biofunctionalization and biological performance of hybrid additive manufactured titanium implants for orthopaedic applications: a review. J. Mech. Behav. Biomed. Mater. 2020;105:103671. https://doi.org/10.1016/j.jmbbm.2020.103671.

[2] Horandghadim N, Khalil-Allafi J, Urgen M. Influence of tantalum pentoxide secondary phase on surface features and mechanical properties of hydroxyapatite coating on NiTi alloy produced by electrophoretic deposition. Surf Coating Technol 2020;386:125458. https://doi.org/10.1016/j.surfcoat.2020.125458.

[3] Zhou D, Gao Y, Lai M, Li H, Yuan B, Zhu M. Fabrication of NiTi shape memory alloys with graded porosity to imitate human long-bone structure. JBE 2015;12: 575–82. https://doi.org/10.1016/S1672-6529(14)60147-5.

[4] Wang Z, Wang C, Li C, Qin Y, Zhong L, Chen B, et al. Analysis of factors influencing bone ingrowth into three-dimensional printed porous metal scaffolds: a review. J Alloys Compd 2017;717:271–85. https://doi.org/10.1016/j.jallcom.2017.05.079.

[5] Bartolomeu F, Costa MM, Gomes JR, Alves N, Abreu CS, Silva FS, et al. Implant surface design for improved implant stability – a study on Ti6Al4V dense and cellular structures produced by Selective Laser Melting. Tribol Int 2019;129:272–82. https://doi.org/10.1016/j.triboint.2018.08.012.

[6] Costa MM, Bartolomeu F, Alves N, Silva FS, Miranda G. Tribological behavior of bioactive multi-material structures targeting orthopedic applications. J. Mech. Behav. Biomed. Mater. 2019;94:193–200. https://doi.org/10.1016/j.jmbbm.2019.02.028.

[7] Costa MM, Dantas TA, Bartolomeu F, Alves N, Silva FS, Miranda G, et al. Corrosion behaviour of PEEK or β-TCP-impregnated Ti6Al4V SLM structures targeting biomedical applications. Trans Nonferrous Metals Soc China 2019;29:2523–33. https://doi.org/10.1016/S1003-326(19)65160-5.

[8] Miranda G, Sousa F, Costa MM, Bartolomeu F, Silva FS, Carvalho O. Surface design using laser technology for Ti6Al4V-hydroxyapatite implants. Optic Laser Technol 2019;109:488–95. https://doi.org/10.1016/j.optlastec.2018.08.034.

[9] Costa MM, Lima R, Melo-Fonseca F, Bartolomeu F, Alves N, Miranda A, et al. Development of β-TCP-Ti6Al4V structures: driving cellular response by modulating physical and chemical properties. Mater Sci Eng C 2019;98:705–16. https://doi.org/10.1016/j.msec.2019.01.016.

[10] Bartolomeu F, Sampaio M, Carvalho O, Pinto E, Alves N, Gomes JR, et al. Tribological behavior of Ti6Al4V cellular structures produced by Selective Laser Melting. J. Mech. Behav. Biomed. Mater. 2017;69:128–34. https://doi.org/10.1016/j.jmbbm.2017.01.004.

[11] Melo-Fonseca F, Lima R, Costa MM, Bartolomeu F, Alves N, Miranda A, et al. 45S5 BAG-Ti6Al4V structures: the influence of the design on some of the physical and chemical interactions that drive cellular response. Mater Des 2018;160:95–105. https://doi.org/10.1016/J.MATDES.2018.08.056.

[12] Ma X, Wang H, Xie H, Qu J, Chen X, Chen F, et al. Engineering the porosity and superelastic behaviors of NiTi alloys prepared by an electro-assisted powder metallurgical route in molten salts. J Alloys Compd 2019;794:455–64. https://doi.org/10.1016/j.jallcom.2019.04.166.

[13] Mwangi JW, Nguyen LT, Bui VD, Berger T, Zeidler H, Schubert A. Nitinol manufacturing and micromachining: a review of processes and their suitability in processing medical-grade nitinol. J Manuf Process 2019;38:355–69. https://doi.org/10.1016/j.jmapro.2019.01.003.

[14] Farvizi M, Ebadzadeh T, Vaezi MR, Yoon EY, Kim Y, Kang JY, et al. Effect of starting materials on the wear performance of NiTi-based composites. Wear 2015; 334–335:35–43. https://doi.org/10.1016/j.wear.2015.04.011.

[15] Ao S, Li K, Liu W, Qin X, Wang T, Dai Y, et al. Electrochemical micromachining of NiTi shape memory alloy with ethylene glycol–NaCl electrolyte containing ethanol. J Manuf Process 2020;53:223–8. https://doi.org/10.1016/j.jmapro.2020.02.019.

[16] Shayesteh Moghaddam N, Saghaian SE, Amerinatanzi A, Ibrahim H, Li P, Toker GP, et al. Anisotropic tensile and actuation properties of NiTi fabricated with selective laser melting. Mater Sci Eng A 2018;724:220–30. https://doi.org/10.1016/j.msea.2018.03.072.

[17] Mehrpouya M, Gisario A, Elahinia M. Laser welding of NiTi shape memory alloy: a review. J Manuf Process 2018;31:162–86. https://doi.org/10.1016/j.jmapro.2017.11.011.

[18] Elahinia MH, Hashemi M, Tabesh M, Bhaduri SB. Manufacturing and processing of NiTi implants: a review. Prog Mater Sci 2012;57:911–46. https://doi.org/10.1016/j.pmatsci.2011.11.001.

[19] Andani MT, Saedi S, Turabi AS, Karamooz MR, Haberland C, Karaca HE, et al. Mechanical and shape memory properties of porous Ni50.1Ti49.9 alloys manufactured by selective laser melting. J. Mech. Behav. Biomed. Mater. 2017;68: 224–31. https://doi.org/10.1016/j.jmbbm.2017.01.047.

[20] Saedi S, Turabi AS, Andani MT, Haberland C, Elahinia M, Karaca H. Thermomechanical characterization of Ni- rich NiTi fabricated by selective laser melting. Smart Mater Struct 2016;25:35005. https://doi.org/10.1088/0964-1726/25/3/035005.

[21] Saedi S, Turabi AS, Andani MT, Haberland C, Karaca H, Elahinia M. The influence of heat treatment on the thermomechanical response of Ni-rich NiTi alloys manufactured by selective laser melting. J Alloys Compd 2016;677:204–10. https://doi.org/10.1016/j.jallcom.2016.03.161.

[22] Haberland C, Elahinia M, Walker JM, Meier H, Frenzel J. On the development of high quality NiTi shape memory and pseudoelastic parts by additive manufacturing. Smart Mater Struct 2014;23:104002. https://doi.org/10.1088/0964-1726/23/10/104002.

[23] Elahinia M, Shayesteh Moghaddam N, Taheri Andani M, Amerinatanzi A, Bimber BA, Hamilton RF. Fabrication of NiTi through additive manufacturing: a review. Prog Mater Sci 2016;83:630–63. https://doi.org/10.1016/j.pmatsci.2016.08.001.

[24] Dufils J, Faverjon F, H´eau C, Donnet C, Benayoun S, Valette S. Combination of laser surface texturing and DLC coating on PEEK for enhanced tribological properties. Surf Coating Technol 2017;329:29–41. https://doi.org/10.1016/j.surfcoat.2017.09.028.

[25] Sheiko N, K´ekicheff P, Marie P, Schmutz M, Jacomine L, Perrin-Schmitt F. PEEK (polyether-ether-ketone)-coated nitinol wire: film stability for biocompatibility applications. Appl Surf Sci 2016;389:651–65. https://doi.org/10.1016/j.apsusc.2016.07.159.

[26] Bartolomeu F, Abreu CS, Moura CG, Costa MM, Alves N, Silva FS, et al. Ti6Al4V-PEEK multi-material structures – design, fabrication and tribological characterization focused on orthopedic implants. Tribol Int 2019;131:672–8. https://doi.org/10.1016/j.triboint.2018.11.017.

[27] Bartolomeu F, Buciumeanu M, Costa MM, Alves N, Gasik M, Silva FS, et al. Multi-material Ti6Al4V & PEEK cellular structures produced by Selective Laser Melting and Hot Pressing: a tribocorrosion study targeting orthopedic applications. J. Mech. Behav. Biomed. Mater. 2019;89:54–64. https://doi.org/10.1016/j.jmbbm.2018.09.009.

[28] Sampaio M, Buciumeanu M, Henriques B, Silva FS, Souza JCM, Gomes JR. Tribocorrosion behavior of veneering biomedical PEEK to Ti6Al4V structures. J. Mech. Behav. Biomed. Mater. 2016;54:123–30. https://doi.org/10.1016/j.jmbbm.2015.09.010.

[29] Geetha M, Singh AK, Asokamani R, Gogia AK. Ti based biomaterials, the ultimate choice for orthopaedic implants – a review. Prog Mater Sci 2009;54:397–425. https://doi.org/10.1016/j.pmatsci.2008.06.004.

[30] Chen Q, Thouas GA. Metallic implant biomaterials. Mater Sci Eng R 2015;87:1–57. https://doi.org/10.1016/j.mser.2014.10.001.

[31] Holzwarth U, Cotogno G. Total hip arthroplasty - state of the art, challenges and prospects. 2012. https://doi.org/10.2788/31286.

[32] Buciumeanu M, Almeida S, Bartolomeu F, Costa MM, Alves N, Silva FS, et al. Ti6Al4V cellular structures impregnated with biomedical PEEK - new material design for improved tribological behavior. Tribol Int 2018;119:157–64. https://doi.org/10.1016/j.triboint.2017.10.038.

[33] Levintant-Zayonts N, Starzynski G, Kopec M, Kucharski S. Characterization of NiTi SMA in its unusual behaviour in wear tests. Tribol Int 2019;137:313–23. https://doi.org/10.1016/j.triboint.2019.05.005.

[34] Neupane R, Farhat Z. Wear and dent resistance of superelastic TiNi alloy. Wear 2013;301:682–7. https://doi.org/10.1016/j.wear.2012.11.017.

[35] Neupane R, Farhat Z. Wear mechanisms of nitinol under reciprocating sliding contact. Wear 2014;315:25–30. https://doi.org/10.1016/j.wear.2014.02.018.

[36] Bartolomeu F, Costa MM, Alves N, Miranda G, Silva FS. Additive manufacturing of NiTi-Ti6Al4V multi-material cellular structures targeting orthopedic implants. Optic Laser Eng 2020;134:106208. https://doi.org/10.1016/j.optlaseng.2020.106208.

[37] Bartolomeu F, Costa MM, Alves N, Miranda G, Silva FS. Engineering the elastic modulus of NiTi cellular structures fabricated by selective laser melting. J. Mech. Behav. Biomed. Mater. 2020;110:103891. https://doi.org/10.1016/j.jmbbm.2020.103891.

[38] Bartolomeu F, Dourado N, Pereira F, Alves N, Miranda G, Silva FS. Additive manufactured porous biomaterials targeting orthopedic implants: a suitable combination of mechanical, physical and topological properties. Mater Sci Eng C 2020;107:110342. https://doi.org/10.1016/j.msec.2019.110342.

[39] Bartolomeu F, Fonseca J, Peixinho N, Alves N, Gasik M, Silva FS, et al. Predicting the output dimensions, porosity and elastic modulus of additive manufactured biomaterial structures targeting orthopedic implants. J. Mech. Behav. Biomed. Mater. 2019;99:104–17. https://doi.org/10.1016/j.jmbbm.2019.07.023.

[40] Weißmann V, Wieding J, Hansmann H, Laufer N, Wolf A, Bader R. Specific yielding of selective laser-melted Ti6Al4V open-porous scaffolds as a function of unit cell design and dimensions. Metals 2016;6(7):116. https://doi.org/10.3390/met6070166.

[41] Ran Q, Yang W, Hu Y, Shen X, Yu Y, Xiang Y, et al. Osteogenesis of 3D printed porous Ti6Al4V implants with different pore sizes. J. Mech. Behav. Biomed. Mater. 2018;84:1–11. https://doi.org/10.1016/j.jmbbm.2018.04.010.

[42] Arabnejad S, Burnett Johnston R, Pura JA, Singh B, Tanzer M, Pasini D. High-strength porous biomaterials for bone replacement: a strategy to assess the interplay between cell morphology, mechanical properties, bone ingrowth and manufacturing constraints. Acta Biomater 2016;30:345–56. https://doi.org/10.1016/j.actbio.2015.10.048.

[43] Taniguchi N, Fujibayashi S, Takemoto M, Sasaki K, Otsuki B, Nakamura T, et al. Effect of pore size on bone ingrowth into porous titanium implants fabricated by additive manufacturing: an in vivo experiment. Mater Sci Eng C 2016;59:690–701. https://doi.org/10.1016/j.msec.2015.10.069.

[44] Miranda G, Faria S, Bartolomeu F, Pinto E, Alves N, Peixinho N, et al. A study on the production of thin-walled Ti6Al4V parts by selective laser melting. J Manuf Process 2019;39:346–55. https://doi.org/10.1016/j.jmapro.2018.12.036.

[45] Saedi S, Turabi AS, Andani MT, Moghaddam NS, Elahinia M, Karaca HE. Texture, aging, and superelasticity of selective laser melting fabricated Ni-rich NiTi alloys. Mater Sci Eng A 2017;686:1–10. https://doi.org/10.1016/j.msea.2017.01.008.

[46] Li DY. A new type of wear-resistant material: pseudo-elastic TiNi alloy. Wear 1998; 221:116–23. https://doi.org/10.1016/S0043-1648(98)00269-5.

[47] Yan L, Liu Y. Wear behavior of austenitic NiTi shape memory alloy. Shape Memory and Superelasticity 2015;1:58–68. https://doi.org/10.1007/s40830-015-0008-1.

[48] Lin HC, Liao HM, He JL, Chen KC, Lin KM. Wear characteristics of TiNi shape memory alloys. Metall Mater Trans A 1997;28:1871–7. https://doi.org/10.1007/s11661-997-0117-3.

[49] Tillmann W, Momeni S. Tribological performance of near equiatomic and Ti-rich NiTi shape memory alloy thin films. Acta Mater 2015;92:189–96. https://doi.org/10.1016/j.actamat.2015.04.006.

[50] Koike H, Kida K, Santos EC, Rozwadowska J, Kashima Y, Kanemasu K. Self-lubrication of PEEK polymer bearings in rolling contact fatigue under radial loads. Tribol Int 2012;49:30–8. https://doi.org/10.1016/j.triboint.2011.12.005.

[51] Bartolomeu F, Buciumeanu M, Pinto E, Alves N, Carvalho O, Silva FS, et al. 316L stainless steel mechanical and tribological behavior — a comparison between selective laser melting, hot pressing and conventional casting. Additive Manufacturing 2017;16:81–9. https://doi.org/10.1016/j.addma.2017.05.007.

[52] Bartolomeu F, Buciumeanu M, Pinto E, Alves N, Silva FS, Carvalho O, et al. Wear behavior of Ti6Al4V biomedical alloys processed by selective laser melting, hot pressing and conventional casting. Trans Nonferrous Metals Soc China 2017;27:829–38. https://doi.org/10.1016/S1003-6326(17)60060-8.

[53] Zhang F, Zheng L, Wang Y, Zhang H. Effect of Ni content and Hf addition on the unlubricated wear performance of Ni-rich NiTi alloys. Intermetallics 2019;112:106548. https://doi.org/10.1016/j.intermet.2019.106548.

CHAPTER 7

NiTi Laser Textured Implants with Improved In Vivo Osseointegration: An Experimental Study in Rats

M.M. Costa[a], A. Miranda[b,c], F. Bartolomeu[a], O. Carvalho[a], S. Matos[d], G. Miranda[e], F.S. Silva[a]

[a]Center for MicroElectroMechanical Systems (CMEMS-UMinho), University of Minho, Campus de Azurém, 4800-058 Guimarães – Portugal

[b]Life and Health Sciences Research Institute (ICVS), School of Medicine, University of Minho, Campus de Gualtar, 4710-057 Braga, Portugal;

[c]ICVS/3B's - PT Government Associate Laboratory, Braga/Guimarães, Portugal

[d]Center for Innovation and Research in Oral Sciences (CIROS), Faculty of Medicine, University of Coimbra, FMUC, Portugal

[e]CICECO, Aveiro Institute of Materials, Department of Materials and Ceramic Engineering, University of Aveiro, 3810-193 Aveiro, Portugal

Abstract

Laser surface texturing is a versatile approach for manufacturing implants with suitable surfaces for osseointegration. This work explores the use of laser to fabricate NiTi textured implants, testing two different groove-based designs. Their performance was evaluated *in vivo* through implantation in Sprague Dawley rats' femur, being then analyzed after 4 and 12 weeks of implantation. Push-out experiments and histological characterization allowed to assess bone-implant bond and osseointegration and to compare the laser textured solutions with non-textured NiTi. Histology showed that, at 4 weeks of implantation, mainly immature woven bone was present whilst at 12 weeks a more mature bone had developed. Considering the largest implantation time (12 weeks), results showed extraction forces considerably higher for textured implants (G2 and G3). Moreover, when comparing G2 and G3, it was found that G2 (having the highest textured surface area) displayed the maximum extraction force among all groups, with an increase of 212% when compared to non-textured implants (G1).

These results prove that the design and manufacturing technology are effective to promote an improved bone-implant bond, aiming the development of orthopedic implants.

Keywords: NiTi; Laser Surface Texturing; *In vivo* Studies; Osseointegration; Implants

7.1. Introduction

Total Hip Arthoplasty, THA, is a widely performed surgical procedure to promote a pain-free mobility and hip-joint functionality [1,2]. Every year, these total artificial joint replacements are performed in more that 1.4 million patients worldwide and this number tends to further increase, which means that it is extremely important to ensure implant longevity, by optimising and enhancing bone-implant fixation [1–3].

To assure this bone-implant fixation, the bone growth towards the implant surface and its attachment, commonly referred as osseointegration, is a fundamental aspect for implants long-term clinical success [1,4]. This process is normally associated with a cascade of biological events that occur after medical implant placement into the bone. Briefly, these events begin with blood interaction with the implant to generate a blood clot, that is a result of clotting factors activation that promotes osteogenic cells migration. This blood clot will act as a provisional matrix and adhere to the implant surface, playing a fundamental role on bone growth and osseointegration [5,6]. In fact, it is extremely important that cell adhesion to the implant is guaranteed, once it is the

interaction between bone and implant surface that will allow an adequate stress distribution from the implant to the bone [5,6].

Dense titanium and its alloys, like Ti6Al4V, are still the first choice for hip implants once they own adequate mechanical properties and biocompatibility [7]. However, there is still some problems arising from these that may lead to implant failure. Since Ti6Al4V Young's Modulus is still high ($\approx$ 110 GPa) when compared to that of cortical bone (10-30 GPa), the stresses that are applied to the implant are not transmitted properly to the bone, which leads to bone resorption and further, implant loosening [7,8].

Equiatomic nickel-titanium (NiTi) alloy, besides having the necessary mechanical properties for such applications, when compared with Ti6Al4V materials, it also displays lower Young's Modulus, which will reduce the existing mismatch between implant and bone [9,10]. Despite that, NiTi also presents outstanding properties making it suitable for a variety of biomedical applications, i.e., it presents shape memory effect and superelasticity, displays high corrosion and wear resistance and excellent biocompatibility [11–14]. Nowadays, NiTi are commercially used in dental devices such as orthodontic wires, endodontic rotary files, and also in the biomedical field such as surgical-assisted devices (endoscopes, stone and blood clots retrievers, vena cava filters) and implantable devices such as stents and heart valves [11,12,15]. Moreover, it also has been applied in load-bearing applications such as spinal correctors, vertebral spacers, etc [16].

As bioinert materials, they are not capable to further elicit bone regeneration. In this sense, several studies are being performed to enhance cell adhesion and osseointegration of titanium alloys by changing its surface features once it is through its surface that the bond between implant and bone must occur [1,5,8,17,18].

It has been proved that surface design (e.g. topography) is critical to osteoblast adhesion and, therefore, a strong biological interaction between implant and bone [1,5,6,19]. In this sense, many surface modification techniques have been applied, as anodic oxidation, grit blasting, sand blasting, acid etching, applying coatings, etc [3,5]. However, these techniques are very non-specific and can bring some contaminations to the material surface (e.g. sand blasting), not allowing to produce a surface with a controlled and defined topography [3,8].

Laser surface texturing is a promising alternative to these conventional methods once it is possible to alter surface topography with high precision and efficiency to achieve a completely controlled design [5,20]. Laser technology reshapes the material surface into a desired topography to enhance surface roughness, highly reported as a crucial parameter for cell adhesion and,

consequently, osseointegration [3]. In this regard, laser approaches are highly explored in literature to achieve materials with a surface topography either at micro- and nano-scale level, aiming biomedical applications [1,5,8,14,18,19]. Among all the surface features found in literature (holes [21,22], pits [23], etc), the most commonly used are grooves and ridges in which cells have the tendency to align and spread [19,24,25].

There are some published studies that evaluate NiTi biological performance either in vitro and/or in vivo aiming orthopedic implantations, using different strategies or fabrication techniques.

Yeung et al. [26] altered surface chemistry of NiTi specimens with plasma immersion ion implantation to obtain nitrogen and oxygen-treated surfaces to assess their cytocompatibility and performance in vivo. Comparable in vitro cell proliferation was found between nitrogen-treated and untreated groups, however, when implanted in rabbits' femur, results indicate higher new bone formation on nitrogen-treated specimens compared with oxygen-treated and untreated ones. In a similar study, the same group of authors assessed the cytocompatibility and performance in vivo of nitrogen and carbon plasma-treated NiTi specimens and concluded that, despite cell growth differences was not significant between groups, bone formation on treated samples was found higher [27]. Another study from Chi-Ho also performed surface chemistry modification, by nitriding NiTi using laser, to improve hydrophilicity and biological response revealing that cell attachment, spreading and proliferation was enhanced on laser-treated groups [28]. In other study, Muhonen et al. [13] evaluated the bone response of sol-gel-derived titania-silica coated intramedullary NiTi nails using shape memory to assure a higher implant contact with bone after implantation, and successfully enhancing bone–implant attachment and biocompatibility. Liu et al. [29] implanted porous NiTi/Ti and dense NiTi/Ti in rabbits femur/tibia and assessed bone ingrowth and interfacial bonding strength. Results indicate that the porous groups have higher bonding strength than the dense ones, being porous NiTi more favorable to fast osseointegration than porous Ti, under the same conditions.

An in vitro study, performed by Chan and his co-authors evaluated the effect of laser-induced surface features regarding morphology, adhesion and viability of mesenchymal stem cells and revealed that these surface features (roughening, anisotropic dendritic pattern and Ni oxidation) improved cell attachment and viability in the laser-melted zone [30]. Li et al. [20] also employed laser to fabricate micro and nanostructures on NiTi sheets and concluded that, after nanosecond laser irradiation, the oxide film formed provided a suitable cell growth environment being these surface features desirable for cell attaching, spreading and proliferation.

Besides the abovementioned studies, to the authors best knowledge, literature regarding in vivo performance of NiTi alloys by laser surface texturing aiming orthopedic implants are scarce.

In this sense, in the present study, a laser approach was used to create surface-grooved textured NiTi implants aiming orthopaedic applications. The aim of this study is to assess implant performance *in vivo* by comparing its bone-implant strength and osseointegration with non-textured implants. Three different types of surface topographies were prepared (non-textured ("machined") and two different micro-textured implants) and inserted into Sprague Dawley rats' femurs that were further characterized, after two different timepoints, 4 and 12 weeks. Characterization consisted in mechanical push-out tests followed by scanning electron microscope imaging of the removed implants and qualitative histological evaluation of bone-implant interfaces.

7.2. Experimental details

7.2.1. Implants fabrication

In the present study, three types of implants were used: one non-textured and two textured, all using NiTi wires purchased from Memry GmbH as starting material, having a diameter of 1.4 mm ± 0.013 mm and 25 mm ± 0.5 mm length.

The non-textured NiTi implants, belonging to group 1 (G1), are NiTi wires as purchased from the manufacturer and will act as control group (Figure 7.1).
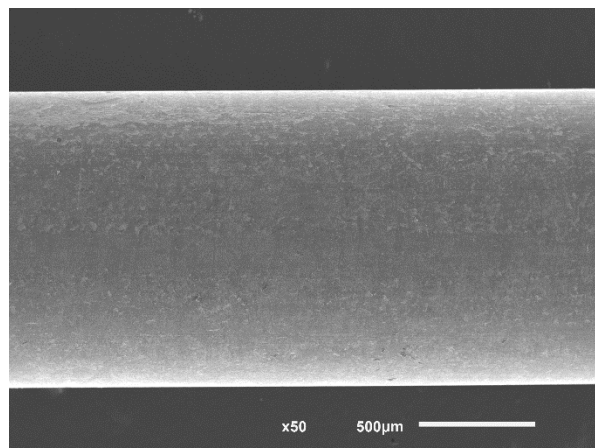
Figure 7.1 - Non-textured NiTi implant (G1).

A Nd:YAG laser from OEM Plus (working with a wavelength of 1064 nm and 6 W maximum power) was used to manufacture two typed of textured surfaces along the surface of the NiTi wires. This laser, with a spot diameter of 3 μm, is a pulsed laser, meaning that surface texturing is achieved by a sequence of pulses. During laser machining, the NiTi wires were attached to a motor,

rotating at ≈ 10 Hz, and the nozzle of the assisted argon flow was placed next to the wires to remove laser-formed debris (Figure 7.2(A)).

The design used to create these textured implants, as depicted in Figure 7.2(B), consisted of overlapping lines in which each line differs in wobble amplitude and number of passages. This strategy aims not only to produce grooves with a more rounded shape but also to distribute the laser energy during machining. In this sense, a sequence of 10 different lines, overlapped, were machined with ≈ 6 W laser power and scan speed of 2 mm s^{-1}, in which each line has a different wobble amplitude, ranging from 25 to 340 µm, and number of passages that varied from 10 to 100, as can be observed in the table presented in Figure 2(B). At the end, a final finishing passage was performed by scanning 50 rectangles in the border of each groove to eliminate powder accumulation on the walls and consequently, create cleaner cuts.

This strategy allowed to produce two types of textures, that differs in terms of distance between grooves. In this sense, group 2 (G2) has a groove width of 398.05 ± 5.14 µm, depth of 248.66 ± 39.50 µm and wall thickness of 183.44 ± 5.97 µm, while group 3 (G3) has a groove width, depth and wall thickness of 397.17 ± 4.70 µm, 236.00 ± 26.87 µm and 479.64 ± 10.13 µm, respectively.
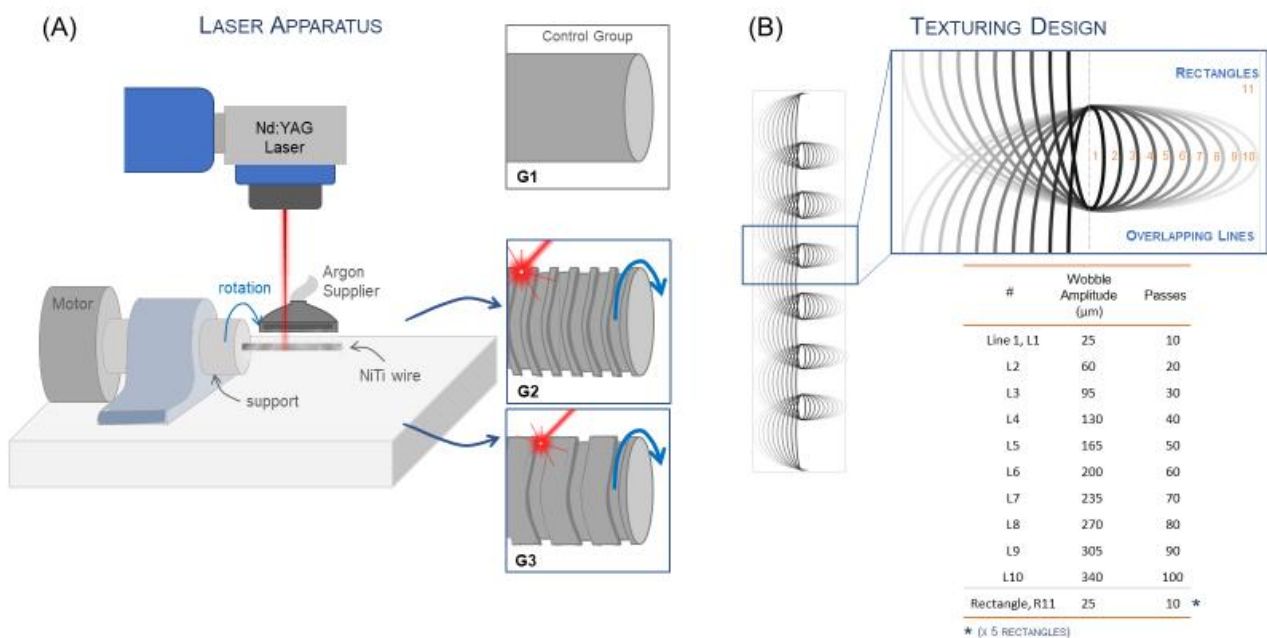
Figure 7.2 - Schematic representation of (A) laser apparatus and (B) strategic design for textures manufacture.

7.2.2. In vivo experiments

7.2.2.1. Pre-clinical model

Thirty-four Male Sprague Dawley rats (Charles River, Barcelona, Spain), with an average body weight of 480.30 ± 53.89 g, were included in this study. Animals were kept in a facility with controlled environmental conditions (22 ± 2 °C, humidity 50-60% and artificial 12h light/dark cycle). Each pair of animals were kept in a cage and irradiated food and sterilized water available *ad libitum*. Enrichment and nesting material were provided. All animal experiments were conducted following the EU Directive 2010/63/EU, approved by the Animal Ethics Committee of the Institution where the study was performed, SECVS 132/2016, and by the national competent authority for animal protection *Direção Geral de Alimentação e Veterinária*, DGAV/010117. All the personnel involved in the procedures are approved as competent for animal experimentation by DGAV and the facilities approved by the national competent authority DGAV/014070.

7.2.2.2. Surgical Procedure

Rats with 16 to 18 weeks-old were anesthetized by administrating a combination of ketamine (75 mg kg^{-1}; Ketamidor, Richter Pharma AG, Austria), medetomidine (0.5 mg kg^{-1}; VetPharma Animal Health, Spain), intraperitoneally. Analgesia was provided pre-operatively by the administration of buprenorphine (0.05 mg kg^{-1}; Richter Pharma AG, Austria), subcutaneously. The animals were positioned in left lateral recumbency, their fur was shaved in the right leg and disinfected with chlorhexidine, as schematically represented in image 1 of Figure 7.3. Each animal randomly received an implant in the right femur. Afterwards, a skin incision was made (Figure 7.3, Image 2), followed by an incision on the muscles *Tensor fasciae lata* and *Vastus lateralis*, parallel to the muscle fibers. An incision was made into the joint capsule, the patella was luxated medially, and the distal epiphysis of the femur exposed (Figure 7.3, Image 3). Drills with ascending lengths were used to create a small defect in the *trochlear sulcus* of the femur and then create a cavity through the longitudinal axis of the femur (Figure 7.3, Image 4). The NiTi implants were press fit, axially, into the newly drilled hole, as shown in Image 5 of Figure 7.3. Finally, the patella was put back in place and the joint capsule muscles and skin were closed in layers with resorbable suture (Figure 7.3, Image 5). Animal recovery included the subcutaneous administration of a reversal agent atipamezole (1 mg kg^{-1}; Antisedan, Orion Corporation, Finland). The animals were kept under red light to avoid hypothermia until the animal fully recovers from the anesthetic effect.

Post-operative analgesia was guaranteed by the administration of a non-steroid anti-inflammatory carprofen (5 mg kg^{-1}; Rimadyl, Zoetis, Portugal) for 3 days and complemented with buprenorphine on post-operative day 1. Antibiotherapy was provided by the subcutaneous administration of enrofloxacine (5 mg kg^{-1}; Baytril, Bayer, Portugal).

At predefined timepoints, 4 and 12 weeks, animal's euthanasia were performed using an over dosage of sodium pentobarbital (150 mg kg^{-1}; Eutasil, CEVA, France). Subsequently, the rat's paw was harvested, the soft tissues carefully removed, and the bone-implant specimens were observed by x-ray (SEDECAL APR VET equipment). Part of the samples from the same group were taken immediately to push-out tests, while the other was fixed with 10% formaldehyde solution to assure tissue preservation for further histological characterization.
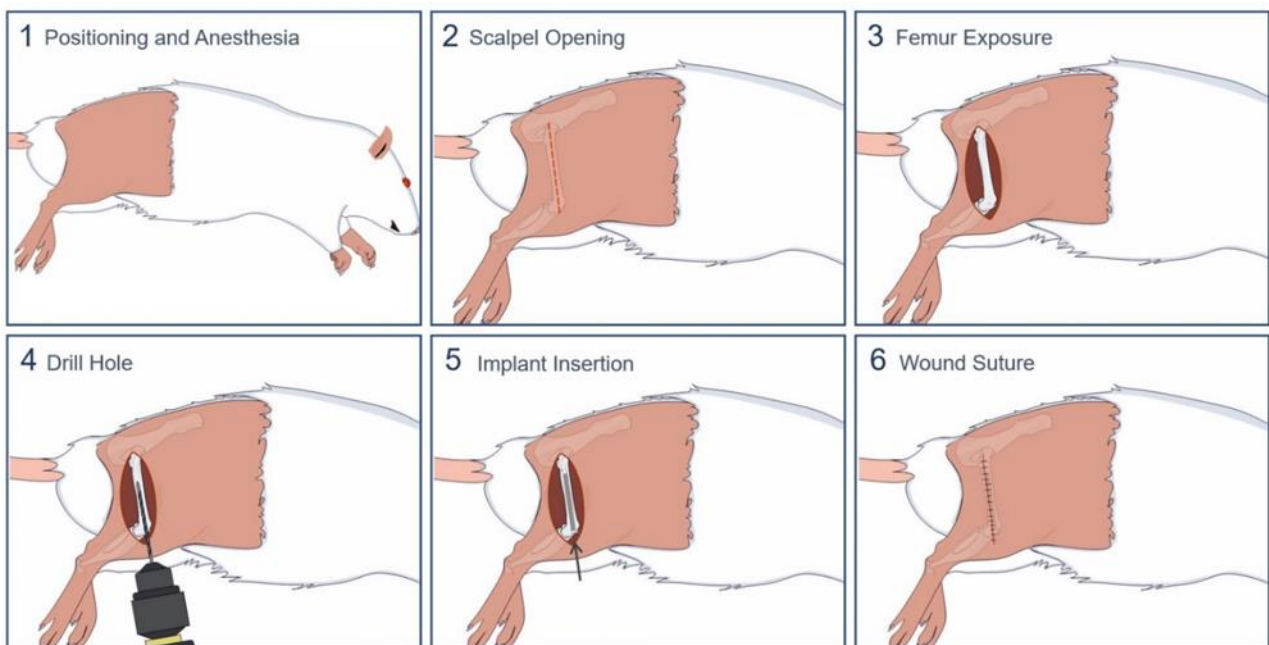
Figure 7.3 - Surgical procedure and implantation.

7.2.3. Push-out tests
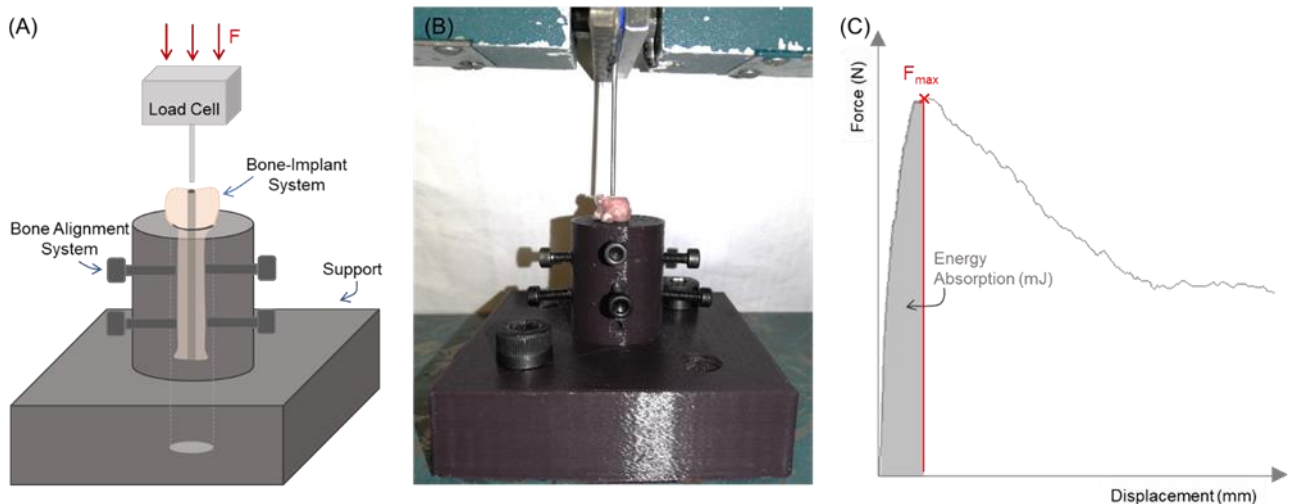
Figure 7.4 - Push-out assay. (A) schematic representation and (B) real image of push-out setup and (C) Load–displacement curve (grey area represents energy absorption).

As previously stated, immediately after removing samples from the animal (implant + femur), part of the samples from the same group were subjected to push-out characterization. Implant push-out test was conducted in order to assess the osseointegration of the implants, i.e., the bonding between the implant and the surrounding bone tissue. In this sense, to perform push-out tests, it was necessary to carefully cut the femur to expose both surfaces of the implant. Afterwards, the implant was pushed using a custom-made apparatus, schematically represented in Figure 7.4(A), in which the bone is placed inside the support, as represented, and the alignment of the implant along the vertical axis of the crosshead device was assured by a screw system placed around the support. It is important to highlight that this custom-made system will avoid any motion in X and Y axis while the load is being applied. This apparatus was fixed to the testing machine and a special metallic nail was fixed to the crosshead device with a diameter smaller than that of implant. Figure 7.4(B) displays real image of the final apparatus, ready for the test. Each sample was loaded at constant crosshead speed of 5 mm min^{-1} using a universal testing machine (Hounsfield, H100KS). The applied load was recorded constantly using a load cell with a range of 2.5 kN. The load and displacement data were recorded, and force-displacement curve was obtained using QMAT 3.51 software. From these curves, the maximum push-out force (F_{max}) and energy absorption (E_a) were obtained. The energy absorption during push-out tests was calculated as the integral of force-displacement curve from 0 up to the displacement corresponding to the maximum force. Figure 7.4(C) exhibits the maximum push-out force (F_{max}) and the area used to determine energy absorption during the test (E_a). Statistical analysis was performed by using mixed-

167

ANOVA analysis with differences between groups compared with the post hoc Bonferroni test to assess the statistically significant differences on push-out force and energy absorption results between all the produced specimens under study. Statistical significance was defined for $p < 0.05$ (95% confidence value).

7.2.4. Surface Characterization

The surface of the produced implants, before *in vivo* experiments and after push-out tests, were characterized by Scanning Electron Microscopy (SEM). After push-out tests, the 4 weeks timepoint and 12 weeks timepoint implants of each group and the respective bones cavities were analyzed by SEM. To observe the bone cavities where implants were inserted, after push-out testing, it was necessary to cut all the bones to expose the cross-section. Afterwards, it is important to highlight that, for SEM analysis, the bones and implants were dehydrated through a sequence of solutions with increasing alcohol concentrations (30%, 50%, 70%, 90% and 100%), remaining in each solution for half an hour, and then, dried in vacuum. Energy Dispersive X-ray spectroscopy (EDX) analysis was also carried out, to assess chemical composition.

7.2.5. Histology Evaluation

For histological characterization, immediately after harvest, the samples were fixed in 10% formaldehyde solution for tissue preservation. Afterwards, fixed samples were cleaned with water to remove all the residues from the fixed solution and then dehydrated in a series of alcohol concentrations (60%, 80%, 96%, 100% and 100%, for 3 days each). Subsequently, Technovit 7200 VLC® solutions were used to defat the samples, using a sequence of 70/30, 50/50, 30/70, 0/100 and 0/100 % alcohol/Technovit 7200 VLC® concentrations also for 3 days each and polymerization occurred (Exakt® 520 Light polymerization unit, Germany). The cutting of the samples was processed with the Exakt Cutting apparatus (Exakt Band System 300 CL/CP, Germany) along the longitudinal axis, according to Figure 7.5 schematic. The samples were then polished (with SiC papers of 1000, 1200, 2500 and 4000 FP) till displaying a thickness around ≈100 μm and, finally, stained with toluidine blue.
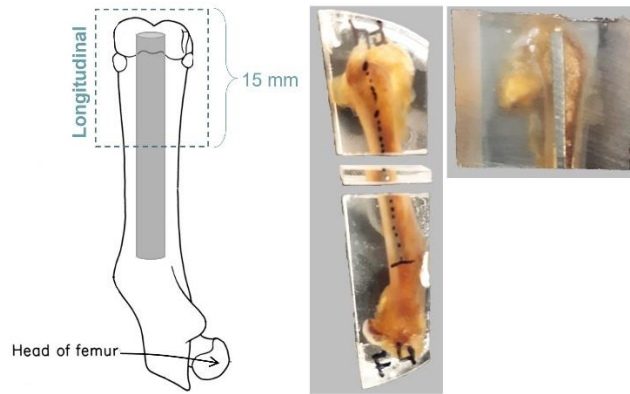
Figure 7.5 - Schematic representation of the cuts made for histological characterization.

7.3. Results and discussion

In this study, three types of NiTi implants were studied and characterized in terms of biomechanical and biological characterization. Implant osseointegration is highly dependent on either primary stability (mechanical anchoring) and secondary stability (biological response). This study targets on primary stability by creating textured implants (G2 and G3) to improve the so-called mechanical anchoring at the early stages of the implantation and consequently, enhance secondary stability. In this sense, NiTi non-textured implants were used as control groups (G1). Figure 7.6 shows SEM micrographs of the final G2 and G3 implants and their respective dimensions.

G2	Mean ± SD
a (μm)	398.05 ± 5.14
b (μm)	183.44 ± 5.97
c (μm)	248.66 ± 39.50

G3	Mean ± SD
a (μm)	397.17 ± 4.70
b (μm)	479.64 ± 10.13
c (μm)	236.00 ± 26.87
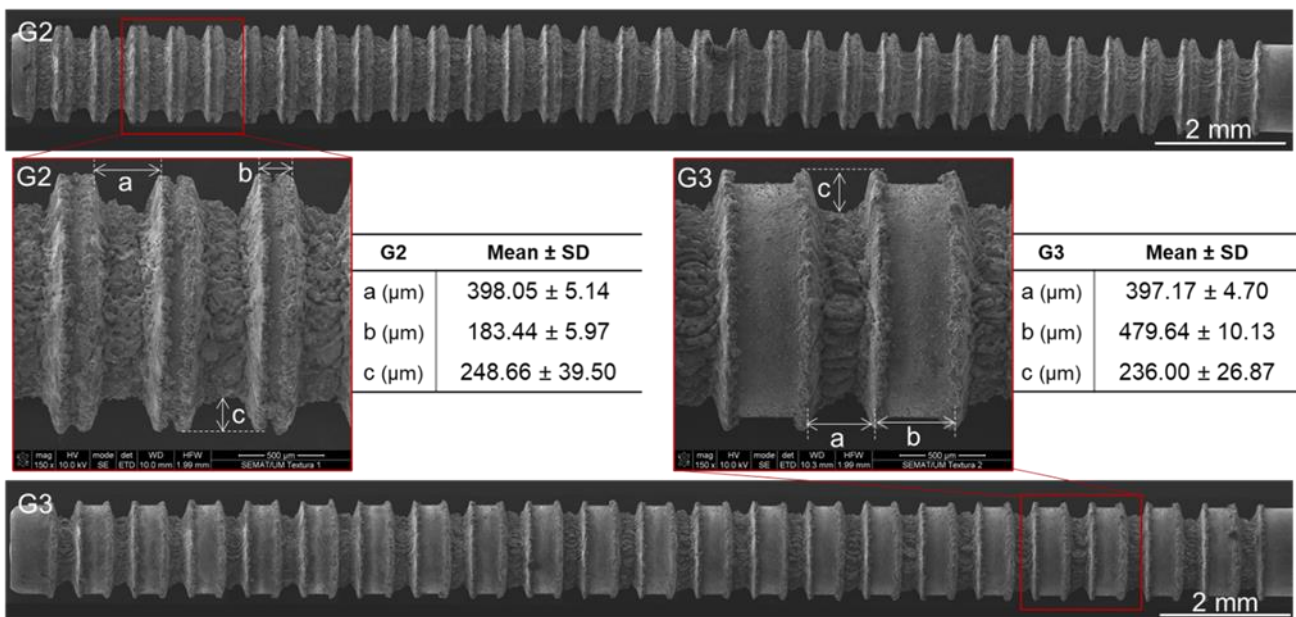
Figure 7.6 - SEM micrographs of G2 and G3 laser textured implants before *in vivo* implantation and respective obtained dimensions in μm (a=groove width, b=wall thickness and c=depth).

When analyzing Figure 7.6, it can be concluded that the adopted laser technology is a versatile and efficient approach to create a texture along the implant with high degree of reproducibility. By comparing G1 (Figure 7.1) with G2 and G3 it can be observed that the surface topography is drastically different in these structures, once the surface area in contact with body environment is significantly higher, which may be an asset in terms of bone growth and mineralization. G2 and G3 were designed to have similar groove width and depth and different wall thickness, once G3 has a higher distance between grooves, having, therefore, lower surface area, when compared to G2.

The aim of this study is to create solutions for orthopedic hip implant replacement, focusing on surface modifications. In this context, it is important to evaluate these NiTi implants performances in relevant models. Thus, these three groups were implanted in the femur of Sprague Dawley rats for 4 and 12 weeks. It is important to mention that, in humans, the majority of patients that undergo implant surgery are adults, and this needs to be taking into consideration when choosing the age of the animal for the *in vivo* experimental model. Roach et al. [31] studied the growth plates of femurs and tibiae in different aged-rats and concluded that, until 5 weeks of age, rats are young and in a period of rapid growing, and the height of the growth plate was the highest whereas at 8-16 weeks-old rats, this height decreased (period where growth is slowing down and the animal is in adulthood). In this regard, for the present study, 16-18 weeks-old rats were used. Moreover, to replicate the implantation process, NiTi implants were press-fitted into the medullary cavity of rats' femur being then positioned in the epiphysis and diaphysis regions, although the focus of this analysis is on the epiphysis region, where there is the highest osseointegration for an effective load transfer. From the authors' point of view, this orientation of implantation along the longitudinal axis of the femur is important once most studies in literature that carry out similar *in vivo* implantations usually insert their solutions in a transversal orientation to that of the femur, which is not correlated with clinical functional setting.

Being rats a smaller animal species, it has an advantage over larger ones of being fast healers, which will significantly reduce the time of the study [32,33]. In fact, Wancket et. al [32] stated that, a large tibial defect in rats can be repaired, fully, within 12 weeks while, in humans, this phenomenon normally takes from 32 up to 52 weeks. In the present study, 4 and 12 weeks of implantation were used as an early stage of bone formation up to its theorical fully reconstitution, respectively. Also, these timepoints were already vastly explored in literature for this animal model in similar studies [33–37].

The animals had no postoperative complications, and none indicated signs of inflammation or infection. Their recovery was quick, and it is important to highlight that they were not deprived of any movement.

As shown in Figure 7.7, that displays radiographic images of the three groups after 4 and 12 weeks of implantation, in all groups, implants seem to integrate satisfactorily with the bone, and none displayed signs of bone callus formation. A radiographic visual inspection may indicate that G1 has lower bone integration, when compared with the other groups, since empty spaces (darker translucent areas) between the implant and the bone are more easily observed.
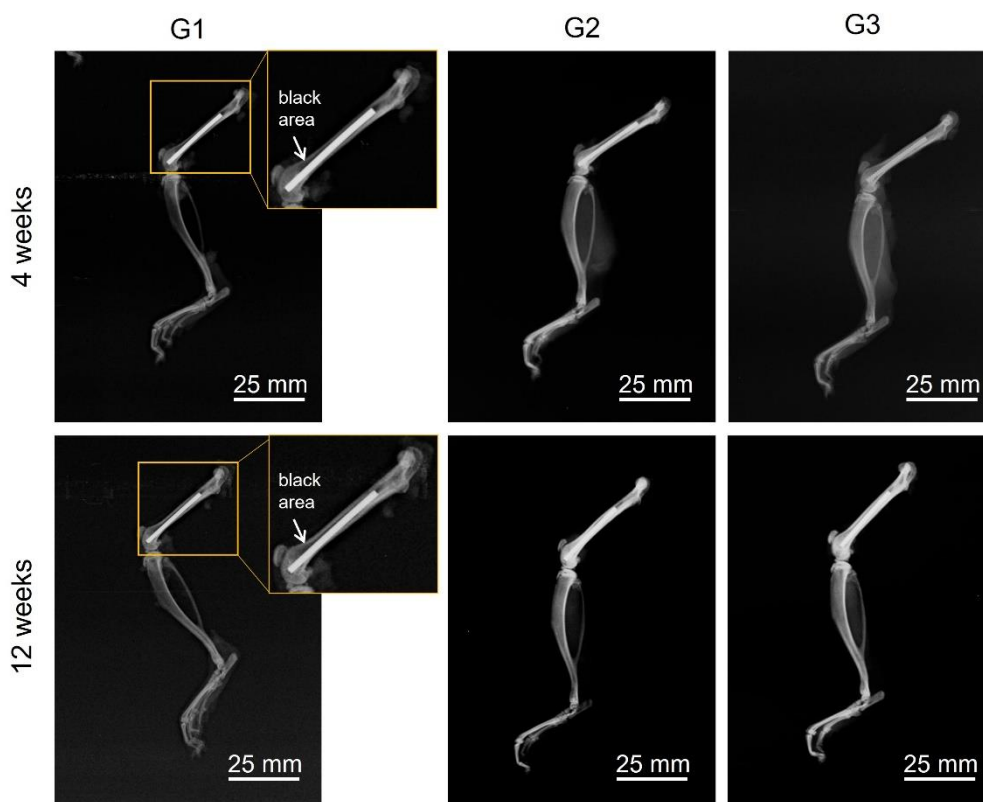
Figure 7.7 - Radiographic images of the leg of Sprague Dawley rats after the implantation times (4 and 12 weeks) with NiTi implants (G1, G2 and G3).

Besides histological analysis, mechanical characterization is also extremely important to assess the performance of the produced implants in terms of osseointegration [38]. In one hand histology provides information regarding different tissues present at the interface implant-bone while mechanical characterization (more precisely, push-out tests) allows to assess the bone-implant fixation. In this regard, maximum push-out force for all the groups, after 4 and 12 weeks of implantation time, are depicted in Figure 7.8. The amount of energy that the interface implant-bone can absorb before failure was also determined and results are presented in Table 7.1.
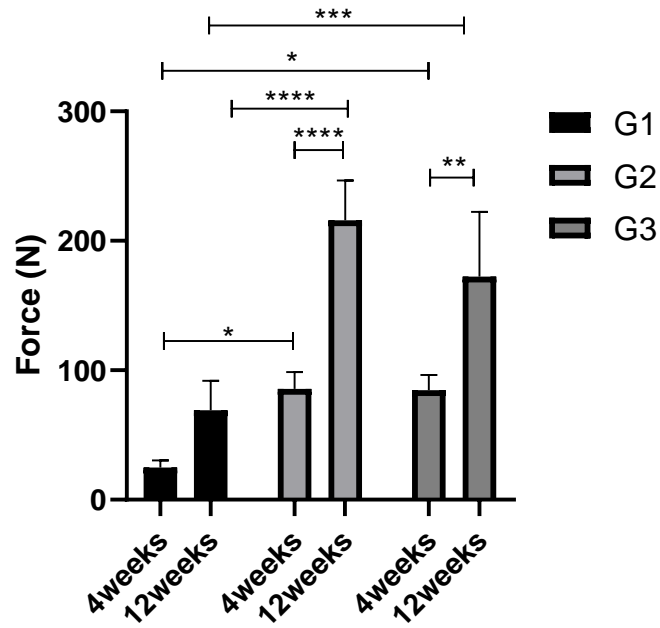
Figure 7.8 - Push-out results regarding maximum force for the different groups, at each timepoint. Values shown as mean ± SD. *-p < 0.05; **- p < 0.01; *** - p < 0.001; **** - p < 0.0001.
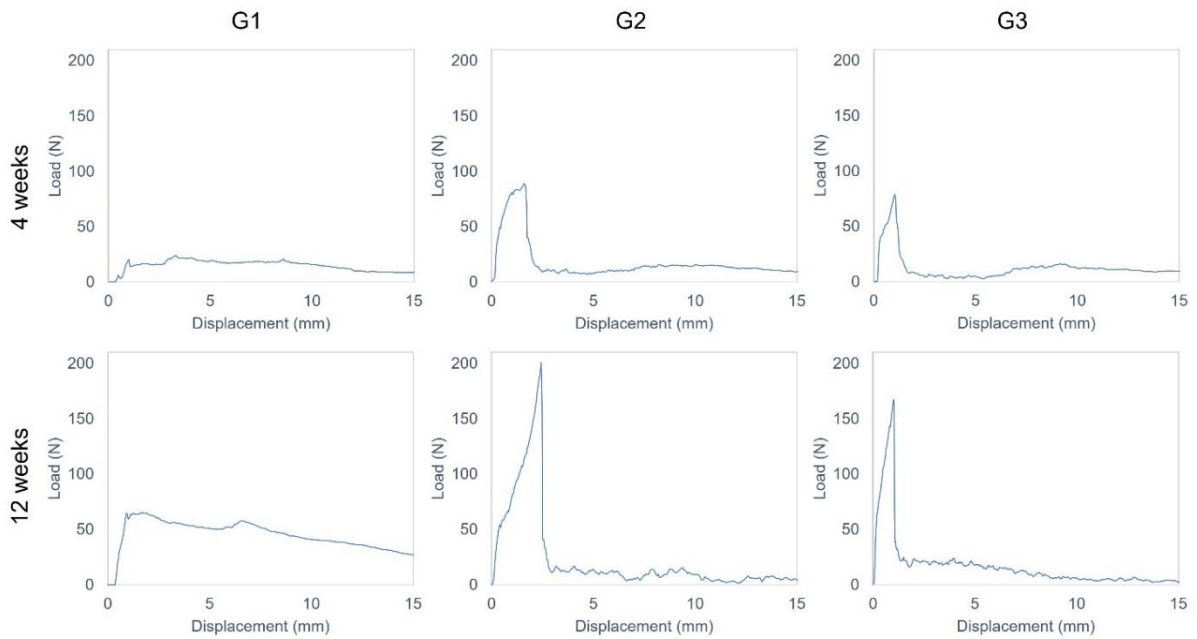
Figure 7.9 - Typical load-displacement curves for all groups and timepoints.

Table 7.1 - Energy absorption to failure (E_a) for the different groups at each timepoint.

Group	Timepoint (weeks)	E_a (mean ± SD), mJ
G1	4	70.37 ± 33.95
	12	63.64 ± 13.33
G2	4	78.15 ± 27.24
	12	158.57 ± 48.88
G3	4	60.37 ± 21.88
	12	109.67 ± 17.89

As shown in Figure 7.8, it is possible to observe a clear increase in push-out maximum force from 4 to 12 weeks of implantation time for all groups. G1, G2 and G3 have a percentual increase of 178%, 152% and 104%, respectively, from 4 to 12 weeks, indicating that bone osseointegration increase with time, as expected. In a statistical point of view, between 4 and 12 weeks, there were statistically significant differences for G2 and G3 groups. These values are in accordance with the ones found in energy absorption results, in which higher energy was found at 12 weeks of implantation. This result was not observed for the G1 group, however, since the standard deviation for this group is quite high, this may be the reason for such conclusion. Statistically, regarding energy absorption results, G2 was the one that displayed statistically differences comparing the implantation timepoints (p=0.0253). Moreover, when analyzing the load-displacement curves displayed in Figure 7.9, it is possible to observe that at 4 weeks of implantation the push-out force required for implant extraction is considerably low when compared with the longest timepoint, especially for G2 and G3 group. When observing the behavior of the curves, it is visible that, despite G2 and G3 group are characterized by a peak followed by an instant drop, conversely to G1 that seems to sustain the load for a longer period, the load is significantly higher, in both implantation timepoints, which will be further translated in higher energy necessary for implant extraction, as shown in Table 7.1. It is worth mentioning that, when evaluating implant push-out behavior, the maximum push-out force is not the only aspect that needs to be addressed, but also the energy that the implant can sustain before its failure [37].

In the present study, the highest value both for maximum force and energy absorption was found for G2 group, for both timepoints. In fact, surface area may be a reason for this outcome. G1 group, being a non-textured implant, has a surface area of around 109.96 mm^2. Taking into consideration the measurements of Figure 7.6, surface areas for G2 and G3 group, analytically determined, were approximately 148.83 mm^2 and 134.97 mm^2, respectively. In this regard, it can be concluded that G2 has the highest surface area in contact with the surrounding tissue, when

compared with the other groups, meaning that, possibly, there is a stronger bonding between implant and bone. In this sense, the higher surface area found for G2 may justify the higher average push-out force and energy values, as can be observed in Table 7.1 and load-displacement curves present Figure 7.9.

Comparing G2 and G3 with G1 group, it can be concluded that, both timepoints have a drastically increase in maximum force results. After 4 weeks of implantation, the percentual increase of maximum push-out force for G2 and G3 groups was 245% and 241% compared to G1, respectively, while at 12 weeks this increase for G2 was 212% and for G3 was 149%, being statistically significant for both timepoints when compared with G1. Among groups, G2, at 12 weeks of implantation, was also the one in energy absorption results that displayed statistically significant differences when compared with G1 (p=0.0029). This behavior is aligned with what was found in the literature where Liu et al, [29] studied the interfacial bonding strength of titanium implants (porous NiTi, porous Ti, dense NiTi and dense Ti) implanted, for 15 weeks, in the femur/tibia of rabbits, and concluded that the highest bonding strength was found for porous materials. At 15 weeks of implantation, they reported a maximum push-out force of 41 and 357 N for dense and porous NiTi, respectively.

Studies in literature regarding biomechanical behavior of NiTi implants are scarce, however several studies report that surface roughness plays a crucial role at cartilage and bone tissue anchoring in implants [39–41], in which a smoother surface enhances fibroblast and epithelial cell adhesion, while a rougher surface promote osteoblastic proliferation [41].

As already mentioned, primary stability highly depends on implant design, that, consequently, is also related with the mechanical properties of the surrounding bone tissue. This means that higher mechanical anchorage is found for cortical bone, when compared with trabecular bone [39]. To ensure this bonding between the implant and bone, it is not only important to guarantee a bone-implant fixation, but also a minimal implant micro-motion once it is this mobility that enhances fibrous tissue formation and therefore hinder osseointegration [39]. In this sense, for a long-term clinical success of an implant, bone quality is one of the main factors to take in consideration, because bone changes in terms of mechanical properties [39]. For this reason, histological analysis is fundamental to assess the type of tissues formed after implantation in order to understand bone formation dynamics, the quality of the new formed bone and correlate these aspects with the design and surface of an implant.

Histological sections of the implants and bone tissues can be seen in Figure 7.10. An initial analysis allowed to conclude that, for both timepoints, no inflammatory or adverse responses were detected at the interfaces. As shown in Figure 7.10, either for 4 or 12 weeks, all the tested groups displayed a good bonding with bone growth towards the implant suggesting that the implantation process did not bring any cytotoxic effect.

At 4 weeks of implantation, despite G1 displayed an extensive involvement of new bone formed around the implant, the areas of direct contact are focused on immature bone interposed with areas with highly vascularized connective tissue. Moreover, it can also be observed that this bone anchorage occurs mainly in the epiphysis and metaphysis region, when compared with diaphysis area where bone apposition is composed of a thin layer of immature woven bone. On the contrary, G2 group exhibit a vast bone proliferation in the grooves, especially in the epiphysis region, in which these bone invaginations assume a direct contact with the implant surface. Similarly, G3 group had an extensive osteointegration in the epiphysis, with higher proliferation inside the grooves, displaying an early stage of bone maturation.

After 12 weeks of implantation, it is possible to observe a higher osseointegration on G1 group, with areas having direct contact with implant surface, in which the lacunar areas of connective tissue that were observed in the earliest timepoint are now filled with new bone, thus creating a continuous layer of mineralized tissue around the implant (even in the diaphysis region). When observing the histological slides for G2 and G3 group, at 12 weeks of implantation, an increment in the maturation process of new bone was observed, particularly inside the grooves. The mineralized tissue formed has a more organized architecture, having characteristics similar to lamellar bone. Moreover, bridging can also be observed between the bone that is deposited directly on the implant surface and the internal cortical of epiphysis area and even in the medullary cavity at diaphysis area.

In this sense, a demarcation can be distinguished between the original cortical bone and the newly formed bone (the latter it is marked by an intense purple color). This demarcation can be clearly seen at 4 weeks of implantation, since at this timepoint, the bone is characterized mainly by immature woven bone. This type of immature bone, is typically constituted by collagen fibers that are dispersed in a random orientation, being further remodeled into a mature bone with a more lamellar configuration where the collagen fibers are parallelly oriented [39]. This type of mature bone can be more visible at 12 weeks of implantation, as expected. Furthermore, when observing the textured groups, G2 and G3, it is possible to observe that bone tissues grow also into

the laser-created grooves. When correlating these observations with the push-out tests results, the increased surface area of these textured implants and the bone growth into these grooves was found to enhance implant stability, once higher push-out maximum forces were measured for these groups.
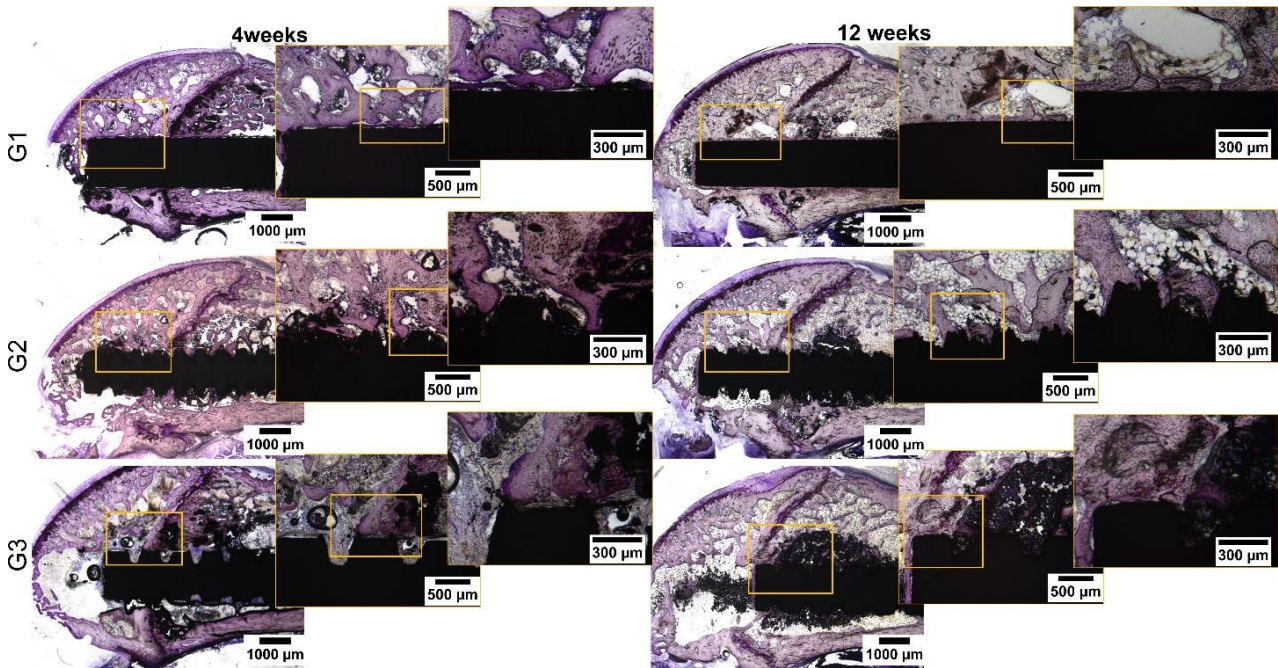
Figure 7.10 - Histological sections of the implants and bone tissues after 4 and 12 weeks of implantation.

After push-out tests, SEM and EDS analysis were performed in all of the extracted implants and bone cavities. EDS results are depicted in Figure 7.11 for G1 group and Figure 7.13 for G2 and G3 groups, revealing the presence of calcium and phosphorus elements, characteristic of bone inorganic phase. This analysis allows to infer on the amount of bone adhered to the implant surface. As seen in Figure 7.11, it is clear that Ti and Ni elements (from the implant material) are clearly detected whilst, in Figure 7.13, the presence of elements associated to bone tissue (e.g. calcium and phosphorus) is clear, indicating higher amounts of bone tissue adhered to these textured implants. By analysing G1 implant and corresponding bone cavity SEM images (Figure 7.11 and Figure 7.12, respectively), a "clean" implant and a smooth bone surface indicate an incipient bone-implant bond, proving that the implantation time influences bone integration, which is in agreement of what was previously discussed regarding push-out results. At 12 weeks of implantation, it is visible that bone fracture surface is rougher, when compared to 4 weeks of implantation, which means that a better interfacial bonding is achieved at higher implantation timepoint. Accordingly,

the higher amount of bone adhered to the implant surface is found after 12 weeks implantation (see Figure 7.11).

Comparing the images of G2 and G3 (Figure 7.13) implants, with the ones of G1, a significantly higher amount of biological tissue adhered to their surface is found. Per se, this suggests that surface texturing has a positive effect on bone apposition. When regarding bone fracture surfaces in Figure 7.12, a smoother topography was found which shows that the bonding between the implant and bone is not as effective as in textured groups (G2 and G3) where, as shown in Figure 7.14, these surfaces are rougher and typical of bone fragile fracture.

Concerning the textured implants surfaces, Figure 7.13, it is also visible the effect of the implantation time, since greater amounts of bone deposited on the surface is observed after 12 weeks. At 4 weeks of implantation, it is still visible the original surface of the implant, while at 12 weeks, a higher amount of biological tissue covers the implant surface. This effect is more evident in G3 group where, even at 12 weeks, part of the surface of the implant it is still visible (corresponding to the smoother part of the original NiTi wire and not the groove). Moreover, this behavior is coincident with the textured implant that displayed lower energy absorption which means that the interfacial bond in this group is not as effective as on G2 group. This may indicate that the bone has a preference to adhere and grow in a rougher surface, as the one displayed inside the grooves. This phenomenon was already discussed, being proved that a rougher surface tends to enhance osteoblastic proliferation [5,24,41].

In conclusion, these implant and bone fracture surfaces suggest that, among all groups, G2 implant is the one that developed a more effective bond with the adjacent bone. This observation is aligned with the results found for mechanical tests in which G2 was the one that displayed the highest maximum push-out force and energy absorption in push-out experiments. Taking advantage of laser versatility, many other different textures with different dimensions and geometries may be produced and tested to enhance bone-implant adhesion, as these can influence cell proliferation and induce bone growth through localized deformations induce in the bone by the implant.
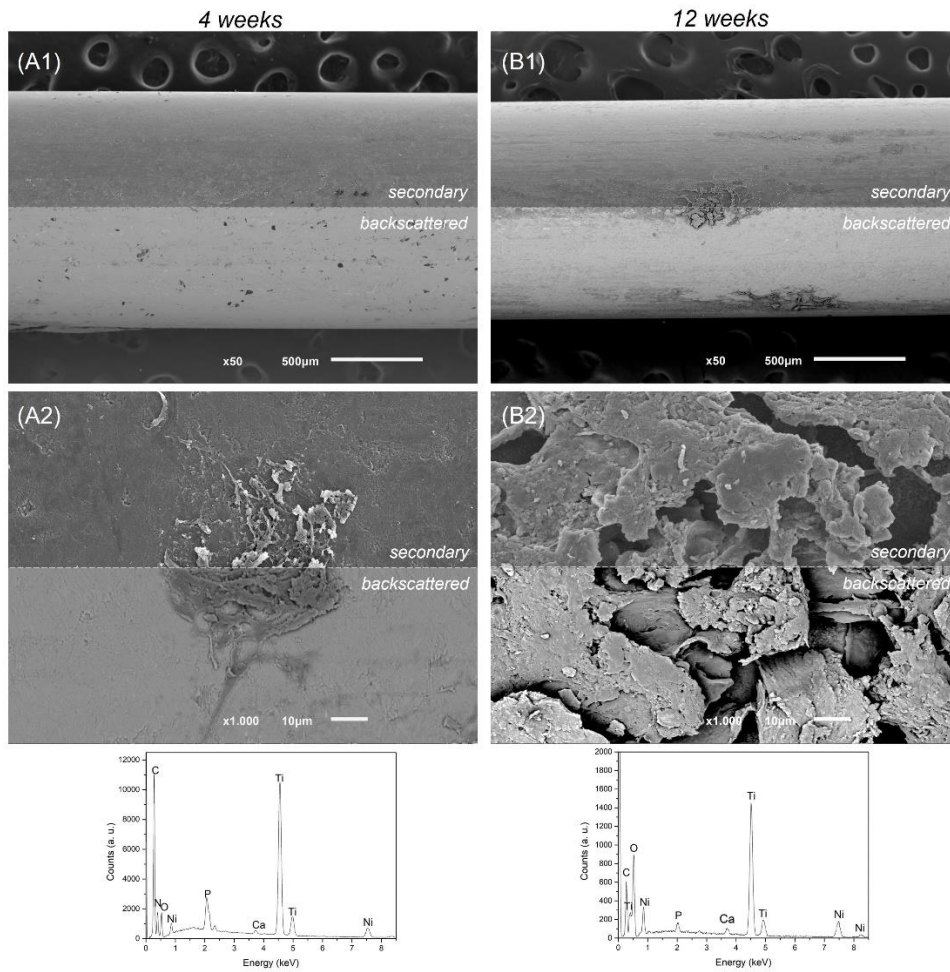
Figure 7.11 - SEM micrographs and EDS spectra of G1 specimens, after push-out tests, for (A) 4 weeks and (B) 12 weeks.
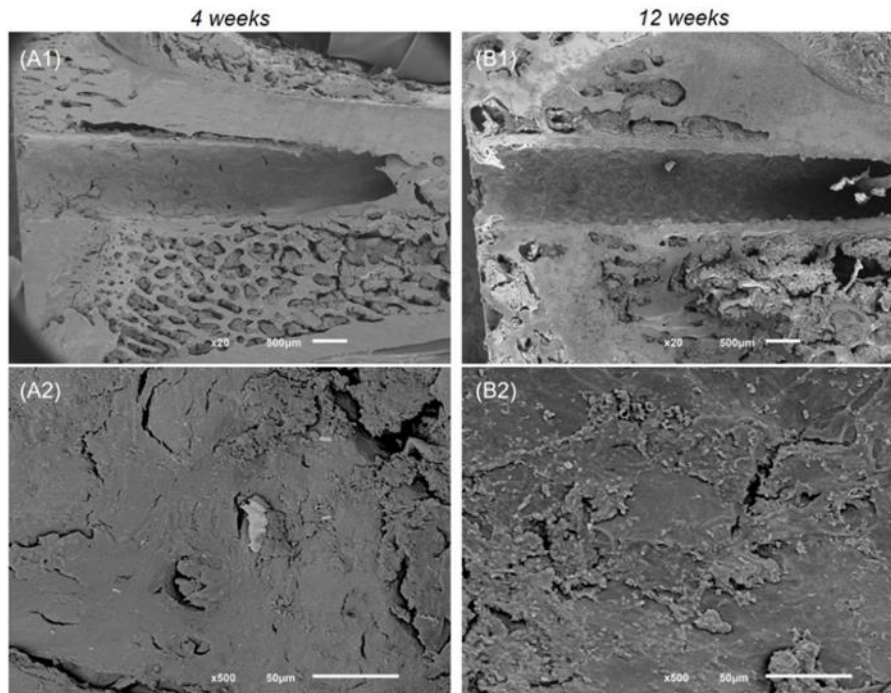
Figure 7.12 - SEM micrographs of bone cavity for G1, after push-out experiments, for (A) 4 weeks and (B) 12 weeks: number 1 corresponds to secondary mode and number 2 to back-scattered mode.
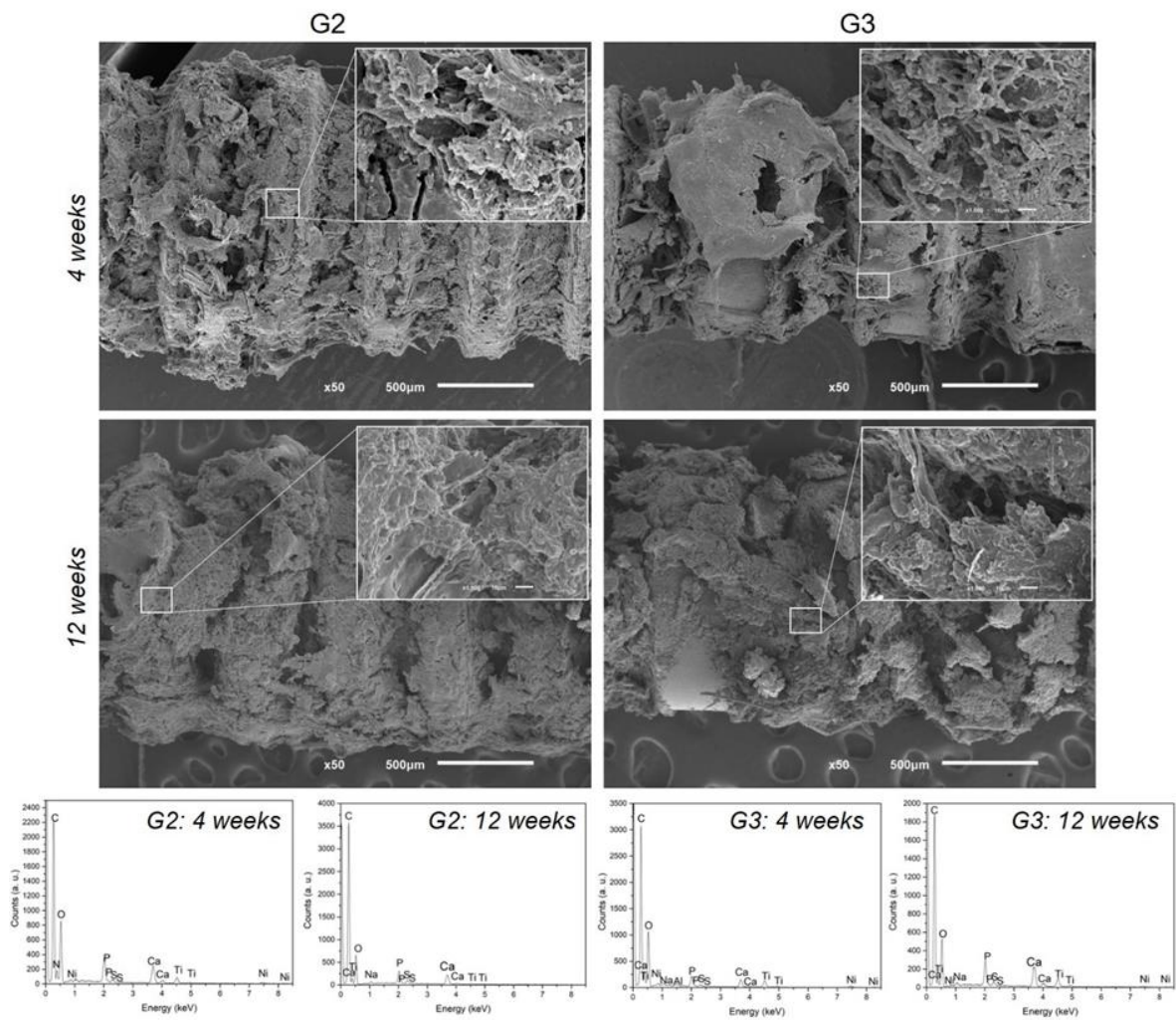
Figure 7.13 - SEM micrographs and EDS spectra of G2 and G3, after push-out tests, for 4 and 12 weeks.
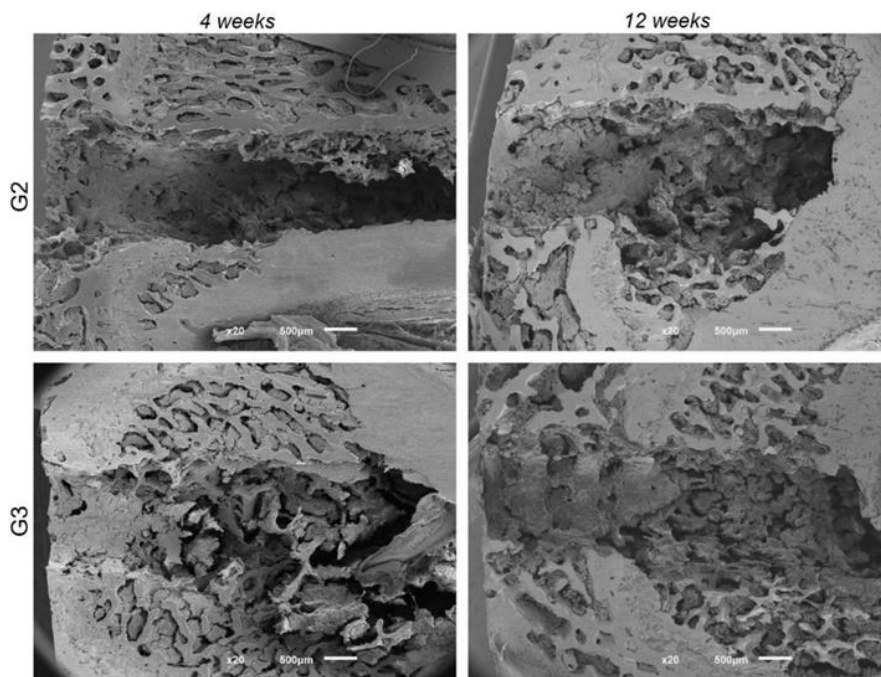
Figure 7.14 - SEM micrographs of bone cavity for G2 and G3, after push-out experiments, for the different timepoints: 4 and 12 weeks.

179

7.4. Conclusions

In the present work, two different implant designs (G2 and G3) were manufactured by using a laser surface texturing approach and implanted *in vivo*, being mechanical and biologically characterized, and compared with non-textured implants. Histological imaging proved that, 4 weeks of implantation, was not a sufficient implantation timepoint for a mature bone formation. After 4 weeks of implantation the maximum push-out force for G2 and G3 was 245% and 241% higher than that found for G1 (non-textured). At this early stage, no significant differences were found between the two groove-based designs (G2 and G3), however, at 12 weeks of implantation, G2 was found to display the highest extraction force, 212% higher than G1, against 149% for G3. Accordingly, G2 energy absorption was the highest, allowing to conclude that the bone-implant bonding in this group is considerably higher. To sum, both laser textured implants displayed higher maximum push-out force and energy, when compared with non-textured, being G2 group, that has the highest surface contact area, the one that showed the best results among all groups. These results prove that the studied laser textured implants are highly effective to enhance bone regeneration that will improve the bond between implant and the adjacent bone and, therefore, improve the longevity of orthopedic implants.

References

[1] C. Wedemeyer, H. Jablonski, A. Mumdzic-Zverotic, H. Fietzek, T. Mertens, G. Hilken, C. Krüger, A. Wissmann, H. Heep, R. Schlepper, M.D. Kauther, Materialia 6 (2019).

[2] M.M. Costa, R. Lima, F. Melo-Fonseca, F. Bartolomeu, N. Alves, A. Miranda, M. Gasik, F.S. Silva, N.A. Silva, G. Miranda, Materials Science and Engineering C 98 (2019) 705–716.

[3] M.J. Coathup, G.W. Blunn, N. Mirhosseini, K. Erskine, Z. Liu, D.R. Garrod, L. Li, Journal of Orthopaedic Research 35 (2017) 820–828.

[4] A. Marques, G. Miranda, D. Faria, P. Pinto, F. Silva, Ó. Carvalho, Journal of the Mechanical Behavior of Biomedical Materials 97 (2019) 375–384.

[5] J. Frostevarg, R. Olsson, J. Powell, A. Palmquist, R. Brånemark, Applied Surface Science 485 (2019) 158–169.

[6] F. Bartolomeu, M.M. Costa, J.R. Gomes, N. Alves, C.S. Abreu, F.S. Silva, G. Miranda, Tribology International 129 (2019) 272–282.

[7] F. Bartolomeu, J. Fonseca, N. Peixinho, N. Alves, M. Gasik, F.S. Silva, G. Miranda, Journal of the Mechanical Behavior of Biomedical Materials 99 (2019) 104–117.

[8] D. Faria, C.S. Abreu, M. Buciumeanu, N. Dourado, O. Carvalho, F.S. Silva, G. Miranda, Journal of Biomedical Materials Research - Part B Applied Biomaterials 106 (2018) 1534–1545.

[9] J.W. Mwangi, L.T. Nguyen, V.D. Bui, T. Berger, H. Zeidler, A. Schubert, Journal of Manufacturing Processes 38 (2019) 355–369.

[10] Q. Chen, G.A. Thouas, Materials Science and Engineering R: Reports 87 (2015) 1–57.

[11] J. Sevcikova, M. Pavkova Goldbergova, Biometals 30 (2017) 163–169.

[12] C.W. Müller, R. Pfeifer, T. El-Kashef, C. Hurschler, D. Herzog, M. Oszwald, C. Haasper, C. Krettek, T. Gösling, Journal of Orthopaedic Research 28 (2010) 1671–1676.

[13] V. Muhonen, S. Kujala, A. Vuotikka, V. Ääritalo, T. Peltola, S. Areva, T. Närhi, J. Tuukkanen, Acta Biomaterialia 5 (2009) 785–793.

[14] C.H. Hung, F.Y. Chang, T.L. Chang, Y.T. Chang, K.W. Huang, P.C. Liang, Optics and Lasers in Engineering 66 (2015) 34–40.

[15] M. Mehrpouya, A. Gisario, A. Brotzu, S. Natali, Optics and Laser Technology 108 (2018) 142–149.

[16] E. Rupérez, J.M. Manero, L.A. Bravo-González, E. Espinar, F.J. Gil, Materials 9 (2016).

[17] F. Mangano, L. Chambrone, R. Van Noort, C. Miller, P. Hatton, C. Mangano, International Journal of Biomaterials 2014 (2014).

[18] C.G. Moura, O. Carvalho, L.M.V. Gonçalves, M.F. Cerqueira, R. Nascimento, F. Silva, Materials Science and Engineering C 104 (2019) 109901.

[19] L. Tiainen, P. Abreu, M. Buciumeanu, F. Silva, M. Gasik, R. Serna Guerrero, O. Carvalho, Journal of the Mechanical Behavior of Biomedical Materials 98 (2019) 26–39.

[20] S. Li, Z. Cui, W. Zhang, Y. Li, L. Li, D. Gong, Materials Letters 255 (2019) 126591.

[21] N. Mirhosseini, P.L. Crouse, M.J.J. Schmidth, L. Li, D. Garrod, Applied Surface Science 253 (2007) 7738–7743.

[22] J. Li, H. Liao, B. Fartash, L. Hermansson, T. Johnsson, Biomaterials 18 (1997) 691–696.

[23] S. Çelen, C. Efeoğlu, H. Özden, Physics Procedia 12 (2011) 245–251.

[24] S. Mukherjee, S. Dhara, P. Saha, International Journal of Advanced Manufacturing Technology 76 (2015) 5–15.

[25] M. Hirao, K. Sugamoto, N. Tamai, K. Oka, H. Yoshikawa, Y. Mori, T. Sasaki, Journal of Biomedical Materials Research - Part A 73 (2005) 213–222.

[26] K.W.K. Yeung, R.Y.L. Chan, K.O. Lam, S.L. Wu, X.M. Liu, C.Y. Chung, P.K. Chu, W.W. Lu, D. Chan, K.D.K. Luk, K.M.C. Cheung, Surface and Coatings Technology 202 (2007) 1247–1251.

[27] K.W.K. Yeung, Y.L. Chan, K.O. Lam, X.M. Liu, S.L. Wu, X.Y. Liu, C.Y. Chung, W.W. Lu, D. Chan, K.D.K. Luk, P.K. Chu, K.M.C. Cheung, Materials Science and Engineering C 28 (2008) 454–459.

[28] C.H. Ng, N. Rao, W.C. Law, G. Xu, T.L. Cheung, F.T. Cheng, X. Wang, H.C. Man, Surface and Coatings Technology 309 (2017) 59–66.

[29] X. Liu, S. Wu, K.W.K. Yeung, Y.L. Chan, T. Hu, Z. Xu, X. Liu, J.C.Y. Chung, K.M.C. Cheung, P.K. Chu, Biomaterials 32 (2011) 330–338.

[30] C.W. Chan, I. Hussain, D.G. Waugh, J. Lawrence, H.C. Man, Materials Science and Engineering C 42 (2014) 254–263.

[31] H.I. Roach, G. Mehta, R.O.C. Oreffo, N.M.P. Clarke, C. Cooper, Journal of Histochemistry and Cytochemistry 51 (2003) 373–383.

[32] L.M. Wancket, Veterinary Pathology 52 (2015) 842–850.

[33] E.A. Horner, J. Kirkham, D. Wood, S. Curran, M. Smith, B. Thomson, X.B. Yang, Tissue Engineering: Part B 16 (2010) 263–271.

[34] J. Irish, A.S. Virdi, K. Sena, M.A. McNulty, D.R. Sumner, Journal of Orthopaedic Research 31 (2013) 800–806.

[35] C. Castellani, R.A. Lindtner, P. Hausbrandt, E. Tschegg, S.E. Stanzl-Tschegg, G. Zanoni, S. Beck, A.M. Weinberg, Acta Biomaterialia 7 (2011) 432–440.

[36] S. Bose, D. Banerjee, A. Shivaram, S. Tarafder, A. Bandyopadhyay, Materials and Design 151 (2018) 102–112.

[37] E.K. Tschegg, R.A. Lindtner, V. Doblhoff-Dier, S.E. Stanzl-Tschegg, G. Holzlechner, C. Castellani, T. Imwinkelried, A. Weinberg, Journal of the Mechanical Behavior of Biomedical Materials 4 (2011) 766–775.

[38] X. Lin, S. Yang, K. Lai, H. Yang, T.J. Webster, L. Yang, Nanomedicine: Nanotechnology, Biology, and Medicine 13 (2017) 123–142.

[39] F. Marco, F. Milena, G. Gianluca, O. Vittoria, Micron 36 (2005) 630–644.

[40] M. Meischel, J. Eichler, E. Martinelli, U. Karr, J. Weigel, G. Schmöller, E.K. Tschegg, S. Fischerauer, A.M. Weinberg, S.E. Stanzl-Tschegg, Journal of the Mechanical Behavior of Biomedical Materials 53 (2016) 104–118.

[41] L. Salou, A. Hoornaert, G. Louarn, P. Layrolle, Acta Biomaterialia 11 (2015) 494–502.

CHAPTER 8

Osseointegration Assessment of Multi-Material Ti6Al4V-βTCP Implants: An Experimental Study in Rats

M.M. Costa[a], A. Miranda[b,c], F. Bartolomeu[a], O. Carvalho[a], S. Matos[d], F.S. Silva[a], G. Miranda[e]

[a]Center for MicroElectroMechanical Systems (CMEMS-UMinho), University of Minho, Campus de Azurém, 4800-058 Guimarães – Portugal

[b]Life and Health Sciences Research Institute (ICVS), School of Medicine, University of Minho, Campus de Gualtar, 4710-057 Braga, Portugal;

[c]ICVS/3B's - PT Government Associate Laboratory, 4710-057 Braga/Guimarães, Portugal

[d]Center for Innovation and Research in Oral Sciences (CIROS), Faculty of Medicine, University of Coimbra, FMUC, 3000-075 Coimbra, Portugal

[e]CICECO, Aveiro Institute of Materials, Department of Materials and Ceramic Engineering, University of Aveiro, 3810-193 Aveiro, Portugal

Abstract

In the present study, mono- and multi-material laser textured Ti6Al4V implants were manufactured and characterized in vivo to explore their applicability in orthopedic implants. Laser surface texturing is used for manufacturing grooved Ti6Al4V implants while a pressure-assisted sintering technique is employed to impregnate beta-tricalcium phosphate (βTCP) into grooves for an improved bioactivity. After implantation into Sprague Dawley rat's femur for 4 and 12 weeks, bone-implant fixation and osseointegration are assessed, by performing push-out tests and histological characterization. Histological characterization showed bone formation around all implants, characterized by immature bone at 4 weeks of implantation and a more mature bone after 12 weeks. The maximum push-out forces are higher for the textured and multi-material solution, when compared to non-textured implants right after 4 weeks of implantation (p<0.05). After 12 weeks, multi-material implant displayed higher fracture energy when compared to non-textured implants (p<0.05).

Results revealed that laser surface texturing and bioactive multi-material solutions are highly effective to promote bone regeneration and enhance bone-implant fixation for further application in orthopedic implants.

Keywords: in vivo, laser surface texturing, multi-material, osseointegration, Ti6Al4V-βTCP

8.1. Introduction

Bone tissue, despite being a self-regenerating tissue, when diseased due to joint pathologies or trauma, can lead to irreversible defects that compromise its overall biomechanical function and bring to the patient severe pain, loss of mobility and disabilities.[1–3] In these cases, to overcome these side effects, patients resort to total joint arthroplasties.[1,4] Statistical data report that every year, more than 1.4 million people worldwide are subject to total hip replacement, and this number tend to increase with time.[5,6]

Ti6Al4V is the most widely used hip implant material due to its outstanding properties, as high corrosion resistance, strength and biocompatibility.[7–11] Ti6Al4V implants, after implantation, will react with the adjacent bone tissue, that is, the blood interactions with the implant will activate clotting factors that, in turn, lead to a clot formation.[7,12,13] Consequently, osteogenic cells will migrate, differentiate, and start the healing process, which is fundamental to achieve bone growth

and osseointegration, presently described as a direct contact between the living bone and implant.[7,13,14]

In cases of trauma, injury, or in this case, prosthesis implantation, the maintenance of bone homeostasis and its functionality restoration is made by the immune system, being up to 20% of immune cells present in bone (like macrophages). As mentioned, bone healing is initiated by a blood clot and an invasion of immune cells. Among cells, macrophages will have an important role in recruitment of bone forming cells. It is important to mention that these macrophages will undergo polarization in an anti- or pro-inflammatory phenotype that will indicate if they help on active regeneration or inflammation, respectively.[15] In this sense, macrophages will interact with bone cells and this interplay is important for bone formation and repair.[16] The immune cells will secrete signaling substances that attract mesenchymal stem cells and ultimately their differentiation to control the osteogenic process. Additionally, osteoblasts mineralization for further bone osteogenesis is also a part of the regulatory role of the immune system.[15] It is already published that, in implantology, depending on the used biomaterial, these immune reactions will determine if they act towards osteogenesis or reject the material.[15]

In fact, although the clinical success of total hip arthroplasties in terms of function and mobility restoration, the long-term success of implants is compromised by the loss of fixation between implant and bone. This will lead to mechanical loosening of the implant and, consequently, to the need to perform revision surgeries.[12]

To promote an interaction with bone with the immune system, and assure implant osseointegration for implant longevity to be achieved, topography, and chemistry modification are extremely attractive.[9,15,17]

Many studies have stated that bone-to-implant contact and osseointegration significantly increase on modified-implant surfaces.[4,18] In fact, it was already reported that rough surfaces enhance osteoblast differentiation, adhesion, and proliferation when compared with smooth ones.[1,7,13] This means that rough surfaces enhance bone matrix deposition and therefore a faster osseointegration.[19] Many techniques have been used for surface modification (e.g. anodic oxidation, grit blasting, sand blasting, acid etching, applying coatings, etc[5,8,20]) however, the obtained surface topography is totally random and uncontrolled, and, in some cases, the used technique can bring some contaminations to the material surface.[10,17,20]

In this sense, laser surface texturing has been widely used for surface modification of biomaterials. The unique features of lasers allow to perform surface modification with high degree

of complexity and precision and without surface contamination, making it an outstanding substitute to conventional methods.[10,11,21] Laser texturing process begins with the application, using laser, of a high energy density on the surface to promote material ablation that in turn, create a texture with a predefined design.[11,17] Several studies state that cell behavior is enhanced in laser textured surfaces and, cell spreading, and adhesion can vary depending on the texture feature (holes, pits, grooves, etc).[8,21–23] An in vitro study performed by Lee et al.,[24] used femtosecond laser to induce sub-micron periodic structures (300, 620, and 760 nm) on titanium, that were then tested in vitro and compared with unmodified control specimens. Although cell metabolism was found similar in laser-modified surfaces and control group, alkaline phosphatase on the former was remarkably increased with cell displaying a more elongated shape with a perpendicular alignment in these surfaces. Among texture features, the most common textures are grooves, being reported that, in these features, cells not only align and adhere to the groove but also have the tendency to spread.[25] In fact, Luu et al.[26] indicated that the performed surface grooves drove macrophages to an anti-inflammatory response, in a pro-healing phenotype, as described previously in this manuscript.

Moreover, there are studies in literature reporting the impact of laser modification on the mechanical anchorage of titanium implants. Palmquist et al.[27] assessed bone-bonding on partly laser-modified implants and compared with machined screw implants. Briefly, laser modification was performed on the thread's valleys of the machined screw implants. These implants were then implanted in rabbits for 6 months, revealing an increased removal torque in laser-modified when compared with machined implants. Similarly, in a different paper,[28] Palmquist and his co-workers obtained a similar outcome in laser-modified implants, having higher removal torque after 8 weeks of implantation in a rabbit model. Besides, it was also found that the fracture during torsion tests, on the laser-modified implants, happened in the bone and not at implant-bone interface. Comparable results are found in Brånemark and Shah studies.[29,30] Cho et al.[31] also evaluated the differences between laser-treated and machined titanium screw implant in an 8-week in vivo experiment and achieved a higher removal torque for the laser-treated group. Using a different approach, Omar et al.[32] produced titanium threaded implants, machined and anodically oxidized, implanted in Sprague Dawley rats for 6, 14, and 28 days, and results revealed an increased breakpoint torque on the oxidized implants after all timepoints. Wang et al.[33] produced macropore structures for in vivo implantation in rabbits, using selective laser melting. They concluded that, for each timepoint, higher fixation was obtained for all porous groups, when compared with the compact implant.

In this sense, gathering surface topography modification and calcium phosphates like βTCP, allows to introduce bioactivity to the implant once these materials are very similar with the natural phase of bone.[6,10,34] These materials are known for their brittle nature and low mechanical properties, reason why they are abundantly reported in literature as coatings.[6,10,34] However, coating delamination during implantation is an already reported issue,[6,10,34,35] thus being very important to found new strategies that may overcome this drawback.

The present study aims to gather laser surface texturing with bioactive impregnation to create a novel multifunctional component. In this sense, Ti6Al4V implants surface will be laser-textured, then performing βTCP impregnation inside the grooves, using a press and sintering technique. This new strategy will promote a mechanical interlocking between the metal and the bioactive materials (avoiding bioactive detachment) that, consequently, enhance osseointegration by given an adequate surface texture and a bioactive material aiming to be resorbed and replaced by newly formed bone. In this paper, non-textured implants, texture implants, and textured-impregnated implants will be fabricated. In vivo studies, after 4 and 12 weeks of implantation, will allow to assess these implants osseointegration by means of push-out tests and histological characterization.

8.2. Experimental section

8.2.1. Implant's manufacture

In the present study, different Ti6Al4V implants were fabricated and tested to assess their potential as hip implants. In this context, Ti6Al4V wires with 1.6 mm diameter and 25 mm length were purchased (*Titanium Products Limited*) and used as control groups and for fabricating laser-textured implants. Figure 8.1 shows a micrograph of these as-purchased wires, named throughout the paper as S1.
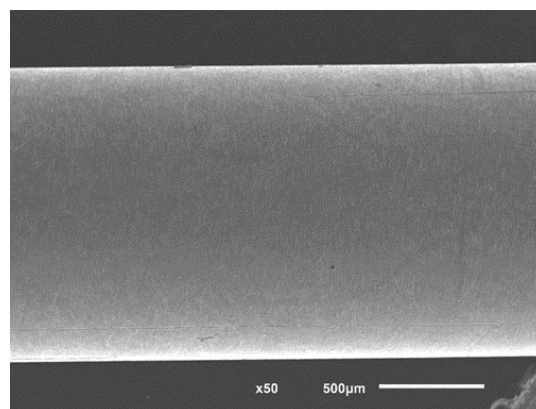
Figure 8.1 - Original surface of Ti6Al4V wire (corresponding to S1).

The second group of samples used in this paper, S2, was surface textured wires obtained by laser machining. For this group, Nd:YAG laser OEM Plus with a laser spot size of 3 μm, working at a wavelength of 1064 nm and with a maximum power 6 W was used. This type of lasers use a sequence of pulses to texture the surface of the material, in which the quality of the cut was highly dependent on laser parameters.[11] For surface texturing around Ti6Al4V wires, a custom-made apparatus was developed, with supports being manufactured to adapt the wires to the laser motor. Figure 8.2(A) shows an illustration of the apparatus used for surface texturing. Briefly, with the supports manufactured, the wires were attached to the laser motor that was rotating at a speed of 3 s revolution[-1]. Argon was used as assisted flow during machining to avoid surface oxidation. A sequence of grooves was machined along the wire, in which each groove consists of 10 overlapping lines that differ in the number of passes and wobble amplitude. As seen in Figure 8.2(B), 10 overlapped lines were designed and performed at a power of ≈ 0.6 W and a scan speed of 2 mm s^{-1}, where wobble amplitudes and number of passes ranged from 25 to 340 μm and 10 to 100, respectively. This process was repeated 24 times. This design strategy will generate a final texture with a more rounded shape and a more evenly distribution of the laser energy during machining. The obtained specimen, corresponding to S2 group, has the following average dimensions: groove width (a)=421.62 ± 5.57 μm; wall thickness (b)=264.41 ± 8.10 μm, and groove depth (c)=179.27 ± 22.91 μm (see Figure 8.2 (C)), all obtained from 63 to 69 measurements. Figure 8.3 displays surface roughness measurements after surface laser texturing obtained by performing 3D Optical Profilometry using a *Sensofar S-neox equipment*, (surface ISO 25178, 2012), coupled to a *SensoSCAN* software.

The last group of this study corresponds to a multi-material implant in which textured Ti6Al4V wires obtained in the same manner as S2, were impregnated with a bioactive material, βTCP powder, obtained from Trans-Tech, Inc. βTCP powder was mixed with acetone ultrasonically (for 10 s), to obtain a viscous solution (≈ 50% (w/v)). Then, this solution was poured onto an acrylic plate and the Ti6Al4V wire was rolled against the solution with an upper acrylic plate, thereby forcing the bioactive material to occupy the available space in the grooves. Finally, the Ti6Al4V-βTCP implants were sintered in a furnace, under argon atmosphere, at 1100 °C for 2h with a heating and cooling rate of 5 °C min^{-1}. Figure 8.4(A) shows a schematic representation of the impregnation process. This final group, corresponding to Ti6Al4V laser-machined impregnated with βTCP was referred throughout this paper as S3.
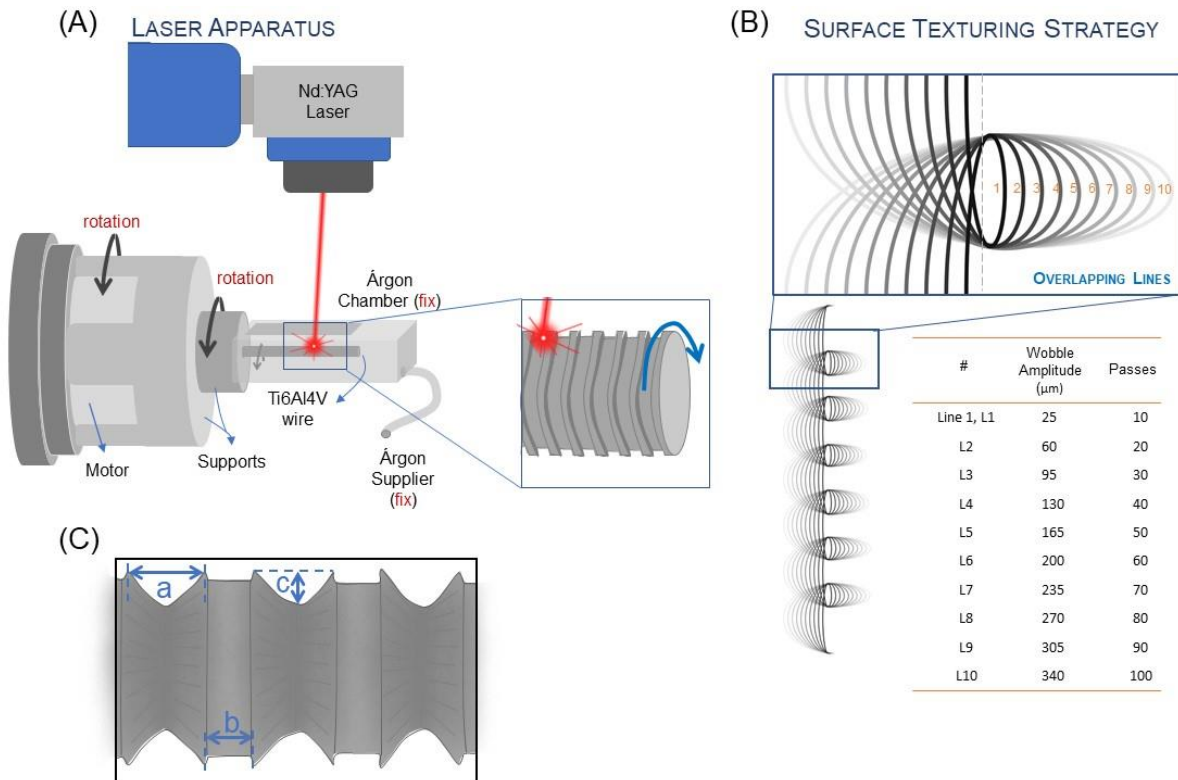
Figure 8.2 - Schematic representation of A) laser machining apparatus, B) strategy for textures machining, and C) dimensions measurements (a=groove width, b=wall thickness, and c=groove depth).

	Sa (µm)	Sq (µm)	Sz (µm)
Z1	2.31 ± 0.62	2.94 ± 0.72	17.13 ± 5.20
Z2	5.08 ± 0.87	6.51 ± 0.99	36.26 ± 4.01
Z3	7.28 ± 1.37	9.15 ± 1.61	54.82 ± 8.79
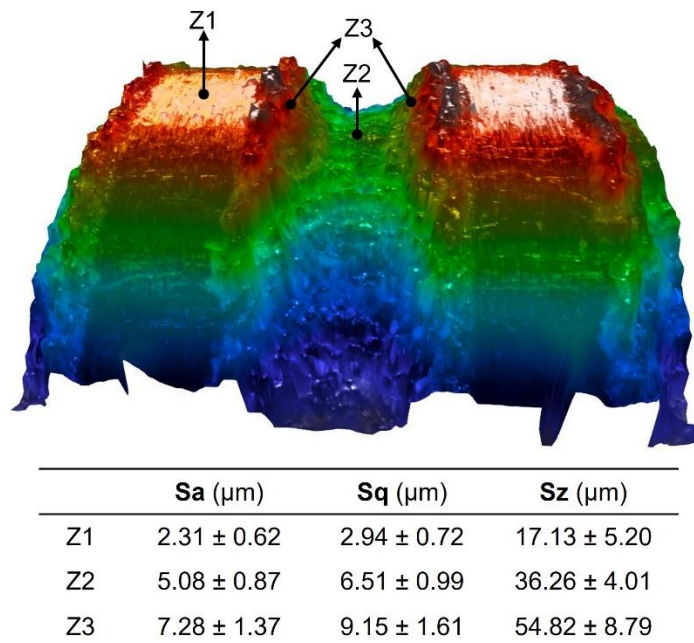
Figure 8.3 - Surface roughness measurements after laser-modification procedure. Results are displayed as mean ± standard deviation.

Lastly, before testing, Ti6Al4V as-manufactured (S1), Ti6Al4V laser-machined (S2) and Ti6Al4V laser-machined impregnated with βTCP (S3) implants (Figure 8.4(B)) were cleaned in ultrasounds.
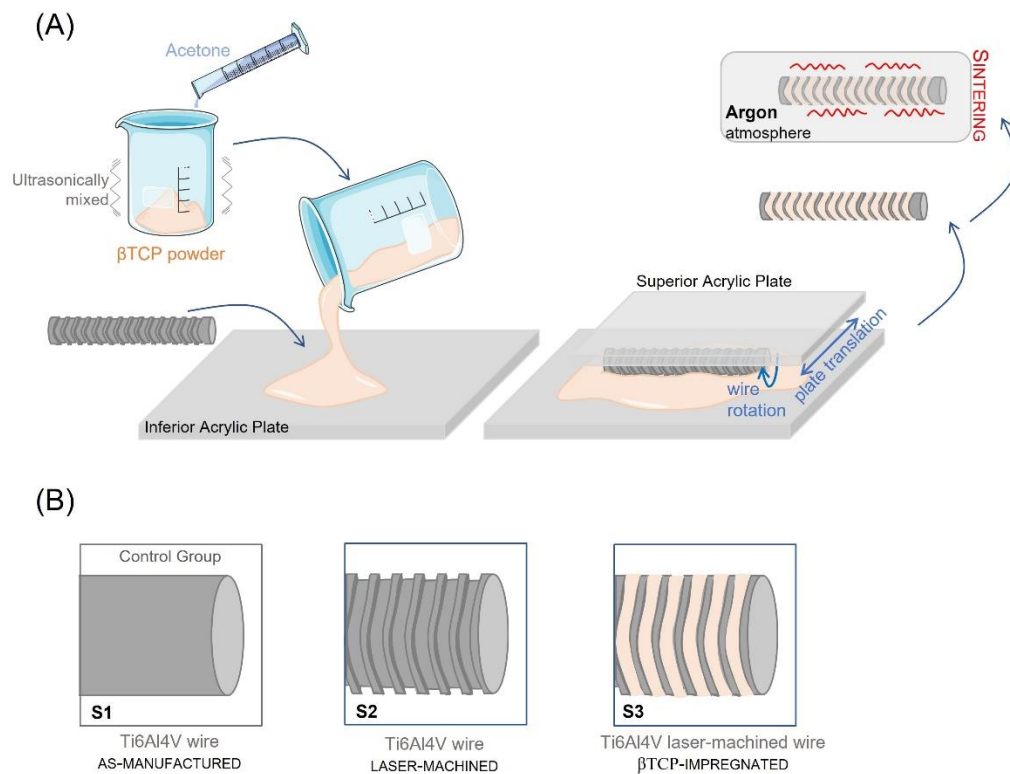
Figure 8.4 - Illustration of the A) impregnation process of laser-machined Ti6Al4V wires and B) final groups used in the present study.

8.2.2. In Vivo Experiments

8.2.2.1. Pre-Clinical Model

In this study, thirty male Sprague Dawley rats (Charles River, Barcelona, Spain), having a weight body average of 515.41 ± 37.64 g were used. The animals were maintained in an animal-controlled facility in terms of temperature (22 °C), humidity (50-60%) and artificial 12 h light/dark cycle (from 8:00 a.m. to 8:00 p.m.). Moreover, not only irradiated food and sterilized water were available ad libitum but also enrichment and nesting material were provided. Moreover, these experiments were carried out following EU Directive 2010/63/EU and approved either by Animal Ethics Committee of the Institution, SECVS 132/2016, and by Direção Geral de Alimentação e Veterinária (national competent authority for animal protection), DGAV/010117. It is important to address that all the staff involved were approved by DGAV as capable to conduct the animal experiments and the facilities approved by the national competent authority DGAV/014070.

8.2.2.2. Surgical Procedure

The surgical procedure followed a sequence of steps that are schematically represented in Figure 8.5. The procedure started by anesthetizing intraperitoneally the animals, ranging between

16 to 18 weeks old, with a combination of 75 mg kg^{-1} ketamine (Ketamidor, Richter Pharma AG, Austria) with 0.5 mg kg^{-1} of medetomidine (Sededorm, VetPharma Animal Health, Spain). Pre-operatively analgesia (0.05 mg kg^{-1} buprenorphine, Richter Pharma AG, Austria) was also administrated, subcutaneously. At this age range, the rats are in adulthood, which was an important aspect to mimic implantation in adult humans, since it was already reported in literature that the growth of the growth plate starts to cease and its thickness to decrease at a rats' age between 8 and 16 weeks.[36]

Then, the animal's fur of the right leg was shaved, as can be seen in the first step of Figure 8.5, the skin disinfected with chlorohexidine solution, and placed (left lateral recumbency) in a heating plate that was kept at 37 °C during the entire surgical procedure. Posteriorly, second step of Figure 8.5, a skin incision was made and, to assess the femur, third step of Figure 8.5, the muscles (*Tensor fasciae lata* and *Vastus lateralis*) were also cut, parallel to the muscle fibers. The joint capsule was, afterward, cut and the patella luxated medially to expose the distal epiphysis of the femur. Afterward, a defect in the trochlear sulcus of the femur was made using drills with ascending lengths, thus making a hole along femurs' longitudinal axis (fourth step of Figure 8.5). The Ti6Al4V implants were then press-fitted, axially, the patella repositioned, and the muscles and skin sutured, with absorbable suture (fifth and sixth step of Figure 8.5). It was important to mention that the groups were randomly assigned for each animal that receive only one implant in the right femur, for either 4 or 12 weeks of implantation. The implant was positioned longitudinally in the epiphysis and diaphysis region, since, in the author's opinion, it was a closer approximation to real implantation procedure in humans, contrary to most related studies found in the literature, which implantation was performed in a transversal orientation. Nevertheless, as epiphysis was the region where highest osseointegration occurs, the analysis will be mainly focused on this area.

For animal recovery, 1 mg kg^{-1} of a reversal agent atipamezole (Antisedan, Orion Corporation, Finland) was administrated subcutaneously, and the animals were placed under red-light to avoid hypothermia during anesthesia recovery process.

Finally, the animals were placed in their home cages and analgesia was guaranteed in the first days pos-operatively. At day 1 post-operatively, buprenorphine was administrated to the animals, complemented with 5 mg kg^{-1} administration of a non-steroid anti-inflammatory carprofen (Rimadyl, Zoetis, Portugal). For the following 3 days post-operatively only carprofen was administered and signs of pain and discomfort were daily accessed in order to adjust the analgesic

protocol if needed. Moreover, antibiotherapy was also supplied using 5 mg kg^{-1} of enrofloxacine (Baytril, Bayer, Portugal), that was administrated subcutaneously.

The experimental endpoint and animal euthanasia was performed after two different predefined timepoints (4 and 12 weeks), by an overdosage administration of 150 mg kg^{-1} of sodium pentobarbital (Eutasil, CEVA, France). Finally, bone-implant system was harvested, by collecting the right leg and removing all the soft tissues, and further taken for radiographic analysis. Afterwards, a batch of samples of the same group was taken to immediate push-out tests (n=6, 3 for each timepoint), and the other batch preserved in a 10% formaldehyde solution for later histological characterization (n=4, 2 for each timepoint).
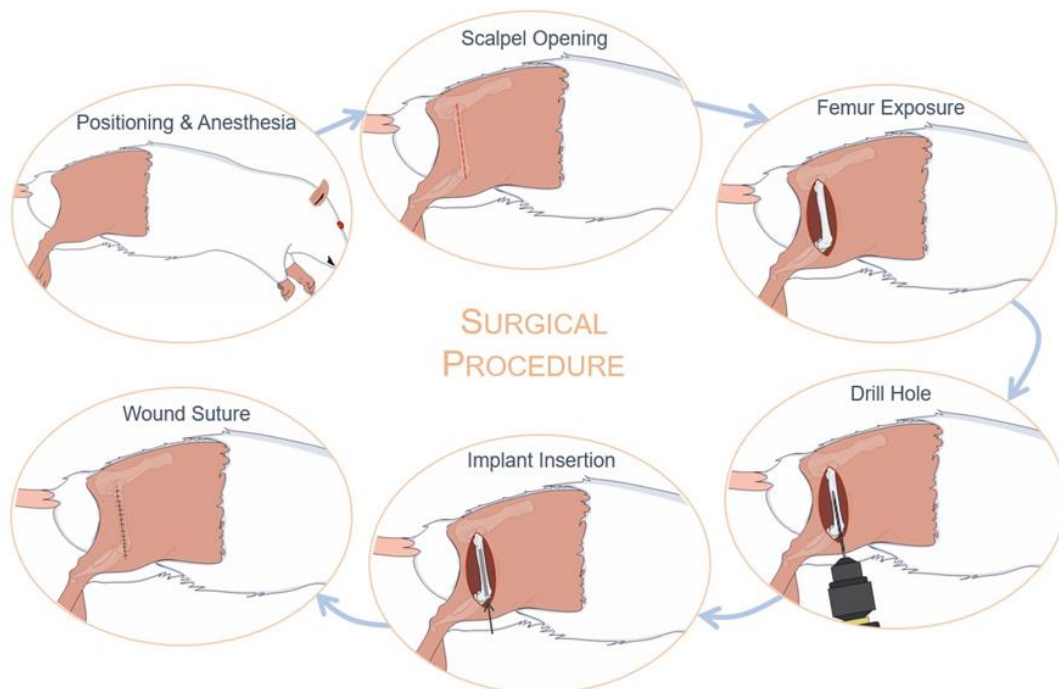
Figure 8.5 - Schematic representation of the sequence of steps adopted in the surgical procedure.

8.2.3. Push-out Tests

Push-out assays were performed, as mentioned, exactly after rat's euthanasia and radiographic analysis. The aim of these tests was to assess the fixation between the implant and surrounding bone for all the three groups. Figure 8.6(A),(B) displays a real image and a schematic illustration of the apparatus used to perform push-out tests, respectively. Briefly, to perform these tests, it was important to cut the femur, carefully, to access the top and bottom surfaces of the implant to further push the implant out of the bone. In this sense, a custom-made apparatus was developed in which the bone was placed inside a support and aligned with a screw system placed around it. This procedure needs to be done in order to guarantee that the crosshead device was perfectly aligned with the implant, in the vertical axis. The support was then fixed to the machine,

to prevent X and Y axis movement during the test. A metal punch having a diameter lower than that of the implant was fixed to the crosshead in order to extract the implant. The loading was performed using a universal testing machine, Hounsfield (H100KS), with a constant crosshead speed of 5 mm min^{-1} while a load-cell (range of 2.5 kN) was recording the applied load along the displacement. After the test, a force-displacement curve was obtained (QMAT 3.51 software) where it was determined the maximum push-out force (F_{max}) and fracture energy (E). F_{max} was determined directly from the force-displacement curve while E was obtained from the integral of the curve from 0 up to fracture, that is, the area under the load-displacement curve from 0 up to fracture.
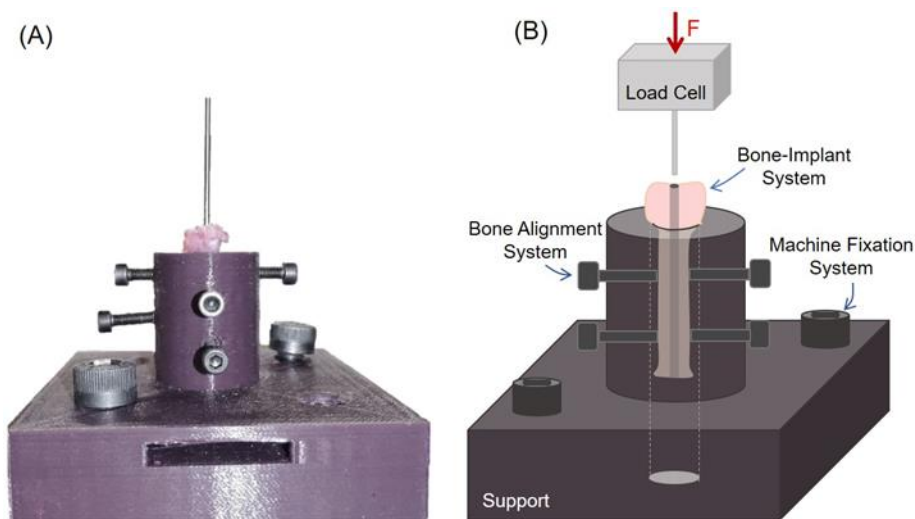
Figure 8.6 - A) Real image and B) illustration of push-out apparatus.

8.2.3.1. Statistical Analysis

Statistical analysis was performed on GraphPad Prism 8 software, by using 2 way-ANOVA with differences between groups compared with the post hoc Bonferroni test to assess the statistically significant differences on push-out force and fracture energy results between all the produced specimens under study. The results were displayed as mean ± standard deviation, considering a sample size of 3 for each statistical analysis. Statistical significance was defined for $p < 0.05$ (95% confidence value).

8.2.4. Surface Characterization

Before animal experiments, the specimens from groups S1, S2, and S3 were observed by scanning electron microscopy (SEM). After push-out tests, the full extracted implant (length = 25 mm) and respective bone cavity where the implant was inserted were observed by SEM, using a JSM.6010LV equipment from JEOL at an accelerating voltage of 10-15 kV, under high vacuum, after coating the samples with Au. Bone cavities exposure was possible by cutting the femur

longitudinally until achieving a clear cross-section. Since it was a biological material, with bone remains and cells, it was important to dehydrate the bones and the implants for SEM analysis. In this sense, prior to SEM, all the bones and implants have gone through a sequence of alcohol solutions, with increasing concentrations (30%, 50%, 70%, 90%, and 100%) for half an hour (each), and finally dried in vacuum. Surface chemical composition of the implants was assessed by energy dispersive x-ray spectroscopy, EDS, from Oxford Instruments Inc (X-act) at an accelerating voltage of 15 kV (acquisition time= 50 s), in an area corresponding to a magnification of 150x, to detect the presence of biological tissue on the implant surface.

8.2.5. Histological Evaluation

After implant harvest, tissue preservation was guaranteed in 10% formaldehyde solution for further histological characterization. To obtain the histological slides, these fixed samples were cleaned in water to remove formaldehyde solution residues and consequently dehydrated in 60%, 80%, 96%, 100% and 100% alcohol concentrations remaining three days in each solution. To remove the fat from the samples, Technovit 7200 VLC solutions were employed, that is, a sequence of 70/30, 50/50, 30/70, 0/100, and 0/100% alcohol/Technovit 7200 VLC concentrations for 3 days each was used follow by polymerization (Exakt 520 Light polymerization unit, Germany). Afterward, the samples were cut longitudinally and transversely, using a Exakt Cutting apparatus (Exakt Band System 300 CL/CP, Germany), according to Figure 8.7. Lastly, the samples were polished up to ≈100 µm thickness, using SiC papers (1000, 1200, 2500 and 4000 FP), and stained with toluidine blue.
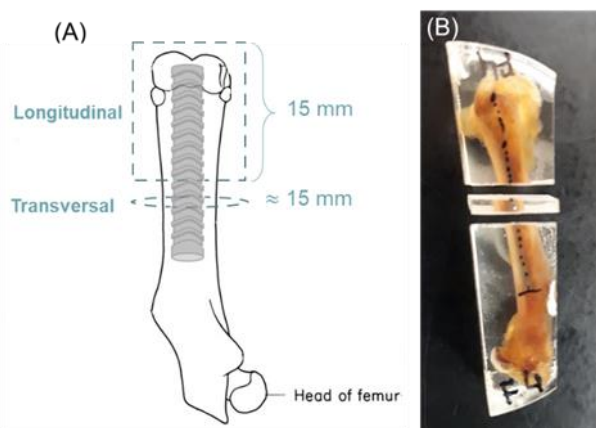
Figure 8.7 - Schematic representation of the cuts made for histological characterization.

8.3. Results and Discussion

For the present study, dense Ti6Al4V implants (S1) and textured implants (S2 and S3) were studied, and their biomechanical and biological performance was assessed. As already mentioned, the first group will act as control group (dense Ti6Al4V non-textured implants), while the second corresponds to textured Ti6Al4V implants and the third to textured Ti6Al4V implants with grooves filled with bioactive βTCP, creating, therefore a multi-material solution. Figure 8.8 shows SEM images of the fabricated implants (S1, S2, and S3).
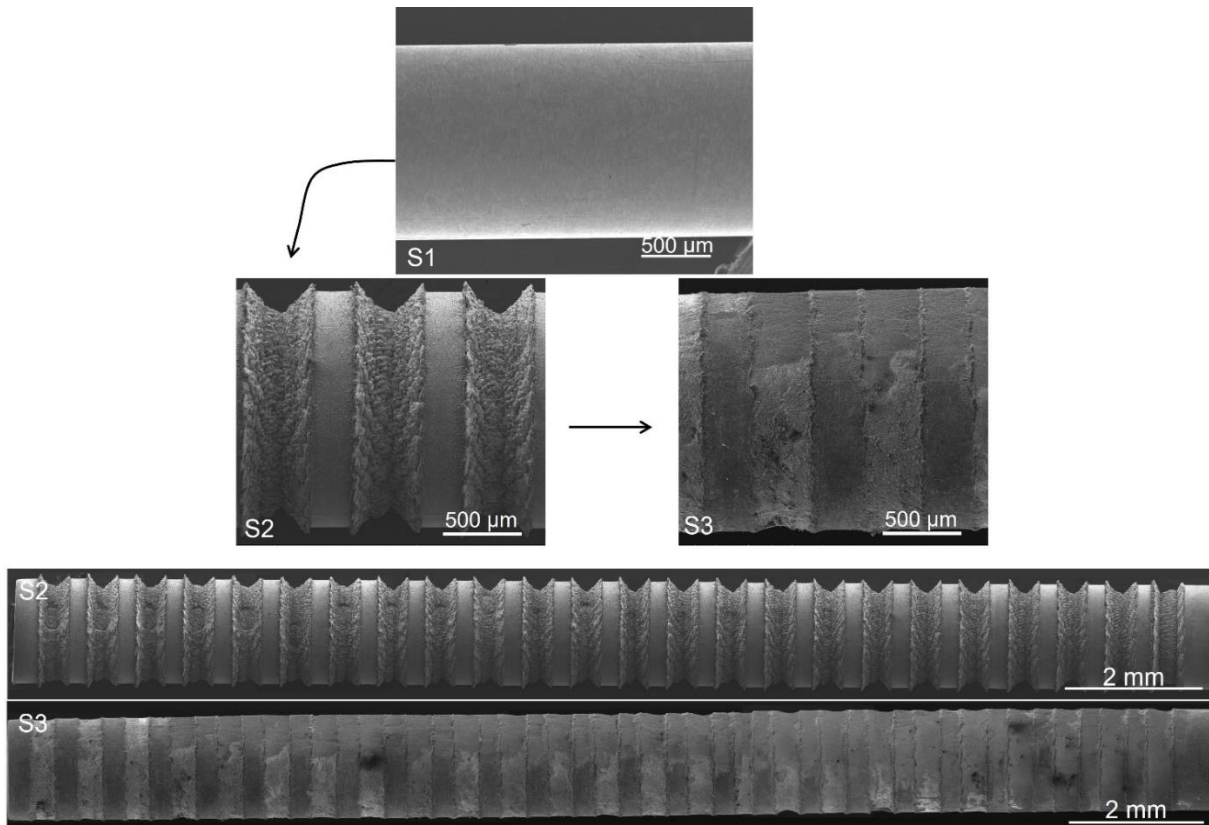
Figure 8.8 - SEM micrographs of S1 (Ti6Al4V as-received), S2 (Ti6Al4V laser-machined), S3 (Ti6Al4V-βTCP), before in vivo implantation. Bellow the magnified images, SEM images of S2 and S3 of full implants are indicated.

First, from these micrographs it is possible to observe that the grooves are very similar between them along the implant, indicating the versatility, efficiency, and high degree of reproducibility of the adopted technique for surface modification of these Ti6Al4V implants. Moreover, by observing the multi-material implant (S3), it is visible that the experimental procedure used to introduce the bioactive material inside the grooves was effective for obtaining a uniform allocation of the bioactive. This type of multi-material implants, where the bioactive material is incorporated into grooves instead of being used as surface coating has the advantage of preventing the delamination of the bioactive, a common drawback upon implantation.

By introducing bioactivity to the implant, it is possible to improve the biological interaction between the implant and the surrounding tissue. It is known that implant osseointegration depends on either primary and secondary stability, that is related with the mechanical anchoring between the implant and bone, and the biological response of the surrounding tissue, respectively. Immediately after implantation, the implant is mechanically held by the bone, the so-called primary stability, highly dependent on the design of the implant. Afterward, osteoclastic cells resorb the injured bone, causing a drop of the primary stability, and osteoblastic activity will promote the formation of woven bone, phenomenon commonly named as secondary stability.[20,37] In this sense, while the second group (S2) targets the mechanical anchoring of the implant to the bone, the third group (S3) aims not only to promote a mechanical anchoring to the bone but also to accelerate the biological processes and achieve a faster osseointegration.

To evaluate these Ti6Al4V implant's performance in a biological environment, the three groups were implanted for 4 and 12 weeks in Sprague Dawley rats' femur and assessed in terms of mechanical and histological characterization. Using this animal model, it is possible to obtain results in a shorter period of study since rats are fast healers and it was already reported that they have the ability to repair a large tibial defect within 12 weeks.[38] In this sense, 4 and 12 weeks were used as implantation timepoints since, despite being very usual in literature for similar studies, they theoretically allow to mimic an initial phase of bone regeneration and a phase where it is completed.

It is important to mention that all animals recovered very quickly; they could move freely inside the cage, and none presented signs of inflammation or infection. Before mechanical tests, the rat's legs were radiographically observed and the respective images for all groups can be seen in Figure 8.9. Apparently, all groups integrate in a satisfactory way into the bone, since, macroscopically, no bone callus was formed and no signs of osteolysis were observed. For a better understanding of what is happening in all groups after 4 and 12 weeks of implantation, in a microscopic manner, further histological analysis was performed.

Although histological analysis being a great indicator of bone formation, by displaying qualitatively the different bone tissues at the implant-bone interface, in this type of studies, mechanical characterization, such as push-out tests, can help to quantify the implant fixation.[39–41] This bone-implant fixation, can be measured, as mentioned, by performing push-out tests, to obtain maximum push-out load. In this sense, Figure 8.10 represents the maximum push-out force values for S1, S2, and S3 groups while Figure 8.11 displays representative load-displacement curves for

all groups for both timepoints. Table 8.1 shows average values of fracture energy obtained for S1, S2, and S3 groups. Both maximum push-out force and energy values are represented as average values of three repetitions, per group.
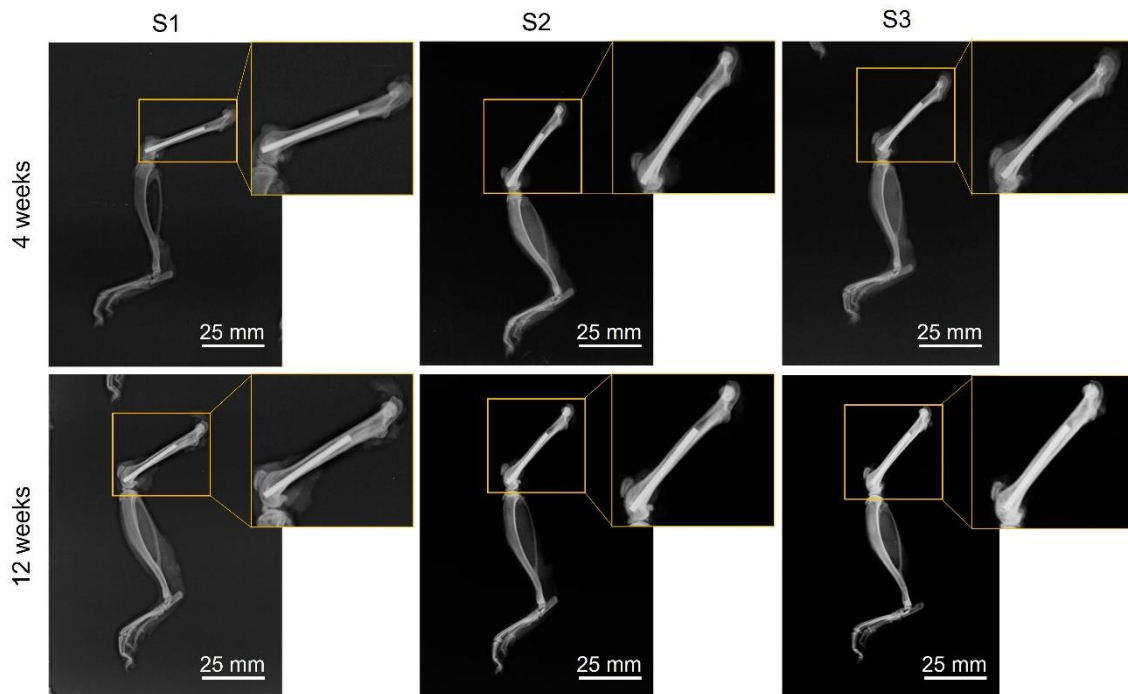
Figure 8.9 - Radiographic images of bone-implant system after in vivo experiments for S1 (Ti6Al4V as-received), S2 (Ti6Al4V laser-machined), S3 (Ti6Al4V-βTCP), after 4 and 12 weeks of implantation.
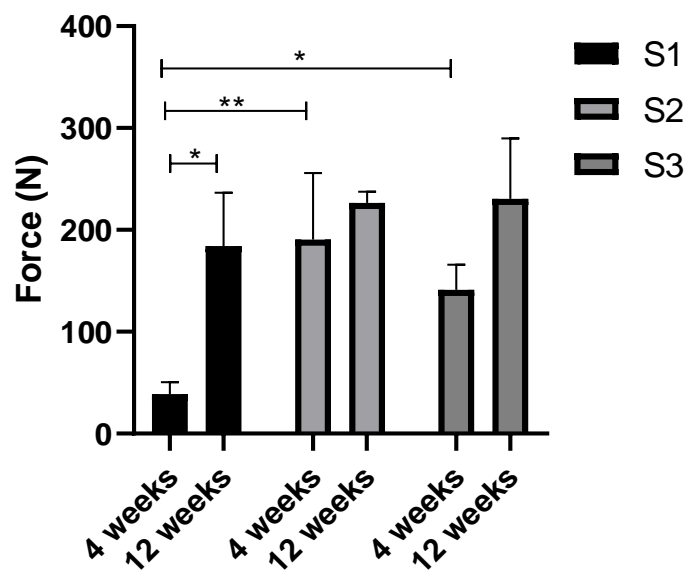
Figure 8.10 – Maximum push-out force for S1 (Ti6Al4V as-received), S2 (Ti6Al4V laser-machined), S3 (Ti6Al4V-βTCP) obtained from push-out tests, after 4 and 12 weeks of implantation, being values shown as mean ± SD. *- $p < 0.05$; **- $p < 0.01$ (n=3).
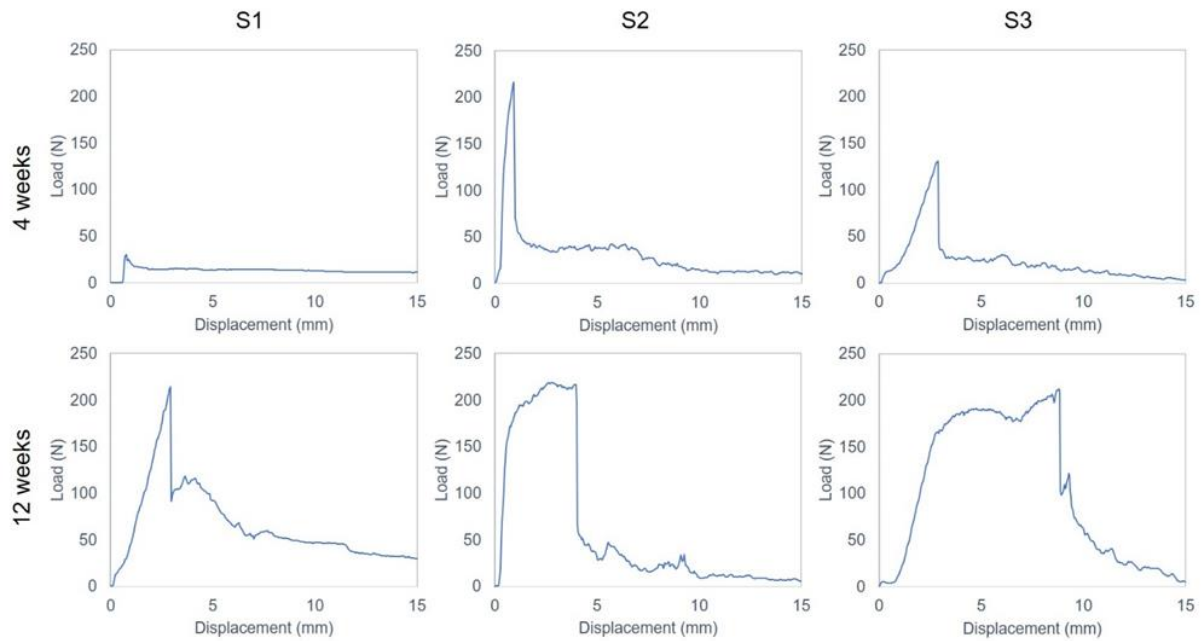
Figure 8.11 - Typical load-displacement curves for S1 (Ti6Al4V as-received), S2 (Ti6Al4V laser-machined), S3 (Ti6Al4V-βTCP), after 4 and 12 weeks of implantation.

Table 8.1 - Fracture energy (E) for the different groups at each timepoint (n=3).

Group	Timepoint (weeks)	E (mean ± SD) [mJ]
S1	4	18.07 ± 18.88
	12	223.37 ± 66.91
S2	4	174.25 ± 90.18
	12	757.21 ± 227.89
S3	4	323.69 ± 280.21
	12	940.01 ± 370.50

From Figure 8.10 results, it is visible that the average maximum push-out force values increase with implantation time, being the percentual increase for S1, S2, and S3 of 375%, 19%, and 63%, respectively. This increase of maximum push-out force with implantation time is in accordance with many studies reported in literature.[42,43] However, from a statistical point-of-view, regarding force, only S1 group was statistically different when comparing both implantation timepoints (p=0.0372). Regarding fracture energy statistics, the opposite was observed, with only S2 and S3 being statistically different from 4 to 12 weeks of implantation (p(S2)=0.0377 and p(S3)=0.0297). These differences in statistical results are related with a high standard deviation found between groups, nevertheless the tendency to an increase push-out force with implantation time can be perceived.

When compared to S1, S2, and S3 have higher average maximum force, for both implantation times. At 12 weeks of implantation, only a slight difference in average maximum push-out force was observed, once the values of S2 and S3 are 23% and 25% higher than S1, respectively, not being found statistically different. On the contrary, the highest difference happened at 4 weeks of implantation, where S2 and S3 displayed 392% and 264% higher maximum push-out force than S1, respectively, being statistically different (p(S2)=0.0033 and p(S3)=0.0421). These values sustain the rapid osseointegration capacity of S2 and S3 groups, that S1 is not able to achieve, which may enable an earlier loading of the implant, since this will integrate with the bone more quickly. Moreover, when comparing load-displacement curves (Figure 8.11), it can be observed that at the earliest timepoint, the push-out force required for extraction corresponds to an isolated peak followed by an almost instantaneous drop, whilst at 12 weeks of implantation, specially for S2 and S3 group, a load plateau is observed, indicating higher energy necessary for rupture and implant extraction. This behavior is in accordance with the average fracture energy values (Table 8.1), where higher energy is required to fracture after 12 weeks of implantation, specially for S2 and S3 groups. When compared with S1 group, statistical analysis only revealed, at 12 weeks of implantation, significant differences for S3 group (p=0.0186). This increase in average values for S2 and S3 in comparison with S1 implants is related with the surface topography of the implants. In fact, these findings are confirmed by previous studies already published, that indicate increased removal torque, and therefore, bone anchorage, on laser-modified surfaces. [27-31] As mentioned, implant design is extremely important for bone osseointegration, in which the mechanical anchoring of the implant is favored on rougher/porous surfaces.[44] Similar trends were found in literature.[33,45] Ran et al.[45] developed Ti6Al4V implants with different pore dimensions, via Selective Laser Melting, having implanted them into rabbit femur's and compared the results with dense Ti6Al4V implants. All porous materials displayed significantly higher shear bond strength at the interface compared with dense, after either 4 or 12 weeks of implantation. It is widely reported in literature that rough surfaces enhance osteoblastic cell adhesion, proliferation and differentiation.[20,44,46] Yet, it is not only important to have bone growth towards the implant, as the quality and biomechanical properties of the new bone formed are essential.[47] During peri-implant healing, fibrous tissue may be formed, due to high mobility of the implant, and being this process faster than bone apposition, it can compromise the overall osseointegration process and promote implant failure.[20,47]

When comparing S2 with S3, although not statistically significantly different, at 4 weeks of implantation, S2 is the one with the highest push-out force, in average. This can be related with the fact that S2 have a higher surface area in contact with the surrounding tissue, while, in S3 group, the grooves are filled (completely or partially due to bioactive resorption) with the bioactive material, thus reducing the exposed surface area. However, this behavior does not happen at 12 weeks of implantation. In the same manner, despite not being statistically different, when comparing S2 and S3, at 12 weeks of implantation, S3 average values are the highest in push-out force and, when observing load-displacement curve and fracture energy values, S3 was also the one that requires higher amount of energy to fracture. This may be an indicator that, at this point, the bioactive material is playing a role in the osseointegration process and being resorbed by the bone, enhancing therefore osteogenesis. It is important to highlight that bioresorption is a biological process mediated by cells (osteoclasts but also macrophages) that depends on the response of cells to their environment.[48]

Bose et al.[46] studied the interfacial bone-implant bonding strength on a doped calcium phosphate coating on a porous titanium. These materials were implanted in Sprague Dawley rats and interfacial shear strength increase from 4 to 10 weeks of implantation. It was also concluded that, after 4 weeks, the shear modulus of CaP coated porous Ti rods was the highest compared with the ones without the coating, and this statement was further confirmed by histological tests that revealed an enhanced osteogenesis in these specimens. In another study, the in vitro and in vivo performance of a bioactive composite implants (Ti6Al4V/TiC/HA having a porous structure) was also assessed by Choy et al.[49] In vitro results revealed that the composite promotes a suitable environment for MC3T3-E1 cells to adhere, proliferate and differentiate. Moreover, when implanted in rabbits' tibiae, histological findings indicate that the composite with the bioactive material displayed better bone-implant interface when compared with the one without (Ti6Al4V/TiC implant).

To sum, besides at 12 weeks of implantation, the average values for the maximum push-out force for all groups is not statistically significantly different, by analyzing the curves and fracture energy values, it is possible to verify the type of bone fixation that is associated to the different implants, and, in this study, it can be observed that the bone anchorage mechanism between implants is different. As stated by Tschegg et al.,[50] the maximum push-out force values are not the most important factor when analyzing implant performance, but the amount of energy that the implant can sustain before rupture. In S1 group, implant-bone anchorage is strong but fragile,

which means that bone is integrated with implant surface however when maximum load is surpassed, there is a sudden decrease of the load (interface failure). With this fragile behavior found in S1 group, implant will no longer be attached to the bone, which can promote the beginning of bone resorption process, and consequently, lead to implant failure. In S2 and S3 groups, where the curves are characterized by higher fracture energy, bone resorption is more difficult to occur since there is load transfer between implant and bone. In these groups, especially in S3, the implant can sustain the load while keeping implant stability. In S2 group, as mentioned, this can be related with a higher mechanical interlocking that is achieved by new bone growth into the laser-machined grooves while, in S3 it can also be related with bioactive material chemical affinity that led to better implant-bone fixation.

In the present study, the longitudinal and transversal histological sections of the implant-bone interface can be observed in Figure 8.12 and Figure 8.13, respectively. By observing this figure, it is possible to detect that neither group elicit a cytotoxic effect on the bone once all implants integrate well with the nearby bone tissue with no visible signs of adverse responses at the interface.

At the earliest timepoint, it is visible that S1 displayed an extensive uniform deposition of immature bone around the implant however it is characterized by a thin bone layer with multiple areas not displaying direct contact with implant surface, being instead filled with highly vascularized connective tissue. Conversely, by introducing laser textured grooves (S2 group), a vast deposition of new bone in direct contact with implant surface is observed, with pronounced bone proliferation inside the grooves. This indicates that these textures will act as osteoinductive areas that are filled with new immature bone, launching bone bridges in contact with native bone present in the bone-implant interface. Moreover, these bone invaginations inside the grooves also exhibit a direct contact with the implant surface, also having areas with richly vascularized connective tissue. When observing S3 group at 4 weeks of implantation, similarly to S2 group, there is osteodeposition around the implant surface, however, as expected, the growth of new bone inside the textures is less pronounced, essentially because the grooves are now filled with the bioactive material. Nevertheless, there are multiple zones in these depressions already in direct contact with immature bone at the implant surface, alternating with zones of highly vascularized connective tissue.

When increasing the implantation time, a noticeable evolution in S1 occurs, regarding not only the bone-implant contact, that is higher after 12 weeks, but also a greater degree of bone maturation. It is also observed a thin layer of organized lamellar bone surrounding the implant and,

in the central and distal portion of the implant, located in the medullary cavity of the diaphysis, there is a significantly reduced osseointegration with focused areas of immature bone. In S2 group, at 12 weeks of implantation, it is visible an almost complete osseointegration in the epiphysis and diaphysis area in which the bone that is in direct contact with the implant surface displays an advanced degree of maturation characterized by lamellar bone, almost completely filling the grooves. It is also observed, in multiple regions, bone projections of mineralized tissue at the implant interface towards the periphery, resulting in an increased bone anchorage. For this implantation time, S3 group exhibits a similar behavior in terms of bone remodeling when compared with S2 however, when comparing the two implantation times, it is visible a higher bone growth inside the grooves being more evident its topography that is now filled with new bone. This indicates, as mentioned, that the bioactive material was replaced by new bone with an advanced degree of maturation.

Overall, in all implants, it is noticeable new bone formation, characterized by immature woven bone, in the bone-implant interface (lighter purple) being this more visible at 4 weeks of implantation. This coloration, characteristic of an immature bone is related with the collagen fibers that are dispersed in a random orientation. With time, this type of bone tissue is remodeled into a lamellar bone in which the collagen fibers are aligned parallelly to each other being this type stronger than the woven bone. After 12 weeks of implantation, the demarcation line between the original bone and the new formed bone is not so pronounced, which means that the woven bone was remodeled to a more mature lamellar bone (that has the same constitution as the original cortical bone).

As mentioned, the laser-produced grooves increase the implant surface area and as seen in histological images, bone was allowed to grow inside these textures, which will, consequently, improve implant mechanical stability and, consequently, higher push-out forces/energy will be needed to remove the implant (as proven by push-out results). By impregnating the textures with bioactive materials, at 4 weeks of implantation, the grooves are almost imperceptible in the histological images, however, statistically significant differences were found in maximum push-out force between this group (S3) and the non-textured implants group (S1). This behavior may be related with the beginning of the bioactive resorption process and its replacement by new bone in specific sites of the implant. At 12 weeks of implantation, the produced grooves are then visible indicating that the bioactive material was resorbed and replaced by newly formed bone.
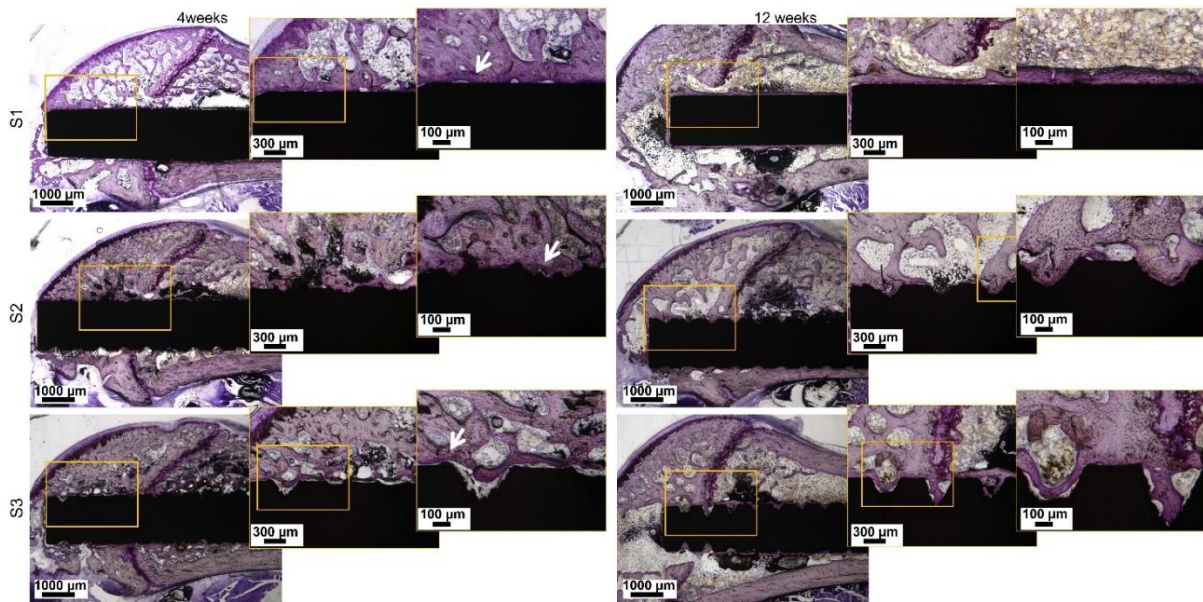
Figure 8.12 – Representative histological longitudinal sections of all implants and bones after 4 and 12 weeks of implantation at 3 different magnifications. Black areas correspond to the metallic implants and pink areas to bone. White arrows indicate the region where is possible to distinguish the original bone and new bone formed.
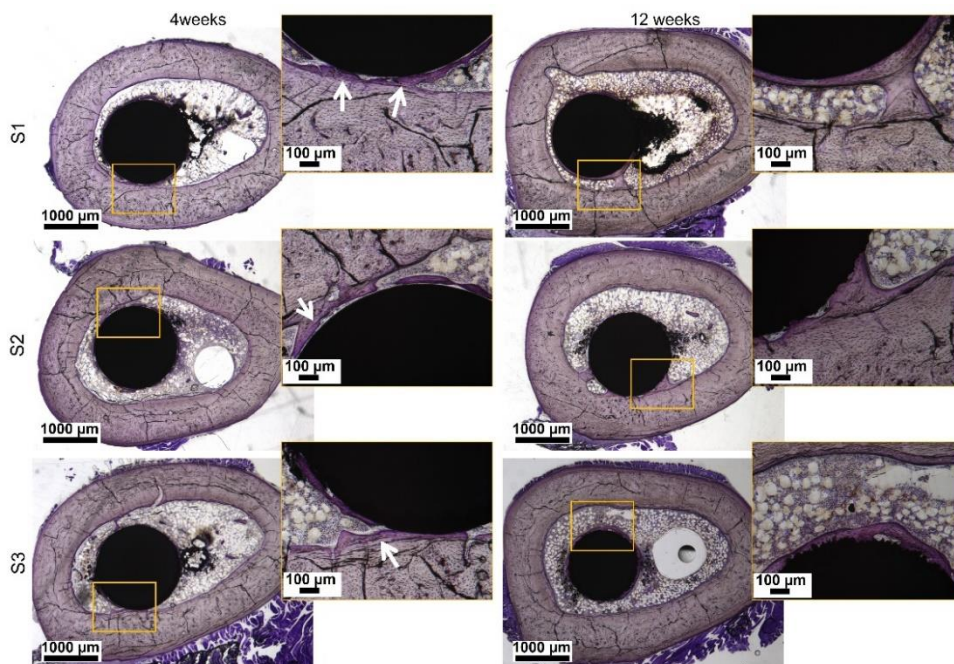
Figure 8.13 – Representative histological transversal sections of all implants and bones after 4 and 12 weeks of implantation at 3 different magnifications. Black areas correspond to the metallic implants and pink areas to bone. White arrows indicate the region where is possible to distinguish the original bone and new bone formed.

Lastly, SEM and EDS analysis were performed on all groups, after push-out tests, for both timepoints. In all EDS spectra for both Figure 8.14 and Figure 8.15 it is possible detect bone tissue elements, namely calcium and phosphorus, that are present in the inorganic phase of bone which means that bone tissue adhered to implants from the three groups. Additionally, it can be also observed that, in the non-textured implants (Figure 8.14), EDS analysis easily detect the elements

of the implant material, namely Ti, Al, and V, conversely to the other groups (Figure 8.15) meaning that higher amounts of bone are attached to the surface of S2 and S3 group.

Besides SEM images of the removed implants, the bone cavities where these were implanted were also observed. Figure 8.14 and Figure 8.16 shows S1 implants and bone cavities SEM micrographs, respectively, for both times of implantation. Both figures indicate that, with the increase of implantation time, more bone adhered to the implant surface. In fact, it is clear that, when compared with 4 weeks, more bone attached to the implant surface is observed at 12 weeks of implantation and a rougher bone fracture surface is obtained, which are good indicators of higher interfacial fixation. These results are in accordance with what was previously stated for push-out tests.

When comparing S1 group with the other two, some significantly changes can be visible. Looking at S2 and S3 implants from Figure 8.15, the micrographs shows that the amount of bone tissue adhered to the implant drastically increase. Bone fracture surfaces of S2 and S3 implants can be observed at Figure 8.17 and, in comparison with S1, these are extremely different being much more destructive and rougher. This may justify the higher maximum push-out force, fracture energy, and load-displacement curves for these groups, due to a higher bone-implant mechanical interlocking being necessarily higher energy to promote rupture. It is possible to indicate, by analyzing implants micrographs and bone cavities that the fracture in S2 and S3 group does not occur on the bone-implant interface, but on the bone, indicating that this interface in both groups is not a fragile area. This outcome is also described in previous reported studies in literature.[28–30]

By analyzing S2 and S3 micrographs, it can be also concluded that the implantation time also has a positive effect on bone apposition and adherence once, in both groups, it is still visible the original implant surface at 4 weeks of implantation whilst, at 12 weeks, higher amount of bone tissue covers the implant surface. It is visible that, at 12 weeks of implantation, the highest amount of bone apposition was found for S3 group. This finding suggests that at 12 weeks, bioactive resorption has occurred to some extent, improving the implant osteointegration and creating higher implant-bone fixation.

Overall, these results suggest that the addition of the bioactive material and creation of a multi-material solution is an asset to enhance osteogenesis process and guarantee an effective long-term bone-implant fixation, proving its potential use in orthopedic implants.
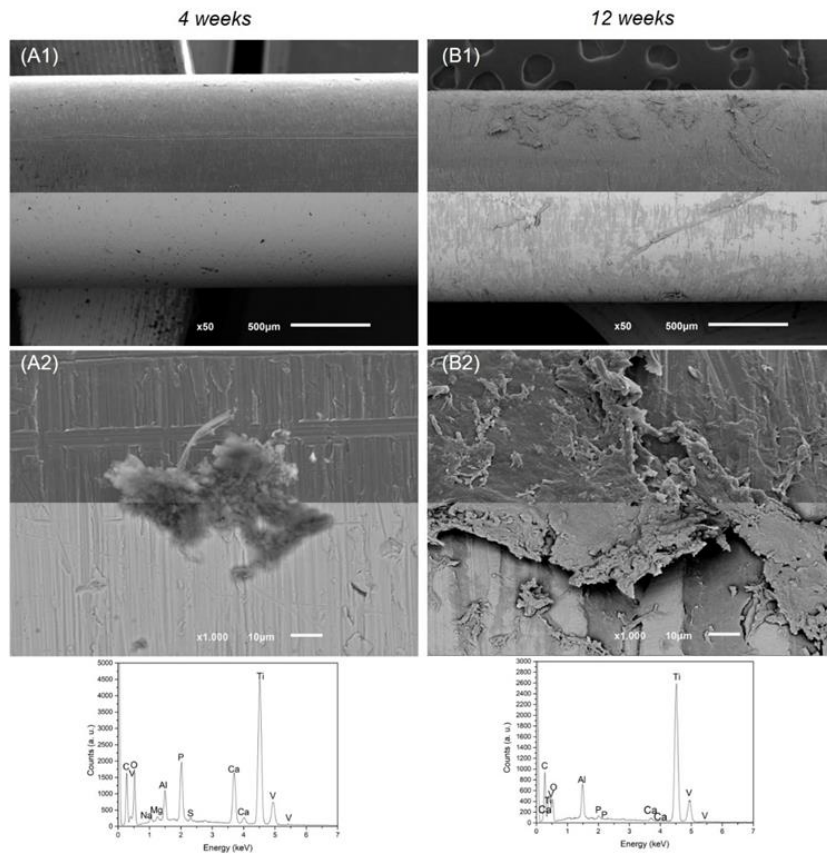
Figure 8.14 - SEM micrographs and EDS spectra of S1, after push-out tests, for A) 4 weeks and B) 12 weeks.
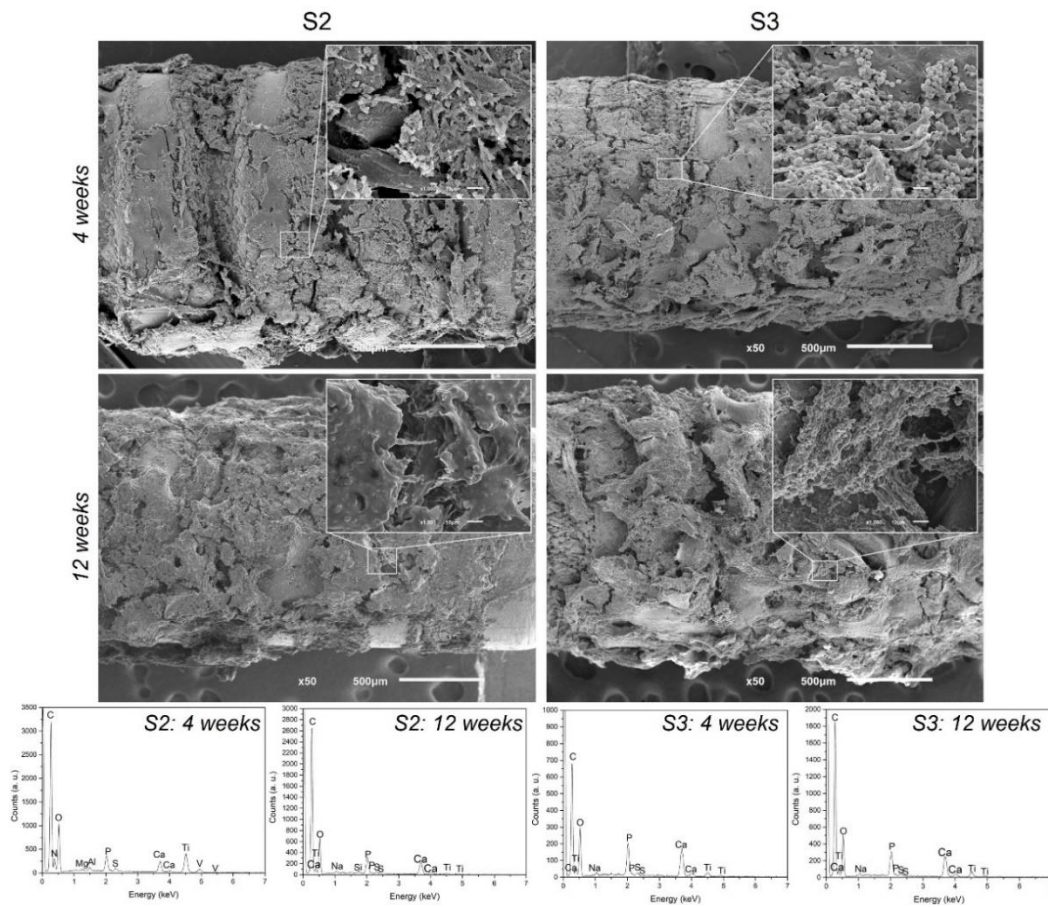
Figure 8.15 - SEM micrographs and EDS spectra of S2 and S3, after push-out tests, for 4 and 12 weeks.
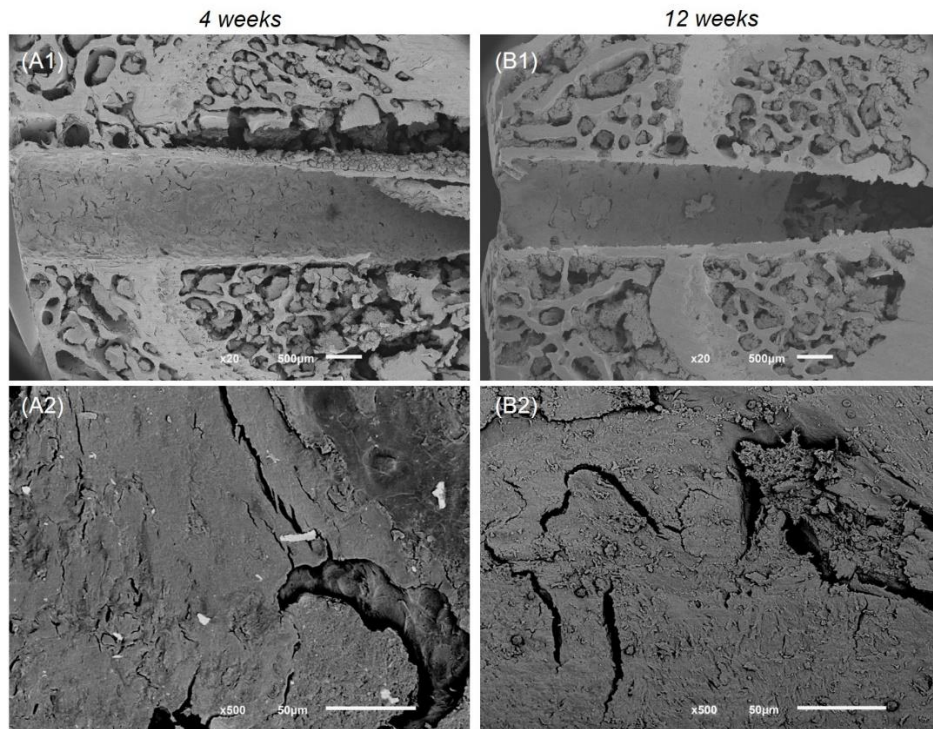
Figure 8.16 - SEM micrographs of bone cavity for S1, after push-out experiments, for A) 4 weeks and B) 12 weeks: number 1 corresponds to secondary mode and number 2 to back-scattered mode.
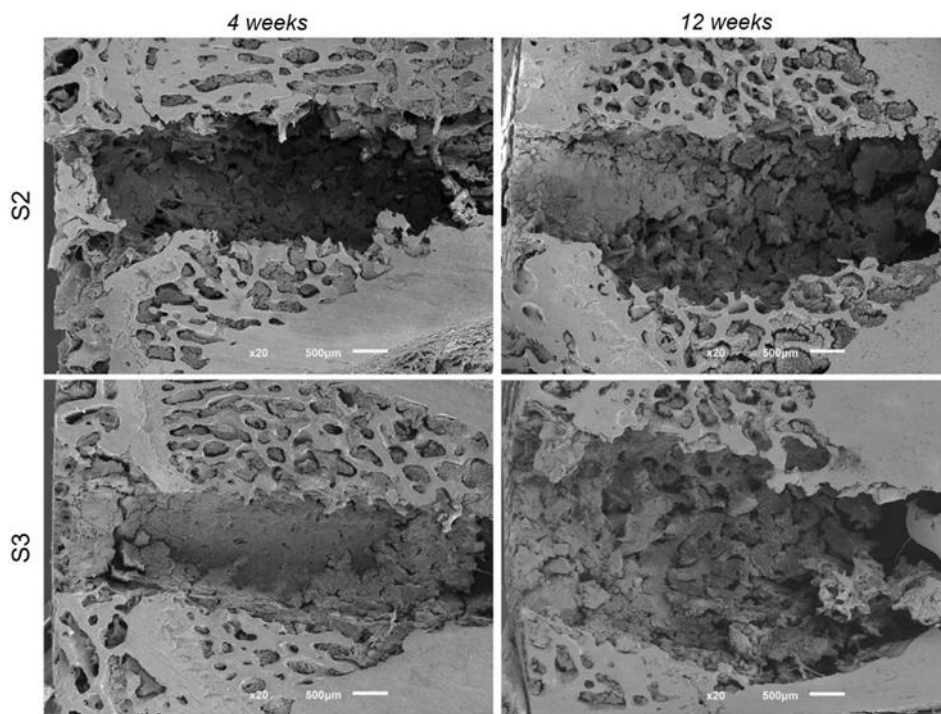
Figure 8.17 - SEM micrographs of bone cavity for S2 and S3, after push-out experiments, for the different timepoints: 4 and 12 weeks.

8.4. Conclusions

From the present study, the following conclusions can be drawn:

• Laser surface texturing was used to manufacture Ti6Al4V laser textured implants with high degree of reproducibility.

• The processing route used to produce the multi-material group and, thus, introduce the bioactive material inside the grooves was successfully achieved.

• In vivo experiments revealed that, at 4 weeks of implantation, textured (S2) and bioactive textured (S3) implants displayed higher maximum push-out forces, with statistically significant differences ($p<0.05$), when compared with non-textured implants (S1).

• After 12 weeks of implantation, the multi-material implants (S3) where the only group exhibiting statistical differences, when compared with non-textured implants, by displaying higher fracture energy.

• Overall, these findings indicate that the multi-material bioactive group is an extremely attractive solution for orthopedic implants since it considerably enhances implant–bone fixation.

References

[1] P. Pou, A. Riveiro, J. del Val, R. Comesaña, J. Penide, F. Arias-González, R. Soto, F. Lusquiños, J. Pou, Procedia Manufacturing 2017, 13, 694.

[2] U. Holzwarth, G. Cotogno, Total Hip Arthroplasty – State of the Art, Challenges and Prospects, Publications Office of the European Union, Luxembourg 2012.

[3] Z. S. Tao, W. S. Zhou, X. W. He, W. Liu, B. L. Bai, Q. Zhou, Z. L. Huang, K. K. Tu, H. Li, T. Sun, Y. X. Lv, W. Cui, L. Yang, Mater. Sci. Eng., C 2016, 62, 226.

[4] H. E. Götz, M. Müller, A. Emmel, U. Holzwarth, R. G. Erben, R. Stangl, Biomaterials 2004, 25, 4057.

[5] C. Wedemeyer, H. Jablonski, A. Mumdzic-Zverotic, H. Fietzek, T. Mertens, G. Hilken, C. Krüger, A. Wissmann, H. Heep, R. Schlepper, M. D. Kauther, Materialia 2019, 6, 100266.

[6] M. M. Costa, R. Lima, F. Melo-Fonseca, F. Bartolomeu, N. Alves, A. Miranda, M. Gasik, F. S. Silva, N. A. Silva, G. Miranda, Mater. Sci. Eng., C 2019, 98, 705.

[7] F. Bartolomeu, M. M. Costa, J. R. Gomes, N. Alves, C. S. Abreu, F. S. Silva, G. Miranda, Tribol. Int. 2019, 129, 272.

[8] S. Mukherjee, S. Dhara, P. Saha, Int. J. Adv. Des. Manuf. Technol. 2015, 76, 5.

[9] J. C. M. Souza, M. B. Sordi, M. Kanazawa, S. Ravindran, B. Henriques, F. S. Silva, C. Aparicio, L. F. Cooper, Acta Biomater. 2019, 94, 112.

[10] D. Faria, C. S. Abreu, M. Buciumeanu, N. Dourado, O. Carvalho, F. S. Silva, G. Miranda, J. Biomed. Mater. Res., Part B 2018, 106B, 1534.

[11] C. G. Moura, O. Carvalho, L. M. V. Gonçalves, M. F. Cerqueira, R. Nascimento, F. Silva, Mater. Sci. Eng., C 2019, 104, 109901.

[12] M. Hirao, K. Sugamoto, N. Tamai, K. Oka, H. Yoshikawa, Y. Mori, T. Sasaki, J. Biomed. Mater. Res., Part A 2005, 73, 213.

[13] J. Frostevarg, R. Olsson, J. Powell, A. Palmquist, R. Brånemark, Appl. Surf. Sci. 2019, 485, 158.

[14] F. A. Shah, P. Thomsen, A. Palmquist, Acta Biomater. 2019, 84, 1.

[15] J. M. Sadowska, M. P. Ginebra, J. Mater. Chem. B 2020, 8, 9404.

[16] Q. Gu, H. Yang, Q. Shi, Journal of Orthopaedic Translation 2017, 10, 86.

[17] M. J. Coathup, G. W. Blunn, N. Mirhosseini, K. Erskine, Z. Liu, D. R. Garrod, L. Li, Journal of Orthopaedic Research 2017, 35, 820.

[18] A. Bandyopadhyay, A. Shivaram, S. Tarafder, H. Sahasrabudhe, D. Banerjee, S. Bose, Ann. Biomed. Eng. 2017, 45, 249.

[19] F. Mangano, L. Chambrone, R. Van Noort, C. Miller, P. Hatton, C. Mangano, Int. J. Biomater. 2014, 2014, 461534.

[20] L. Salou, A. Hoornaert, G. Louarn, P. Layrolle, Acta Biomater. 2015, 11, 494.

[21] S. Çelen, C. Efeoğlu, H. Özden, Phys. Procedia 2011, 12, 245.

[22] N. Mirhosseini, P. L. Crouse, M. J. J. Schmidth, L. Li, D. Garrod, Appl. Surf. Sci. 2007, 253, 7738.

[23] J. Li, H. Liao, B. Fartash, L. Hermansson, T. Johnsson, Biomaterials 1997, 18, 691.

[24] B. E. J. Lee, H. Exir, A. Weck, K. Grandfield, Appl. Surf. Sci. 2018, 441, 1034.

[25] L. Tiainen, P. Abreu, M. Buciumeanu, F. Silva, M. Gasik, R. Serna Guerrero, O. Carvalho, J. Mech. Behav. Biomed. Mater. 2019, 98, 26.

[26] T. U. Luu, S. C. Gott, B. W. K. Woo, M. P. Rao, W. F. Liu, ACS Appl. Mater. Interfaces 2015, 7, 28665.

[27] A. Palmquist, L. Emanuelsson, R. Brånemark, P. Thomsen, J. Biomed. Mater. Res., Part B 2011, 97, 289.

[28] A. Palmquist, F. Lindberg, L. Emanuelsson, R. Brånemark, H. Engqvist, P. Thomsen, J. Biomed. Mater. Res., Part A 2010, 92, 1476.

[29] R. Brånemark, L. Emanuelsson, A. Palmquist, P. Thomsen, Nanomedicine 2011, 7, 220.

[30] F. A. Shah, M. L. Johansson, O. Omar, H. Simonsson, A. Palmquist, P. Thomsen, PLoS One 2016, 11, e0157504.

[31] S. A. Cho, S. K. Jung, Biomaterials 2003, 24, 4859.

[32] O. M. Omar, M. E. Lennerås, F. Suska, L. Emanuelsson, J. M. Hall, A. Palmquist, P. Thomsen, Biomaterials 2011, 32, 374.

[33] H. Wang, K. Su, L. Su, P. Liang, P. Ji, C. Wang, J. Mech. Behav. Biomed. Mater. 2018, 88, 488.

[34] M. M. Costa, F. Bartolomeu, N. Alves, F. S. Silva, G. Miranda, J. Mech. Behav. Biomed. Mater. 2019, 94, 193.

[35] C. F. Dunne, K. Roche, B. Twomey, K. T. Stanton, Mater. Lett. 2016, 176, 185.

[36] H. I. Roach, G. Mehta, R. O. C. Oreffo, N. M. P. Clarke, C. Cooper, J. Histochem. Cytochem. 2003, 51, 373.

[37] P. Kuzyk, E. Schemitsch, Indian Journal of Orthopaedics 2011, 45, 108.

[38] L. M. Wancket, Vet. Pathol. 2015, 52, 842.

[39] X. Lin, S. Yang, K. Lai, H. Yang, T. J. Webster, L. Yang, Nanomedicine 2017, 13, 123.

[40] B. Elmengaard, J. E. Bechtold, K. Søballe, Biomaterials 2005, 26, 3521.

[41] S. Nganga, A. Ylä-Soininmäki, L. V. J. Lassila, P. K. Vallittu, J. Mech. Behav. Biomed. Mater. 2011, 4, 1797.

[42] T. Yu, H. Gao, T. Liu, Y. Huang, C. Wang, Mater. Sci. Eng., C 2020, 108, 110406.

[43] C. Castellani, R. A. Lindtner, P. Hausbrandt, E. Tschegg, S. E. Stanzl-Tschegg, G. Zanoni, S. Beck, A. M. Weinberg, Acta Biomater. 2011, 7, 432.

[44] M. Meischel, J. Eichler, E. Martinelli, U. Karr, J. Weigel, G. Schmöller, E. K. Tschegg, S. Fischerauer, A. M. Weinberg, S. E. Stanzl-Tschegg, J. Mech. Behav. Biomed. Mater. 2016, 53, 104.

[45] Q. Ran, W. Yang, Y. Hu, X. Shen, Y. Yu, Y. Xiang, K. Cai, J. Mech. Behav. Biomed. Mater. 2018, 84, 1.

[46] S. Bose, D. Banerjee, A. Shivaram, S. Tarafder, A. Bandyopadhyay, Mater. Des. 2018, 151, 102.

[47] F. Marco, F. Milena, G. Gianluca, O. Vittoria, Micron 2005, 36, 630. [48] S. V. Dorozhkin, Ceram. Int. 2015, 41, 13913.

[49] M. T. Choy, C. Y. Tang, L. Chen, C. T. Wong, C. P. Tsui, Mater. Sci. Eng., C 2014, 42, 746.

[50] E. K. Tschegg, R. A. Lindtner, V. Doblhoff-Dier, S. E. Stanzl-Tschegg, G. Holzlechner, C. Castellani, T. Imwinkelried, A. Weinberg, J. Mech. Behav. Biomed. Mater. 2011, 4, 766.

CHAPTER 9

Multi-Material Cellular Structured Orthopedic Implants Design: In Vitro and Bio-Tribological Response

Submitted to Applied Materials Today

M.M. Costa[a], R. Lima[b,c], N. Alves[d], N.A. Silva[b,c], M. Gasik[e,f], F.S. Silva[a], F. Bartolomeu[a,1], G. Miranda[g,h,1]

[a]Center for MicroElectroMechanical Systems (CMEMS-UMinho), University of Minho, Campus de Azurém, 4800-058 Guimarães – Portugal

[b]Life and Health Sciences Research Institute (ICVS), School of Medicine, University of Minho, Campus de Gualtar, 4710-057 Braga, Portugal

[c]ICVS/3B's - PT Government Associate Laboratory, Braga/Guimarães, Portugal

[d]Centre for Rapid and Sustainable Product Development Polytechnic Institute of Leiria, Rua General Norton de Matos, Apartado 4133, 2411-901 Leiria – Portugal

[e]School of Chemical Engineering, Aalto University Foundation, FI-00076 Espoo, Finland

[f]Seqvera Ltd., Helsinki, Finland

[g]CICECO, Aveiro Institute of Materials, University of Aveiro, 3810-193 Aveiro, Portugal

[h]Department of Materials and Ceramic Engineering, University of Aveiro, 3810-193 Aveiro, Portugal

[1] Co-last authorship

Abstract

In this study, Selective Laser Melting (SLM) was used to produce mono-material Ti64Al4V- and NiTi-cubic cellular structures with an open-cell size and wall thickness of 500 μm and 100 μm, respectively. Bioactive beta-tricalcium phosphate (βTCP) and polymer poly-ether-ether-ketone (PEEK) were used to fill the produced structures open-cells, thus creating multi-material components. These structures were characterized *in vitro* in terms of cell viability, adhesion, differentiation and mineralization. Also, bio-tribological experiments were performed against bovine plate to mimic the moment of implant insertion. Results revealed that metabolic activity and mineralization were improved on SLM mono-material groups, compared with control group. All cell metrics were improved with the addition of PEEK, conversely to βTCP where no significant differences were found. These results suggest that the proposed solutions can be used to improve implants performance.

Keywords: Multi-Material structures; NiTi-based; Ti6Al4V- based; *in vitro*; bio-tribological experiments

9.1. Introduction

Hip implants, as currently applied in the human body, are dense metallic components aiming to replace an injured joint, in order to recover joint functionality and restore pain-free mobility to the patient [1,2]. However, hip implants have limited lifespan, especially in younger patients that have a more active lifestyle which will lead, eventually, to implant failure and consequently the need to resort to revision surgeries that are more expensive and painful for the patient [2–4].

Among all complications that can occur that lead to implant failure, loss of fixation between the implant and bone is one of the most prevailing [3,5]. Commercially available dense hip implants are markedly different from natural bone, from both mechanical and biomechanical points of view. In fact, there is a stiffness mismatch between the existing implant metallic materials and bone, which leads to a phenomenon called stress shielding effect [3,6–9]. Briefly, in an artificial joint, when a load is applied, it is mainly transmitted through the implant and less stress is transmitted to the surrounding bone [3,9,10]. Due to this effect, bone starts to resorb, leading to implant loosening and its consequent failure. Besides, a non-uniform contact pressure between implant and bone can also lead to the same outcome. Lastly, implant micro-motions together with a poor wear resistance of implant materials can lead to wear particles release to the surrounding bone [3,6,8,9].

In order to overcome these problems, adding porosity to the implant, in a controlled manner, is a very attractive solution since it allows implant stiffness tailoring to values close to that of bone [7]. Despite being the most used material in implantology, Ti6Al4V (Ti64) offers several advantages, including mechanical strength, high biocompatibility and corrosion resistance however its elastic modulus is still high when compared to that of bone [2,3,6,11–15]. In this sense, by creating porous implants, it is possible to decrease the modulus of a Ti64 component, and reduce the stress shielding effect [10]. This controlled porosity can be achieved by manufacturing the implant through Additive Manufacturing techniques, particularly Selective Laser Melting (SLM). By SLM it is possible to manufacture, in a layer-by-layer process, components with high degree of complexity from CAD data [3,6,13–16]. Besides elastic modulus tailoring, this interconnected porosity will also assure nutrients flow and vascularization for cells to adhere and proliferate, thus allowing bone to grow towards and into the implant (mechanical interlocking) [3,5,13–15,17]. Ran et al. [18] evaluated the *in vitro* biological performance of different Selective Laser Melted porous Ti6Al4V implants (500, 700 and 900 μm pore sizes), and concluded that scaffolds with lower open-cell sizes were suitable for cell adhesion whilst higher sizes are beneficial for cell proliferation. It is also reported that these structures allow nutrients and oxygen supply for vascularization and osteogenesis, crucial aspects for promoting bone ingrowth, that, in turn, is extremely important to enhance bone-implant fixation. In a different study, this outcome was also reported by Yang et al. [19] that analyzed *in vitro* response of porous Ti6Al4V implants with different pore sizes fabricated by Laser Beam Melting, concluding that best cellular growth, migration and adhesion was found for both 350 and 500 μm pore size groups. Chen et al. [20], when analyzing the effect of pore size of Ti6Al4V structures on cell proliferation, osteogenesis and bone ingrowth, *in vitro* and *in vivo*, revealed that the scaffolds have no cytotoxic effect on cells, being 500 μm pore size the one that displayed greatest cell proliferation, differentiation and bone ingrowth.

Nickel-titanium (NiTi) alloy is an interesting material for such applications once it has high corrosion resistance, high biocompatibility and two attractive and special properties, shape memory effect and superelasticity [3,5,6,16,21–24]. When compared with Ti64, NiTi elastic properties are lower and its wear resistance superior, thus reducing the stress shielding effect and wear debris release, respectively. On the other hand, its shape memory effect can also be used to assure a uniform contact pressure between implant and bone [5,6,21].

The creation of multi-material solutions can be extremely advantageous when it is intended to fulfill different requirements in different regions of a same component. In this way, it will be

possible to gather different properties that a single material would not be able to possess [2]. For instance, poly-ether-ether ketone (PEEK) is a polymeric material that, besides being biocompatible and having high corrosion resistance, also owns an excellent wear resistance, being very attractive to enhance implant wear performance [5,13,25]. On the other hand, bioactive β-tricalcium phosphate (βTCP) is also very interesting for such application once both Ti6Al4V and NiTi are bioinert, meaning that they do not elicit a biological response when implanted [2,4,14]. Conversely, βTCP, as a bioactive material and being very similar to the mineral phase of bone, will interact with the biological environment and induce a faster osseointegration [2,13,14,24]. Zheng et al. [26] evaluated the biocompatibility and mineralization *in vitro* of PEEK scaffolds and PEEK-HA composites manufactured by additive manufacturing and showed that, although both options displayed good cytocompatibility, the addition of hydroxyapatite enhanced cell adhesion and mineralization. Park et al. [27] manufactured βTCP-PCL scaffolds by 3D bioprinting, with different concentrations and showed an improved cell proliferation and alkaline phosphatase (ALP) activity in the composite scaffolds, especially with higher βTCP concentrations, when compared to no-bioactive groups. Similarly, Harb et al. [28] performed PMMA-TiO$_2$ and PMMA-ZrO$_2$ coatings, modified with hydroxyapatite and βTCP on Ti6Al4V implants, revealing an enhanced ALP activity and calcium concentration on the coating and even higher for the coating with the bioactive materials included, when compared with Ti6Al4V.

However, both PEEK and βTCP mechanical properties are not suitable for load-bearing applications [2,14,29], in this sense, combining them with stronger materials like Ti64 and/or NiTi, will guarantee the necessary biological and mechanical requirements.

In this context, creating mono- and multi-material solutions to bring multi-functionality to implants and overcome the current implant problems, aiming to create implants for life, is the main focus of the present study. In this sense, SLM will be used to manufacture NiTi and Ti64 cellular structures that will be further impregnated either by PEEK or βTCP. With these solutions it is possible to meet specific requirements like lowering implant elastic properties and promoting bone ingrowth through the interconnected porosity, improve wear resistance by introducing materials as NiTi and PEEK or add bioactivity through βTCP incorporation.

For that purpose, in the following study, different solutions gathering different materials were manufactured and characterized *in vitro* to assess cell viability, adhesion and metabolic activity and its potential differentiation and mineralization as well as their implant-bone tribological interaction at the moment of implantation.

9.2. Experimental Details

9.2.1. Specimens Fabrication

In the present study, seven different groups were designed and manufactured and further characterized with details being presented in Table 9.1.

Table 9.1 - Group description and fabrication method.

Group	Description	Fabrication Method
G1	Ti64 SLA	Cast SLA-treated
G2	Ti64 SLM	SLM
G3	Ti64-βTCP	SLM+PS
G4	Ti64 -PEEK	SLM+HP
G5	NiTi	SLM
G6	NiTi-βTCP	SLM+PS
G7	NiTi-PEEK	SLM+HP

SLA – Sandblast-acid etching; PS – press and sintering;
HP – hot pressing.

As a representation of commercially available implant, dense Ti64 cast/forged commercial rod, obtained from *Titanium Products (United Kingdom)*, having 6 mm diameter, was cut and exposed to sandblast-acid etching process (SLA) to display a moderate roughness topography frequently used in implants (between 2 and 4 μm) [2,30,31]. These specimens were sandblasted with spherical alumina particles and further acid etched in a 32% HCL, 96% $H2_sO_4$ and H_2O (2,1,1) solution, for 5 minutes at 65 °C ± 4°C and ultrasonically cleaned in isopropanol for 5 minutes. This group, schematically represented in Figure 9.1 (A) will be named throughout this manuscript as G1.

For cellular structures manufacture, Ti64 and NiTi were used as base materials in which Ti64 (ELI – grade 23) starting powder, with a spherical morphology, were purchased from *SLM solutions*, with a particle size (d50) of 46.94 μm, and NiTi powder was obtained by atomizing (at *TLS technique GmbH, Germany*) a $Ni_{50.8}Ti_{49.2}$ ingot (at.%) from *SAES Smart Materials*, using an electrode induction-melting gas atomization (EIGA) technique. The final powder displayed a spherical morphology with a particle size, d50, of 47.5 μm. NiTi and Ti64 cellular structures were designed and fabricated using an SLM equipment (*SLM solutions, model 125HL*) with an 400W Ytterbium-fiber laser with 87 μm diameter. The process occurred under argon atmosphere, with a heated platform at 200°C, using the 90 W laser power, 600 mm/s scan speed, 30 μm layer thickness and 90 μm scan spacing. Figure 9.1 (B) illustrates the SLM manufacturing process used

for Ti64 and NiTi cellular structures. These Ti64 and NiTi cellular structures, CAD designed with an open-cell size of 500 μm and wall thickness of 100 μm, will be used as G2 and G5 groups, respectively, and will also act as base specimens for multi-material production.

Multi-material specimens were produced by impregnating into these cellular structures either βTCP or PEEK. For that purpose, βTCP spherical powder with a d50 of 2.26 μm was purchased from *Trans-Tech, Inc*. while PEEK powder, d50 of 50 μm, having an irregular shape was obtained from *Evonik Industries (Germany)*. For multi-material structures with βTCP the process begins by mixing the bioactive powder with acetone to create a viscous solution (≈ 36% (w/v)). This solution and the cellular structures were inserted inside a 10 mm (diameter) steel die and a hydraulic press was used, at a pressure of ≈74 MPa, for 10 minutes to force the entrance of the solution into the structures. The multi-material specimens were then sintered in a tubular furnace at 1100°C for 2h, at a heating rate of 8 °C/min, in an argon atmosphere for NiTi-βTCP specimens and high vacuum for Ti6Al4V-βTCP specimens. Regarding multi-material structures with PEEK hot pressing (HP) technique was used for the structure's impregnation. In this process, PEEK powder and the NiTi or Ti6Al4V cellular structures were inserted inside an 8 mm graphite die, following by its positioning inside a hot pressing equipment. Under vacuum, a residual pressure was firstly applied to accommodate the powder and the temperature was raised up to 380°C (above PEEK melting point (345°C)). The induction heating was turned off and when the temperature reaches 300°C, a pressure of around 10 MPa was applied for approximately 15 seconds to force the polymer to fill the open cells. After repeating this cycle two times, the specimen was allowed to cool till room temperature. Figure 9.1 (C) and (D) displays a schematic representation of βTCP and PEEK impregnation process, respectively.

Additionally, a final group of multi-material samples, named throughout the manuscript as bimetallic, were manufactured and will act as a proof-of-concept by introducing a next level of multi-material multi-functionality. In this context, NiTi-Ti64 multi-material bimetallic cellular structures were produced by SLM according to the following steps: a NiTi region was firstly printed, up to a predefined layer number; the fabrication process was stopped and all the excess/loose NiTi powder was removed from the platform and replaced by Ti64 powder, manually; Ti6Al4V region was then printed on top of the previously manufactured NiTi, up to the final layer designed in the CAD data. The processing parameters used were selected according to the ones defined for mono-material production and were: 90 W laser power, 600 mm/s scan speed, 30 μm layer thickness and 90 μm scan spacing, which corresponds to an energy density of 55.6 J/mm³. These final samples

CAD files had an open cell and wall thickness of 500 μm and 100 μm, respectively. Afterwards, for tri-material production, NiTi-Ti64 specimens' open-cells were filled with PEEK following the same process used for G4 and G7 groups. Similarly, NiTi-Ti64-βTCP specimens were produced similarly to G3 and G6 groups.

Before characterization, all groups were polished with SiC abrasive papers up to P4000, ultrasonically cleaned with isopropanol, dried in vacuum for 30 minutes and stored in a desiccator until characterization.
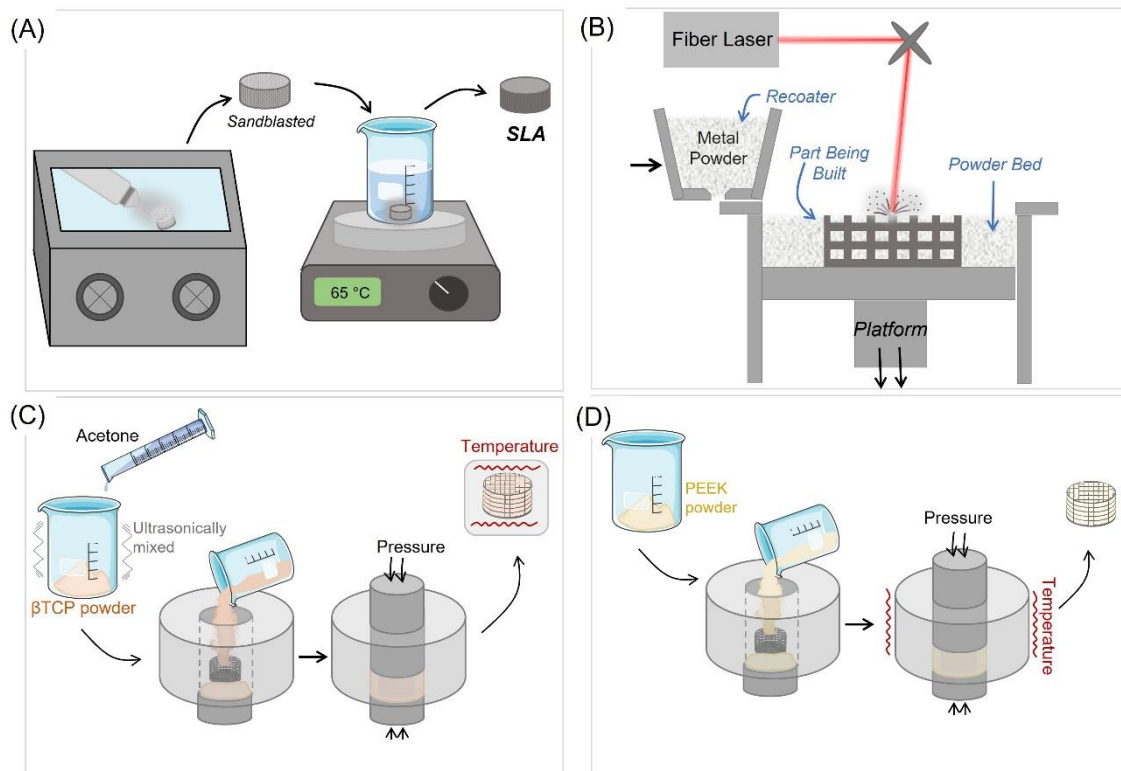
Figure 9.1 - Schematic representation of the fabrication methods for the produced specimens (A) Sandblast Acid Etching (SLA); (B) SLM; (C) βTCP and (D) PEEK impregnation.

9.2.2. Morphological and Crystallographic Characterization

The surface morphology of specimens from the different groups was observed by means of Scanning Electron Microscopy (SEM), before and after biological and bio-tribological tests. Moreover, X-ray diffraction analysis (XRD) was also performed on the produced specimens, before characterization, using a *Bruker AXS D8 Discover (USA)* equipment from 10 to 90°, with a step size and counting time of 0.02° and 1s, respectively. Energy-dispersive X-Ray spectroscopy analysis (EDS) was also used, when needed, after bio-tribological tests in specific sites of the specimens to assess material transfer.

9.2.3. *In Vitro* Experiments

9.2.3.1. Cytotoxicity Assessment

The short-term cytotoxicity of the produced scaffolds was performed according to Silva et al. [32], in triplicate. The scaffolds were placed in minimum essential medium (MEM) and extracted after 24 hours, 7 and 28 days. In all tests, material weight-to-extract fluid rate was constant (0.2 g/ml) and after each time point the extracts were filtered through a 0.45 mm pore-size filter.

9.2.3.1.1. Cell Culture

Rat lung fibroblasts-L929 cell line from European Collection of Cell Cultures were seeded in a 24-well plate (n=3, 5×10^3 cells/well) and then cultured at 37°C in a humidified atmosphere with 5% CO_2, for 24 hours in Dulbecco's modified Eagle's medium (DMEM) culture medium (*Sigma, Missouri, USA*). This media was supplemented with 10% fetal bovine serum (FBS) (*Gibco, Barcelona, Spain*) and 1% antibiotic-antimycotic mixture (*Sigma*).

9.2.3.1.2. MEM Extraction Test

Twenty-four hours after cell seeding, the culture medium was removed from the wells and replaced by the MEM extraction fluid. The L929 cultures were then incubated for 72 hours at 37°C in a humidified atmosphere with 5% CO_2. Live cells were stained with calcein-AM (1 mg/ml; *Molecular Probes, Eugene, OR*) and nonviable cells with propidium iodide (0.1 mg/ml; *Molecular Probes*). After incubation for 15 min at 37°C in a humidified atmosphere with 5% CO_2, cultures were observed under a fluorescence microscope (*BX-61; Olympus, Hamburg, Germany*). Latex extracts were used as negative controls for cell survival, whereas standard culture medium was used as positive control.

9.2.3.2. Dynamic Direct Contact Assay

Cell attachment and proliferation can be assessed by direct contact assay in order to evaluate the *in vitro* biocompatibility of the scaffolds [33]. Human Mesenchymal Stem Cells (hMSCs) derived from human bone marrow (*Lonza, Switzerland*) were cultured as monolayers in Alpha minimum essential medium (α-MEM). This medium was supplemented with 10% FBS and 1% antibiotic-antimycotic mixture, in sterile T175 tissue culture flasks.

Cell seeding was performed as previously described [34]. Briefly, the P6 hMSCs were trypsinized, centrifuged and resuspended in α-MEM medium. Subsequently, 50μl of medium

containing 1×10^5 cells were seeded on top of the scaffold. One hour after cell seeding, 750 µl of culture medium was added to each well and cell-scaffold were incubated 24 hours in static conditions. After 24 hours cultures in static conditions were changed to orbital shaking (100 rpm) and kept for 7 days in a humidified atmosphere at 37°C, containing 5% CO_2, with medium changes every 3 days.

9.2.3.2.1. Alamar Blue Viability Assay

Cell viability was determined by Alamar Blue cell viability reagent (*Invitrogen, Massachusetts, USA*). The assay solution was prepared by adding 1/10th of cell viability reagent in α-MEM medium. This solution was added to cell-scaffold for 4 hours at 37°C, containing 5% CO_2, protected from direct light in dynamic conditions. The fluorescence was measured (excitation at λ=560 nm; emission at λ=590 nm) with fluorescence spectrophotometer (*Varioskan Flash; Thermo Scientific, Massachusetts, USA*).

9.2.3.2.2. Cell Distribution and Morphology

After 7 days of culture, the distribution and morphology of the hMSCs were evaluated using phalloidin/DAPI staining [35]. Phalloidin labels cytoskeleton (red) whereas the nucleus is stained with DAPI (blue). After cells fixation with 4% paraformaldehyde (PFA; *Sigma, Missouri, USA*) for 30 min at room temperature, the cell-scaffold structure was washed and sliced. Both the top and the sliced scaffold structures were incubated with 0.1µg/ml of phalloidin (*Sigma, Missouri, USA*) and 1µg/ml of DAPI (*Sigma, Missouri, USA*) during 30 min. Finally, scaffolds were washed with PBS and observed under a confocal microscope (*Fluoview FV 1000; Olympus, Hamburg, Germany*).

9.2.3.3. Osteogenic Differentiation

Cell differentiation was performed accordingly Westhrin et al. [36]. Briefly, hMSCs were cultured at 37°C in a humidified atmosphere containing 5% CO_2 in α-MEM, 10% FBS and 1% antibiotic-antimycotic mixture. To induce osteogenic differentiation the media was supplemented with bone morphogenetic protein 2 (BMP-2, 300 mg/ml, *Millipore, Massachusetts, USA*), ascorbic acid (0.05 mM), dexamethasone (10-8 M) and glycerophosphate (10 mM). Cells for differentiation purposes were used before passage 8.

9.2.3.3.1. Alizarin Red Staining and Quantification

Alizarin Red S (AR; *Sigma, Missouri, USA*), an anthraquinone dye, has been widely used to evaluate calcium deposits in cell culture. The AR staining is quite versatile because the dye can be extracted from the stained monolayer of cells and readily assayed. We have applied this quantification assay to the osteogenesis induction of hMSCs. Cells were cultured in different media, α-MEM and osteogenic differentiation media for 15 days and fixed with PFA 4% and AR staining and quantified for mineral deposit using. The AR staining was performed after removal of the fixative and wash the cell-scaffold 3 times with deionized water (dH_2O). After completely remove the dH_2O, 40 mM AR was added to each well and incubated at room temperature (RT) for 30 min with gentle orbital shaking. The dye is then removed, and the cell-scaffold were washed 5 times with dH_2O, and photomicrographs were taken in brightfield microscopy (*Leica MZ FLIII; Leica, Germany*).

In order to quantify the calcium mineralization, after photomicrographs acquisition, 10% acetic acid (*Sigma, Missouri, USA*) was added to each well and incubated at RT for 30 min while shaking. Then each cell-scaffold was vortex for 30 seconds, and heated at exactly 85°C for 10 min. Samples were incubated on ice for 5 min, and centrifuges at 20.000 g for 15 min. After centrifugation, 500 µl of supernatant was transfer to a new tube and 200 µl of 10% ammonium hydroxide (*Sigma, Missouri, USA*) was added. Aliquots of 150 µl of samples and standards were measured in triplicates in a 96-well plate, and absorbance read at 405 nm with the plate reader (*NanoQuant Infinite M200; Tecan, Switzerland*).

9.2.4. Implant-Bone Interaction Tests

The main purpose of this tests is to mimic, as close to reality as possible, the tribological behavior that occurs during hip implant insertion. For this test, a custom-made apparatus was made consisting of a polymeric support for the specimens, rigidly fixed to a load cell, and an acrylic device fixed to the tribometer where rectified femoral young bovine bone plates were mounted, as shown schematically in Figure 9.2.
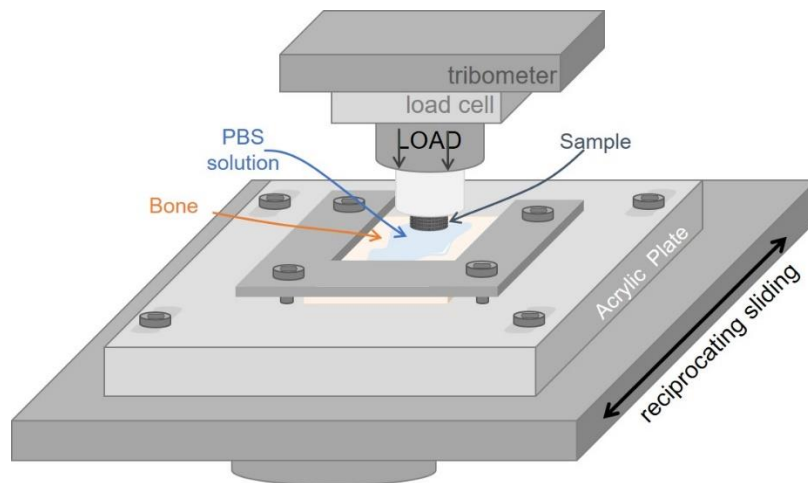
Figure 9.2 - Schematic illustration of the apparatus for bone-implant interaction experiments.

The experiments were carried out in a flat-on-flat reciprocating sliding configuration, using a tribometer from *Bruker (UMT-2 model, USA)*.

Three distinct moments were analyzed during these tests, specifically regarding static initial (Si), implantation (I) and final static (Sf) periods. Briefly, at the moment of implantation, there is a counterforce to the insertion movement, referred as frictional force, being this phenomenon replicated in these bio-tribological tests as static initial. Then, the moment of implant insertion into the bone cavity happens, in which, at this stage, an interaction between the implant and bone occurs (implantation test). This test was performed for a sliding distance of 100 mm in order to mimic the distance commonly used in implant surgeries [31,37,38]. Static final test aims to evaluate the final stability of the implant, i.e., after implant positioning, there is a final frictional force that will dictate the stability of the implant that is in literature named as primary stability [14,38,39]. For all three tests a normal load of 50 N was used, using Phosphate-Buffered Saline (PBS) solution, that was kept in a water bath at 37 °C, as lubrication fluid to mimic the physiological conditions during implantation. After each test, the samples were ultrasonically cleaned in isopropanol for 2 minutes to remove loose debris resultant from the bio-tribological tests.

9.2.5. Statistical Analysis

Statistical analysis was performed on *GraphPad Prism 8 software*, by using one way-ANOVA with differences between groups compared with the post hoc Bonferroni test to assess the statistically significant differences on bone-implant interactions and *in vitro* results between all the produced specimens under study. The results were displayed as mean ± standard deviation. Statistical significance was defined for $p < 0.05$ (95% confidence value).

9.3. Results and Discussion

9.3.1. Morphological and Crystallographic Characterization

In the present study, NiTi and Ti64 were used as powdered base materials to manufacture cellular structures by means of Selective Laser Melting and thus produce mono- and multi-material structures. Further PEEK or βTCP impregnation were performed as previously described. Figure 9.3 shows SEM images of top surfaces of all the produced cellular structured specimens and also Ti64 SLA group (G1), sandblasted and acid-etched, to represent the commercial solution currently used in hip implants.

When observing the SEM images from Figure 9.3, some dimensional deviations between the CAD model and the fabricated part are clearly noticed, namely lower open-cell sizes and larger wall thicknesses on SLM-produced specimens. These cubic-like specimens have open-cell sizes and wall thicknesses for NiTi structures of 384.2 ± 21.6 and 187.4 ± 22.9 μm and for Ti64 structures of 387.1 ± 33.6 and 178.1 ± 23.8 μm, respectively, similarly to previously reported studies from this group of authors for similar specimens and processing conditions [6,11]. In fact, literature extensively reports this phenomenon, inherent to SLM process, related with the partial melting of the powder particles next to the laser melted track. This leads to thicker walls and consequently smaller open-cells [5,6,18,40,41].

Multi-material groups revealed that the impregnation strategies used for both βTCP or PEEK impregnation were successfully accomplished, as the bioactive/polymeric material is mechanically imprisoned inside the open-cells, making its detachment more difficult as usually happens when the materials are applied as coatings.

Besides, it is important to highlight that the fabrication of high-quality NiTi specimens is challenging and only a limited group of authors reports its effective fabrication by this technology. In this sense, the NiTi-SLM parts produced in this study, also demonstrate the efficiency of the processing parameters used to produce this material and structures.
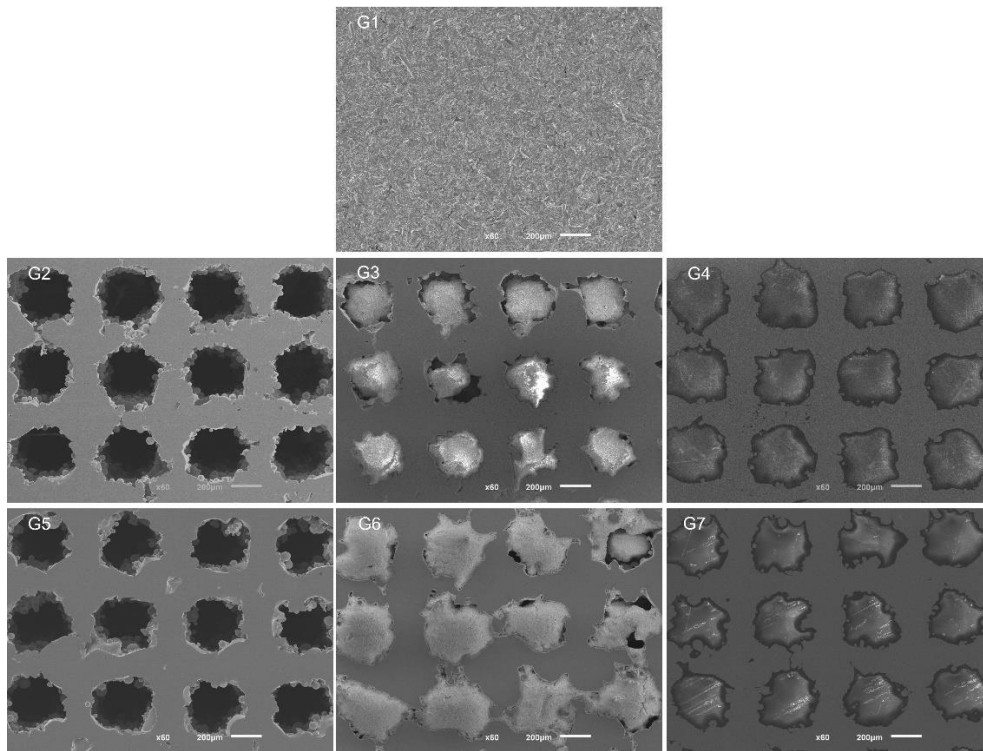
Figure 9.3 - SEM micrographs of G1-Ti64 SLA, G2-Ti64 SLM, G3-Ti64-βTCP, G4- Ti64-PEEK, G5- NiTi, G6- NiTi- βTCP and G7-NiTi-PEEK specimens.

Figure 9.4 and Figure 9.5 show the XRD spectra of Ti64-based and NiTi-based specimens, respectively. It is known that Ti64 is a β+α alloy, the body-centered cubic (BCC), known as β-phase, and the hexagonal close-packed (HCP) structure, α-phase [13,42,43]. When observing the Ti64-based specimens XRD spectra (Figure 9.4) both phases are detected in all groups. Comparing Ti64 SLA (G1) and Ti64 SLM (G2), despite presenting both phases, the intensities of the peaks slightly differ, which may indicate that the amount of each phase is different. In fact, it is reported in literature that Ti64 microstructure highly depends on the processing cooling rate [44,45]. While commercial cast Ti64 alloy, G1, is typically characterized by α phase and small amounts of β phase, in SLM, the high temperature gradients and fast cooling rate of the process will lead to the formation of α' phase [42,44–46]. In this sense, when regarding HCP crystalline structure, when analyzed in XRD, it can indicate the presence of α or α' phases, which cannot be distinguished in the spectra [2,3,13,42].

Regarding the NiTi-based specimens (Figure 9.5), NiTi group (G5) displays the main peaks corresponding to austenitic phase of NiTi, cubic – B2 phase (reference pattern no. 03-065-5746). Moreover, martensitic phase is not a clearly detected neither the formation of other intermetallic phases. Conversely, when observing NiTi- βTCP spectra (G6), there are some peaks that can be attributable to martensitic B19' phase, according to pattern no. 00-035-1281. Additionally, NiTi$_2$

and Ni_3Ti peaks can also be detected, considering the XRD reference patterns no. 01-072-0442 and 03-065-2038, respectively. This means that the experimental procedure used for βTCP sintering, where high temperatures are used, may act as a heat treatment step to the NiTi. Literature reports that heat treatment between 300-500°C will result in Ni_4Ti_3 phase formation, however, when the temperature increases to higher temperatures, it will lead to Ni_4Ti_3 dissolution into Ni_3Ti [47–49].

Finally, analyzing all the multi-material spectra in both figures (Ti64-βTCP, Ti64-PEEK, NiTi-βTCP and NiTi-PEEK), all the additional peaks detected are attributed to βTCP and PEEK materials, according to βTCP XRD pattern no. 009-0169 and XRD PEEK patterns found in literature [5,13,46].
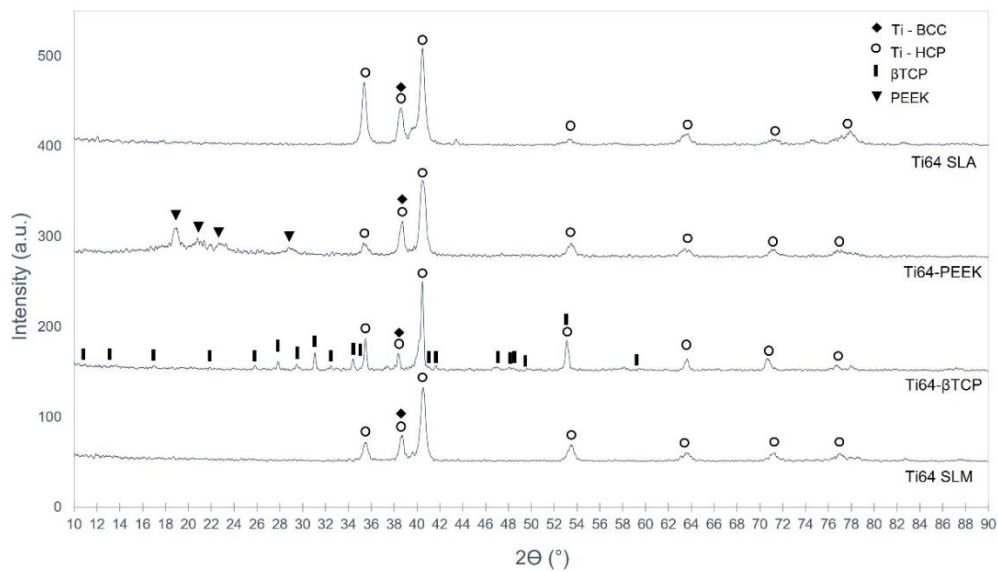
Figure 9.4 - XRD patterns for Ti64-based specimens.
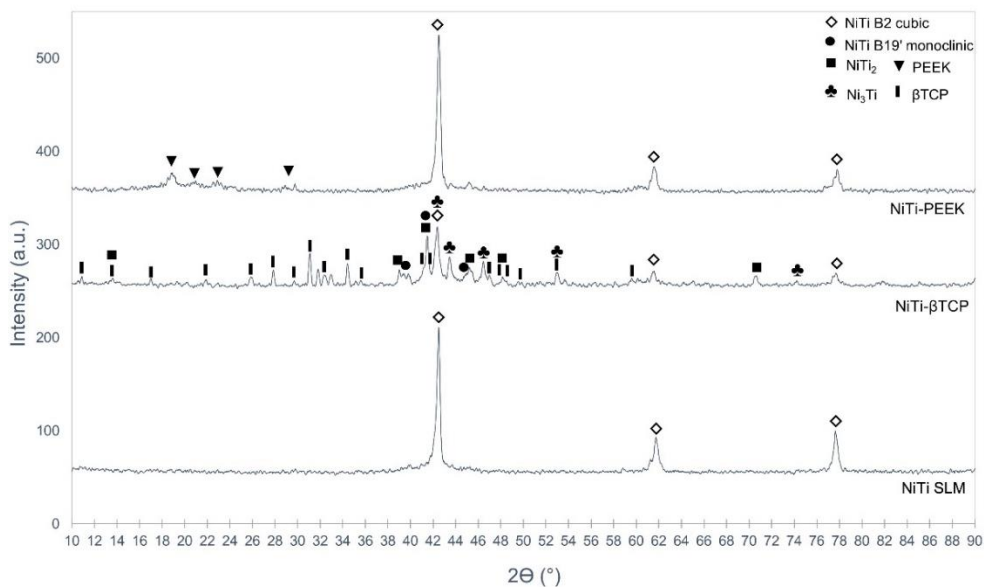
Figure 9.5 - XRD patterns for NiTi-based specimens.

9.3.2. *In Vitro* Analysis

9.3.2.1. Cell Viability

Right after implantation, a complex cascade of biological events will occur and, depending on implant's design, material and surface morphology, bone formation on and into its surface will take place. These biological events involve cell attachment, proliferation, differentiation and mineralization [27,50]. Nevertheless, before all this, it is first important to understand if the selected implant material would bring any toxic effect to the host tissue, i.e., if the material can provide a suitable environment for these cellular events to occur.

In this sense, to evaluate the cytotoxic effect of the produced specimens, i.e., the toxic effect of the products released from the specimens during incubation with MEM, L929 cells were cultured for 72h with the different MEM extracts (24h, 7 and 28 days for each condition) and live/dead staining performed (Figure 9.6).
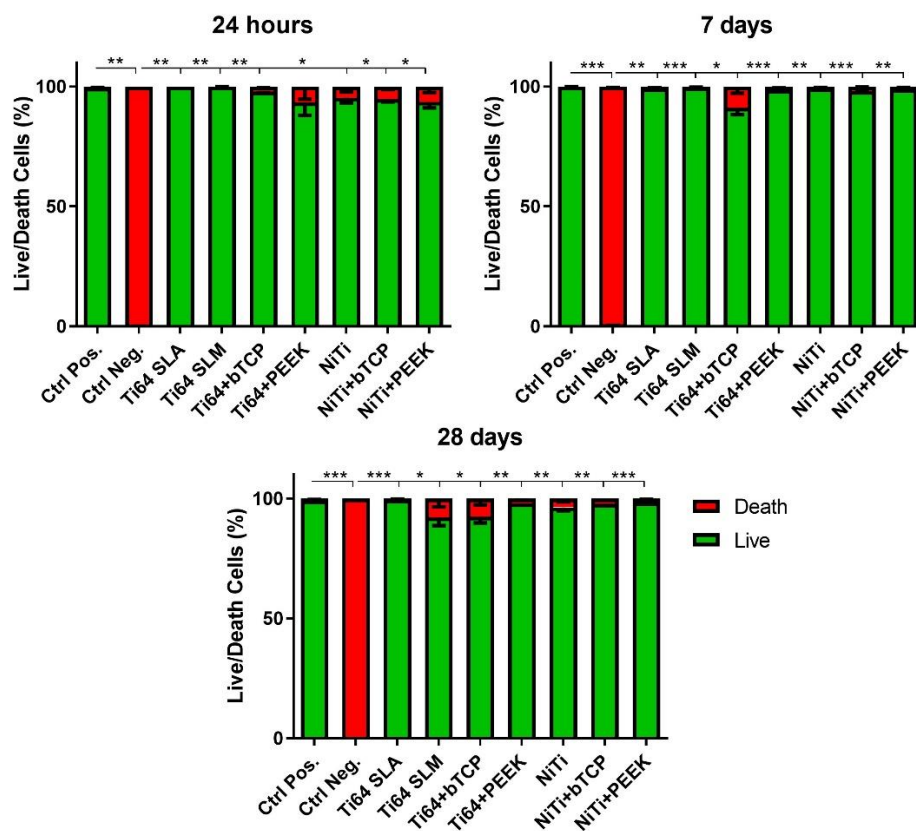
Figure 9.6 - Cell viability of L929 cells after cultured for 72h in the specimens' leachables released for the cultured medium during 24 h, 7 and 28 days. Values shown as mean ± SD. * - p < 0.05; ** - p < 0.01; *** - p < 0.001.

As shown in Figure 9.6, live/dead results revealed an average percentage of live cells in all groups above 90% even for the higher timepoint (28 days), which shows that all the produced

specimens did not induced cytotoxicity. Statistical analysis confirms such conclusion since no significant statistical differences were found between groups. Nevertheless, 24h after cell culture, all groups displayed statistically significant differences when compared with the negative control, with exception for Ti64-PEEK group. However, this outcome is not found on the ensuing timepoints. In this sense, results indicate that the adopted processing strategies (SLM, HP and PS) and the addition of a second material (βTCP or PEEK) had no significant effect on cell cytotoxicity, especially when compared with the available commercial solution (SLA).

9.3.2.2. hMSCs Adhesion and Metabolic Activity

Phalloidin/DAPI and Alamar blue assays were used to assess hMSCs cells morphology and metabolic activity when cultured for 7 days under dynamic conditions, with media renewal every 3 days. Fluorescence images of the groups and respective metabolic quantification after the experiments can be observed for Ti64-based groups and NiTi-based groups in Figure 9.7 and Figure 9.8, respectively.

When regarding Ti64-based groups, Figure 9.7, results indicate statistically significant differences between Ti64 SLA and SLM groups, with the latter presenting higher cell metabolic activity (p=0.0374), meaning that the cells have a preference over the architecture presented in G2-SLM group. It is worth mentioning that, despite SLA being the commercial solution nowadays used in orthopedics widely reported in literature as a surface modification that leads to an improved cellular response, the present results reveal a positive effect on the cellular activity on cellular structured group that has a polished surface condition. When analyzing Figure 9.8 graph for NiTi-based groups, a similar tendency is observed with NiTi group having higher metabolic activity than Ti64 SLA, although statistical analysis revealed no differences. This can be related with higher exposed surface area found in SLM groups, when compared with SLA (G1). This open interconnected architecture provides a suitable environment for free-flow of culture media and for the delivery to cells of the necessary nutrients and oxygen for them to proliferate. The fluorescence images of cell morphology indicate the actin cytoskeleton (red color) stained by Phalloidin, while cell nuclei is visible in blue (stained by DAPI). In both figures (Figure 9.7 and Figure 9.8) it is visible, especially at higher magnification, that cells migrate and proliferate inside the open-cells, corroborating the metric results. Despite cell density on G1-Ti64 SLA is higher, this is observed in a single plane, conversely to the mono-material cellular groups (G2 and G5) where cells can be found inside the open-cells, in fact a great indicator for further bone ingrowth. These findings are

in accordance with studies found in literature, that indicate that a porous, interconnected network enhance cell migration, proliferation and differentiation [18,19,27]. Ran et al. [18] stated that these porous structures facilitate nutrients and oxygen transport, crucial aspects for vascularization and osteogenesis for further bone ingrowth that, subsequently, will increase implant-bone fixation.

When observing multi-material Ti64-based groups, no significant differences were found between mono-material (G1 and G2) and Ti64-PEEK group (G4), however a pronounced metabolic activity decrease was observed in Ti64-βTCP (G3), that were statistically different from the remaining groups (p<0.0001). On NiTi-based specimens, a general similar trend is observed, however no significant differences were found among groups. Fluorescence images may help clarify such results, since in G3-Ti64 βTCP group, lower cell density is found adhered to the specimen, when compared with other groups, while in G6-NiTi βTCP this observation is not as pronounced. Regarding PEEK-impregnated specimens (G4 and G7), despite the open cells are fully impregnated with the polymeric material, higher density of cells is found in these groups which may be an indicator that PEEK has a positive effect on cell adhesion.
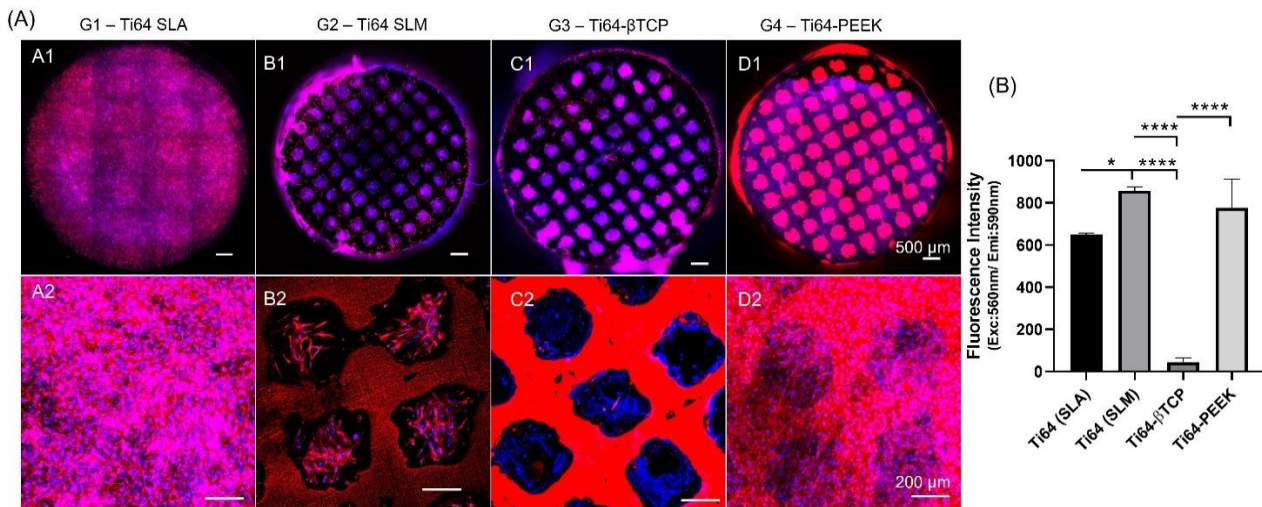
Figure 9.7 - (A) Fluorescence images of phalloidin/DAPI hMSCs staining after culturing under dynamic conditions for 7 days, at 2 different magnifications. (B) Metabolic activity results for cells cultured in Ti64-based specimens. Values shown as mean ± SD. * - p < 0.05; **** - p < 0.0001.
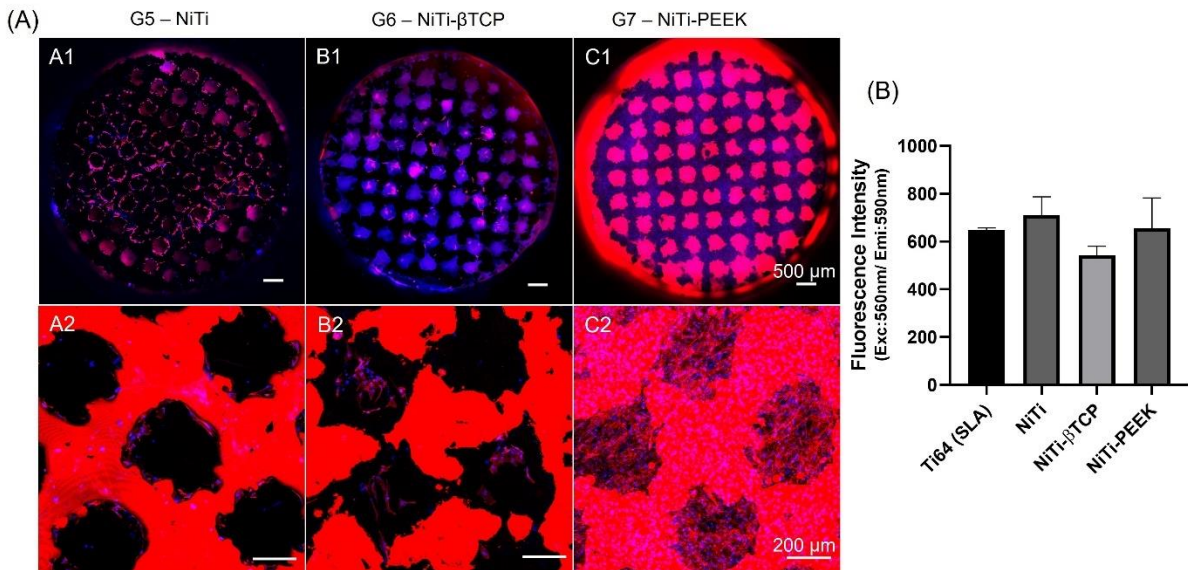
Figure 9.8 - (A) Fluorescence images of phalloidin/DAPI hMSCs staining after culturing under dynamic conditions for 7 days, at 2 different magnifications. (B) Metabolic activity results for cells cultured in NiTi-based specimens. Values shown as mean ± SD.

9.3.2.3. hMSCs Differentiation and Mineralization

After cell viability and hMSCs adhesion and metabolic activity, cell differentiation and mineralization were evaluated by Alizarin Red assay tests.

Alizarin red (AR) was used to detect calcium deposits on the specimens and detect extracellular matrix mineralization by mature osteoblasts [51,52]. Figure 9.9 and Figure 9.10 show images of alizarin red staining after cell culture for 15 days in Ti64-based and NiTi-based groups, respectively. For comparison purposes, the assay was performed in three different conditions with cells being cultured using an α-MEM or an osteogenic media, and a control condition where no cells were used, aiming to evaluate the reliability of the test. Results regarding quantitative AR analysis are in Figure 9.11.

When observing Alizarin Red staining it is possible to conclude that, in the osteogenic media, all the produced specimens, after 15 days, presented some degree of mineralization. AR quantifications prove this outcome by presenting, in both Ti64-based and NiTi-based groups (Figure 9.11 (A) and (B), respectively), higher mineralization in osteogenic media when compared to α-MEM media, as expected. This trend is visible in all groups, although significant differences were only found on Ti64-PEEK (p=0.0002) and NiTi-PEEK (p=0.0158) groups. Similarly, it is also visible that, when comparing with the control, higher values of mineralization were detected on osteogenic media, although no significant differences were found, except for Ti64-PEEK (p=0.0002) and NiTi-PEEK (p=0.0147). It is expected that, in control assays, no mineralization occurs once, in these samples, no cells were included. However, an increased AR was found on Ti64 SLM and NiTi

groups, being statistically different, in the NiTi-based specimens, when compared with Ti64 SLA (p=0.0327) and NiTi-PEEK (p=0.0436) groups. This outcome should be related with these groups' architecture, since the interconnected porous structure will difficult the cleaning step of the protocol.
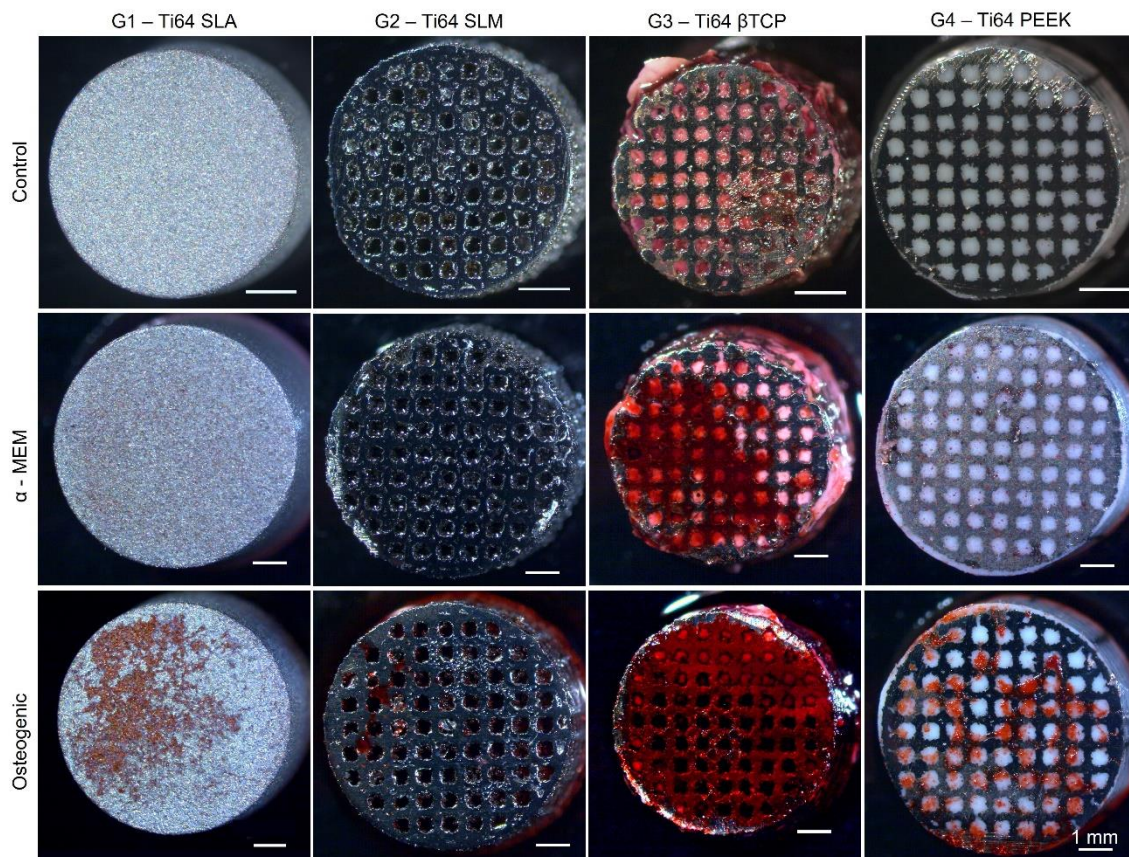
Figure 9.9 - Alizarin Red staining on Ti64-based specimens on control (no cells), α-MEM and osteogenic media.

By observing AR results for α-MEM media, a trend can be observed, with increased AR for Ti64- and NiTi-SLM groups (G2 and G5), when compared with SLA, with statistical differences found for the later (p=0.0097). An increased AR for PEEK-impregnated specimens was found, although not having significant differences, in comparison with SLA.

Figure 9.10 - Alizarin Red staining on NiTi-based specimens on control (no cells), α-MEM and osteogenic media.
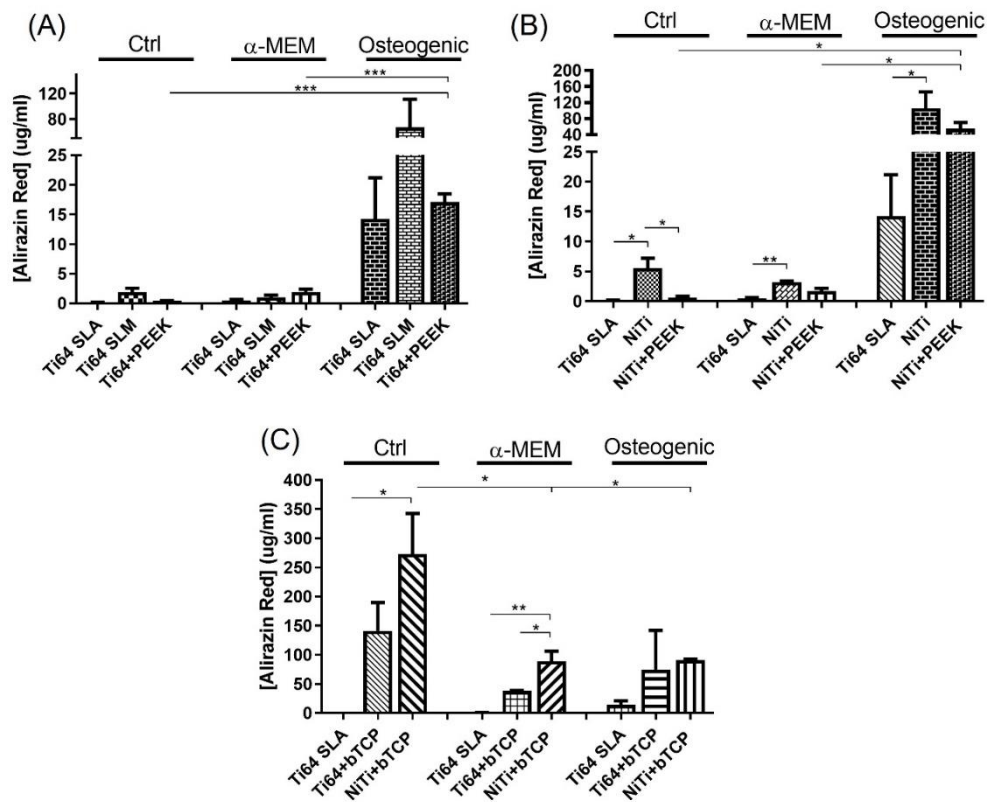
Figure 9.11 - Alizarin Red quantification for (A) Ti64-based, (B) NiTi-based groups and (C) Groups with βTCP for the different media after 15 days cell culture. Values shown as mean ± SD. * - p < 0.05; ** - p < 0.01; *** - p < 0.001.

When regarding the osteogenic media, no statistical differences were found among groups, in exception to NiTi that display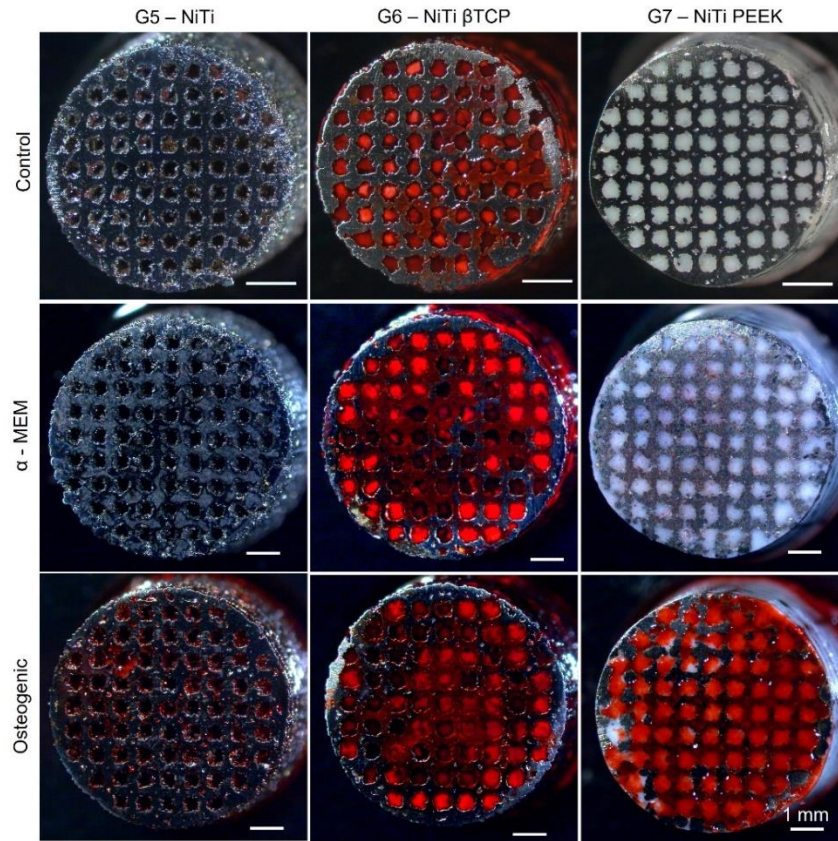s higher AR when compared with Ti64 SLA (p=0.0143), however, a similar trend can be detected with higher AR found for mono-material SLM groups and multi-material PEEK-impregnated ones, when compared to SLA. These results are in agreement with AR staining, where higher mineralization can be detected in PEEK-impregnated groups, in both osteogenic media and α-MEM, than in SLA. In SLM groups, these findings are not so visible to detect on the specimen's surface, indicating that mineralization may be occurring inside the structures. It is important to highlight that, in α-MEM, PEEK-impregnated groups already present some degree of mineralization, compared with the remaining groups, suggesting its enhanced ability to induce mineralization, without the addition of the osteogenic elements.

In fact, by observing Figure 9.9 and Figure 9.10, apparently, the groups with high degree of mineralization were the ones having βTCP as the surface is homogeneously distributed with deposits of calcium. As seen in Figure 9.11 (C), higher average values of mineralization with and without osteogenic factors were found, when compared with the remaining groups, in exception to NiTi-based groups in the osteogenic media, still being the second highest group. Compared with control Ti64 SLA group, statistical analysis only revealed significant differences for NiTi-βTCP group, with higher AR values found for the later (p=0.0085), although the tendency for higher values on βTCP groups is perceivable. However, it is important to highlight that βTCP already has calcium in its composition, and since AR detects calcium deposits, this could lead to a spontaneous dyeing. In this sense, the control results help on understanding the effect of this spontaneous dyeing in mineralization, since, in this condition, AR assays were performed in all groups without cells, as mentioned. Results, both from AR staining and quantification indicate that this test is not suitable for quantifying mineralization on calcium-based specimens once it is possible to identify "mineralization" even in the groups that were not in contact with cells, although significance was only detected on NiTi-βTCP group. In this sense, these results demonstrated that AR staining should not be used to quantify mineralization in the scaffold with βTCP, however, if used, the assay must be carried out with the same culture times, without cells, and the results must be presented considering the results obtained from the control.

Overall, results revealed that the scaffolds herein tested did not presented cytotoxic effects and that the proposed design of introducing a porous interconnected structure enhances the overall cellular response in terms of metabolic activity, differentiation, and mineralization, when compared with Ti64 SLA control group. As mentioned, this is related with the ability of such structures to

significantly enhance exposed surface area while providing space for a free-flow of oxygen and nutrients for cells to adhere, proliferate and differentiate, and for further bone to grown onto and into the scaffold. Moreover, as for multi-material specimens, the addition of PEEK has shown a positive effect, in comparison with Ti64 SLA, in terms of cell adhesion, differentiation and proliferation, and presenting an equal or better behavior when compared with SLM groups. Finally, general results revealed that the addition of βTCP does not bring any advantage in terms of improving cellular behavior. In fact, almost all metrics displayed non-significant differences or lower values when adding material. Conversely, several studies in literature report the beneficial effects of adding calcium phosphates for better adhesion and enhanced differentiation and mineralization, when compared with specimens without these materials [26–28,51,53]. In the present study, as mentioned, the addition of calcium phosphates did not bring any additional benefits when compared with the remaining groups. MarcBarb et al. [50] reported similar results when comparing the response of human osteoblasts in additive manufactured implants with traditional machined ones, with and without hydroxyapatite coating. In their study, results revealed that almost all metrics were decreased with the addition of hydroxyapatite and this outcome could be related with the bioactive crystallinity, since, highly crystalline hydroxyapatite is usually associated with lower dissolution that in turn negatively affect cellular adhesion [50,54]. Moreover, Backes et al. [51] also reported that using higher concentrations of βTCP would inhibit cell proliferation, based on previous reported studies [55,56]. It is discussed that higher amount of this bioactive material will decrease calcium and phosphate concentrations in the medium and, in turn, ions will be absorbed on the surface during crystalline growth and mineralization process. On the other hand, if used in lower concentrations, this material will promote cell growth as proteins are being absorbed and cells bonded to the surface. In this sense, literature is controversial when discussing *in vitro* response of bioactive materials, and in fact, this same response could vary depending on several aspects, namely the type of cells used and corresponding culturing needs, specimens production methods, surface conditions, etc [50]. Thus, it is also important to add that, *in vivo* experiments should be important to perform in further studies, to understand the behavior of such materials in a closer-to-reality conditions.

9.3.3. Implant-Bone Interaction Tests

When regarding implants implantation process, it is important to guarantee a good fixation to the surrounding bone for the osseointegration process to occur. For that purpose, the stability

of an implant is assured if primary and consequently secondary stability are guaranteed. During implantation, the press-fit process is responsible for assuring implant anchorage to the bone being, therefore, mechanically fixed and achieving primary stability [31,38,39,57]. Afterwards, a cascade of biological events will occur that will allow bone to grow at the implant-bone interface to guarantee long-term stability of the implant (secondary stability) [31,38,39]. In this sense, studying the implant-bone interaction during implantation is extremely important to assess implant adhesion and stability after the procedure (primary stability), fact that will influence the long-term success of the implant. Figure 9.12 shows the average static initial, implantation and static final coefficient of friction values, obtained during implant-bone interaction tests against bone plates. As mentioned, the static COF is related with the necessary force to initiate a movement. Static initial and static final COF (primary stability) were assessed. The dynamic coefficient of friction that aims to mimic the resistance to insertion was also assessed.

When analyzing static initial COF for Ti64-based groups (Figure 9.12 (A)) it is possible to observe that, from all groups, Ti64 SLA was the one with highest value, being the difference statistically significant from Ti64-βTCP (p=0.0035) and Ti64-PEEK (p=0.0033) groups. Similarly, higher static initial COF was found for G1 (Ti64 SLA), when compared with the remaining NiTi-based groups, as seen in Figure 9.12 (B), with p values for NiTi, NiTi- βTCP and NiTi-PEEK being 0.0273, 0.0006 and 0.0055, respectively. It has been proved that the tribological behavior is highly influenced by the surface properties of the materials (surface design, roughness) and by the testing conditions namely, applied load, lubrication conditions, etc [31,39,58,59]. When regarding the static coefficient of friction, surface chemical composition and morphology are crucial factors to consider. In this particular case, as mentioned, Ti64 SLA group (G1) exhibits a moderate surface roughness, contrary to the other groups where the walls of the structures have polished surface finishing. This means that, before sliding, the contact between G1 specimens and the bone was through the peaks of the surface, meaning that higher forces were required to initiate the movement. When comparing the mono-material SLM group with multi-material ones, it is found that the former displayed higher static initial COF, being statistically different for Ti64-based groups. Despite NiTi group was not found statistically different than multi-material NiTi-based groups, this tendency of higher static COF for mono-material group can also be observed. Despite all these structures have polished surface finishing, mono-material structures, having open-cells, have lower contact area than multi-material ones, where the cells are filled with bioactive or polymeric material.

This can explain the higher static initial COF, once the lower contact area leads to higher contact pressure and higher forces to start motion.

When regarding dynamic tests COF, no significant differences were found between groups, except for Ti64 SLM (G2) and Ti64 SLA (G1) with higher dynamic COF for the former (p=0.015). Nevertheless, average values indicate an overall trend, with the lowest COF displayed by G1. When sliding starts, after few cycles, surface peaks are polished and the valleys filled with detached bone now adhered to the surface, which will minimize the topography effect and reduce the coefficient of friction.

Theoretically, it is usual that the dynamic COF is lower than the static, however, statistical differences were only found in static initial COF for G1 and G2 group, despite average values show this trend. However, this is not observed for multi-material structures impregnated with βTCP, possibly due to bioactive detachment from the open cells, during sliding, releasing harder particles that will interact with the mating surfaces. When observing final static COF values, it can be concluded that, for all groups, higher values were obtained when compared with dynamic COF, being statistically different. This indicates that a good adhesion to bone has occurred, for all groups, with no significant differences between them.

Figure 9.13 show SEM micrographs of the worn surfaces, using two different magnifications, for all groups specimens. Chemical analysis was also performed to assess bone transfer to the specimens and results from the marked yellow zones in Figure 9.13 can be observed in Table 9.2. In these figures, the sliding directions are indicated by the white arrows. By observing the higher magnification images of the specimens, it is possible to observe, by atomic contrast, two distinct zones, a dark gray and a light gray, corresponding to the bone adhered to the surface and to the metal surface, respectively. For all the tested groups it is possible to conclude that adhesion mechanism occurred, due to bone adherence to the surface, but also abrasion since grooves aligned with the sliding direction are visible in all micrographs. Despite SEM micrographs, adhesion is also proven by EDS analysis since, in all groups, Ca and P (corresponding to bone) are detected. During sliding, the released bone debris will adhere to the specimens' surface and form a new compact tribolayer that will have a major contribution to the tribological behavior. In fact, this newly formed bone layer will smooth the specimens' surface and lower the coefficient of friction. In this study, it is visible that the adhered bone in G1 covers almost the entire surface whilst in the remaining groups this new bone layer extension is lower. As mentioned, this behavior can be

explained by G1 specimens surface roughness, higher than that of polished groups, but also the presence of open cells, during sliding, act as containers for bone wear debris to be collected.

These results indicate that, regarding primary stability, despite not displaying significant differences when compared with the commercially available solution (G1), the benefits arising from the proposed solutions, in terms of allowing bone ingrowth and elastic modulus tailoring make them extremely suitable and attractive for orthopedic applications.
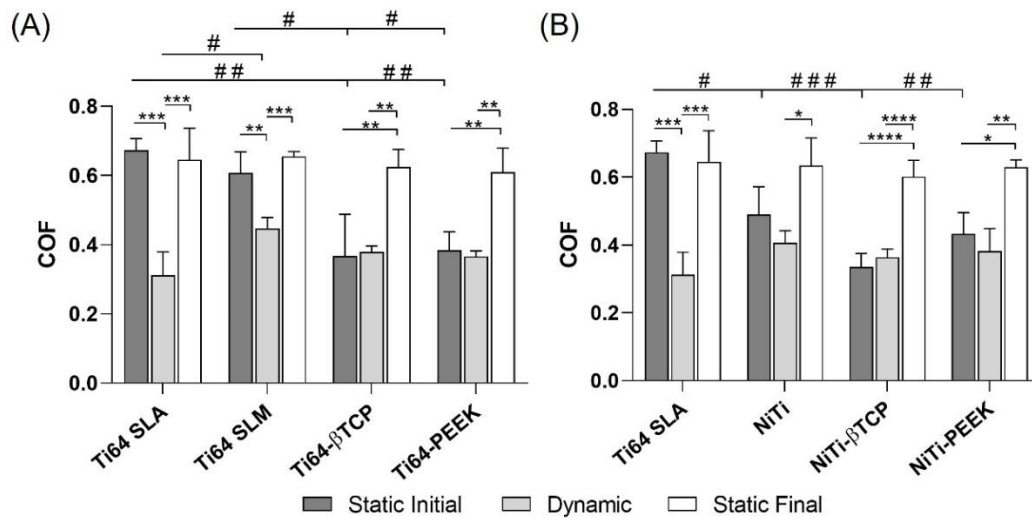
Figure 9.12 - Coefficient of friction (COF) values for static initial, dynamic and static final tests, for (A) Ti64-based specimens and (B) NiTi-based specimens, worn against bone plate. Values shown as mean ± SD. * or # - p < 0.05; ** or ## - p < 0.01; *** or ### - p < 0.001.

Finally, bimetallic specimens were also produced, as shown in Figure 9.14. From these images, it is possible to perceive, especially in the bimetallic group (NiTi-Ti64), the transition between NiTi and Ti64 cellular structure. This was successfully achieved, with a good bond between the two different materials, which, once again, validates the strategy and the processing parameters used. Similarly, the impregnation process was also validated, once the bioactive and polymeric materials were successfully impregnated into the open-cells.
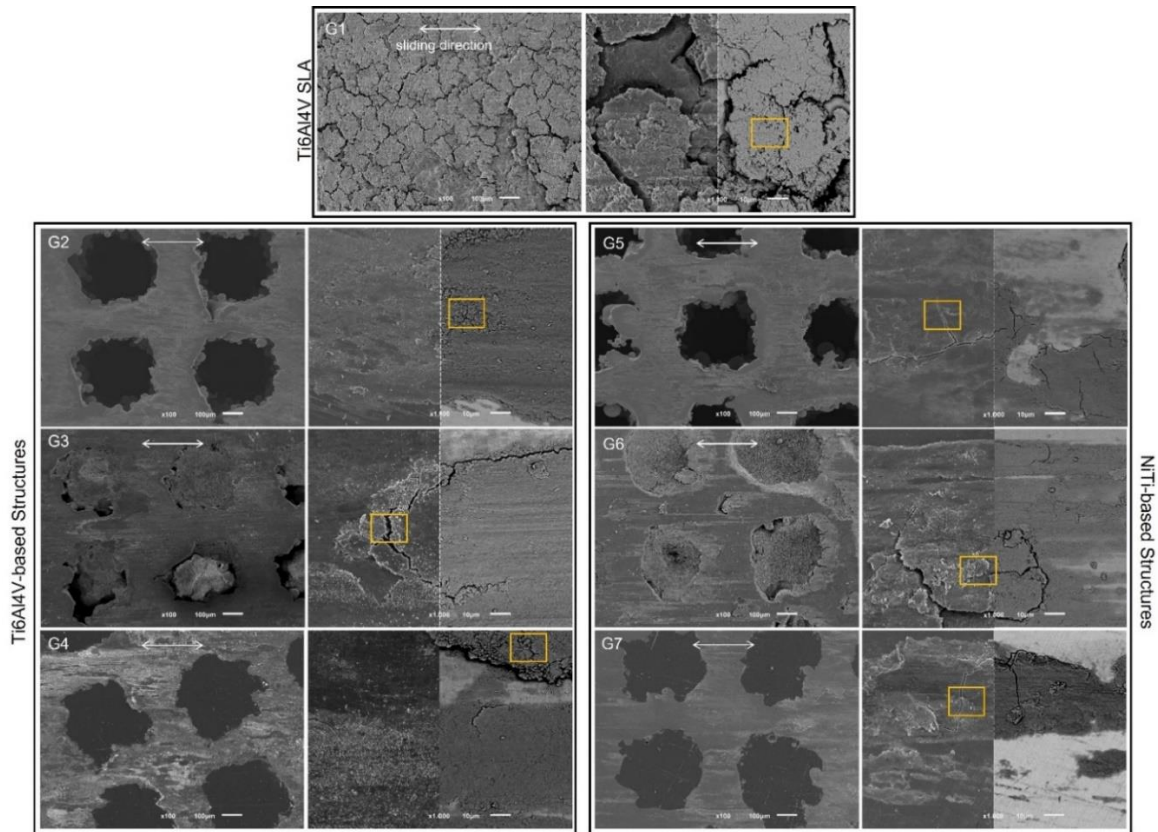
Figure 9.13 - SEM images of worn surfaces for G1-Ti64 SLA, G2-Ti64 SLM, G3-Ti64-βTCP, G4- Ti64-PEEK, G5- NiTi, G6- NiTi- βTCP and G7-NiTi-PEEK groups. Marked yellow squares represent EDS region (see Table 9.2).

Table 9.2 - Chemical composition (in wt. %) of the material transfer zones in all specimens.

Sample Group	Ca	P	Ti	Al	O	C	Others
G1: Ti64 SLA	27.2	14.5	1.5	-	38.3	16.6	1.9
G2: Ti64 SLM	21.4	11.4	10.6	0.7	39.8	13.4	2.7
G3: Ti64-βTCP	21.6	11.4	8.9	0.7	35.9	16.9	4.5
G4: Ti64-PEEK	23.6	13.3	1.2	-	37.9	17.2	6.8
G5: NiTi	27.2	15.1	2.2	-	39.9	12.4	3.3
G6: NiTi-βTCP	25.9	13.1	6.2	-	33.7	15.1	6
G7: NiTi-PEEK	25.5	15.6	1.5	-	37.5	16	3.9
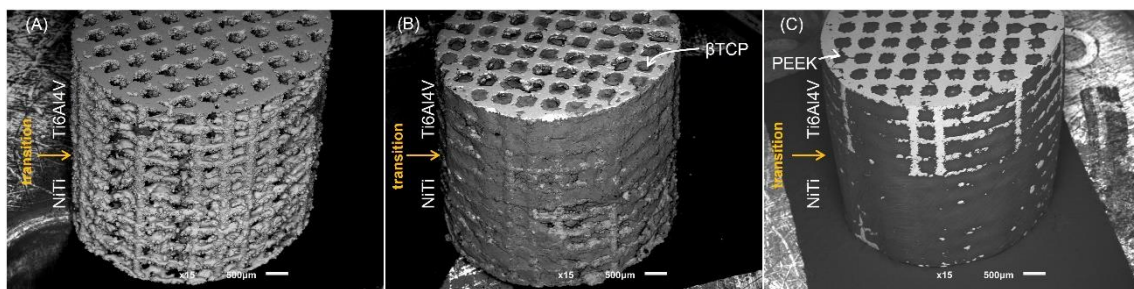
Figure 9.14 - SEM micrographs of bimetallic specimens isometric perspective (A) NiTi-Ti64, (B) NiTi-Ti64-βTCP and (C) NiTi-Ti64-PEEK.

These solutions were fabricated as a proof-of-concept of new approaches to bring multi-functionality to the final component, as schematically represented in Figure 9.15. In detail, by introducing porosity it is expected to enhance the bone-implant mechanical anchoring by promoting bone ingrowth and also tailor the elastic properties of the material. Bartolomeu et al [6,11] reported an elastic modulus for Ti64 and NiTi structures of ≈ 16 GPa and ≈ 4 GPa, respectively. Despite NiTi cellular structure has a lower elastic modulus, when compared to that of cortical bone (ranges between 10 and 30 GPa) [3,5,6,11], it is intended that this material is used on an outer layer of the implant, being the inner part composed of structured Ti64, that displays an elastic modulus within the referred cortical bone range. Moreover, the bioactive and polymeric materials can be added to a final multi-material solution allocated in different regions of the implant, where different requirements exist. Overall, these solutions are developed thinking of a broader goal, that is the fabrication of patient-specific implants that can fulfill local requirements by using different architectures and materials combinations.
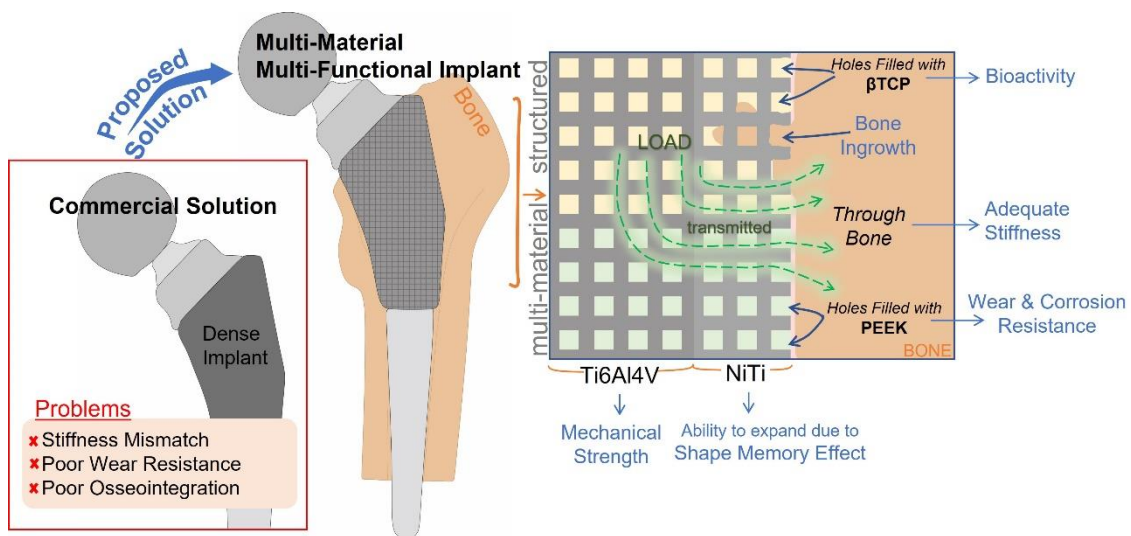
Figure 9.15 - Design concept of multi-material multi-functional hip implant solution.

9.4. Conclusions

In the present study, Ti6Al4V and NiTi cellular structures were successfully produced by Selective Laser Melting. Multi-material specimens, in which βTCP and PEEK were impregnated inside these structures using powder metallurgy techniques (Press and Sintering and Hot Pressing), were also effectively manufactured.

In vitro results revealed enhanced overall cellular response in SLM mono-material structures when compared with bulk SLA. The addition of PEEK provided a positive effect in cell adhesion,

metabolic activity and, subsequently, cellular differentiation and mineralization while βTCP addition seems to bring no advantage regarding cell behavior. Bone-implant interaction tests revealed that, besides Ti64 SLA, was the one displaying higher initial static coefficient of friction, no statistical differences among groups were found regarding primary stability, determined by the final static coefficient of friction.

Overall, the solutions here proposed can help to overcome the problems arising from commercially available choices, by providing adequate stiffness/elastic properties while assuring adequate cellular response without compromising the overall primary stability.

Acknowledgments

References

[1] C. Wedemeyer, H. Jablonski, A. Mumdzic-Zverotic, H. Fietzek, T. Mertens, G. Hilken, C. Krüger, A. Wissmann, H. Heep, R. Schlepper, M.D. Kauther, Laser-induced nanostructures on titanium surfaces ensure osseointegration of implants in rabbit femora, Materialia. 6 (2019) 100266. doi:10.1016/j.mtla.2019.100266.

[2] M.M. Costa, R. Lima, F. Melo-Fonseca, F. Bartolomeu, N. Alves, A. Miranda, M. Gasik, F.S. Silva, N.A. Silva, G. Miranda, Development of β-TCP-Ti6Al4V structures: Driving cellular response by modulating physical and chemical properties, Materials Science and Engineering C. 98 (2019) 705–716. doi:10.1016/j.msec.2019.01.016.

[3] F. Bartolomeu, M.M. Costa, N. Alves, G. Miranda, F.S. Silva, Additive manufacturing of NiTi-Ti6Al4V multi-material cellular structures targeting orthopedic implants, Optics and Lasers in Engineering. 134 (2020) 106208. doi:10.1016/j.optlaseng.2020.106208.

[4] I. Mitra, S. Bose, W.S. Dernell, N. Dasgupta, C. Eckstrand, J. Herrick, M.J. Yaszemski, S.B. Goodman, A. Bandyopadhyay, 3D Printing in alloy design to improve biocompatibility in metallic implants, Materials Today. 45 (2021) 20–34. doi:10.1016/j.mattod.2020.11.021.

[5] M.M. Costa, F. Bartolomeu, J. Palmeiro, B. Guimarães, N. Alves, G. Miranda, F.S. Silva, Multi-material NiTi-PEEK hybrid cellular structures by Selective Laser Melting and Hot Pressing: Tribological characterization, Tribology International. 156 (2021) 106830. doi:10.1016/j.triboint.2020.106830.

[6] F. Bartolomeu, M.M. Costa, N. Alves, G. Miranda, F.S. Silva, Engineering the elastic modulus of NiTi cellular structures fabricated by selective laser melting, Journal of the Mechanical Behavior of Biomedical Materials. 110 (2020) 103891. doi:10.1016/j.jmbbm.2020.103891.

[7] E. Alabort, D. Barba, R.C. Reed, Design of metallic bone by additive manufacturing, Scripta Materialia. 164 (2019) 110–114. doi:10.1016/j.scriptamat.2019.01.022.

[8] S. Solanke, V. Gaval, S. Sanghavi, In vitro tribological investigation and osseointegration assessment for metallic orthopedic bioimplant materials, Materials Today: Proceedings. 44 (2021) 4173–4178. doi:10.1016/j.matpr.2020.10.528.

[9] D. Shekhawat, A. Singh, A. Patnaik, Tribo-behaviour of biomaterials for hip arthroplasty, Materials Today: Proceedings. 44 (2021) 4809–4815. doi:10.1016/j.matpr.2020.11.420.

[10] S.Y. Chen, J.C. Huang, C.T. Pan, C.H. Lin, T.L. Yang, Y.S. Huang, C.H. Ou, L.Y. Chen, D.Y. Lin, H.K. Lin, T.H. Li, J.S.C. Jang, C.C. Yang, Microstructure and mechanical properties of open-cell porous Ti-6Al-4V fabricated by selective laser melting, Journal of Alloys and Compounds. 713 (2017) 248–254. doi:10.1016/j.jallcom.2017.04.190.

[11] F. Bartolomeu, J. Fonseca, N. Peixinho, N. Alves, M. Gasik, F.S. Silva, G. Miranda, Predicting the output dimensions, porosity and elastic modulus of additive manufactured biomaterial structures targeting orthopedic implants, Journal of the Mechanical Behavior of Biomedical Materials. 99 (2019) 104–117. doi:10.1016/j.jmbbm.2019.07.023.

[12] D. Faria, C.S. Abreu, M. Buciumeanu, N. Dourado, O. Carvalho, F.S. Silva, G. Miranda, Ti6Al4V laser surface preparation and functionalization using hydroxyapatite for biomedical applications, Journal of Biomedical Materials Research - Part B Applied Biomaterials. 106B (2018) 1534–1545. doi:10.1002/jbm.b.33964.

[13] M.M. Costa, T.A. Dantas, F. Bartolomeu, N. Alves, F.S. Silva, G. Miranda, F. Toptan, Corrosion behaviour of PEEK or β-TCP-impregnated Ti6Al4V SLM structures targeting biomedical applications, Transactions of Nonferrous Metals Society of China. 29 (2019) 2523–2533. doi:10.1016/S1003-6326(19)65160-5.

[14] M.M. Costa, F. Bartolomeu, N. Alves, F.S. Silva, G. Miranda, Tribological behavior of bioactive multi-material structures targeting orthopedic applications, Journal of the Mechanical Behavior of Biomedical Materials. 94 (2019) 193–200. doi:10.1016/j.jmbbm.2019.02.028.

[15] L. Yuan, S. Ding, C. Wen, Additive manufacturing technology for porous metal implant applications and triple minimal surface structures: A review, Bioactive Materials. 4 (2019) 56–70. doi:10.1016/j.bioactmat.2018.12.003.

[16] S. Parvizi, S.M. Hashemi, F. Asgarinia, M. Nematollahi, M. Elahinia, Effective parameters on the final properties of NiTi-based alloys manufactured by powder metallurgy methods: A review, Progress in Materials Science. 117 (2021) 100739. doi:10.1016/j.pmatsci.2020.100739.

[17] P. Gao, B. Fan, X. Yu, W. Liu, J. Wu, L. Shi, D. Yang, L. Tan, P. Wan, Y. Hao, S. Li, W. Hou, K. Yang, X. Li, Z. Guo, Biofunctional magnesium coated Ti6Al4V scaffold enhances osteogenesis and angiogenesis in vitro and in vivo for orthopedic application, Bioactive Materials. 5 (2020) 680–693. doi:10.1016/j.bioactmat.2020.04.019.

[18] Q. Ran, W. Yang, Y. Hu, X. Shen, Y. Yu, Y. Xiang, K. Cai, Osteogenesis of 3D printed porous Ti6Al4V implants with different pore sizes, Journal of the Mechanical Behavior of Biomedical Materials. 84 (2018) 1–11. doi:10.1016/j.jmbbm.2018.04.010.

[19] F. Yang, C. Chen, Q. Zhou, Y. Gong, R. Li, C. Li, F. Klämpfl, S. Freund, X. Wu, Y. Sun, X. Li, M. Schmidt, D. Ma, Y. Yu, Laser beam melting 3D printing of Ti6Al4V based porous structured dental implants: Fabrication, biocompatibility analysis and photoelastic study, Scientific Reports. 7 (2017) 45360. doi:10.1038/srep45360.

[20] Z. Chen, X. Yan, S. Yin, L. Liu, X. Liu, G. Zhao, W. Ma, W. Qi, Z. Ren, H. Liao, M. Liu, D. Cai, H. Fang, Influence of the pore size and porosity of selective laser melted Ti6Al4V ELI porous scaffold on cell proliferation, osteogenesis and bone ingrowth, Materials Science and Engineering C. 106 (2020) 110289. doi:10.1016/j.msec.2019.110289.

[21] J.W. Mwangi, L.T. Nguyen, V.D. Bui, T. Berger, H. Zeidler, A. Schubert, Nitinol manufacturing and micromachining: A review of processes and their suitability in processing medical-grade nitinol, Journal of Manufacturing Processes. 38 (2019) 355–369. doi:10.1016/j.jmapro.2019.01.003.

[22] J. Sevcikova, M. Pavkova Goldbergova, Biocompatibility of NiTi alloys in the cell behaviour, Biometals. 30 (2017) 163–169. doi:10.1007/s10534-017-0002-5.

[23] C.H. Hung, F.Y. Chang, T.L. Chang, Y.T. Chang, K.W. Huang, P.C. Liang, Micromachining NiTi tubes for use in medical devices by using a femtosecond laser, Optics and Lasers in Engineering. 66 (2015) 34–40. doi:10.1016/j.optlaseng.2014.08.001.

[24] M. Dulski, K. Dudek, M. Grelowski, J. Kubacki, J. Hertlein, M. Wojtyniak, T. Goryczka, Impact of annealing on features of BCP coating on NiTi shape memory alloy: Preparation and physicochemical characterization, Applied Surface Science. 437 (2018) 28–40. doi:10.1016/j.apsusc.2017.12.056.

[25] S. Verma, N. Sharma, S. Kango, S. Sharma, Developments of PEEK (Polyetheretherketone) as a biomedical material: A focused review, European Polymer Journal. 147 (2021) 110295. doi:10.1016/j.eurpolymj.2021.110295.

[26] J. Zheng, H. Zhao, E. Dong, J. Kang, C. Liu, C. Sun, D. Li, L. Wang, Additively-manufactured PEEK/HA porous scaffolds with highly-controllable mechanical properties and excellent biocompatibility, Materials Science and Engineering C. 128 (2021) 112333. doi:10.1016/j.msec.2021.112333.

[27] J.S. Park, S.J. Lee, H.H. Jo, J.H. Lee, W.D. Kim, J.Y. Lee, S.A. Park, Fabrication and characterization of 3D-printed bone-like β-tricalcium phosphate/polycaprolactone scaffolds for dental tissue engineering, Journal of Industrial and Engineering Chemistry. 46 (2017) 175–181. doi:10.1016/j.jiec.2016.10.028.

[28] S. V. Harb, N.J. Bassous, T.A.C. de Souza, A. Trentin, S.H. Pulcinelli, C. V. Santilli, T.J. Webster, A.O. Lobo, P. Hammer, Hydroxyapatite and β-TCP modified PMMA-TiO2 and PMMA-ZrO2 coatings for bioactive corrosion protection of Ti6Al4V implants, Materials Science and Engineering C. 116 (2020) 111149. doi:10.1016/j.msec.2020.111149.

[29] G.M. Peñarrieta-Juanito, M. Costa, M. Cruz, G. Miranda, B. Henriques, J. Marques, R. Magini, A. Mata, J. Caramês, F. Silva, J.C.M. Souza, Bioactivity of novel functionally structured titanium-ceramic composites in contact with human osteoblasts, Journal of Biomedical Materials Research - Part A. 106 (2018) 1923–1931. doi:10.1002/jbm.a.36394.

[30] Straumann, Scientific Evidence First Edition (2011), (2011) 1–36.

[31] F. Bartolomeu, M.M. Costa, J.R. Gomes, N. Alves, C.S. Abreu, F.S. Silva, G. Miranda, Implant surface design for improved implant stability – A study on Ti6Al4V dense and cellular structures produced by Selective Laser Melting, Tribology International. 129 (2019) 272–282. doi:10.1016/j.triboint.2018.08.012.

[32] N.A. Silva, A.J. Salgado, R.A. Sousa, J.T. Oliveira, A.J. Pedro, H. Leite-Almeida, R. Cerqueira, A. Almeida, F. Mastronardi, J.F. Mano, N.M. Neves, N. Sousa, R.L. Reis, Development and Characterization of a Novel Hybrid Tissue Engineering–Based Scaffold for Spinal Cord Injury Repair, Tissue Engineering Part A. 16 (2010) 45–54. doi:10.1089/ten.tea.2008.0559.

[33] S. Ribeiro-Samy, N.A. Silva, V.M. Correlo, J.S. Fraga, L. Pinto, A. Teixeira-Castro, H. Leite-Almeida, A. Almeida, J.M. Gimble, N. Sousa, A.J. Salgado, R.L. Reis, Development and characterization of a PHB-HV-based 3D scaffold for a tissue engineering and cell-therapy combinatorial approach for spinal cord injury regeneration, Macromolecular Bioscience. 13 (2013) 1576–1592. doi:10.1002/mabi.201300178.

[34] A. Canha-Gouveia, A.R. Costa-Pinto, A.M. Martins, N.A. Silva, S. Faria, R.A. Sousa, A.J. Salgado, N. Sousa, R.L. Reis, N.M. Neves, Hierarchical scaffolds enhance osteogenic differentiation of human Wharton's jelly derived stem cells, Biofabrication. 7 (2015) 035009. doi:10.1088/1758-5090/7/3/035009.

[35] R. Silva, H. Ferreira, A.C. Carvalho, A.C. Gomes, A. Cavaco-Paulo, Protein microspheres as suitable devices for piroxicam release, Colloids and Surfaces B: Biointerfaces. 92 (2012) 277–285. doi:10.1016/j.colsurfb.2011.11.050.

[36] M. Westhrin, M. Xie, M. Olderøy, P. Sikorski, B.L. Strand, T. Standal, Osteogenic differentiation of human mesenchymal stem cells in mineralized alginate matrices, PLoS ONE. 10 (2015) e0120374. doi:10.1371/journal.pone.0120374.

[37] R.H. Wittenberg, R. Steffen, H. Windhagen, P. Bücking, A. Wilcke, Five-year results of a cementless short-hip-stem prosthesis, Orthopedic Reviews. 5 (2013) 16–22. doi:10.4081/or.2013.e4.

[38] T.A. Dantas, C.S. Abreu, M.M. Costa, G. Miranda, F.S. Silva, N. Dourado, J.R. Gomes, Bioactive materials driven primary stability on titanium biocomposites, Materials Science and Engineering C. 77 (2017) 1104–1110. doi:10.1016/j.msec.2017.04.014.

[39] C.G. Moura, R. Pereira, M. Buciumeanu, O. Carvalho, F. Bartolomeu, R. Nascimento, F.S. Silva, Effect of laser surface texturing on primary stability and surface properties of zirconia implants, Ceramics International. 43 (2017) 15227–15236. doi:https://doi.org/10.1016/j.ceramint.2017.08.058.

[40] F. Bartolomeu, M.M. Costa, N. Alves, G. Miranda, F.S. Silva, Selective Laser Melting of Ti6Al4V sub-millimetric cellular structures: Prediction of dimensional deviations and mechanical performance, Journal of the Mechanical Behavior of Biomedical Materials. 113 (2021) 104123. doi:10.1016/j.jmbbm.2020.104123.

[41] N. Taniguchi, S. Fujibayashi, M. Takemoto, K. Sasaki, B. Otsuki, T. Nakamura, T. Matsushita, T. Kokubo, S. Matsuda, Effect of pore size on bone ingrowth into porous titanium implants fabricated by additive manufacturing: An in vivo experiment, Materials Science and Engineering C. 59 (2016) 690–701. doi:10.1016/j.msec.2015.10.069.

[42] F. Toptan, A.C. Alves, Ó. Carvalho, F. Bartolomeu, A.M.P. Pinto, F. Silva, G. Miranda, Corrosion and tribocorrosion behaviour of Ti6Al4V produced by selective laser melting and hot pressing in comparison with the commercial alloy, Journal of Materials Processing Tech. 266 (2019) 239–245. doi:10.1016/j.jmatprotec.2018.11.008.

[43] F. Melo-Fonseca, R. Lima, M.M. Costa, F. Bartolomeu, N. Alves, A. Miranda, M. Gasik, F.S. Silva, N.A. Silva, G. Miranda, 45S5 BAG-Ti6Al4V structures: The influence of the design on some of the physical and chemical interactions that drive cellular response, Materials & Design. 160 (2018) 95–105. doi:10.1016/J.MATDES.2018.08.056.

[44] F. Bartolomeu, M. Buciumeanu, E. Pinto, N. Alves, F.S. Silva, O. Carvalho, G. Miranda, Wear behavior of Ti6Al4V biomedical alloys processed by selective laser melting, hot pressing and conventional casting, Transactions of Nonferrous Metals Society of China (English Edition). 27 (2017) 829–838. doi:10.1016/S1003-6326(17)60060-8.

[45] F. Bartolomeu, S. Faria, O. Carvalho, E. Pinto, N. Alves, F.S. Silva, G. Miranda, Predictive models for physical and mechanical properties of Ti6Al4V produced by Selective Laser Melting, Materials Science and Engineering A. 663 (2016) 181–192. doi:10.1016/j.msea.2016.03.113.

[46] F. Bartolomeu, M. Buciumeanu, M.M. Costa, N. Alves, M. Gasik, F.S. Silva, G. Miranda, Multi-material Ti6Al4V & PEEK cellular structures produced by Selective Laser Melting and Hot Pressing: a tribocorrosion study targeting orthopedic applications, Journal of the Mechanical Behavior of Biomedical Materials. 89 (2019) 54–64. doi:10.1016/j.jmbbm.2018.09.009.

[47] B.N.K. Reddy, N.K. Udayashankar, The effect of annealing temperature on the structural, morphological, mechanical and surface properties of intermetallic NiTi alloy thin films, Surfaces and Interfaces. 5 (2016) 62–71. doi:10.1016/j.surfin.2016.09.007.

[48] Y. Chen, S. Sun, T. Zhang, X. Zhou, S. Li, Effects of post-weld heat treatment on the microstructure and mechanical properties of laser-welded NiTi/304SS joint with Ni filler, Materials Science and Engineering A. 771 (2020) 138545. doi:10.1016/j.msea.2019.138545.

[49] A. Bhardwaj, M. Ojha, A. Garudapalli, A.K. Gupta, Microstructural, mechanical and strain hardening behaviour of NiTi alloy subjected to constrained groove pressing and ageing treatment, Journal of Materials Processing Technology. 294 (2021) 117132. doi:10.1016/j.jmatprotec.2021.117132.

[50] R.F. MacBarb, D.P. Lindsey, C.S. Bahney, S.A. Woods, M.L. Wolfe, S.A. Yerby, Fortifying the bone-implant interface part 1: An in vitro evaluation of 3D-printed and TPS porous surfaces, International Journal of Spine Surgery. 11 (2017) 105–115. doi:10.14444/4015.

[51] E.H. Backes, E.M. Fernandes, G.S. Diogo, C.F. Marques, T.H. Silva, L.C. Costa, F.R. Passador, R.L. Reis, L.A. Pessan, Engineering 3D printed bioactive composite scaffolds based on the combination of aliphatic polyester and calcium phosphates for bone tissue regeneration, Materials Science & Engineering C. 122 (2021) 111928. doi:10.1016/j.msec.2021.111928.

[52] P. Lei, H. Qian, T. Zhang, T. Lei, Y. Hu, C. Chen, K. Zhou, Porous tantalum structure integrated on Ti6Al4V base by Laser Powder Bed Fusion for enhanced bony-ingrowth implants: In vitro and in vivo validation, Bioactive Materials. 7 (2022) 3–13. doi:10.1016/j.bioactmat.2021.05.025.

[53] G. Peñarrieta-juanito, M. Cruz, M. Costa, G. Miranda, J. Marques, R. Magini, A. Mata, J.C.M. Souza, J. Caramês, F.S. Silva, A novel gradated zirconia implant material embedding bioactive ceramics: Osteoblast behavior and physicochemical assessment, Materialia. 1 (2018) 3–14. doi:10.1016/j.mtla.2018.07.002.

[54] V. Müller, S. Balvay, C. Gaillard, S. Tadier, L. Gremillard, E. Djurado, One-step fabrication of single-phase hydroxyapatite coatings on Ti-alloy implants by electrostatic spray deposition: From microstructural investigation to in vitro studies, Surface and Coatings Technology. 427 (2021) 127805. doi:10.1016/j.surfcoat.2021.127805.

[55] Y. Liu, G. Wang, Y. Cai, H. Ji, G. Zhou, X. Zhao, R. Tang, M. Zhang, In vitro effects of nanophase hydroxyapatite particles on proliferation and osteogenic differentiation of bone marrow-derived mesenchymal stem cells, Journal of Biomedical Materials Research - Part A. 90 (2009) 1083–1091. doi:10.1002/jbm.a.32192.

[56] Y. Nakagawa, T. Muneta, K. Tsuji, S. Ichinose, Y. Hakamatsuka, H. Koga, I. Sekiya, β-Tricalcium Phosphate Micron Particles Enhance Calcification of Human Mesenchymal Stem Cells in Vitro, Journal of Nanomaterials. 2013 (2013) 426786. doi:10.1155/2013/426786.

[57] L. Tiainen, P. Abreu, M. Buciumeanu, F. Silva, M. Gasik, R. Serna Guerrero, O. Carvalho, Novel laser surface texturing for improved primary stability of titanium implants, Journal of the Mechanical Behavior of Biomedical Materials. 98 (2019) 26–39. doi:10.1016/j.jmbbm.2019.04.052.

[58] S. Madeira, A. Barbosa, C.G. Moura, M. Buciumeanu, F.S. Silva, O. Carvalho, Aunps and Agμps-functionalized zirconia surfaces by hybrid laser technology for dental implants, Ceramics International. 46 (2020) 7109–7121. doi:10.1016/j.ceramint.2019.11.203.

[59] D. Faria, B. Henriques, A.C. Souza, F.S. Silva, O. Carvalho, Laser-assisted production of HAp-coated zirconia structured surfaces for biomedical applications, Journal of the Mechanical Behavior of Biomedical Materials. 112 (2020) 104049. doi:10.1016/j.jmbbm.2020.104049.

CHAPTER 10

CONCLUSIONS

This chapter presents the main conclusions that can be drawn from the work developed in this PhD thesis, as well as pointing suggestions for future work and finally listing further contributions to this PhD thesis.

10.1. General Conclusions

This PhD thesis was focused on multi-functional multi-material solutions for implants. Selective Laser Melting and Laser Surface Texturing were used to manufacture interconnected cubic-like metallic cellular structures and laser groove-textured implants, respectively. By using additional processing techniques and strategies, additional materials (Calcium phosphates or PEEK) were added to these Ti-based constructs. Their tribological and biological performance was assessed, keeping in mind their application.

As seen in Chapter 3, cubic-like SLM structures (fabricated using optimal processing parameters, as determined in previous studies) were impregnated with bioactive βTCP by two different strategies, allowing to obtain multi-material structures with two different bioactive percentages (1.58 and 2.98 wt.%). Mono- and multi-material structures were characterized *in vitro* and compared with commercially available dense Ti6Al4V. Roughness measurements revealed higher values found for commercial group, being statistical different from the remaining groups, whilst wettability results indicate that this group is the one with the most hydrophobic behavior. Conversely, SLM specimens displayed hydrophilic surfaces, which is preferable for protein adsorption at implant surface and further enhanced cell performance. *In vitro* results showed that all groups presented no cytotoxic effect to cells, although the addition of βTCP turns the media more alkaline, being the highest found for lower bioactive percentage. The higher contact area between the bioactive material and the medium, in this group, will lead to higher dissolution rate and in turn, higher pH. From this study, it can be concluded that the interconnected porosity allowed cells to grow not only onto but into the implant surface and, higher bioactive percentages are preferable for lowering the pH medium and, consequently, enhance cell adhesion and proliferation.

Using the previously selected procedure for impregnating βTCP (press and sintering), in chapter 3 (press and sintering), chapter 4 aims to evaluate the corrosion behavior of multi-material Ti6Al4V-βTCP cellular structures. Moreover, in this same study, another group of multi-material structures were produced by impregnating the open-cell sizes with polymer PEEK through hot pressing technique. All tested groups corrosion behavior (dense SLM, cellular SLM, Ti6Al4V-βTCP and Ti6Al4V-PEEK) revealed their ability to resist to localized corrosion. Nevertheless, the impregnation process of βTCP and PEEK influenced the corrosion behavior of these structures, since in βTCP group the non-fully impregnation increase the exposed area, leading to difficulties in

electrolyte penetration, whereas in PEEK group, although fully impregnated, the presence of some gaps may act as active zones and promote discontinuities on the passive film.

Following this multi-material bioactive characterization, chapter 5 aimed to assess the tribological response of bioactive materials impregnation (hydroxyapatite and βTCP) on Ti6Al4V cellular structures in a flat-on-flat reciprocating sliding test. Besides performing a typical tribological test for assessing the specimens weight loss, an initial test was performed to mimic the moment of implantation and therefore determined the final stability of the implant after its insertion. Results revealed that, comparing bioactive materials, the one that exhibited higher wear resistance, lower weight loss, was βTCP also having one of the highest static final coefficient of friction, among groups, which indicates that it is a good option for achieving an improved primary stability.

Chapter 6 introduces NiTi alloy, studying the tribological behavior of multi-material NiTi-PEEK cellular structures and compared it with mono-material groups, with differences in CAD design regarding open-cell sizes (500 and 600 µm) and wall thicknesses (100, 150 and 350 µm). The tests, performed in a ball-on-flat reciprocating sliding configuration, revealed that comparing the different porosities, it is observed that higher porosity structures (higher number of open cells on a given area) are collecting the wear debris, acting as containers, thus reducing third body effect and consequently reducing the specific wear rate (higher wear resistance). The addition of PEEK led to an increased wear resistance when compared with mono-material groups, as the specific wear rates were considerably lower.

In Chapter 7, NiTi implants were manufactured also by using a laser-assisted technique, namely laser surface texturing, to obtain NiTi textured implants, with two groove designs, that differ in terms of groove distance and, therefore, surface exposed area. The study aimed to evaluate the bone-implant fixation and osseointegration *in vivo* of the produced implants. For that purpose, these were implanted in Sprague Dawley rats' femur, for two different timepoints (4 and 12 weeks) and characterized in terms of push-out and histological experiments. Higher push-out forces were observed for the textured groups, right after 4 weeks of implantation, when compared with non-textured group, being the highest found for the group with higher exposed area. The bone was allowed to grow inside the grooves, with higher amount of biological tissue found adhered to the surface, thus proving an enhanced bone-implant fixation considerably, that is translated in better push-out results.

Similarly, in chapter 8, laser surface texturing technique was used to produce Ti6Al4V laser textured implants in which the grooves were further filled with bioactive βTCP to obtained multi-

material implants. These implants were also implanted *in vivo*, in rats' femur, and characterized with push-out and histological tests to understand implant-bone fixation and osseointegration as well as the effect of βTCP addition on these metrics, after 4 and 12 weeks of implantation. In this study, as shown in the previous study, laser textured implants had higher push-out force after 4 weeks of implantation, compared with non-textured implants. Although the grooves are filled with bioactive material, being the exposed area reduced, compared to textured implants, this outcome is also observed, suggesting the ability of the bioactive material to enhance the osteogenesis process. For the longer timepoint (12 weeks), multi-material implants were the ones that displayed the highest fracture energy, meaning that bone-implant fixation in these implants is stronger and higher energies are required to its fracture, with fracture occurring at the bone and not bone-implant interface, conversely to non-textured implants.

Lastly, on Chapter 9, by resorting to Selective Laser Melting and Powder Metallurgy techniques, mono- and multi-material were manufactured and NiTi, Ti6Al4V, βTCP- or PEEK-impregnated NiTi or Ti6Al4V structures were obtained. The main focus of this study was to evaluate the *in vitro* performance of these structures, under dynamic conditions, and assess their primary stability after implantation. Cytotoxicity experiments, cell adhesion, metabolic activity, differentiation and mineralization were assessed and bio-tribological experiments against bone performed to replicate as close to reality possible implant insertion and thus evaluate implant primary stability. *In vitro* results indicate that the mono-material cellular structures had an enhanced cellular response when compared with commercially available solutions and the addition of PEEK also had a positive effect regarding cell adhesion, metabolic activity, differentiation and mineralization. βTCP addition did not bring any beneficial effect to overall *in vitro* results, conversely to what is widely reported in literature, being higher crystallinity and amount of βTCP concerns that may be related to such results. Nevertheless, further works should be performed to better understand these results followed by *in vivo* studies to understand their performance under real physiologic conditions. Nevertheless, bone-implant tribological tests revealed that the proposed solutions did not compromise the final primary stability since comparable final coefficient of friction were found in all structures, when compared with commercial solution. This paper also introduces a whole new solution for implant purposes, characterized by bimetallic cellular structures, produced by SLM, that are further impregnated with bioactive and polymeric materials to create tri-material solutions aiming to fulfill the implants drawbacks currently reported. With these structures it is possible to tailor elastic modulus through interconnected porosity while benefit from

Ti6Al4V mechanical properties, NiTi SME/corrosion resistance, bioactivity from βTCP and PEEK corrosion and wear resistance to create therefore a multi-functional implant.

10.2. Suggestions for Future Works

According to the findings of this PhD thesis, some possibilities for future work that can complement this project arise, namely:

- Assess the corrosion behavior of mono-material NiTi structures and its multi-material variants (NiTi-βTCP and NiTi-PEEK) as well as bimetallic structures (Ti64-NiTi);

- Evaluate the biological response of NiTi or Ti64 cellular structures, where a bioactive thin-coating is applied on the outer and inner surfaces in order to provide an adequate media inside the open-cells, and simultaneously provide bioactivity for an enhanced osteoinduction while offering available space for the cells to proliferate and bone to grow inside these structures;

- Evaluate the shape memory effect of NiTi structures by defining suitable heat treatments that can allow to control and adapt the transformation temperatures to body requirements and, therefore, assure a desired bone-implant contact pressure, without compromising bone integrity;

- Perform *in vivo* experiments using cellular structured hip implants, preferably in large-size animal models;

- Design of multi-material implants with local specific properties.

10.3. Further Contributions to this thesis

In addition to the studies developed and described in this PhD thesis, further conference attendances and contributions in other studies were made throughout this thesis, namely:

10.3.1. Conferences

- **M.M. Costa**, F. Bartolomeu, B. Guimarães, N. Alves, G. Miranda, F.S. Silva. Mechanical and Tribological Characterization of NiTi Cellular Structures made by Selective Laser Melting, aiming Orthopedic Implants. 4th Doctoral Congress in Engineering, 27-28 june of 2021, Porto-Portugal (online).

Oral presentation

- **M.M. Costa**, A. Campos, O. Carvalho, F. Bartolomeu, F.S. Silva, G. Miranda. Ti-NiTi Multi-material Parts Fabrication By Laser Machining And Powder Metallurgy. 8th International Conference on Mechanics of Biomaterials and Tissues, 15-19 december 2019, Hawaii-United States

Oral presentation

- G. Miranda, **M. M. Costa**, F. Bartolomeu, F.S. Silva. Assessing the influence of laser parameters on the fabrication of thin-walled Ti6Al4V tubes manufactured by selective laser melting. 8th International Conference on Mechanics of Biomaterials and Tissues, 15-19 december 2019, Hawaii-United States of America

Poster presentation

- **M.M. Costa**, R. Lima, F. Melo-Fonseca, F. Bartolomeu, A. Miranda, N.A. Silva, F.S. Silva, G. Miranda. Ti6Al4V-Bioactive Cellular Structures: A Multi-Material Approach to Enhance Cellular Response. 8th Portuguese Congress of Biomechanics, 15-16 february 2019, Unhais da Serra-Portugal

Oral presentation

Award for best student oral presentation

- **M. M. Costa**, N. A. Silva, S. Almeida, R. Lima, F. Bartolomeu, A. Miranda, O. Carvalho, N. Alves, F. S. Silva, G. Miranda. βTCP-impregnated Ti6Al4V cellular structures: Methodology and In Vitro Bioactivity. 28th Annual Conference of the European Society of Biomaterials, 4-8 september 2017, Athens-Greece

Poster presentation

- **M. M. Costa**, F. Bartolomeu, N. Alves, O. Carvalho, F. S. Silva, G. Miranda. Bioactive impregnation on Ti6Al4V cellular structures produced by Selective Laser Melting. International conference on Powder Metallurgy & Particulate Materials (AMPM2017), 13-15 june 2017, Las Vegas-United States of America.

Oral presentation

10.3.2. Published Articles

- M.B. Da Cruz, J.F. Marques, G.M. Peñarrieta-Juanito, **M. M. Costa**, J.C.M. Souza, R.S. Magini, G. Miranda; F.S. Silva, J.M.M. Caramês, A.S.P. Da Mata. Bioactive-enhanced polyetheretherketone dental implant materials: Mechanical characterization and cellular responses. Journal of Oral Implantology, 2021, Volume 47, Issue 1, Pages 9 – 17. https://doi.org/10.1563/aaid-joi-D-19-00172

- F. Bartolomeu, **M.M. Costa**, N. Alves, G. Miranda, F.S. Silva. Selective Laser Melting of Ti6Al4V sub-millimetric cellular structures: Prediction of dimensional deviations and mechanical performance. Journal of the Mechanical Behavior of Biomedical Materials, 2021, Volume 113, 104123. https://doi.org/10.1016/j.jmbbm.2020.104123

- F. Bartolomeu, **M.M. Costa**, N. Alves, G. Miranda, F.S. Silva. Additive manufacturing of NiTi-Ti6Al4V multi-material cellular structures targeting orthopedic implants. Optics and Lasers in Engineering, 2020, Volume 134, 106208. https://doi.org/10.1016/j.optlaseng.2020.106208

- F. Bartolomeu, **M.M. Costa**, N. Alves, G. Miranda, F.S. Silva. Engineering the elastic modulus of NiTi cellular structures fabricated by selective laser melting. Journal of the Mechanical Behavior of Biomedical Materials, 2020, Volume 110, 103891. https://doi.org/10.1016/j.jmbbm.2020.103891

- M.B. da Cruz, J.F. Marques, B.F. Fernandes, **M.M. Costa**, G. Miranda, A.D.S.P. da Mata, J.M.M. Carames, F.S. Silva. Gingival fibroblasts behavior on bioactive zirconia and titanium dental implant surfaces produced by a functionally graded technique. Journal of Applied Oral Science, 2020, Volume 28, Pages 1 – 10. https://doi.org/10.1590/1678-7757-2020-0100

- F. Bartolomeu, C.S. Abreu, C.G. Moura, **M.M. Costa**, N. Alves, F.S. Silva, G. Miranda. Ti6Al4V-PEEK multi-material structures – design, fabrication and tribological characterization focused on orthopedic implants. Tribology International, 2019, Volume 131, Pages 672 – 678. https://doi.org/10.1016/j.triboint.2018.11.017

- M.B. da Cruz, J.F. Marques, G.M. Peñarrieta-Juanito, **M.M. Costa**, J.C.M. Souza, R.S. Magini, G. Miranda, F.S. Silva, A.D.S.P. da Mata, J.M.M. Caramês. Hard and Soft Tissue Cell Behavior on Polyetheretherketone, Zirconia, and Titanium Implant Materials. The International Journal of Oral & Maxillofacial Implants, 2019, Volume 34, Issue 1, Pages 39 – 46. 10.11607/jomi.6926.

- F. Bartolomeu, M. Buciumeanu, **M.M. Costa**, N. Alves, M. Gasik, F.S. Silva, G. Miranda. Multi-material Ti6Al4V & PEEK cellular structures produced by Selective Laser Melting and Hot Pressing: A tribocorrosion study targeting orthopedic applications. Journal of the Mechanical Behabior of Biomedical Materials, 2019, Volume 89, Pages 54 – 64. https://doi.org/10.1016/j.jmbbm.2018.09.009

-F. Bartolomeu, **M.M. Costa**, J.R. Gomes, N. Alves, C.S. Abreu, F.S. Silva, G. Miranda. Implant surface design for improved implant stability – A study on Ti6Al4V dense and cellular structures produced by Selective Laser Melting. Tribology International, 2019, Volume 129, Pages 272 – 282. https://doi.org/10.1016/j.triboint.2018.08.012

- G. Miranda, F. Sousa, **M.M. Costa**, F. Bartolomeu, F.S. Silva, O. Carvalho. Surface design using laser technology for Ti6Al4V-hydroxyapatite implants. Optics and Laser Technology, 2019, Volume 109, Pages 488 – 495. https://doi.org/10.1016/j.optlastec.2018.08.034

- F. Melo-Fonseca, R. Lima, **M.M. Costa**, F. Bartolomeu, N. Alves, A. Miranda, M. Gasik, F.S. Silva, N.A. Silva, G. Miranda. 45S5 BAG-Ti6Al4V structures: The influence of the design on some of the physical and chemical interactions that drive cellular response. Materials and Design, 2018, Volume 160, Pages 95 – 10515. https://doi.org/10.1016/j.matdes.2018.08.056

- G. Peñarrieta-Juanito, M. Cruz, **M.M. Costa**, G. Miranda, J. Marques, R. Magini, A. Mata, J.C.M. Souza, J. Caramês, F.S. Silva. A novel gradated zirconia implant material embedding bioactive ceramics: Osteoblast behavior and physicochemical assessment. Materialia, 2018, Volume 1, Pages 3 – 14. https://doi.org/10.1016/j.mtla.2018.07.002